INVESTIGATION OF OPPOSED FLOW FLAME SPREAD OVER SOLID FUELS

By

Sarzina Hossain

A DISSERTATION

Submitted to
Michigan State University
in partial fulfillment of the requirements
for the degree of

Mechanical Engineering – Doctor of Philosophy

2021

ABSTRACT

INVESTIGATION OF OPPOSED FLOW FLAME SPREAD OVER SOLID FUELS

By

Sarzina Hossain

The opposed flow flame spread over flat solid fuels is of fundamental importance to the field of fire safety. Several features of opposed flow flame spread are experimentally, numerically and analytically investigated. Thermally thick slab of PolyMethylMethAcrylate (PMMA) was used to study the effects of opposed flow velocity (8-58 cm/s) and fuel thickness (6.6, 12.1 and 24.5 mm). The experiments were conducted with a Narrow Channel Apparatus (NCA) at Michigan State University (MSU). The flame spread rate results show that the maximum flame spread occurs at a lower flow velocity for relatively thicker fuel. The peak flame spread rate for 6.6 mm, 12.1 mm and 24.5 mm occurs at 18.5 cm/s, 12.1 cm/s and 10.3 cm/s, respectively. Several flame spread regimes: thermal, chemical and regressive burning are identified from the results. Flame spread regimes are usually depend on the opposed flow velocity. However, the flame spread rate for newly found regressive burning regime is independent of flow velocities. Visual observation of the flame indicates that the flame intensity augments with flow velocity for all thicknesses of PMMA. The comparison between NCA data and legacy data for similar material (PMMA) and thickness (12.1 mm) demonstrated excellent agreement, subject to the extension of the numerical and theoretical analysis to include relevant features of the flame spread stretch rate theory. The results also demonstrated the effectiveness of the stretch rate theory for markedly different experimental configurations. Although thick slab is used to perform tests, complete burn out of the samples for thickness 6.6 and 12.1 mm are observed at high opposed flow velocities (30±5 cm/s and higher). On contrary, the thickest sample (24.5 mm) did not go through complete burning. This indicates the nature of surface regression and its impact on flame spread rate.

Based on the results, it can be emphasized that the factors controlling the flame front advancement involves both flame spread and surface regression. So, the burnt samples at different opposed flow velocities of 24.5 mm thickness from flame spread study is measured for surface regression depth experimentally. A semi-empirical correlation is developed to relate the flame spread and regression and to determine the mass loss rate from the burnt fuel surface. Mass loss rate is also a key aspect of characterizing the flammability of materials. Results show that the power law dependency of mass loss rate changes with opposed flow velocity. A comparison of power law exponents of current results and results from literature are made. Results demonstrate that the power law dependency at flow velocity 8.2, 10.3 and 12 cm/s is -0.5 which show excellent agreement with legacy work.

Next, another study is conducted on the post-flame-spread 24.5 mm PMMA sample, burnt at opposed flow velocity 15 cm/s. Visual observation of post-burn sample shows the formation of significant number of internal bubbles. Three samples of similar thickness burnt at similar condition were investigated for bubble count and size. Results indicate higher and smaller bubble presence near the leading edge of the flame compared to the trailing edge side. Comparison of bubble size distribution with several distribution function demonstrates that the bubble size shows good agreement with Log-normal distribution function.

Finally, the transient regression rate has been investigated analytically and numerically. The effect of external heat flux simulating flame heat flux is analyzed for PMMA considering it as an ideal-vaporizing solid. Results indicate a strong dependency of heat flux on material regression for a time duration. After a certain time period, the regression rate became insensitive to heat flux change. A scale analysis is performed to compare the analytical-numerical regression rate results with experimental surface regression depth. The predicted regression followed a similar pattern as the experimental surface regression.

This thesis is dedicated to Arif, whose love, support and positive energy have made this journey through graduate school possible. Thank you for always believing in me

ACKNOWLEDGEMENTS

First and foremost, I must thank the individual who introduced me to fundamental fire and combustion research, my advisor Professor Indrek S. Wichman. It is very rare to find someone of profound influence that has such a positive impact on our life. Dr. Wichman's deep afinity and knowledge for science inspire me to become a hard-working person. His guidance and enthusiasm has helped me to learn various aspects of combustion research. There has never been a moment throughout my graduate studies where he has not been there for me. His open door policy and ability to see into the depths of a scientific problem has made my graduate life a pleasure. I hope to continue pursuing this learning and values throughout the rest of my life.

I would like to thank Dr. Giles Brereton, Dr. Elisa Toulson and Dr. Mohsen Zayernouri to serve as the committee members . Their time and support are very appreciated.

I want to express my sincere gratitude to Dr. Sandra L. Olson from NASA and Dr. Fletcher Miller from San Diego State University (SDSU) for their valuable advice and help on my research. The close collaboration with NASA and SDSU was a life-time opportunity for me. I am grateful that I was able to share my ideas, present my work and got valuable feedback from them.

Undergraduate students Sam and Adi at MSU had occassionally helped me to conduct experiments. Students from SDSU, Nick Lage and Peter Spang also provided some logistic support. I would like to take this opportunity to thank them for their time and support.

Lastly, the never ending support from all of my friends and family. My father and mother always instilled the importance of education from a very young age. They have always supported me in each and every aspect of life. I am truly grateful for their sacrifices.

TABLE OF CONTENTS

LIST OF TABLES

LIST OF FIGURES

KEY TO SYMBOLS

a	Stretch rate, $[1/T]$
a_b	Buoyant stretch rate, $[1/T]$
a_f	Forced stretch rate, $[1/T]$
B_0, B_n	Fourier constants
c_f, c_g, c_q	Proportionality constants
c_p	Specific heat, $[L^2/T^2\theta]$
D_{O_2}	Oxygen diffusivity, $[L^2/T]$
d_{avg}	Average bubble diameter, $[L]$
E	Scaling parameter
$(F/A)_{mass,stoi}$	Stoichiometric fuel to air mass ratio
F	Fourier number
Gr	Grashof number
g	Gravity, $[L/T^2] = 9.81 m^2/s$
h	NCA gap height, $[L]$
$h(\tau)$	Dimensionless regression
$h(t)$	Solid-vapor interface position, $[L]$
h_b	Bubble layer depth in each segment, $[L]$
h_c	Heat transfer coefficient, $[M/T^3\theta]$
k	Thermal conductivity, $[ML/T^3\theta]$
k_g	Gas Conductivity, $[ML/T^3\theta]$
k_s	Solid Conductivity, $[ML/T^3\theta]$
L	Arbitary length, $[L]$
L_s	Preheat length, $[L]$
Le	Lewis number
Le_{eff}	Effective Lewis number

l_b	Length of the ROI of a segment, $[L]$
l_f	Length of heat source, $[L]$
$\dot{m}_i''$	Mass flux in, $[M/L^2T]$
$\dot{m}_o''$	Mass loss rate, $[M/L^2T]$
$\dot{m}$	Mass feed rate, $[M/T]$
$\dot{m}_f$	Mass feed rate of fuel, $[M/T]$
$\dot{m}_g$	Mass feed rate of gas, $[M/T]$
$\dot{m}_{ox}$	Consumed mass feed rate of oxygen, $[M/T]$
$\overline{\dot{m}_o''}$	Total mass loss rate, $[M/L^2T]$
N	Number of bubbles
$\overline{Nu}_{l_f}$	Nusselt number based on length l_f
Pe_h	Peclet number for channel flow
Q''	Dimensionless heat flux
$\dot{q}_{cond,s}''$	Heat flux conduction into solid phase, $[M/T^3]$
$\dot{q}_{f+g}''$	Heat flux from flame and hot gases, $[M/T^3]$
$\dot{Q}_P$	Product gas enthalpy rise rate, $[ML^2/T^3]$
$\dot{Q}_{conv}$	Convection heat loss rate, $[ML^2/T^3]$
$\dot{Q}_{flame}$	Total flame heat release rate, $[ML^2/T^3]$
$\dot{Q}_f$	Solid fuel enthalpy rise rate, $[ML^2/T^3]$
$\dot{Q}_g$	Gas enthalpy rise rate, $[ML^2/T^3]$
$\dot{Q}_{in}$	Heat input rate into the control volume, $[ML^2/T^3]$
$\dot{Q}_{loss}$	Total heat loss, $[ML^2/T^3]$
$\dot{Q}_{out}$	Heat rate out of the control volume, $[ML^2/T^3]$
$\dot{Q}_{rad}$	Radiative heat loss rate, $[ML^2/T^3]$
$\widehat{Q}_{loss}$	Dimensionless heat loss
q''	Imposed heat flux, $[M/T^3]$

Re_{l_f}	Reynolds number based on length l_f
$r(t)$	Regression rate, $[L/T]$
s	Flame standoff distance, $[L]$
$T_0(y)$	Temperature profile at the time t_v, $[\theta]$
T_F	Flame temperature, $[\theta]$
T_∞	Surrounding temperature, $[\theta]$
T_s	Surface temperature, $[\theta]$
T_v	Vaporization temperature, $[\theta]$
T_∞	Initial temperature, $[\theta]$
T_{in}	Inlet temperature, $[\theta]$
T_{out}	Outlet temperature, $[\theta]$
$\overline{T}$	Heated segment temperature, $[\theta]$
t_b	Maximum depth of the bubble layer, $[L]$
t_f	Fuel thickness, $[L]$
t_v	Time to attain vaporization temperature, $[T]$
U	Oxidizer velocity, $[L/T]$
U_b	Buoyant velocity, $[L/T]$
U_g	Unburned gas velocity, $[L/T]$
$u(\eta,\tau)$	Dimensionless temperature
$u(y)$	Parabolic velocity distribution
V_f	Flame spread rate, $[L/T]$
V_b	Total bubble volume, $[L^3]$
$V_{cylinder}$	Total volume of equivalent-cylinder bubble, $[L^3]$
$V_{f,max}$	Maximum flame spread rate, $[L/T]$
V_{sphere}	Total volume of equivalent-sphere bubble, $[L^3]$
$\overline{V}_g$	Opposed flow velocity, $[L/T]$
$\widehat{V}_g$	Dimensionless opposed flow velocity

$v(\eta, \tau)$	Arbitrary temperature function
$V_{g,diff}$	Diffusion velocity for oxygen, $[L/T]$
V_r	Relative velocity, $[L/T]$
w	Fuel width, $[L]$
$w(\eta, \tau)$	Arbitrary temperature function
w_b	Width of the ROI of a segment, $[L]$
Y_{ox}	Mass fraction for oxygen
$y = f(x)$	Curved regressing surface function
$\mathcal{L}_v$	Enathalpy per unit mass, $[L/T^2] = 1.6x10^6\ J/kg$

Greek Symbols

α	Thermal diffusivity, $[L^2/T]$
α_{eff}	Effective thermal diffusivity, $[L^2/T]$
α_f	Fuel thermal diffusivity, $[L^2/T]$
α_g	Gas thermal diffusivity, $[L^2/T]$
β	Coefficient of thermal expansion, $[1/\theta]$
Δs	Curved surface incremental area, $[L]$
δ	Thermal tickness, $[L]$
δ_g	Gas preheat length scale, $[L]$
δ_o	Stoichiometric oxygen distance, $[L]$
δ_q	Quenching distance, $[L]$
δ_s	Solid preheat length scale, $[L]$
δ_w	Characteristic dimension along the width of the sample, $[L]$
ϵ	Emissivity
η	Dimensionless length
ν	Kinematic viscosity, $[L^2/T]$
ϕ	Overall equivalence ratio
ψ	Percentage of total bubble volume in each segment

ρ	Density, $[M/L^3]$
ρ_f	Fuel density, $[M/L^3]$
ρ_g	Gas density, $[M/L^3]$
ρ_s	Density of PMMA, $[M/L^3] = 1190\ kg/m^3$
τ	Dimensionless time
τ_v	Dimensionless vaporization time
$\widehat{\delta}_o$	Dimensionless stoichiometric oxygen distance
ξ	Transformed coordinate to immobilize the moving boundary

CHAPTER 1

INTRODUCTION

1.1 Significance of Fire Studies

Combustion is a branch of research that has a great importance both in academe and in practice. The wide applications of combustion occur especially in the energy sector, the automobile industry, cooking and heating (domestic), which make it a blessing. But uncontrolled fire terrifies people: the growing concern of residential, non-residential and wild forest fires and harmful pollution, makes combustion a threat. According to the U.S. Fire Adminstration (USFA), there were 1,318,500 incidents of fires in 2018 [1]. These incidents caused 15,200 injuries and 3,655 deaths. Beyond injuries and deaths, the total cost for the damages was approximately 25.6 billion.

Fire also possess a great risk for spacecraft and can cause huge damage in the international space station (ISS). In this respect, progress in fire safety research is a worthy endeavor. There have been several accidents in spacecraft due to on board fire. On Apollo 1, in 1967 [2] during the launch pad test, a cabin fire broke out and caused severe damage to the vehicle (Figure 1.1 (a)), and three astronauts lost their lives. In 1970, one oxygen tank exploded and damaged all the oxygen supplies, the water and the electrical power systems (Figure 1.1 (b)) on the Apollo 13 mission [3]. In addition, a major fire incident occurred on the Mir Russian Space Station on February 24, 1997 [4]. An oxygen canister ignited and generated poisonous smoke (Figure 1.1 (c)) which threatened the lives of the crew members.

Although much research has been done in regards to fire safety pertinent to earth and space applications, there are still many aspects and features that are not fully understood or explored. A better understanding of the combustion behavior and fire phenomena could provide a guideline for the spacecraft designer to control and possibly prevent some of the devastating accidents discussed above.

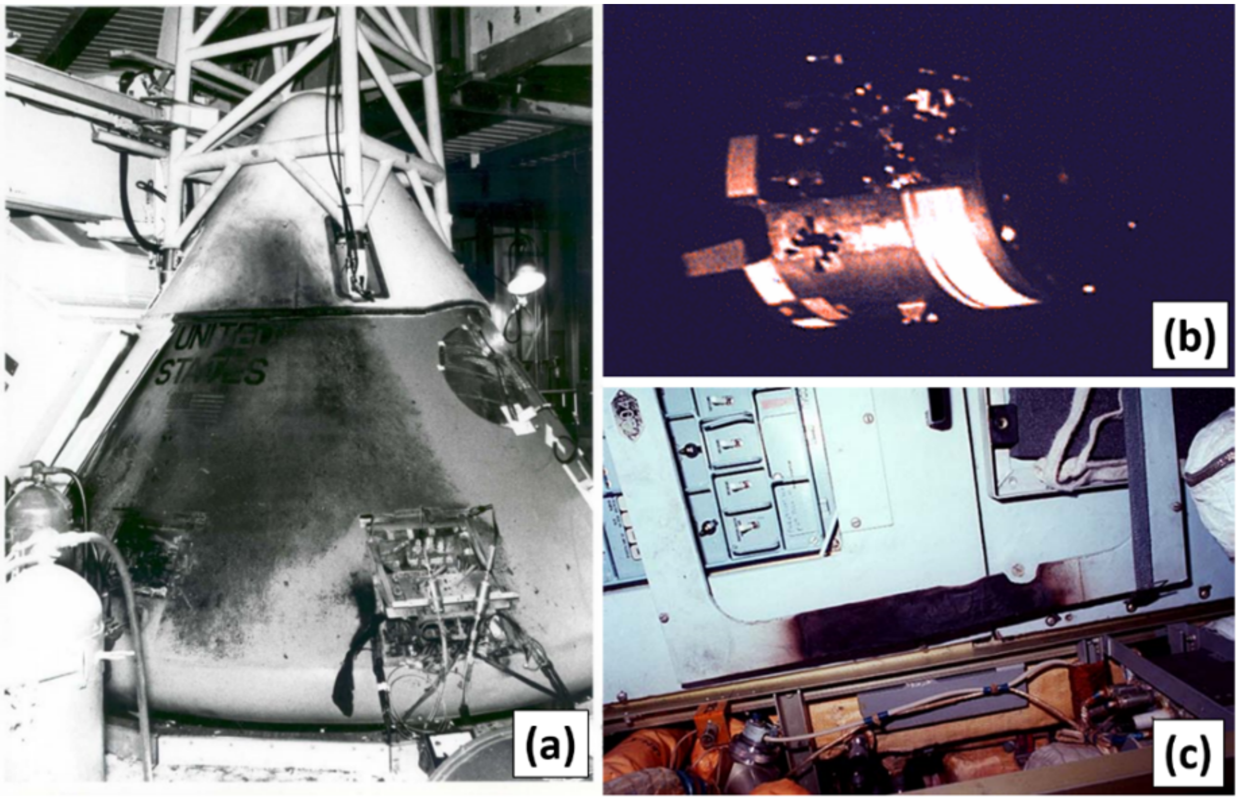

Figure 1.1: (a) Apollo 1 spacecraft after the fire (b) Apollo 13 after accident (c) Mir Russian Space Station oxygen canister

1.2 Diffusion Flames

When a flammable substance undergoes combustion, a flame is produced. Flames are generally classified as premixed and non-premixed flames. If the fuel and oxidizer are mixed prior to ignition it is known as premixed flame. Non premixed flames are widely known as diffusion flames. In a diffusion flame, combustion takes place at the flame surface only, at a front where the fuel meets oxidizer. The oxidizer and fuel diffuse toward each other slowly in a diffusion flame. Heat diffuses from the reaction zone to the fuel and oxygen sides and chemical reactions occur as soon as the fuel and oxidizer touch each other. The burning process generates products that includes soot particles. The formation of soot particles may be higher in this case because often there is not enough oxidizer to react with the fuel. The most common example is the candle flame (Figure 1.2 (a)). During a typical combustion process such as a candle flame on earth, the flow is induced by the buoyancy. The chemical heat release by the flame increases the local gas temperature and creates a density gradient. The buoyant force pushes the low density hot gas upward and entrains fresh air into the reaction zone to sustain combustion.

However, a diffusion flame has a completely different appearance in space. In the absence of gravity and buoyancy, the hot combustion products stay at the fuel surface which results in a spherical shape flame (Figure 1.2 (b)). In other words, the heated gases are not swept upward by a buoyancy-induced gas flow. The result is a blue flame, which indicates lessened soot formation. Typically the diffusion flames in microgravity are laminar unless there is some type of forcing or if the flames are large.

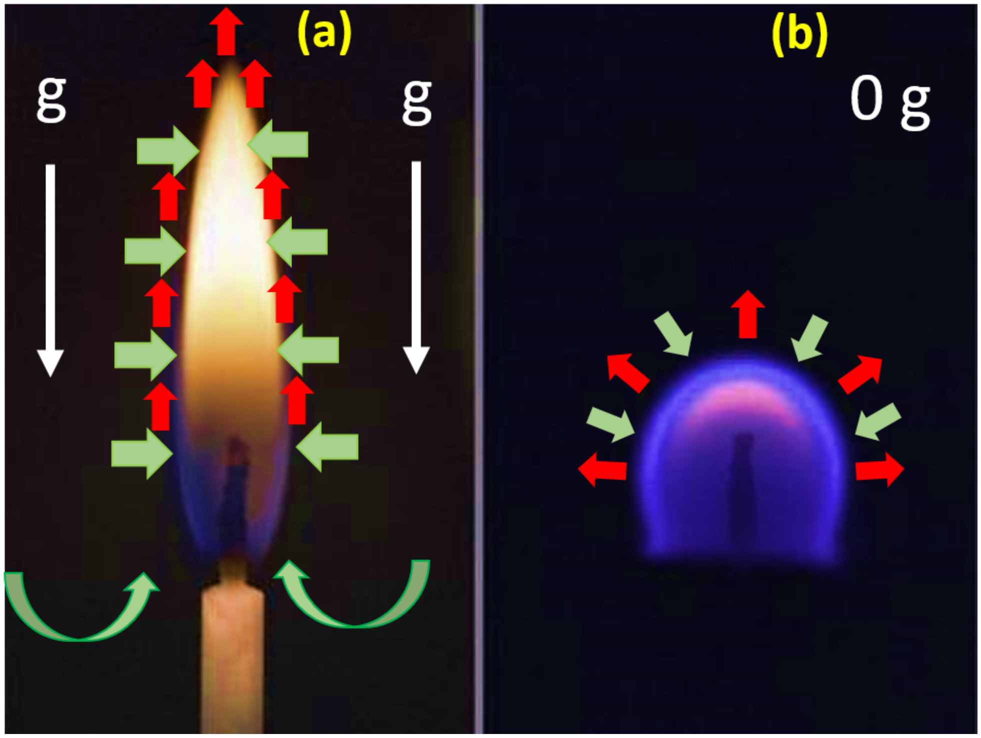

Figure 1.2: An example of a diffusion flame. A candle is lighted (a) on Earth (b) in microgravity. In (a), hot products rise (red arrows) due to buoyancy and draw fresh cool air (green arrows) behind it to form the characteristic of tear-drop shape. In (b), in the absence of buoyancy the hot products do not rise, rather they diffuse outward from the surface and the flame consequently becomes spherical. (Image courtesy of NASA https://www.nasa.gov/sites/default/files/images/586089main_me-candleFlame_full.jpg)

1.3 Opposed Flow Flame Spread

Solid fuel combustion involves many intricate processes that are coupled with each other. Due to the importance of fire safety, flame spread over solid fuels has been a topic of extensive theoretical, computational and experimental studies. The heat generated by the flame initiates the solid fuel pyrolysis and produces flammable volatile gases. The volatile fuel vapor and the surrounding oxidizer create a combustible mixture and feed the flame. The feeding of oxidizer to sustain flame spreading can be achieved in two ways. Some studies were focused on the utilization of surrounding quiescent air as the oxidizer whereas other studies used a forced flow into the system.

Generally, flame spread means the rate of flame movement across a fuel surface. The flame spread mechanism can be classified into two general categories: concurrent flow flame spread and opposed flow flame spread. When the flame advancement is in the same direction as the oxidizer flow it is known as concurrent flow flame spread. In an opposed flow, the direction of flame spread is opposite to the direction of the oxidizer flow.

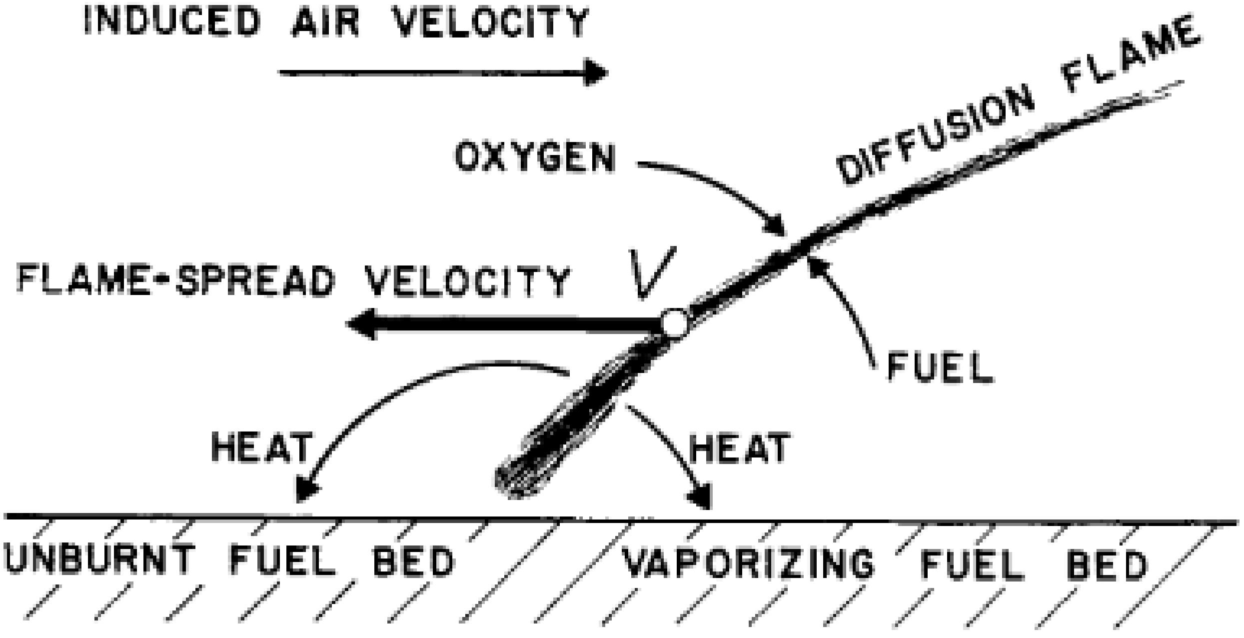

Figure 1.3: Physical description of opposed flow flame spread over a stationary fuel bed.

Opposed flow flame spread over solid fuels is a fundamental area of combustion research. One of the first academic studies of opposed flow flame spread was by deRis [5]. He assumed a fuel bed with an infinite reaction rate for the gas phase reaction and also assumed that the incoming flow was a uniform slug or "Oseen" flow (Figure 1.3). The conclusion of this work was that the flame spread rate is proportional to uniform flow velocity, and groups of thermophysical parameters, and an enthalpy ratio.

Based on deRis's assumption, Williams [6], described that the fire spread phenomena in solids, liquids, and smoldering through porous media in terms of a propagating front. Fernandez-Pello et al. [7] studied the effect of opposed flow velocity for thin and thick fuels. They proposed the Damkohler number, Da, to assess the relative importance of opposed flow velocity and finite-rate gas phase kinetics. Wichman and Williams [8] simplified deRis's model by clarifying the processes that control the flame spread mechanism for which conductive-convective heat transfer are significant and finite rate chemistry is negligible. Later on in 1983, Wichman [9] included finite-rate chemistry in a model and formulated flame spread over solid fuels without flame-sheet approximations. The significance of the velocity gradient also known as the stretch rate, on flame spread rate was one of the important findings of these studies [9, 10]. An review of flame-spread can be found in [11].

1.4 Material Thickness

In engineering, the temperature gradient can be ignored within a thermally thin body (Figure 1.4 left). For thermally thick bodies, the temperature variation throughout the body cannot be ignored (Figure 1.4 right). The flame spread mechanism in an opposed flow is a complex process controlled by the interaction between the solid and gas phases. The opposed flow flame spread process depends importantly on the thickness of the solid fuel. For thermally thin fuels, the front and rear surface temperatures are nearly identical during burning. In this case, if the gas phase chemical kinetics are infinitely fast and the solid decomposition mechanism is simplified [5] a robust and accurate flame spread formula can be derived [11]. Flame spread is generally more complicated to describe for thermally thick materials. Heat transfer equations for time varying transient heat

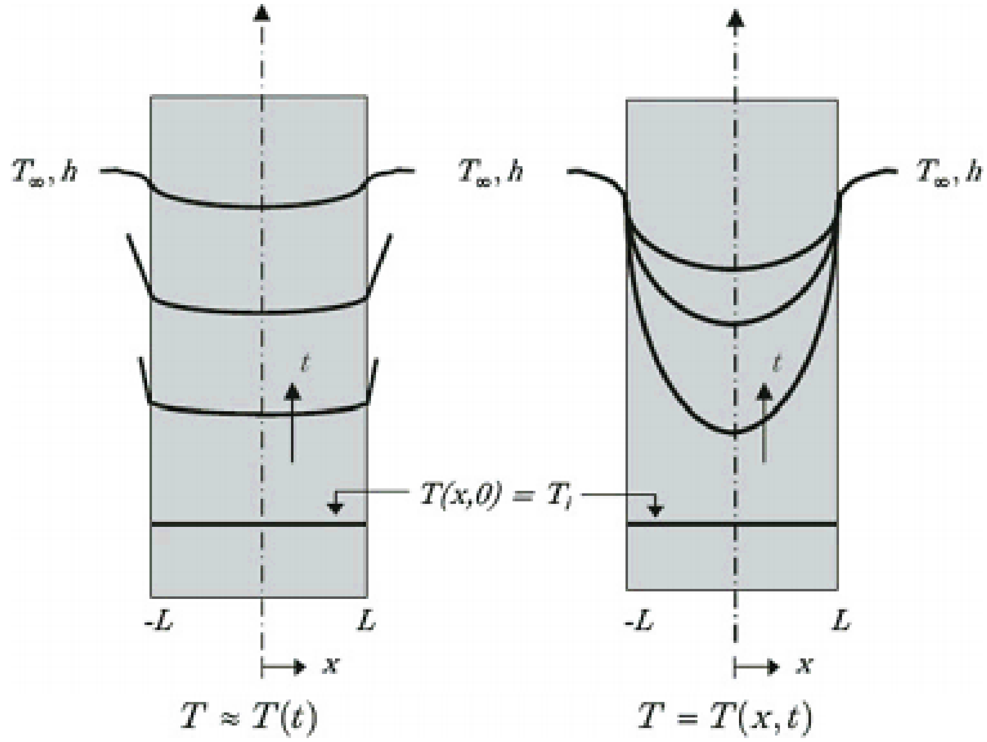

Figure 1.4: Transient temperature distributions for thermally thin and thick bodies. [12]

conduction and the non-spatially uniform temperature field within the material volume are required. For thermally thick fuels, solid decomposition is often dominant and it is not possible to ignore finite-rate condensed-phase chemistry.

In his PhD thesis, deRis first made a theoretically based distinction between opposed flow flame spread over thin and thick fuels. The nondimensional flame spread rate formulation for thin fuels provided by deRis [5] is the following;

$$\overline{V} = \frac{\rho_s c_s L V (T_v - T_a)}{2^{1/2} k_g (T_f - T_v)}, \tag{1.1}$$

and for thermally thick fuels,

$$\overline{V} = \frac{\rho_s c_s k_s V (T_v - T_a)^2}{\rho_g c_p k_g U_m (T_f - T_v)^2}, \tag{1.2}$$

where, ρ_s is the solid phase density, c_s is the solid phase specific heat, k_s is the solid phase thermal conductivity, ρ_g is the gas phase density, c_g is the gas phase specific heat, k_g is the gas phase thermal conductivity, L is the fuel thickness (applicable only for thin fuels), $\overline{V}$ is the flame spread rate, T_v is the vaporization temperature, T_a is the ambient temperature, and T_f is the flame temperature.

An improved analytical flame spread model was developed for thin fuels where the details of solid decomposition were ignored and the gas was assumed to flow toward the flame front in an opposed slug flow [8]. As discussed in the last section, the flame spread rate for thin fuels does not depend on the incoming opposed flow, rather it depends on the velocity distribution of the flow field more importantly the velocity gradient or stretch rate [9, 11, 13].

For a cylindrical geometry, Delichatsios [14] provided an analytical expression for the flame spread rate over a thermally thin rod:

$$V_f = 2c\left(\frac{L_g}{r}\right)\left(\frac{1}{ln(1+\frac{cL_g}{r})}\right)\left(\frac{k_g}{\rho_s c_s r}\right)\left(\frac{T_f - T_p}{T_p - T_\infty}\right). \tag{1.3}$$

For the thermally thick rod

$$V_f = c\left(\frac{L_g}{r}\right)\left(\frac{1}{ln(1+\frac{cL_g}{r})}\right)\left(1-\frac{k_s(T_p - T_\infty)}{\rho_g c_g U_\infty 2r(T_f - T_p)}\right)^{-1}\left(\frac{k_g \rho_g c_g}{k_s \rho_s c_s}\right)\left(\frac{T_f - T_p}{T_p - T_\infty}\right)^2 U_\infty, \tag{1.4}$$

where, V_f is the flame spread rate, U_∞ is the opposed air flow, ρ_s, k_s and c_s are the solid density, thermal conductivity and specific heat, ρ_g, k_g and c_g are the gas density, thermal conductivity and specific heat, T_f, T_p and T_∞ represent the flame, pyrolysis and ambient temperature, L_g is the diffusion length, r is the rod radius and c is a constant.

1.5 Flammability

Generally, flammability refers to the propensity of a substance to ignite easily and burn rapidly, and it is one indicator of the fire hazard. It is not an intrinsic property since it is dependent on the fire conditions. Widely used polymers are inexpensive and tend to be among the most flammable materials.

In solid fuel combustion research, flame spread rate and mass burning/loss rate (fuel regression) are considered as key parameters in evaluating material flammability. They dictate the ability of a material to influence fire growth. The flame spread rate can be affected by external environmental conditions, e.g., flow velocity, pressure, oxygen concentrations and gravity level. The mass loss rate is characterized by the amount of vapor fuel leaving the surface per unit time per unit area. It determines the regression of the solid fuel and affects the flame length. As the sample surface regresses, the gaseous products leave the surface while the local regression rate depends on the local heat feedback rate. Generally, the advancement of a flame front over a solid sample involves both lateral flame spread and transverse fuel surface regression.

1.6 Fire Hazards of Polymers

Polymeric materials have become increasingly popular for different usages. Polymers are chemically formed by combining together a number of monomers. Carbon is the main element but hydrogen, nitrogen, chlorine and oxygen are also used for forming polymers. Polymeric materials are classified into three general categories: thermoplastics, thermosets and elastomers. For the purpose of fire research thermoplastics are of much more interest than thermosets and elastomers. Common examples of thermoplastics are Nylon, PolyEthylene (PE), PolyCarbonate (PC) and PolyMethylMethAcrylate (PMMA). Based on the phase of decomposition, polymers can be generalized as charring and non-charring materials. Generally, cellulosic fuels produce char during burning. Polycarbonate and PMMA are examples of non-charring materials, which produce almost no char during combustion. The fire propagation behavior for charring and non-charring materials is different. Many experiments and numerical simulations of flame spread over solid fuels have been done for paper or other cellulosic fuels, charring materials, and PMMA, a non-charring material. Since fire is an important practical problem, it is crucial to understand and quantify the behavior of polymeric materials in a fire environment to meet and possibly satisfy engineering fire safety requirements.

1.7 Flame Spread Studies in Microgravity

The National Aeronautics and Space Administration (NASA) has limited options to test materials for fire safety in microgravity. The first option is to conduct tests in true microgravity on

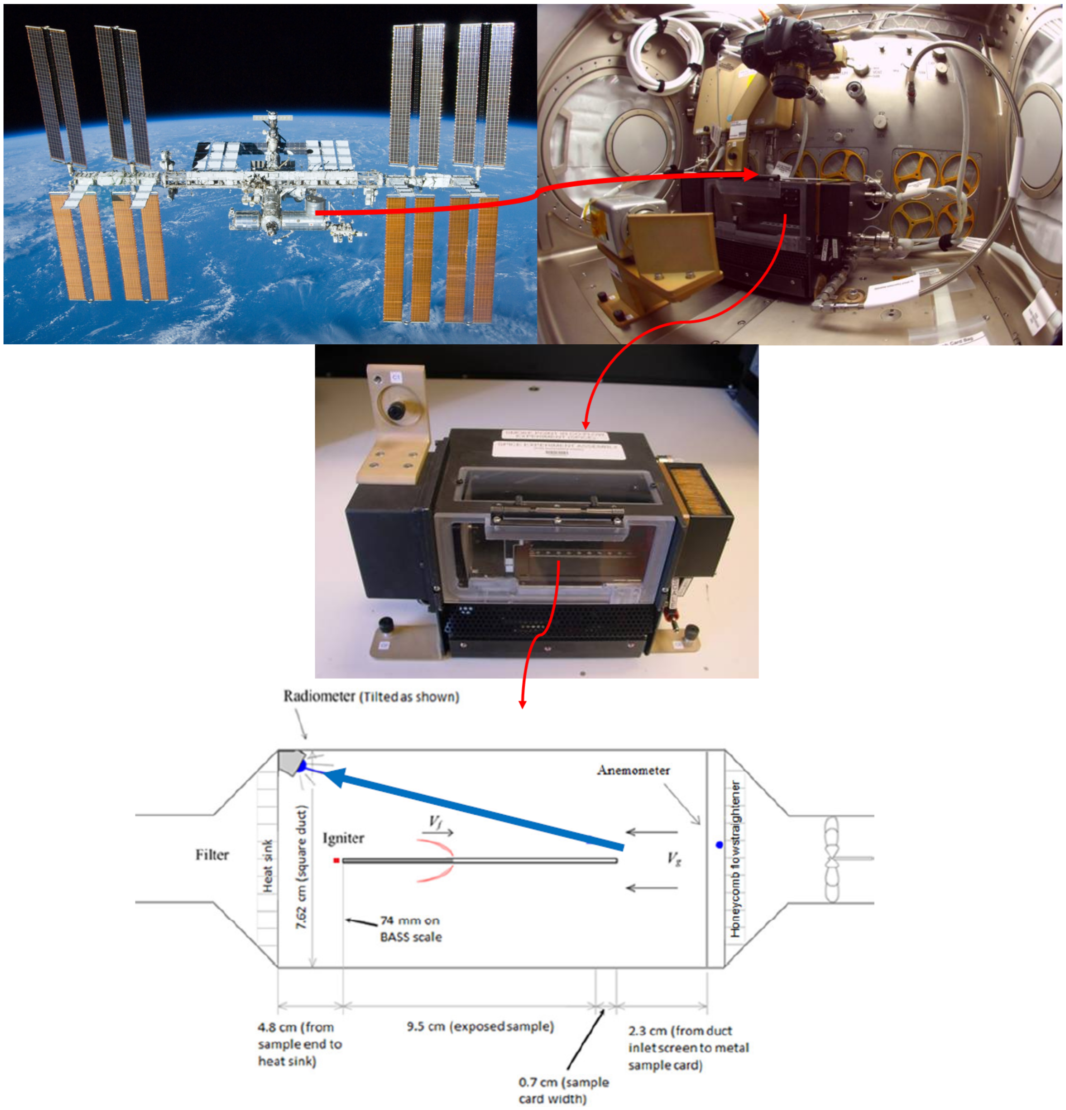

Figure 1.5: Microgravity Science Glovebox (MSG) Facility located in the International Space Station (ISS) shown is the Burning and Suppression of Solids-II (BASS-II) hardware inside the MSG. The schematic of BASS-II shows that flow enters from the right side followed by a honeycomb. Diagnostics include an anemometer for recording the velocity, and a radiometer for the radiation heat flux from the flame. The BASS-II setup can accommodate different fuel shapes (plates, spheres, rods) and different materials (PMMA, other thermoplastics)

the International Space Station (ISS). Several studies [15–18] have been conducted by NASA in actual microgravity in the ISS using the microgravity science glovebox. Such true microgravity tests include projects such as the Burning and Suppression of Solids-II (BASS-II) experiments. Figure 1.5 shows the BASS-II setup, which provides a contained atmosphere on the ISS to conduct fire related experiments.

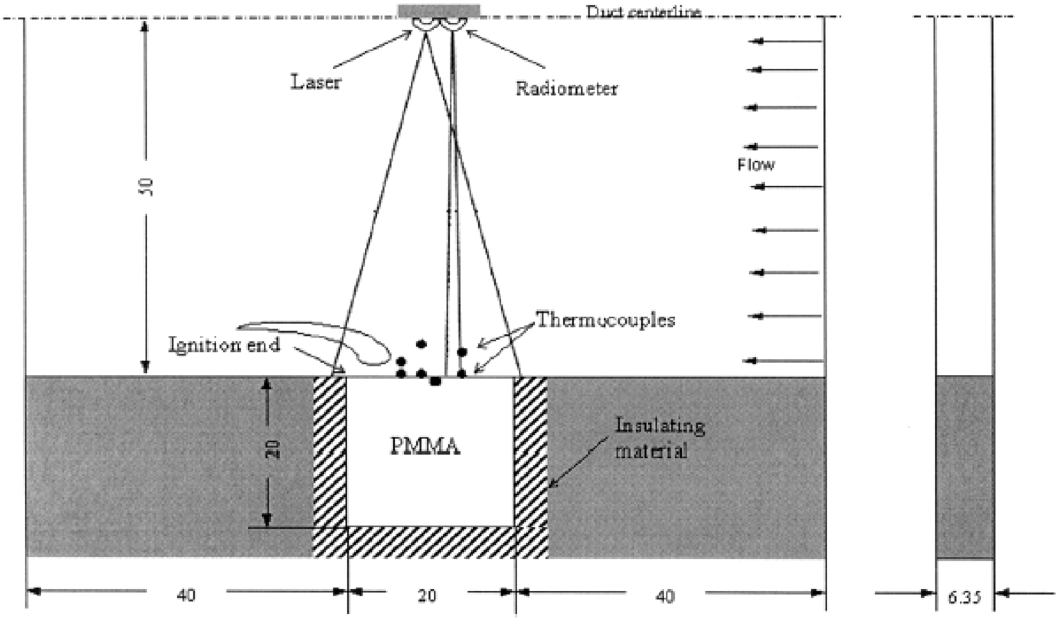

Figure 1.6: Schematic of the DARTFire two mirror image flow tunnel. The samples are placed near the center of gravity of the sounding rocket.

However, it is very expensive to conduct ISS tests. Astronaut time, the cost of transporting apparatus and most importantly ensuring sufficient oxidizer availability are all major hurdles. Another option is to conduct experiments inside a free-falling rocket. This types of experiments were performed under the Diffusive and Radiative Transport in Fires (DARTFire) [19] project. A schematic of the DARTFire setup is shown in Figure 1.6. This setup has two mirror-image flow tunnels of 15 cm long by 10 cm wide by 10 cm height. The thick black PMMA samples were 20 mm long x 20 mm thick x 6.35 mm wide, burnt at flow velocities 5, 10, 15 and 20 cm/s. They studied the effects of low velocity flow, oxidizer concentration, and weak external radiative heat flux on spreading flames over thick PMMA.

One of the available ground based research facilities is NASA's Zero Gravity Research Facility (ZGRF) [20], which can simulate microgravity on earth. Figure 1.7 shows the ZGRF release mechanism, positioned on the vacumm chamber by a crane. The chamber volume is approximately 16600 m^3. The drop tower facility provides a microgravity environment for approximately five seconds. Microgravity flame spread was examined for example in the project called the Analysis of Thermo-diffusive and Hydrodynamic Instabilities in near extinction Atmospheres (ATHINA) [21].

Figure 1.7: Photograph of the Zero Gravity Research Facility (ZGRF) at the NASA Glenn Research Center.

The experiments in the drop tower though expensive, are cheaper than conducting tests in orbit. However, the testing time span is very limited. This limits the microgravity testing to quick burns of thin fuels. It does not allow conducting experiments with thick materials that require a long time to reach a condition of steady flame spread.

Another well-known reduced gravity test facility is the ‘vomit comet’ where the aircraft travels on a parabolic path and during the fall provides about 25 seconds of microgravity [22]. Although this aircraft provides a slightly higher test time span than the drop tower, it is still not sufficient for higher thickness materials.

1.8 Narrow Channel Apparatus (NCA)

It is quite clear that the major challenges associated with the study of microgravity flame spread in the space station are high cost, the required long burning time and, the unavailability of unlimited oxidizer. In addition, the existing ground-based alternatives (drop tower and reduced gravity aircraft) are not effective due to their short testing time. In order to achieve longer burn times, a ground-based testing facility was developed at NASA as an alternative to actual microgravity tests. For spacecraft applications, material flammability is currently evaluated using the NASA-STD-6001B Test 1 [23]. Figure 1.8 (a) shows the schematic of a sample holder inside a vacuum chamber. It is vertically oriented and can accomodate nonmetallic samples of dimensions 30 cm by 6.4 cm. The test is not conducted in either microgravity or even simulated microgravity.

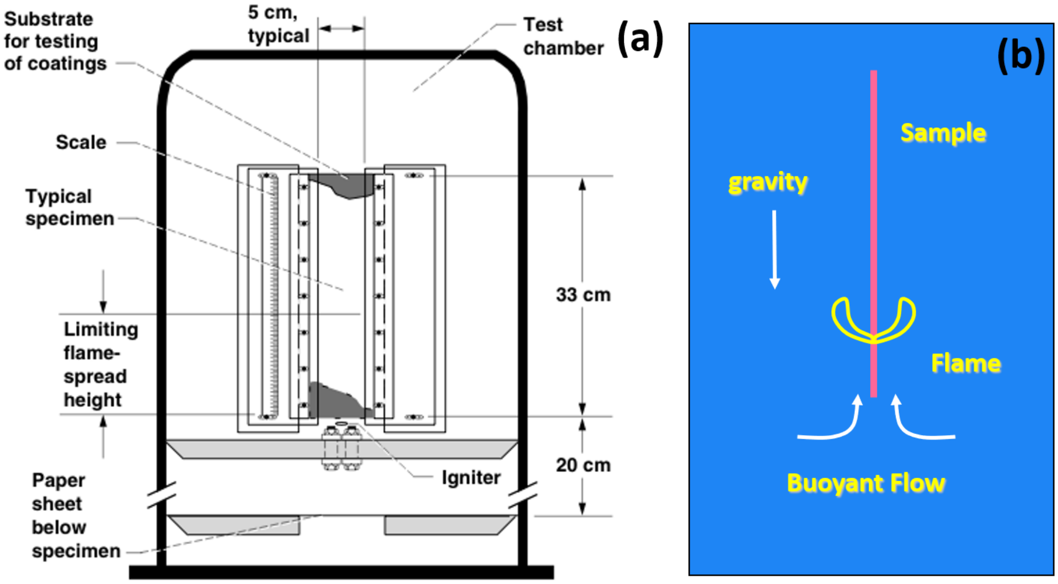

Figure 1.8: (a) Schematic of NASA-STD-6001B Test 1 setup (b) The upward burning concept, used in the NASA-STD-6001B Test 1, which is not a microgravity test.

The main flammability test generates a buoyancy induced flow which is much larger than the flow in a spacecraft environment [24]. Therefore, Test 1 is overly conservative in many cases due to the severity of the 1-g upward burning (Figure 1.8 (b)). Therefore, there is an incentive to develop ground-based test apparatus that can provide information about the behavior of fires relevant to spacecraft ventilation flow rates and atmospheres, and furthermore that are able to produce what can be called “Simulated microgravity flow conditions”. A method to do so, currently called the Narrow Channel Apparatus (NCA), has been under development for fundamental flame spread research efforts. The first developed apparatus to simulate microgravity was constructed at Michigan State University and was known as the Hele-Shaw apparatus [25]. The disadvantage of this device is the large heat sink near the burning sample. An improved version of the Hele-Shaw apparatus is referred as the Narrow Channel Apparatus (NCA). In recent times, it is a well-known apparatus for simulating microgravity flame spread. The flames in the NCA appear visually similar to those that have been studied in actual microgravity environments on the ISS. It also exhibits similar flame spread rates to actual microgravity flames [21]. In the Narrow Channel Apparatus (NCA), the operating gap height is reasonably small (in the order to 3-10mm). In the horizontal orientation of the NCA, the effect of the buoyancy force become negligible due to the small gap height. Therefore, one of the key factors in the design of the NCA is the proper selection of the gap height. (Hossain et al. [26] found the gap height that provides best compromise between buoyancy suppression and heat loss to the NCA is approximately 5 mm. This detail will be discussed in chapter 2.) In addition, the NCA possesses several attractive features that simplify the fluid dynamics during the experiment. For example, the NCA provides a laminar velocity profile that resembles the flow condition in a spacecraft. The flow in the narrow channel is laminar and two-dimensional, except at very high gas velocities, when side boundary conditions may become important. It permits researchers to concentrate on studying the kinetics of the interaction of fire suppressants with well-defined laminar diffusion flames over solid fuels. Different and new versions of this apparatus are being designed and developed at NASA Glenn Research Center, San Diego State University (SDSU) and Michigan State University (MSU). All of these apparatuses are based on the original MSU design [25].

Each new apparatus has been designed and manufactured differently to serve different purposes. Thus, the NCA at SDSU has the capability of testing materials up to 30.5 cm long, 10 mm thick and 50.8 mm wide. The NCA at NASA has a sample holder that can accommodate a 25 cm long and 5 cm wide sample [21]. However, the materials practically used in International Space Station (ISS) are usually thicker and wider. So, it is necessary to design a test facility (NCA) that can test thicker and wider samples which is similar to the actual scale parts used in ISS. Therefore, the primary research objective is to improve the current MSU NCA facility for testing that can replace or supplement the current NASA Standard 6001B Test 1 [23] to improve flame propagation testing and to aid the actual scaled material selection process.

1.9 Dissertation Outline

The studies presented in this dissertation, supported by NASA, consist of experimental exploration, numerical modeling and theoretical calculations and correlations. The ultimate practical goal of this effort is to improve the fire safety protocol in the space station by extending our current understanding of the characteristics of solid fuel combustion. This dissertation also addresses numerous inherent fundamental physical complexities occurring during opposed flame spread over complex, realistic, solid fuels.

This dissertation is organized into eight chapters focusing on different aspects of solid polymer fuel combustion. Following this brief Introduction, Chapters 2 and 3 deal with the analysis of fundamental quantities of opposed flow flame spread over thin and thick fuels, respectively. Chapters 4 and 5 cover the detailed analyses of post burn thick fuels after flame spreading. In chapter 6, a transient regression model is developed under the influence of a constant heat source to mimic the flame. Each chapter (Chapters 2-6) starts with a brief synopsis, motivation/introduction, literature review, description of experimental setup and test methodology. The result are presented and discussed. Lastly, a short summary of each respective chapter (2-6) is provided. Chapter 7, Conclusions, is followed by Chapter 8, Future Work. Finally, the Appendices and the Bibliography for all chapters are listed.

The research in Chapter 2 was conducted at National Aeronautics and Space Administration (NASA) John H. Glenn Research Center at Lewis Field, Cleveland, OH on opposed flow thin fuels, under the microgravity fire safety research program. This chapter primarily deals with the analysis of the role of the gap height and the opposed flow velocity in the NCA for thin fuels. A control volume analysis was adopted for the heat losses from the flame by radiation, convection and enthalpy change of the gases. Several analytical correlations and scaling parameters are formulated to quantify the flame spread process in the NCA. The evidence of a trade-off between buoyant suppression and flame quenching is of particular interest for the further development of NCA and for the perfection of a standard test method. Chapter 2 was published in Combustion and Flame [26] (S. Hossain, I. S. Wichman, G. W. Sidebotham, S. L. Olson, and F. J. Miller. Influence of gap height and flow field on global stoichiometry and heat losses during opposed flow flame spread over thin fuels in simulated microgravity. Combust. Flame, 193:133–144, 2018.).

Chapter 3 presents the study of thick PMMA fuels in the Michigan State University (MSU) NCA at standard ambient conditions over a range of opposed oxidizer flow velocities. The motivation behind this work is to study the flame spread rate of three different thicknesses of PMMA. The experimental results and discussion section includes the visual observation of the flame, burnt sample analysis, flame spread rate measurement and the discussion about the new regressive burning regime where the flame spread rate is independent of the opposed flow velocity. Here, the study also extends to compare the results of different experimental configurations. The flame spread rate results are compared with the similar material (PMMA) and thickness (12.1 mm) results from the literature. Detail numerical and theoretical analysis are conducted for the proper comparison and interpretation of the data. Chapter 3 has been published in Combustion and Flame [27] (S. Hossain, I. S. Wichman, F. J. Miller, and S. L. Olson. Opposed flow flame spread over thermally thick solid fuels: buoyant flow suppression, stretch rate theory, and the regressive burning regime. Combustion and Flame, 219:57 – 69, 2020.).

In Chapter 4, a theoretical correlation is developed to determine the mass loss rate of post-burn PMMA samples of nominal thickness 25.4 mm. This semi-empirical correlation involves the measurement of surface regression depth and flame spread rate. The flame spread rate has already been measured in chapter 3 for 25.4 mm PMMA for a varied range of flow velocities. An image acquisition process is developed and discussed for the surface regression measurement of the post-burn samples. The mass loss rate results are compared with previous literature values. Similar to Chapters 2 and 3, this chapter has its own motivation, literature review, results and discussion and summary sections.

Research in Chapter 5, was also conducted on the post-burn samples. After analyzing the burnt samples, extensive internal bubble formation was observed. This chapter is focused on quantifying the bubble numbers, their distribution, their volume fraction and so on. Digital image analysis was used to count the bubbles and to determine their sizes. Several classes of bubble statistics were studied.

Chapter 6 deals with the development of a theoretical and numerical model of transient regression rate and the scaling analysis that relates the model results to experimental results discussed in Chapter 4. The model provided an understanding of the surface regression rate under various heat fluxes.

In Chapter 7, the key scientific findings of the research in this dissertation are summarized. In Chapter 8 possible future research subjects are briefly discussed.

CHAPTER 2

INFLUENCE OF GAP HEIGHT AND FLOW FIELD ON HEAT LOSSES DURING OPPOSED FLOW FLAME SPREAD OVER THIN FUELS IN SIMULATED MICROGRAVITY

Synopsis

In this chapter, the role of Narrow Channel gap height was evaluated over thin fuels for opposed flow flame spread. The primary goal is to estimate the optimum gap height for Narrow channel which can suppress buoyancy without promoting excessive heat losses to the channel walls. To accomplish the primary objective, the dependence of heat losses as a function channel height and air flow velocities is assessed. The heat loss calculation is based on the control volume analysis from the flame by radiation, convection and enthalpy change of the gases. The evidence of a trade-off between buoyant suppression and flame quenching through heat losses is of interest for the further development and refinement of a standard test method for spacecraft applications. This study was done at the preliminary design stage of MSU narrow channel apparatus. The results provided critical information about the gap height of MSU NCA. It also provided a better insight about the nature of opposed flow flame spread over thin fuels in simulated microgravity conditions. This work has been conducted in collaboration with NASA. All the experiments were performed at NASA's Cleveland, OH facility. The data is organized, analyzed and detailed set of models has been developed at MSU. The following work is also published as journal article in Hossain et al. [26].

2.1 Literature Review

For thermally thin fuels, the flame spread rate in the NCA is compared with NASA's Zero-gravity research facility by varying the total pressure, oxidizer velocity and oxygen concentration [28]. Flames in the NCA look similar to those studied in microgravity and exhibit similar spread rates to microgravity flames for thin fuels where direct comparisons are possible [21]. The flame spread rate has also been measured and compared in normal and microgravity at different pressures in the cylindrical tube geometry [29]. Different channel configurations have been studied to analyze flame front propagation using analytical, numerical and experimental techniques for thin solid fuels [30]. Phenomena such as flame fingering and a low flow quenching limit have been demonstrated in the NCA that are characteristic of actual opposed flow microgravity flame experiments [21]. These phenomena have never been observed in NASA Test 1 [29], which is described in Ref. [31]. In light of the previous work and discussion, there are three major goals of the present study, which addresses only thermally thin fuels samples. One goal is to determine the influence of global combustion stoichiometry on simulated opposed flow microgravity flame spread. This fundamental quantity — its global stoichiometry — characterizes the spread process and clarifies changes that occur in the flame behavior, even though it is well known that the local opposed flow flame spread process is stoichiometric. The first goal is to quantify the various experimentally measured behaviors analytically through correlations and scaling parameters derived from an order-of-magnitude, predominantly control volume analysis. A second goal is to evaluate the role of gap height in the NCA. The evidence of a trade-off between buoyant suppression and flame quenching through heat losses. The gap height will influence flame spread rates, the flame combustion rate, and heat losses to the NCA walls. Since the purpose for diminishing the gap height is to suppress buoyancy so that microgravity conditions might better be simulated, there must be a compromise between decreasing the gap height to suppress buoyancy while simultaneously increasing the heat losses from the flame to values not found in pure microgravity flame spread. A third goal is to quantify the accuracy of flame spread models, e.g. [10]. Because of the nature of the Hagen-Poiseuille flow field in the NCA, the influences of the flow field can be systematically examined, enabling direct comparisons to be made between the Oseen and velocity gradient models.

2.2 Experiment Description

The configuration of the NCA at NASA used for this study (Figure 2.1) has been described extensively elsewhere [21]. In this apparatus the facility air is regulated, filtered and dried prior to

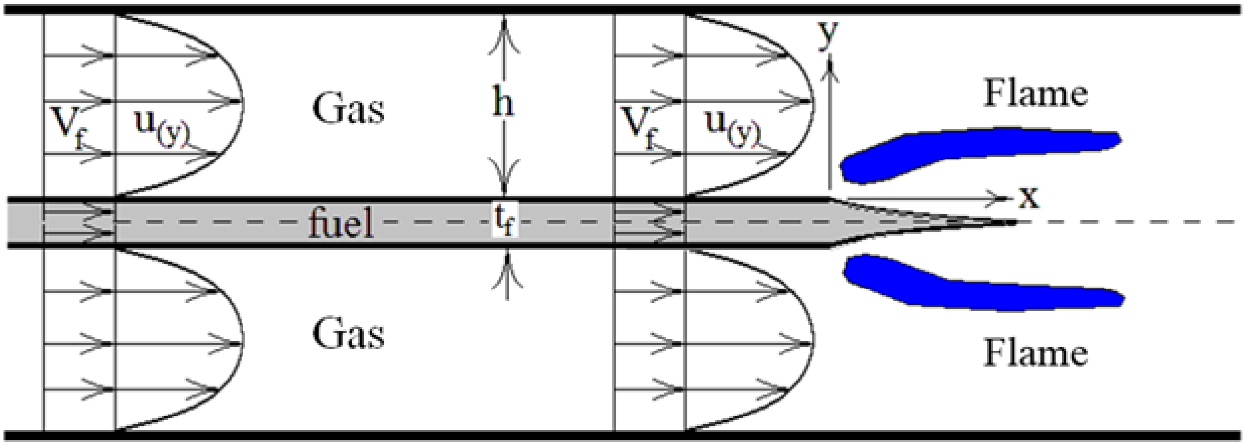

Figure 2.1: Schematic of spreading flame in a narrow channel in flame coordinates. Note the definition of h as the channel half width (for thin samples). The total channel gap height is $2h + t_f$. In a coordinate frame fixed to the flame the opposed flow velocity is $V_f + u(y)$ as shown.

entering a mass flow controller. The flow enters an inlet plenum section that conditions the flow to become a fully developed laminar flow between flat plates. The test section is 38 cm wide by 45 cm long, with a total gap height ($2h + t_f$) that can be adjusted over the range of approximately 3 - 20 mm. A 0.8 mm thick stainless-steel sample holder plate is placed in the center of the test section, with flow on both sides over the thin fuel sample. A 5 cm by 25 cm rectangular slot is cut in the center of the sample holder to accept the thin fuel samples (Whatman 44 filter paper). The desired air flow is established and an igniter wire placed at the trailing edge of the sample is activated, igniting a flame that propagates upstream (to the left in Figure 2.1) toward the supply air. The experiment is videotaped using two cameras. A top view is used to analyze the flame propagation, a side view to investigate flame shape and structure. The videos are analyzed using Spotlight software developed at NASA Glenn [32]. All of the parameter values used in subsequent calculations are shown in Table 2.1.

2.3 Experimental Results

Flame spread rates were measured for four gap heights, h = (3, 5, 7, 9) mm. All flame spread measurement were obtained for a steady spread rate. Several tests were performed to determine the repeatability and reproducibility of the results. Figure 2.2 shows the flame spread rates (cm/s) for these gap heights as a function of the opposed flow velocity. For each gap height, Figure 2.2 shows that there is a velocity that maximizes the flame spread rate. For the two lower gap heights h = (3, 5) mm, lower opposed flows than those indicated by the left-most data points did not support a steady flame and led eventually to extinction. Equipment limitations prevented an upper flow (blow off) limit to be reached except for a gap of 3 mm, in which case a test at 40 cm/s opposed flow produced blow off. For the smallest gap height, h = 3 mm, the flame spread rate is distinctly lower than for the other gap heights. There is an inflection point for the gap heights h = 7 and 9 mm for the lower opposed flow velocity ranges. This behavior mirrors that of classic opposed flow flame spread experiments [7]. This inflection point does not appear for the gap heights h =3, 5 mm. [12]

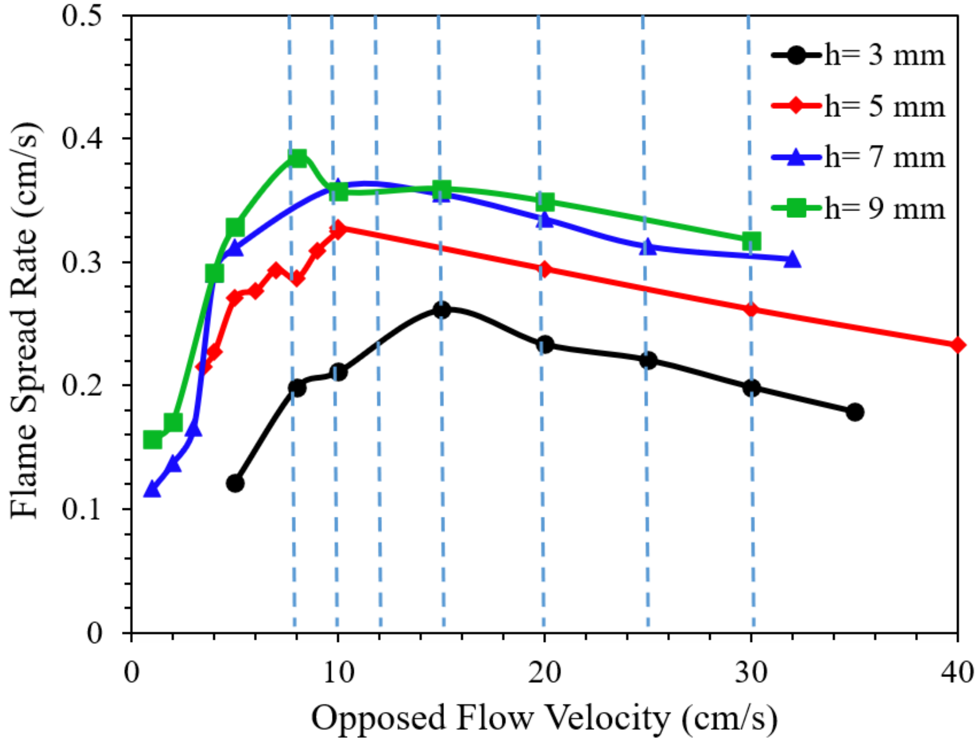

Figure 2.2: Flame spread rate vs opposed flow velocity for thermally thin samples of Whatman 44 filter paper. Note the appearance for each channel height of a single peak spread rate of approximately 0.3 cm/s, which is of the order of 0.1 cm/s. The dashed vertical lines represent flame spread rates that are plotted later as functions of gap height. The experimental error is approximately 5 % for the flame spread measurements.

Figure 2.3 shows side view images as a function of gap height and opposed flow velocity. The asymmetries between the flames at the top and bottom allow a qualitative assessment of buoyancy effects, which tend to steepen the flame angle and alter the concavity of the top flame compared with the bottom flame. The influences of buoyancy appear to be minor for gap heights h = (3, 5) mm, in agreement with the previous research [33, 34].

The lean spreading flames of Figure 2.3 are reminiscent of co-flow diffusion flames in which gaseous fuel flows in a central jet (the horizontal vaporized fuel flow) surrounded by a gas flow under over-all fuel lean conditions. The flame is close to the central axis (the horizontal plane in the spreading flame). This perspective is apparent for the highest opposed flow velocity images of Figure 2.3.

For over-all fuel rich spreading flames, the rate of fuel gasification from the sample by the flame exceeds the stoichiometric requirement of the gas (oxidizer) being delivered by the inflow. All of the inflow oxygen is consumed, with excess fuel still available for combustion. Thus, the vitiated gaseous fuel downstream of the flame is capable in principle of supporting a secondary diffusion flame if it were to encounter a fresh oxidizer supply there. This type of behavior has been observed in opposed flow flame spread in polyvinyl-chloride tubes [29, 35]. Fuel rich spreading flames in the NCA are reminiscent of co-flow inverse diffusion flames, where an oxidizer flow is surrounded by a fuel flow in excess of the stoichiometric oxygen requirement. In the NCA, the flame closes on the containing wall, which behavior is apparent for the lowest opposed flow velocity images in Figure 2.3.

In addition to the NCA data gathered here, RITSI (Radiative Ignition and Transition to Spread Investigation) data from a previous set of microgravity tests in the microgravity Glovebox [36] are used for comparing the current on-earth NCA data with actual microgravity data. The duct height for the RITSI tests was 47.5 mm is 5.3 times larger than the largest gap height (9 mm) in the NCA.

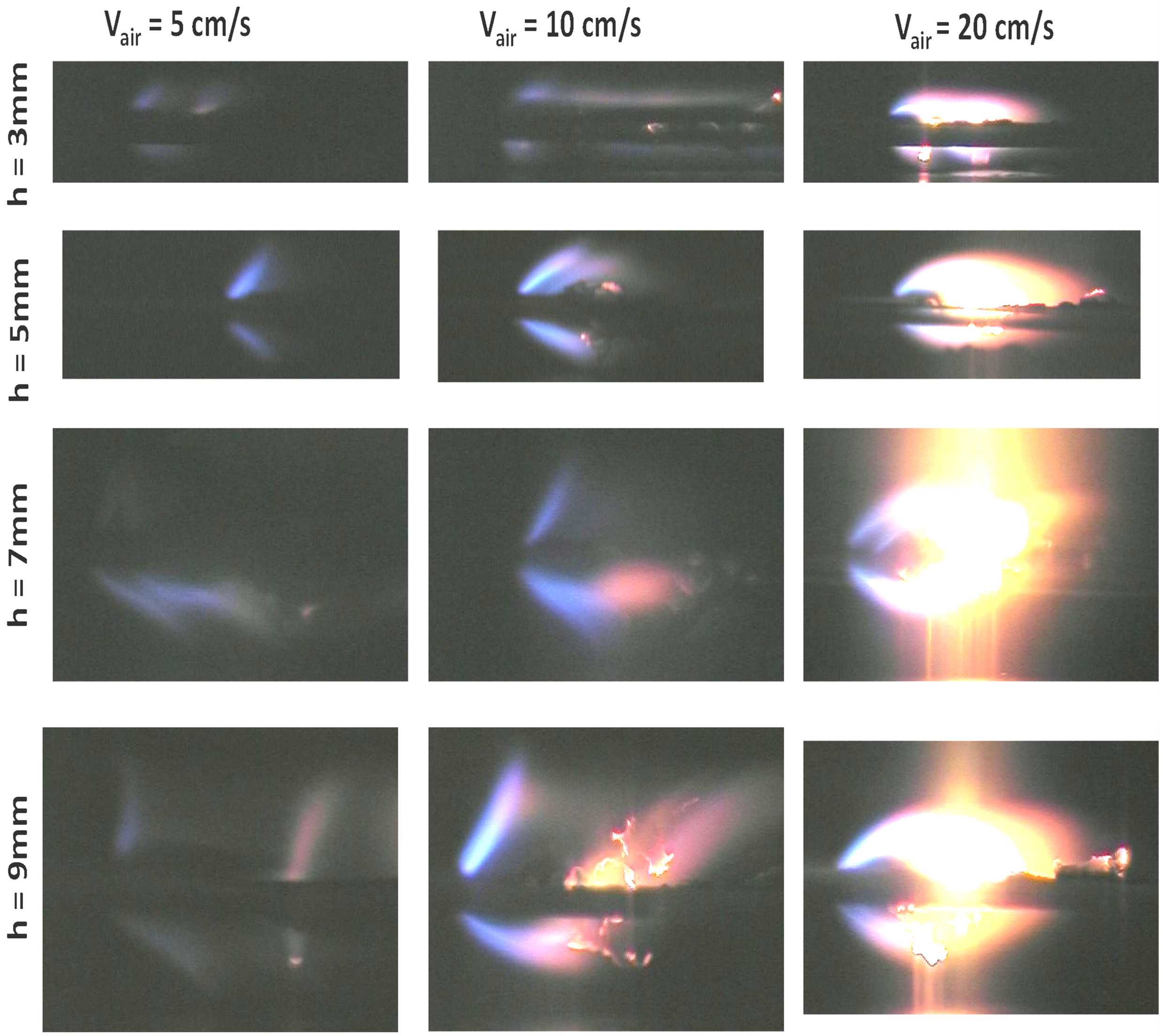

Figure 2.3: Side view flame images from the NCA at various air velocities and gap heights. (Camera settings were identical for each test, so that relative flame brightness could be compared). For higher gap heights and lower flow velocities, the flames approach greater vertically.

2.4 Results and Discussions

2.4.1 Theoretical Analysis and Correlations: Global Stoichiometry

2.4.1.1 Overall NCA Stoichiometry

The overall stoichiometry of a flame spreading in the NCA can be transparently defined because the oxidizer flow is geometrically confined. This is in contrast with a spreading flame in an

Table 2.1: Parameter values used for calculations. The solid fuel is Whatman 44 filter paper whose thickness is indicated. The inflow gas is air at 298 K and 1 atm.

Quantity	Symbol	Value	Units	Sources
Fuel density	ρ_f	435	kg/m^3	[21]
Fuel thickness	t_f	0.00017	m	
Fuel width	w	0.0508	m	
Fuel molecular weight	$\mathrm{M}W_f$	162	kg/mol	[21]
Stoichiometric fuel to air mass ratio	$(F/A)_{mass,stoich}$	0.196		
Oxidizer density	ρ_g	1.18	kg/m^3	[12]
Gas absolute viscosity	μ_g	1.98E-05	kg/m/s	[12]
Gas thermal conductivity	k_g	0.023	W/m/K	[12]
Gas specific heat	$C_{p,g}$	1005	J/kg/K	[12]
Gas thermal diffusivity	α_g	1.93E-05	m^2/s	[12]
Oxygen diffusivity	D_{O_2}	2.20E-05	m^2/s	[12]
Solid fuel thermal conductivity	k_f	0.15	W/m/K	[12]
Fuel specific heat	$C_{p,f}$	2500	J/kg/K	[12]
Fuel thermal diffusivity	α_f	1.38E-07	m^2/s	[12]
Surface temperature	T_s	700	K	[21]
Mass fraction for oxygen	Y_{ox}	0.23		
Emissivity for cellulose	ϵ	0.85		[21]
Stefan–Boltzman constant	σ	5.67E-08	W/m/K^4	[12]

open environment whose overall fuel lean stoichiometry has little meaning or consequence. In the following development, the fundamental stoichiometry relations for the confined, steady and spreading flame are derived.

Consider first mass conservation. The mass feed rate of fuel from the sample in flame-fixed coordinates is $\dot{m}_f = \rho_f V_f t_f w$. The mass feed rate of gas (air) in flame coordinates is $\dot{m}_g = 2\rho_g(V_f + \overline{V}_g)hw$. Here ρ_f is the fuel density, ρ_g is the gas density, t_f is the fuel thickness, V_f is the flame velocity, and $\overline{V}_g$is the average flow velocity and w is the sample width. The factor '2' for the gas feed rate is used to account for the symmetry of flame spread with flow on top and bottom sides of the sample. After rearrangement, the global flame equivalence ratio (fuel-to-air feed ratio normalized by its stoichiometric value) can be written in terms of four dimensionless quantities,

$$\phi = \left(\frac{\rho_f}{\rho_g}\right)\left(\frac{t_f}{2h}\right)\left(\frac{V_f}{V_f + \overline{V}_g}\right)\left(\frac{1}{(F/A)_{mass,stoich}}\right) \tag{2.1}$$

The global NCA equivalence ratio given by Eq. (2.1) depends on material parameters (ρ_f and ρ_g), on the channel and sample geometry (h and t_f), and on the flow dynamics of the flame spread process (V_f and $\overline{V}_g$).

This correlation is applied to the experiment. The fixed parameters areρ_f, ρ_g, t_f, and the fuel-to-oxidizer stoichiometric mass ratio for cellulose ($C_6H_{10}O_5$) in air has the value 0.196, see Table 2.1. The variable parameters are h, V_f and $\overline{V}_g$.

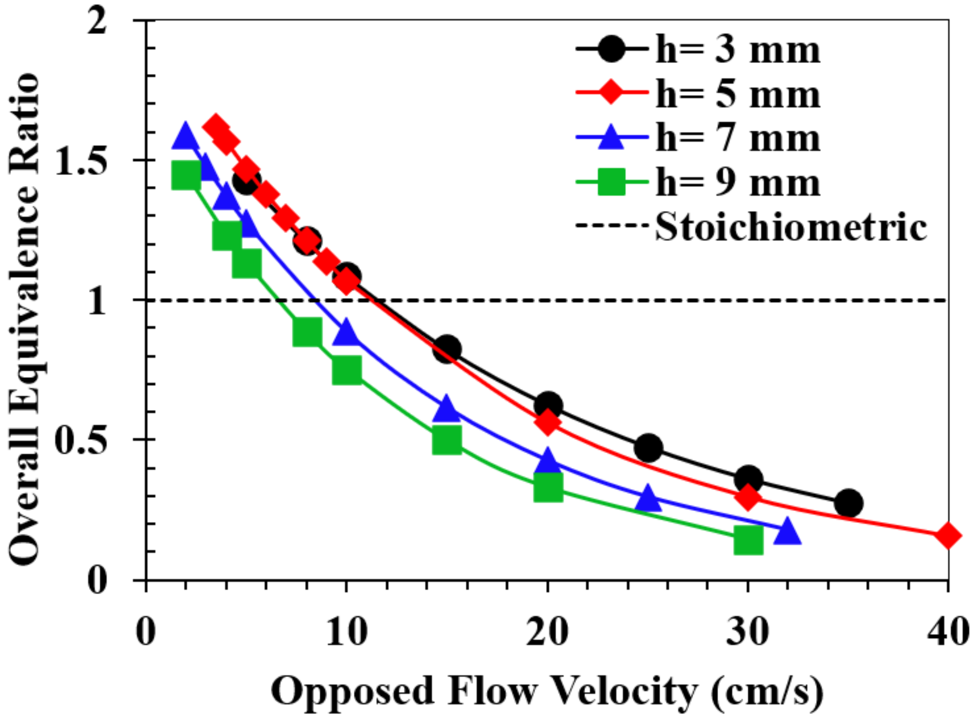

Figure 2.4: Overall equivalence ratio versus opposed flow velocity plotted from Eq. (2.1).

Figure 2.4 Overall equivalence ratio versus opposed flow velocity plotted from Eq. (2.1). The equivalence ratio given by Eq. (2.1) is plotted against $\overline{V}_g$ in Figure 2.4 for the four NCA gap heights (excluding points which show obvious buoyancy effects for the larger h's) to determine whether the sample experiences globally rich, stoichiometric or lean combustion. As seen, the equivalence ratio is generally a monotonically decreasing function of the gas flow rate, $\frac{\partial\phi}{\partial\overline{V}_g} < 0$. That is, the overall stoichiometry become leaner as the flow $\overline{V}_g$ increases, even in the slower flows (see the left part of Figure 2.2) where the flame speed V_f increases with $\overline{V}_g$. Also, the larger are the h values the leaner are the flames. As expected, the added gas inflow moves the combustion process toward an over-ventilated state. At low inflow speeds, an over-all fuel rich NCA stoichiometry occurs for all values of h. The transition from overall rich to overall lean occurs in the approximate range 6-11 cm/s of the average gas inflow.

2.4.1.2 Stoichiometric Distance

Here a new quantity is defined, called the stoichiometric distance, which is particular to the channel flow geometry. The stoichiometric distance is a measure of the required oxidizer (air) inflow for obtaining globally (not locally) stoichiometric combustion. Its numerical value, in the form of a dimensionless ratio, determines whether the required oxidizer inflow for stoichiometric combustion is not met (fuel rich), is met (stoichiometric), or is exceeded (fuel lean).

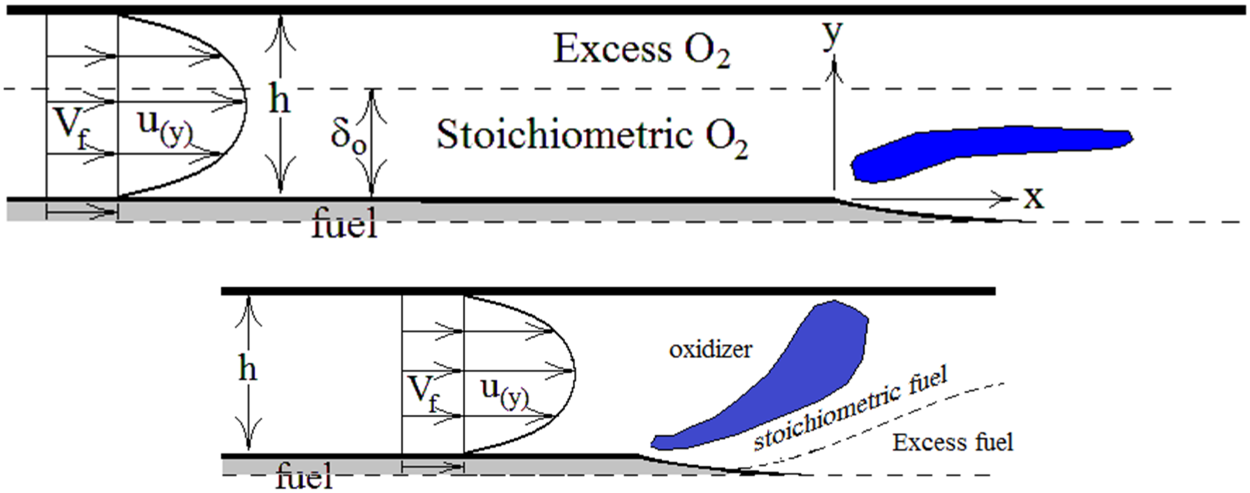

Figure 2.5: Schematic of an overall lean (top) and rich (bottom) flames. The centerline of the fuel is treated as a line of symmetry.

The calculation of the stoichiometric distance begins by positing the existence of a fictitious transverse distance from the fuel surface, δ_0, within which stoichiometric oxygen enters the flame (Figure 2.5). If the channel height h is smaller than δ_0 the global combustion process cannot possibly be stoichiometric: it will always be fuel rich for the given airflow velocity.

$$\dot{m}_{g,stoich} = 2\rho_g w \int_{y=0}^{\delta_0} (V_f + u)\,dy = \frac{\dot{m}_f}{(F/A)_{mass,stoich}} \tag{2.2}$$

Introducing the Hagen-Poiseuille parabolic velocity distribution $u(y) = 6\pi y(1-y)$ into Eq. (2.2) (note: y = 0 is located at the sample surface, see Figure 2.1 and $\overline{u}$ mean flow velocity which is equal to $\overline{V}_g$ in this analysis), integrating and then rearranging the result yields a cubic equation for δ_0, which is written in dimensionless form as

$$K_3\hat{\delta}_0^3 - K_2\hat{\delta}_0^2 - K_1\hat{\delta}_0 + K_0 = 0 \tag{2.3}$$

where $\hat{\delta}_0 = \delta_0/h$, $K_0 = \left(\frac{\rho_f}{\rho_g}\right)\left(\frac{t_f}{2h}\right)\left(\frac{V_f}{\overline{V}_g}\right)\left(\frac{1}{(F/A)_{mass,stoich}}\right)$, $K_1 = \frac{V_f}{\overline{V}_g}$, $K_2 = 3$ and $K_3 = 2$.

Figure 2.6 shows a plot of the stoichiometric distance against the opposed flow velocity. Consistent with the result of Figure 2.4, Eq. (2.3) is solved for $\phi < 1$(globally lean) numerically and plotted. However, for $\phi > 1$ (globally reach) the stoichiometric distance, δ_0 should be greater than the gap height, h which is unrealistic. Therefore, when $\phi > 1$ the stoichiometric distance, δ_0 is set equal to the gap height, h. For higher gap heights the stoichiometric distance is higher, which is opposite to the behavior of the overall equivalence ratio. In the light of this discussion, it can be written as $K_0 = \phi(1 + K_1)$ after combining Eqs. (2.1) and (2.3) and then solve for ϕ:

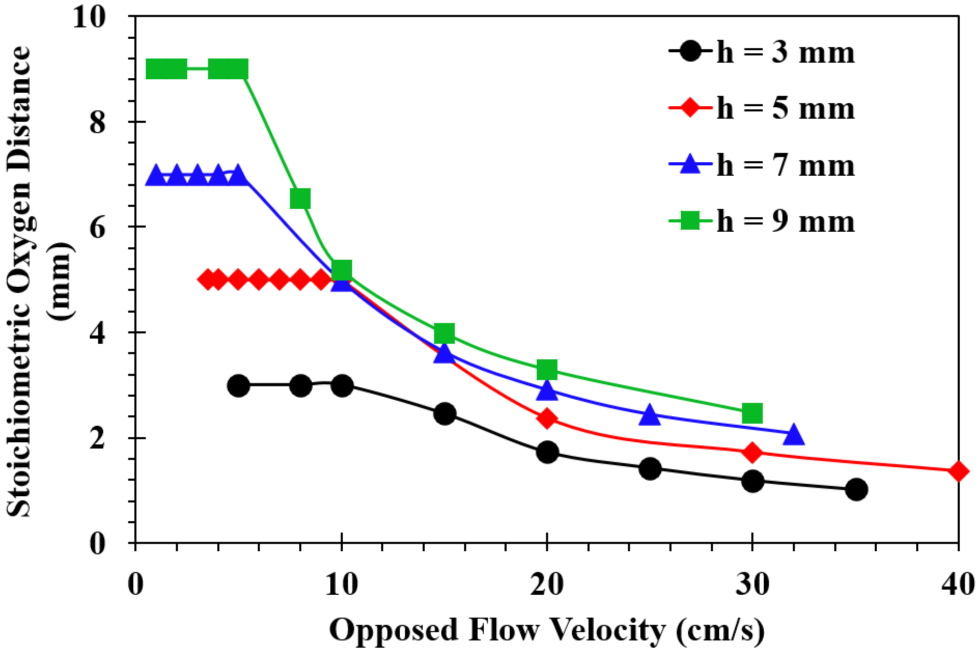

Figure 2.6: Stoichiometric distance versus opposed flow velocity. The highest channel height ($h = 9mm$) exhibits the highest stoichiometric distance while the lowest channel height ($h = 3mm$) shows lowest stoichiometric distance.

$\phi = \frac{3\hat{\delta}_0^2 + K_1\hat{\delta}_0 - 2\hat{\delta}_0^3}{1+K_1}$.

Since the ratio of the spread rate to the opposed flow is of order 10^{-2}, so $K_1 << O(1)$ is used and the approximate form of this equation is written as follows

$$2\hat{\delta}_0^3 - 3\hat{\delta}_0^2 + \phi = 0 \tag{2.4}$$

This simplified parameter-free Eq.(2.4) is solved numerically and plotted against ϕ as shown in Figure 2.7.

2.4.2 Theoretical Analysis and Correlations: Length Scales and Opposed Flow

2.4.2.1 Solid Preheat Length Scale

Figure 2.8 is a schematic of the flame in the vicinity of the leading edge that shows several characteristic length scales. These include the flame quenching distance δ_q and the preheating distances in the solid and gas phase, called δ_s and δ_g, respectively. A coordinate system that is fixed to the flame front is also shown.

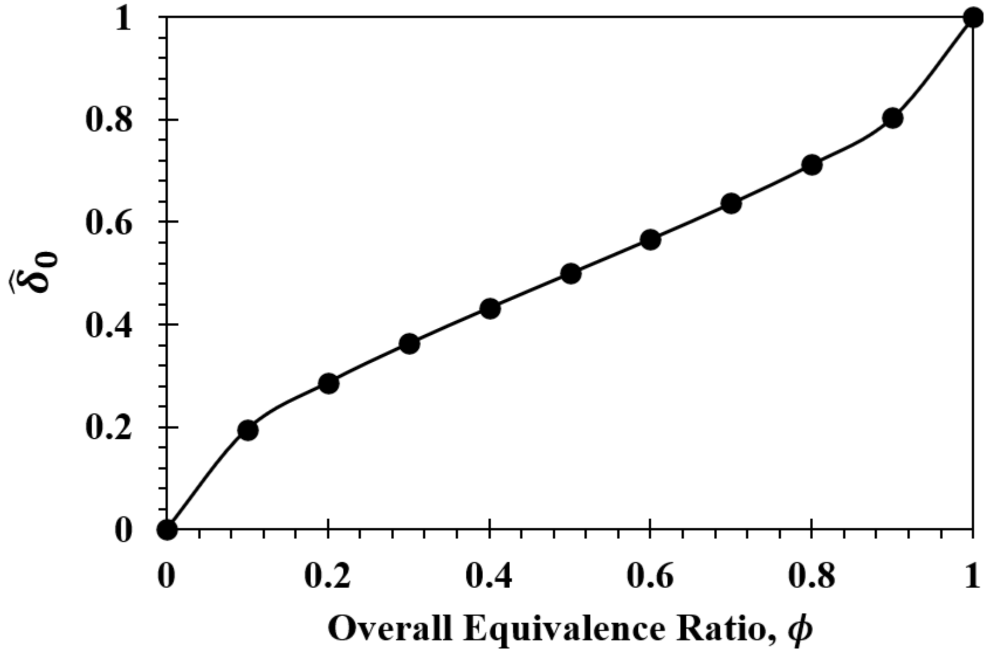

Figure 2.7: Dimensionless stoichiometric distance as a function of the overall equivalence ratio from Eq. (2.4).

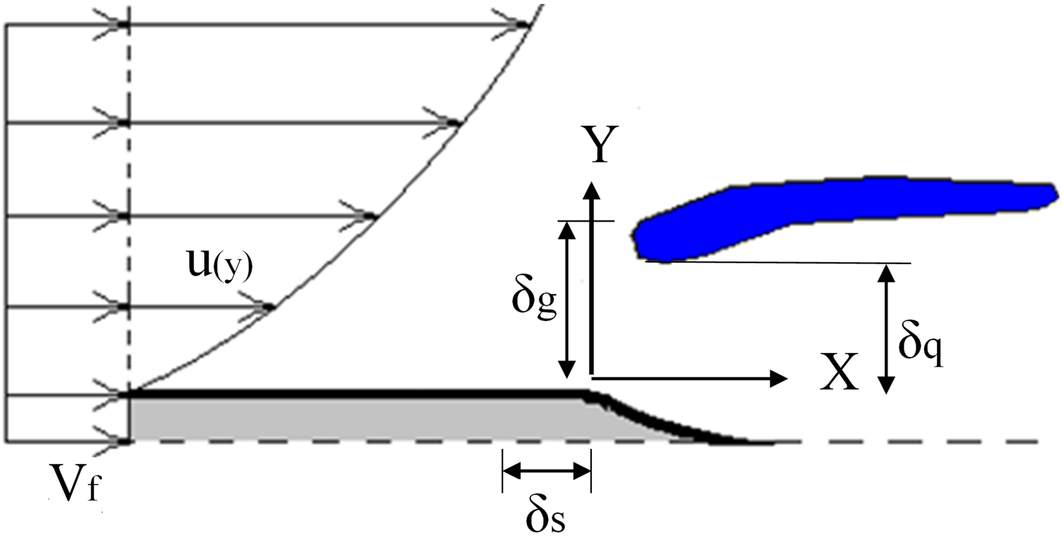

Figure 2.8: Flame schematic defining the gas and solid length scales, along with the flame quenching distance. The latter measures distance between the surface and the point at which the spreading flame quenches.

In the solid phase, the heat conducted forward from the gasifying region raises the temperature of the solid fuel samples from the ambient temperature (T_∞) to the gasification temperature (Tv). By neglecting heat transfer from the gas phase preheating region to the solid, an energy balance for this preheat region is written as $(\rho_f V_f t_f w) c_{p,f} (T_v - T_\infty) \sim \frac{k_f t_f w (T_v - T_\infty)}{\delta_s}$. This yields the following expression for the characteristic solid preheat distance,

$$\delta_s \sim \frac{\alpha_f}{V_f} \tag{2.5}$$

Where, $\alpha_f = \frac{k_f}{\rho_f c_{p,f}}$ is the solid fuel thermal diffusivity. By introducing an order unity constant to account for the proportionality, c_s, the solid preheat length of Eq. (2.5) becomes $\delta_s = c_s \frac{\alpha_f}{V_f}$. In the spreading flame, especially at low opposed flow rates, there is an additional potentially important source of heat from the gas preheat region to the solid fuel. Nevertheless, it is instructive to quantify the magnitude of the characteristic preheat distance solely from a balance between heat conduction through the solid and solid-phase convection.

2.4.2.2 Gas Preheat Length Scale

In contrast with the solid, the gas velocity feeding the flame is not clearly defined, because it varies with the transverse distance from the surface (Figure 2.5 2.5 and Figure 2.8 2.8). This variation is important because the flames shown in Figure 2.3 2.3 generally reside inside the velocity boundary layer. An energy balance for heat flux for the preheat region of characteristic dimension δ_g can be written as $\rho_g V_r c_{p,g}(T_F - T_\infty) \sim \frac{k_g(T_F - T_\infty)}{\delta_g}$ where $V_r = V_f + U_g$ is the relative velocity at the flame leading edge. Therefore

$$\delta_s \sim \frac{\alpha_g}{V_r} = \frac{\alpha_g}{V_f + U_g} \tag{2.6}$$

Where, $\alpha_g = \frac{k_g}{\rho_g c_{p,g}}$ is the thermal diffusivity of the gas mixture and a gas velocity U_g has been included that may be evaluated using different models. Conceptually, this velocity is observed – or felt – by the leading edge of the flame, which is displaced from the solid at the quenching distance, δ_q.

Four different models for Ug are developed here. The first model (model 1) is the Oseen approximation of constant or slug-flow velocity [5, 8]. The second model (model 2) is the constant velocity gradient, negligible flame speed ($V_f \rightarrow 0$) approximation [9, 10, 13] in which $V_r \sim U_g$. The hird model (model 3) is the constant velocity gradient approximation [9, 10, 13] without the restriction to negligible flame speed. Here, $V_r = V_f + U_g$. The fourth model (model 4) is the parabolic (Hagen-Poiseuille) flow in the NCA.

The Oseen approximation employs a constant gas phase velocity, for which the opposed gas flow velocity at the leading edge of the flame is the mass average slug flow velocity, $\overline{V}_g$ [5, 8]. The gas phase characteristic length for model 1 is

$$\delta_{g,Oseen} \sim \frac{\alpha_g}{V_f + \overline{V}_g} \tag{2.7}$$

The conceptual difficulty with this model is that the flame hugs closely to the wall, hence the slug or average velocity is larger than what the flame experiences near its leading edge. In fact, the gas velocity observed by the flame at its leading edge (at the quenching distance δ_q) is the most appropriate velocity to use [10, 13]. The no slip condition and the existence of a quenching layer suggests that the gas velocity experienced by the flame can be approximated by the velocity gradient multiplied by the quenching distance [10]. Using this velocity as the relative velocity in the expression for the gas-phase preheat length gives

$$\delta_{g,LinGrad} \sim \frac{\alpha_g}{V_f + \frac{du}{dy}|_{y=0}\delta_q} \tag{2.8}$$

For the narrow channel, the velocity gradient at the wall is characterized by the Hagen-Poiseuille parabolic gas flow profile. Inserted into Eq. (2.8), it yields

$$\delta_{g,LinGrad} \sim \frac{\alpha_g}{V_f + \frac{6\overline{V}_g \delta_q}{h}} \tag{2.9}$$

In the following section, the quenching distance and gas preheat distance are shown to have the same basic functionality. For this reason, it is assumed that they are proportional,

$$\delta_q = c_q \delta_g \tag{2.10}$$

Substitution of Eq. (2.10) into Eq. (2.9) followed by algebraic rearrangement yields a quadratic equation for the gas preheat length (normalized by the channel width), viz.

$$\hat{\delta}_g^2 + B_1 \hat{\delta}_g - B_0 = 0 \tag{2.11}$$

where $\hat{\delta}_g = \frac{\delta_g}{h}$, $B_1 = \left(\frac{1}{6c_q}\right)\left(\frac{V_f}{\overline{V}_g}\right)\left(\frac{\delta_g}{h}\right)$ and $B_0 = \left(\frac{c_g}{6c_q}\right)\left(\frac{\alpha_g}{\overline{V}_g h}\right)$. Here, “Linear Gradient Model A” refers to model 2, when V_f is neglected in comparison with $\overline{V}_g$ in either Eq. (2.9) or Eq. (2.11). Inclusion of the flame spread rate term V_f yields “Linear Gradient Model B,” or model 3. The physical solution of the quadratic Eq. (2.11) is

$$\frac{\delta_{g,LinGradB}}{h} = \frac{-1}{12c_q}\left(\frac{V_f}{\overline{V}_g}\right) + \sqrt{\frac{1}{144c_q^2}\left(\frac{V_f}{\overline{V}_g}\right)^2 + \frac{c_g}{6c_q}\left(\frac{\alpha_g}{\overline{V}_g h}\right)} = \frac{-K_1}{12c_q} + \sqrt{\left(\frac{K_1}{12c_q}\right)^2 + \frac{c_g}{6c_q}\left(\frac{\alpha_g}{\overline{V}_g h}\right)} \tag{2.12}$$

Neglecting the flame spread rate in comparison with the opposed gas velocity, i.e., recalling that $K_1 << O(1)$, yields the ‘A’ result, which is a more compact solution, and which adequately captures the problem physics,

$$\frac{\delta_{g,LinGradA}}{h} = \sqrt{\frac{c_g}{6c_q}\left(\frac{\alpha_g}{\overline{V}_g h}\right)} \tag{2.13}$$

The last term of Eq. (2.13) contains the inverse of a Peclet number for the channel flow, $Pe_h = \frac{\overline{V}_g h}{\alpha_g}$. The functionality of the dimensionless gas preheat length for Eq. (2.13) is therefore $\frac{\delta_{g,LinGradA}}{h} = O(\frac{1}{\sqrt{Pe_h}})$, where it is assumed that $\sqrt{\frac{c_g}{6c_q}}$. In the dimensional form of Eq. (2.13), the values of the two proportionality constants c_g and c_q could in principle be determined from a rigorous analysis and/or obtained empirically from detailed experimental flame structure measurements. For convenience, for lack of information, and because a detailed discussion of these factors is beyond the scope of this work, they are set equal to unity. Eq. (2.13), with $c_g = c_q$, predicts that for the same opposed flow velocity a flame in a higher channel (larger h), with its smaller velocity gradient, will result in larger gas preheat and quenching distances. The final or fourth model for the narrow channel apparatus (NCA) accounts for the curvature in the Hagen-Poiseuille velocity profile, and in Eq. (2.6) employs the known velocity at the quenching distance for the relative velocity felt by the flame leading edge. Thus, $\delta_{g,NCA} = \frac{\alpha_g}{V_f + \left(\frac{6\overline{V}_g \delta_q}{h}\right)\left(1 - \frac{\delta_q}{h}\right)}$. Substituting Eq. (2.10) for the quenching distance and rearranging yields a cubic equation for the gas preheat length normalized by the channel height,

$$\hat{\delta}^3_{g,NCA} + C_2 \hat{\delta}^2_{g,NCA} - C_1 \hat{\delta}_{g,NCA} + C_0 = 0 \tag{2.14}$$

where $\hat{\delta}_{g,NCA} = \frac{\delta_{g,NCA}}{h}$, $C_2 = \frac{1}{c_q}$, $C_1 = \left(\frac{1}{6c_q^2}\right)\left(\frac{V_f}{\overline{V}_g}\right)$, $C_0 = \left(\frac{c_g}{6c_q^2}\right)\left(\frac{\alpha_g}{6\overline{V}_g}\right)$

A scaling analysis of Eq. (2.14) is performed in the Appendix (Eq. A.1) to produce an analytical expression for δ_g (model 4). A summary of the four models for the gas preheat length is found in Table 2.2

A comparison of the gas phase length scales is shown in Figure 2.9 for the case of gap height h = 5 mm (a) and h = 9 mm (b). Figure 2.9 (a) and Figure 2.9 (b) show that the Oseen approximation (model 1) deviates substantially from the other three models (models 2-4). Conversely, the agreement between models 2-4 is excellent over the entire flow range. Therefore, the key approximations of the linear gradient ‘A’ model, namely, a constant velocity gradient near the leading edge of the

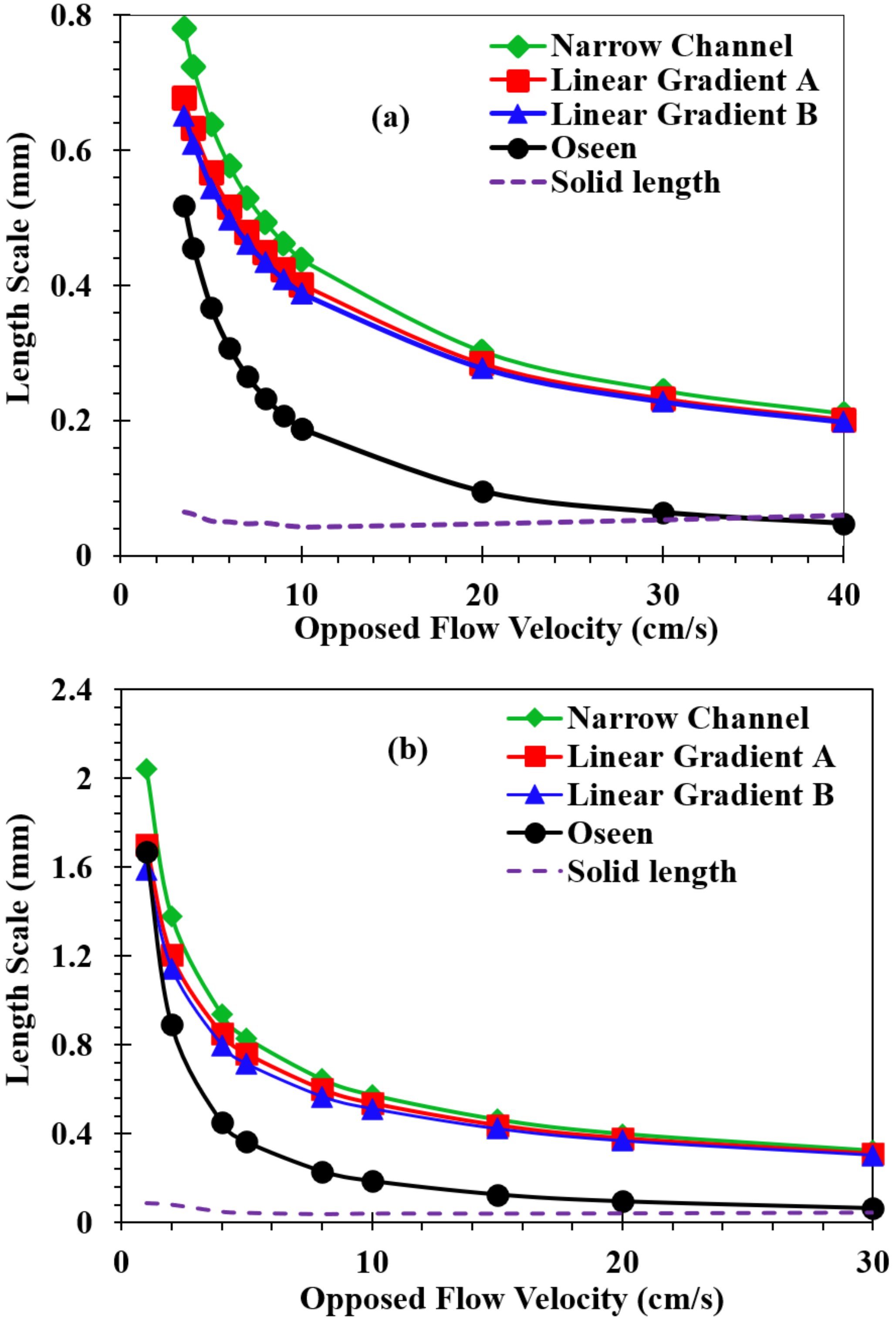

Figure 2.9: Characteristic solid and gas preheat length scales. (a) For channel height h = 5 mm. (b) For channel height, h = 9 mm. The Oseen model (model 1) approaches the three velocity gradient models (models 2 - 4) only at the lowest opposed flow velocities shown.

flame, and a flame velocity much less than the opposed gas velocity (at the leading edge) appears to be valid even for the lowest opposed velocities that still support flame spread. Also, from Figure 2.9 (b) for gap height h = 9 mm, at the lowest opposed flow velocity of 1cm/s, the Oseen model shows good agreement Linear gradient A and Linear gradient B models. As seen, the agreement is better for h = 9 mm than h = 5 mm for the lowest opposed flow velocity.

Table 2.2: Models 1–4 for the velocity observed by the flame in flame-fixed coordinates. Each model produces a different characteristic gas phase characteristic length.

Model	Opposed flow velocity in flame coordinates	Gas phase characteristic length, δ_g
Model 1 (Oseen)	Average flow velocity	$\delta_s \sim \frac{\alpha_g}{V_r} = \frac{\alpha_g}{V_f+U_g}$
Model 2 (Linear Gradient A)	Velocity at quenching layer (assumed constant velocity gradient with $V_f \ll V_{ox}$)	$\delta_{g,LinGradA} = \sqrt{\frac{c_g}{6c_q}\left(\frac{\alpha_g h}{\overline{V}_g}\right)}$
Model 3 (Linear Gradient B)	Velocity at quenching layer (assumed constant velocity gradient, V_f retained)	$\delta_{g,LinGradB} = \frac{-h}{12c_q}\left(\frac{V_f}{\overline{V}_g}\right)$ $+h\sqrt{\frac{1}{144c_q^2}\left(\frac{V_f}{\overline{V}_g}\right)^2+\frac{c_g}{6c_q}\left(\frac{\alpha_g}{\overline{V}_g h}\right)}$
Model 4 (Parabolic Channel Flow)	Velocity at quenching layer, (parabolic velocity profile)	$\delta_{g,NCA} = \sqrt{\frac{c_g}{6c_q}\left(\frac{\alpha_g h}{\overline{V}_g}\right)}$ $x\left[1+\frac{\sqrt{c_g c_q}\sqrt{\frac{\alpha_g}{6\overline{V}_g h}}}{\frac{1}{\sqrt{c_g c_q}}\frac{V_f}{\overline{V}_g}\sqrt{\frac{6\overline{V}_g h}{\alpha_g}}+2}\right]$

2.4.2.3 Comparison of Solid Length Scale and Gas Length Scale

Figure 2.10 shows the solid and gas preheat lengths of Eqs. (2.5) and (2.14), respectively, versus $\overline{V}_g$ for the four gap heights on logarithmic axes. The gas preheat lengths, calculated using the NCA model of Eq. (2.14) are an order of magnitude larger than the solid preheat lengths. Even though the characteristic gas phase velocity is much bigger than the solid velocity, the larger thermal diffusivity

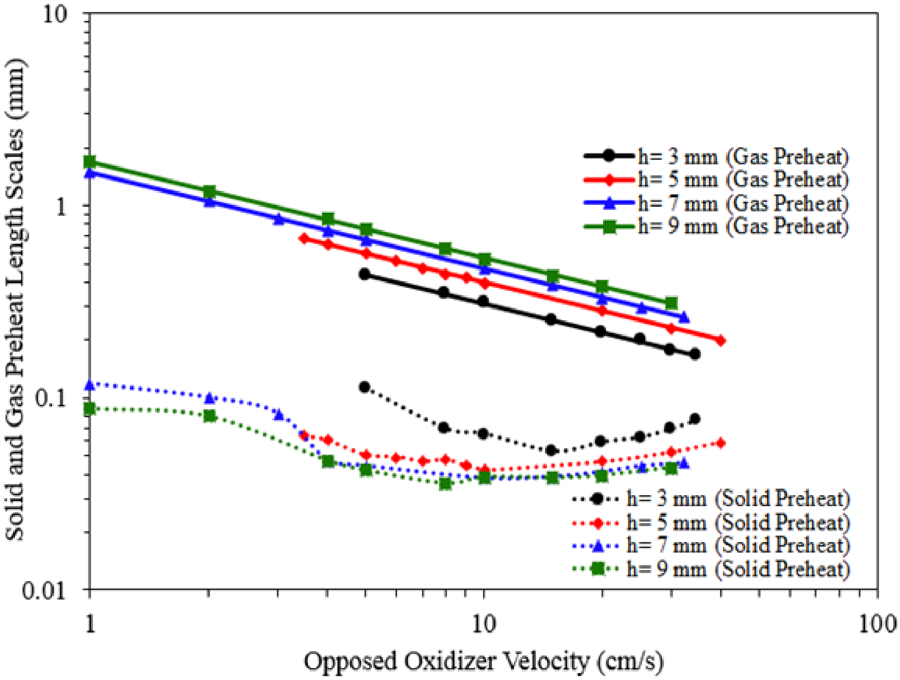

Figure 2.10: Characteristic preheating lengths for channel heights h = (3, 5, 7, 9) mm on a log-log scale. The gas phase length (using the NCA model) is an order of magnitude larger than the solid phase length except when $\overline{V}_g$ increases to values larger than O (10 cm/s).

of the gases still produces a much larger δ_g than the calculated δ_s. The result, $O(\delta_g) >> O(\delta_s)$), indicates that there is an important mechanism for preheating the solid from the gas preheat layer. Since the sample fuel is thin, the path for the heat transfer through solid phase is restricted. Most of the heat transfer occurs by conduction through the gas phase, or by radiation. This aspect of predominant heat transfer through the gas phase was discussed in an excellent early review of flame spread [37]. Nevertheless, the higher is the opposed flow, the (relatively) smaller is the gas preheat layer. Also, the greater is the gap height, the (relatively) larger is the gas preheat layer due to the diminished velocity gradients near the wall. It is expected that for this case the Oseen model (model 1), despite its structural unreality, would provide acceptable flame spread rate predictions.

2.4.2.4 Normalization of the Flow Velocity

The opposed flow velocity can be normalized by using a diffusion velocity for oxygen, defined as

$$V_{g,diff} = \frac{D_{o_2}}{\delta_g} \tag{2.15}$$

where D_{o_2} is the diffusion coefficient of oxygen into the gas mixture. It follows that a dimensionless opposed flow velocity may be defined as

$$\hat{V}_g = \left(\frac{\delta_g \overline{V}_g}{\alpha_g}\right)\left(\frac{\alpha_g}{D_{o_2}}\right) \tag{2.16}$$

which equals unity when $\overline{V}_g = \frac{D_{o_2}}{\delta_g}$ is substituted from Eq. (2.15). Here the Lewis number, $Le = \alpha/D$ has been introduced by multiplying and dividing by α_g. For the Linear Gradient 'A' model (with $V_f << \overline{V}_g$) the use of Eq. (2.13) for δ_g gives

$$\hat{V}_g = \sqrt{\frac{c_g}{6c_q}\left(\frac{\alpha_g h}{\overline{V}_g}\right)}\left(\frac{\overline{V}_g}{\alpha_g}\right) Le = \sqrt{\frac{c_g}{6c_q}} Le \sqrt{\left(\frac{\overline{V}_g h}{\alpha_g}\right)} \tag{2.17}$$

The above $\hat{V}_g$ has the functionality

$$\hat{V}_g = C.Le.Pe^{1/2} \tag{2.18}$$

A variant of Eqs. (2.17) and (2.18) was originally derived from a theoretical analysis of flame spread into an opposed linear velocity gradient flow [10, 13]. The analysis produced an estimate for the proportionality indicated here and also produced a correlation that described finite-rate chemistry influences on flame spread [9]. The consequences of this model were analyzed and compared with data using several flame spread correlations [13]. The finite chemistry aspects were studied in detail in [9]. The physico-inuitive analysis developed here does not utilize the governing equations but uses concepts of engineering modeling to develop the general formula of Eq. (2.14) which is simplified for linear velocity gradient flows to produce Eq. (2.13). The latter result, as mentioned, is also the consequence of a rigorous analysis [9, 10, 13].

In Figure 2.11 the overall flame equivalence ratio is plotted against the dimensionless opposed flow velocity. Below a dimensionless opposed flow velocity of approximately one (1), the flames are rich with the constants c_g and c_q of Eqs. (2.12), (2.13) set to unity. In order to normalize the dimensionless velocity to unity, C = 0.5 is used in Eq. (2.18). The vertical dashed line is placed

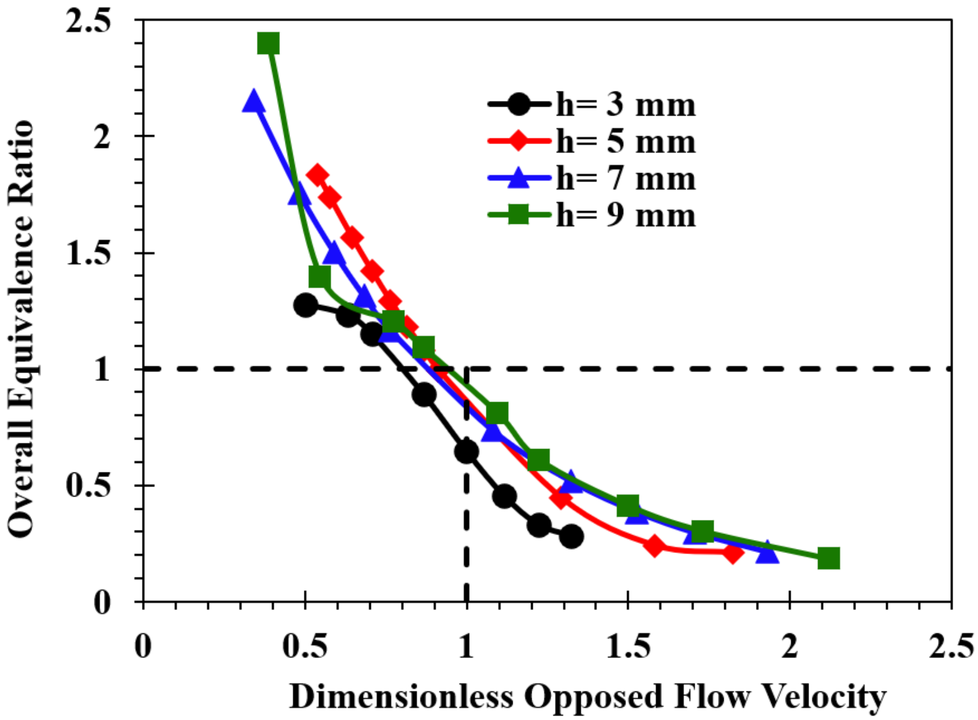

Figure 2.11: Overall equivalence ratio versus dimensionless opposed flow velocity. The horizontal dashed line is the stoichiometric condition separating lean from rich flames. The vertical dashed line represents the dimensionless opposed flow velocity of unity. The latter has been formed as the ratio of average flow velocity and characteristic diffusion velocity, see Eqs. (2.15) and (2.16).

where the dimensionless opposed flow velocity is unity, that is, where the opposed flow velocity equals the diffusion velocity. There is good correlation for gap heights h =(5, 7, 9) mm, whereas the case h = 3 mm deviates, an effect attributed in the next section to a higher heat loss. The horizontal dashed line separates over-all lean from rich flames.

2.4.3 Theoretical Analysis and Correlations: Heat Losses

2.4.3.1 Heat generation

There are two cases to consider for the calculation of the total heat generation by combustion in the NCA: (1) When $\phi > 1$ there is excess fuel available for combustion. All of the oxidizer is used to burn fuel. In this case, $\delta_0 > h$. An insufficient quantity of oxidizer is available for combustion of the fuel. (2) When $\phi = 1$ the stoichiometry permits all of the oxidizer to burn all of the available fuel. This case produces $\delta_0 = h$, meaning that the stoichiometric oxygen distance equals the NCA gap height. (3) When $\phi < 1$ (as illustrated in Figure 2.5) there is excess oxidizer available. This produces $\delta_0 < h$, which allows all of the fuel to be consumed. These cases were evaluated separately: $\phi \geq 1$: For the excess fuel and stoichiometric cases (1) and (2), respectively, $\phi \geq 1$ so that $\frac{\delta_0}{h} = 1$. The heat release by the flame is given by

$$Q_{flame} = \dot{m}_{ox} \triangle h_{ox}$$

Here $\dot{m}_{ox} = 2\rho_g Y_{ox}(V_f + \overline{V}_g)$ is the mass flow rate of oxidizer into the NCA and $\triangle h_{ox}$ is the heat release for the fuel on a per oxygen mass basis, given by approximately 13.1 MJ/kgO2 as the lower heating value [38].

$\phi < 1$: This case requires that the available oxidizer and therefore the heat release must be diminished by the factor $\delta_0/h < 1$, viz.

$$Q_{flame} = \dot{m}_{ox} \frac{\delta_0}{h} \triangle h_{ox}$$

Thus, the heat release by the flame can be written as:

$$\dot{Q}_{flame} = \left\{ \begin{array}{cc} 2\rho_g Y_{ox}(V_f + \overline{V}_g) hw \triangle h_{ox} & \phi \geq 1 (\delta_0 = h) \\ 2\rho_g Y_{ox}(V_f + \overline{V}_g) hw \frac{\delta_0}{h} \triangle h_{ox} & \phi < 1 (\delta_0 < h) \end{array} \right\} \tag{2.19}$$

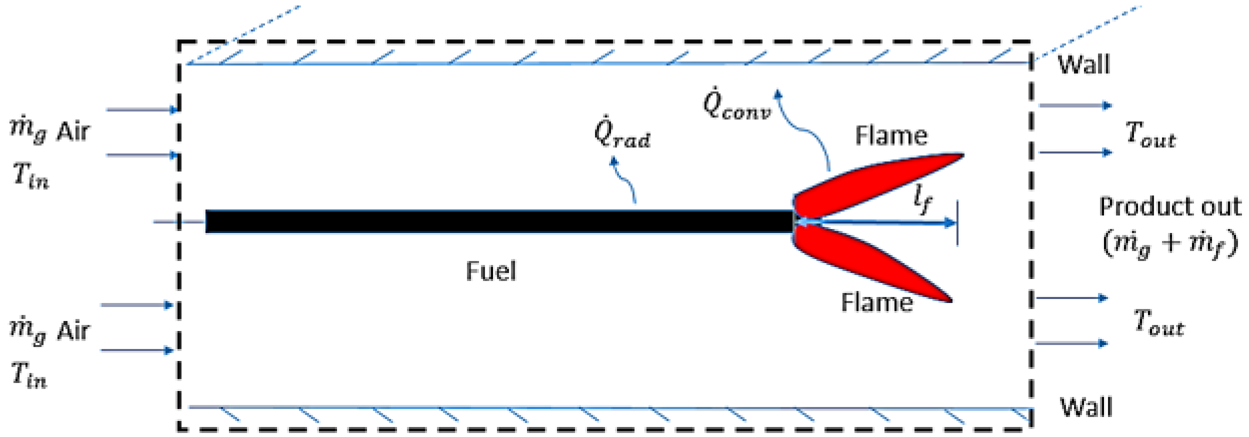

Figure 2.12: Schematic of the narrow channel apparatus where the dashed line represents the control volume of the system.

2.4.3.2 Heat Loss

The following control volume analysis describes quantitatively the heat losses in the NCA. In, Figure 2.12 oxidizer enters the system from the left side at temperature T_{in}, velocity $\overline{V}_g$ and mass flow rate $\dot{m}_g$. During combustion, the oxidizer reacts with the solid fuel as product gases leave the control volume. The mass flow rate out of the system is written as $\dot{m}_g + \dot{m}_f$.

The expressions for the contributions to the energy balance are: Heat input into the control volume:

$\dot{Q}_{in} = \dot{m}_g cp,g(T_{in} - T_\infty) = \rho_g \overline{V}_g (hw) cp,g(T_{in} - T_\infty)$

Heat release rate leaving the control volume:

$\dot{Q}_{out} = \dot{Q}_{rad} + \dot{Q}_{conv} + \dot{Q}_P$

Here, $\dot{Q}_{rad}$ is the heat loss to the ambient by radiation, $\dot{Q}_{conv}$ is the heat loss to the wall due to convection and $\dot{Q}_P$ is the enthalpy rise of the product gases. The total heat loss is given by

$\dot{Q}_{loss} = Q_{out} - Q_{in} = \dot{Q}_{rad} + \dot{Q}_{conv} + \dot{Q}_P - \rho_g \overline{V}_g (hw) cp,g(T_{in} - T_\infty)$

where the oxidizer inlet temperature T_in is taken to be equal to T_∞. Thus

$$\dot{Q}_{loss} = \dot{Q}_{rad} + \dot{Q}_{conv} + \dot{Q}_P \tag{2.20}$$

In the following subsections the three terms on the RHS of Eq. (2.20) are discussed.

2.4.3.3 Radiative Heat Loss

The heat loss by radiation to the ambient is evaluated from the expression

$\dot{Q}_{rad} = \epsilon \sigma w h (T_s^4 - T_\infty^4)$

where ϵ is the emissivity of the fuel, wh is the surface area of the fuel, σ is the Stefan-Boltzman constant and T_s is the surface temperature which can be taken as the fuel pyrolysis temperature.

2.4.3.4 Convective Heat Loss

The convective loss to the NCA walls is now evaluated. In a previous study, Elipidorou et al. [39] produced an expression for the convective heat transfer to the walls of a channel when one of the walls was a finite-length heat source and the entire other wall was a heat sink. To evaluate the convection loss term for the NCA a similar approach is considered here. The upper NCA wall is understood as the heat sink, and the flame, which essentially occurs as a heated region trailing the burning sample (Figure 2.1 and Figure 2.12), is understood as the finite-length heat source. Symmetry of the configuration allows evaluation of the heat loss to only one wall. The flame length l_f corresponds to the the length of the heat source.

For laminar flow, the Nusselt number in a channel with a finite heat source (flame) is given by Elipidorou et al. [39] as $\overline{Nu}_{l_f} = 1.166 Re_{l_f}^{0.393}$, where $Re_{l_f} = \frac{\overline{V}_g l_f}{\nu}$. In this steady state analysis, the temperature of the heated segment is $\overline{T} = \frac{T_F + T_\infty}{2}$. Thus, the heat losses from the flame to one NCA wall are given by

$$\dot{Q}_{conv} = h_c l_f w(\overline{T} - T_\infty) = \overline{Nu}_{l_f} kw(\overline{T} - T_\infty) = 1.166 \left(\frac{\overline{V}_g l_f}{\nu} \right)^{0.393} kw(\overline{T} - T_\infty)$$

2.4.3.5 Product Gas Enthalpy Rise

To evaluate this term, the enthalpy rise of both the fuel and oxidizer are calculated. The enthalpy rise of the solid fuel leaving the control volume is $\dot{Q}_f = \dot{m}_f c_{p,f}(T_{out} - T_\infty) = \rho_f t_f w V_f c_{p,f}(T_{out} - T_\infty)$. The enthalpy rise of the oxidizer entering the control volume is $\dot{Q}_g = \dot{m}_g c_{p,g}(T_{out} - T_\infty) = \rho_g \overline{V}_g (hw) c_{p,g}(T_{out} - T_\infty)$. The net enthalpy rise of the product gases is therefore given by, $\dot{Q}_P = \dot{Q}_f + \dot{Q}_g = \rho_g \overline{V}_g (hw) c_{p,g}(T_{out} - T_\infty) + \rho_f t_f w V_f c_{p,f}(T_{out} - T_\infty)$

2.4.3.6 Total Heat Loss

After substituting $\dot{Q}_{rad}$, $\dot{Q}_{conv}$ and $\dot{Q}_P$ in Eq. (2.20), the total heat loss by the flame is obtained as

$$\dot{Q}_{loss} = \epsilon \sigma w h (T_s^4 - T_\infty^4) + 1.166 \left(\frac{\overline{V}_g l_f}{\nu} \right)^{0.393} kw(\overline{T} - T_\infty) + \rho_g \overline{V}_g (hw) c_{p,g}(T_{out} - T_\infty) + \rho_f t_f w V_f c_{p,f}(T_{out} - T_\infty) \tag{2.21}$$

2.4.3.7 Dimensionless Heat Loss

The dimensionless ratio of heat losses to flame heat generation is $\hat{Q}_{loss} = \frac{\dot{Q}_{loss}}{\dot{Q}_{flame}}$. Substitution of Eq. (2.19) and (2.21) results in

$$\hat{Q}_{loss} = \kappa \left\{ \begin{array}{cc} 1 & \phi \geq 1 \\ \frac{1}{\frac{\delta_0}{h}} & \phi < 1 \end{array} \right\} \tag{2.22}$$

where

$$\kappa = \frac{\epsilon \sigma w h (T_s^4 - T_\infty^4) + 1.166 \left(\frac{\overline{V}_g l_f}{\nu}\right)^{0.393} k w (\overline{T} - T_\infty)}{2\rho_g Y_{ox} (V_f + \overline{V}_g) h w \triangle h_{ox}} + \frac{\rho_g \overline{V}_g (hw) c_{p,g} (T_{out} - T_\infty) + \rho_f t_f w V_f c_{p,f} (T_{out} - T_\infty)}{2\rho_g Y_{ox} (V_f + \overline{V}_g) h w \triangle h_{ox}} \tag{2.23}$$

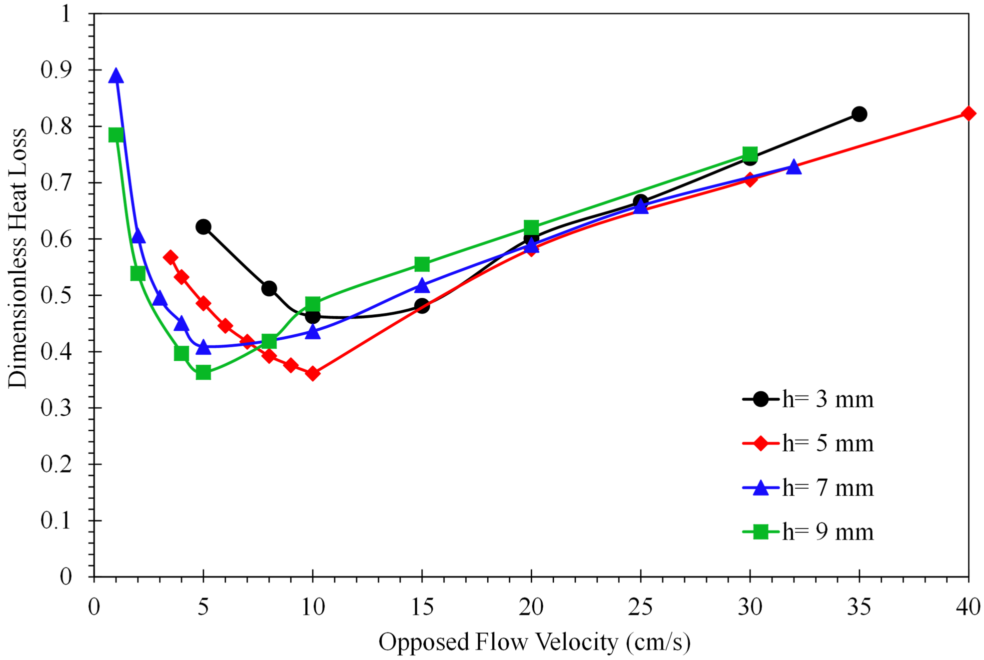

Figure 2.13: Dimensionless heat loss versus opposed flow velocity for gap heights (h=3,5,7 and 9) mm.

This dimensionless heat loss is plotted as a function of the opposed flow velocity in Figure 2.13 for NCA. In this plot Eq. (2.22) is the ordinate for $\phi \geq 1$ and $\phi < 1$. This figure shows that the heat losses attain a minimum value for all gap heights. Although it appears that the heat losses

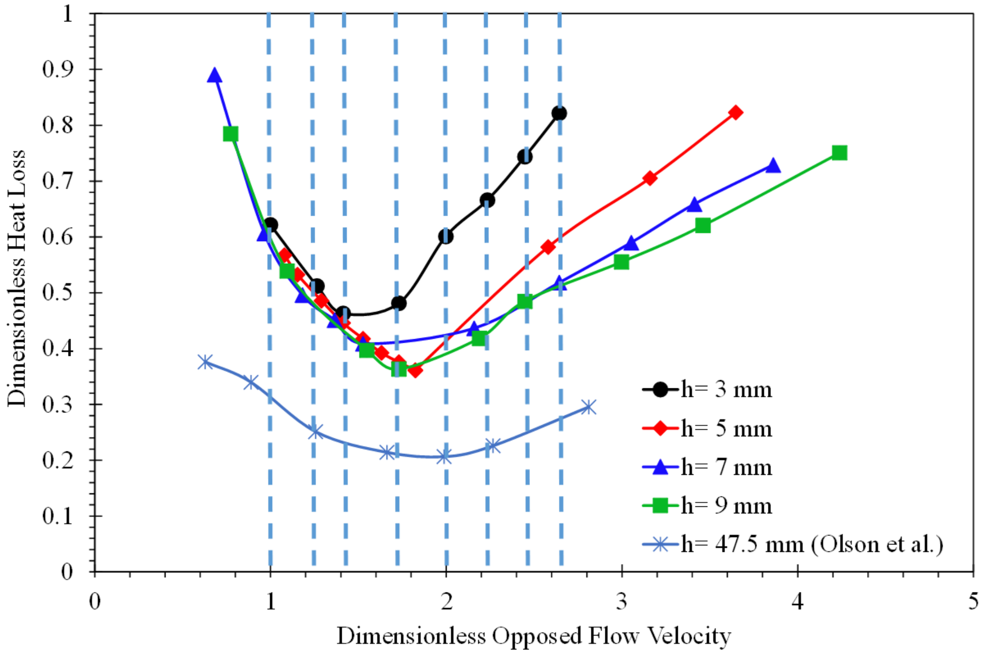

Figure 2.14: Dimensionless heat loss versus dimensionless opposed flow velocity, Eq. (2.18). Ratios of the dimensionless heat loss are evaluated at the dashed lines at selected values of the dimensionless opposed flow velocity. The curve for h = 47.5 mm represents one RITSI test in actual microgravity [36]. The value C=1 is used in Eq. (2.18).

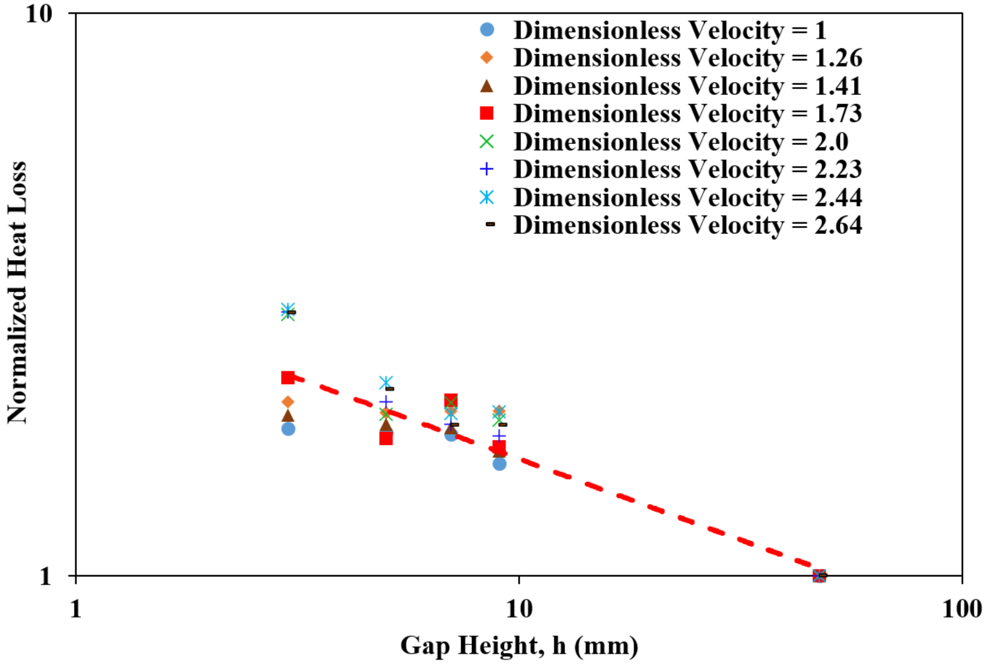

Figure 2.15: Nondimensional heat loss data from Figure 2.14 normalized with the RITSI data for microgravity testing with channel height h = 47.5 mm. The correlation is given by Eq. (2.24).

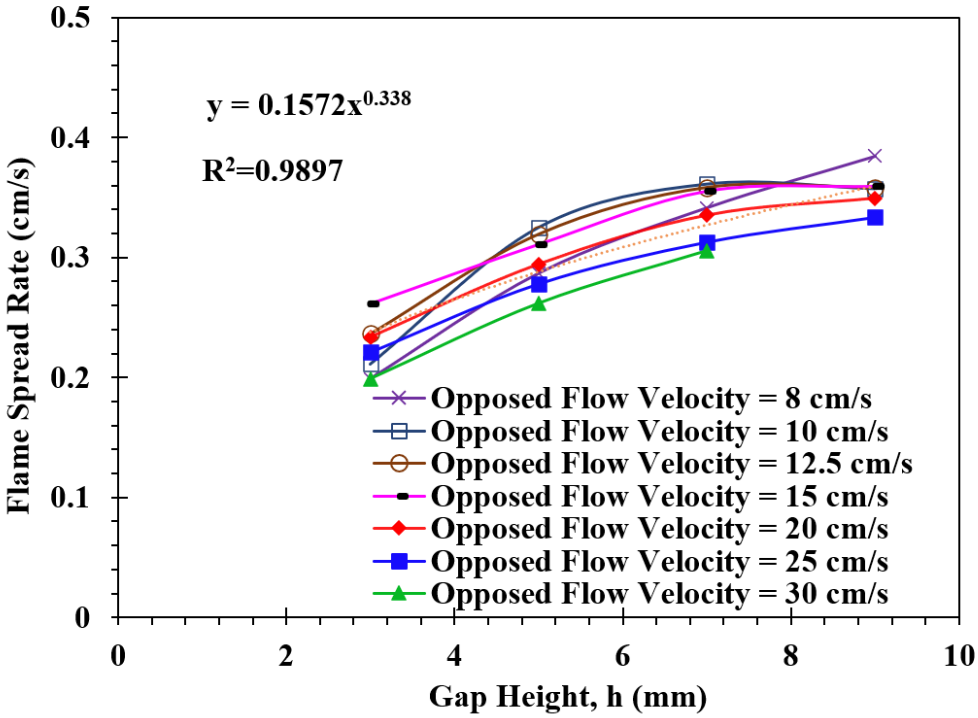

Figure 2.16: Flame spread rate versus gap height for different opposed flow velocities taken from the data of Figure 2.2 (vertical dashed lines).

for h = 7, 9 mm become large at the lowest opposed flow velocities (of order 1 cm/s) it must be noted that the flames for h = 3, 5 mm are already extinguished. Stated differently, the data for small velocities of $O(1) cm/s$ for h=7 and 9 mm are largely inconsequential because, due to the high heat losses for h = 3 and 5 mm, these flames have already extinguished for $\overline{V}_g$ less 5 cm/s and 3.5 cm/s, respectively. For the higher velocity ranges $\overline{V}_g \sim 15 - 35 cm/s$ for all gaps, the heat loss is always smallest when h=5 mm . In Figure 2.14 the dimensionless velocity $\hat{V}_g$ given by Eq. (2.18) is used as the abscissa. This allows comparison of the relative heat losses by a common standard. Shown also are the RITSI data of Olson et al. for actual microgravity experiments [36]. This graph shows several things: (1) The relative heat losses for $h = 3mm$ are always the largest; (2) The minimum of the heat losses occurs for $h = 3mm$ at a significantly lower $\hat{V}_g$ than the other h values; (3) The $h = 7$ and $9mm$ cases are virtually indistinguishable meaning that by $h = 7mm$ we already have a "high" channel; (4) Nevertheless, the RITSI data are still far lower in terms of overall heat loss.

In Figure 2.15, the dimensionless heat loss is normalized with the microgravity RITSI data.

This figure shows the dependence of the dimensionless heat losses on the channel height. The data, taken from the vertical dashed lines shown in Figure 2.14 and assembled in Figure 2.15, generate the empirical correlation

$$\hat{Q}_{loss} = \frac{3.12}{h^{0.28}} \tag{2.24}$$

This correlation is compared with the analytical content of Eq. (2.22). The dependence of the flame spread rate on the channel height is found from examination of the data in Figure 2.2 (vertical dashed lines) and it produces the correlation shown in Figure 2.16, namely $V_f = 0.16h^{0.338}$. This is an approximately $V_f \sim h^{1/3}$ functional dependence, which compares well functionally with the experimental dependence given by Eq. (2.24), which can be written in order-of-magnitude form as $\hat{Q}_{loss} \propto V_f \propto h^{-1/3}$.

2.5 Summary

A scaling analysis shows that flames at low flows become fuel rich when the forced flow becomes of comparable magnitude with the diffusive flow Figure 2.11. The heat loss increases as the quenching distance increases relative to the gap height at low flow, thereby increasing conductive losses to the confining walls. The theory leading to Eqs. (2.12) and (2.17) produces results that are in agreement with previous modeling efforts [9, 10, 13]. This agreement is encouraging, since flame spread in spatially variable velocity fields is a relatively unexplored research topic.

Buoyancy suppression is achieved by making the gap narrow. However, narrowing the gap increases heat losses to the confining walls as shown in Figure 2.13 and Figure 2.14. Of the cases investigated, a gap height h $\approx$ 5 mm between fuel and confining wall yields a good compromise between buoyancy suppression and wall heat losses in the Narrow Channel Apparatus.

There are two aspects of flame spread research that are of broader significance in this work than correlating experimental results with an integral model. In the first aspect, this work addresses a central problem of classical flame spread, in which the velocity field plays a major role. How best to accommodate the velocity profile has been a question ever since the theory of flame spread was put forward by deRis [5].

Subsequent to the Oseen flow theory of deRis, the velocity gradient theory was developed in the 1980s [9, 10, 13]. Verification and validation of its predictions has been scant because measurements are difficult and familiarity with the theory is challenging. This chapter provides viable experimental measurements for verification, and in addition develops a simplified, accessible version of that theory. Comparisons between the three versions of the velocity gradient theory and also with the Oseen theory points not only to the relative benefits of the velocity gradient theory but also to the appropriate uses of the Oseen theory. Figure 2.9. a, b show that the Oseen curve approaches closest to the velocity gradient curves as the opposed flow decreases, as should be expected for these two theories.

Additional details of the flame spread mechanism can be discussed in the context of this model, such as quenching distance theory for describing the approach of diffusion flame leading edges to the cold surfaces over which they spread [40, 41]. In the current work the order unity constants c_g and c_q are set equal to unity. In the articles referenced above on diffusion flame leading edges these “constants” depend on the chemical features of the problem, such as the activation energy and other reaction rate parameters. Important basic physics has been subsumed in these parameters.

Heat losses and their dependence on the channel height h are evaluated. Although it was shown by examination of the velocity profiles that the velocity gradient theory accounted for the flow physics, the dependence of the flame spread rate on channel height h cannot be deduced simply from $V_f \propto \sqrt{\frac{du}{dx}}$, which implies that in the flame spread formula for narrow channel flames there must be a heat-loss factor and a finite-chemistry factor that account for the additional h-dependence.

This thin fuel study will be extended for thick fuel in Chapter 3. The investigation involved extensive testing, numerical analysis and theoretical formulation. Experiments are performed here at Michigan State University. Cast PMMA is considered as fuel sample. The primary objective of the experimental work is to assess the flame spread rate as a function of sample thickness and opposed flow velocity. The results are compared with literature by performing numerical analysis. Furthermore, a theoretical correction is introduced to improve the comparison.

CHAPTER 3

OPPOSED FLOW FLAME SPREAD OVER THERMALLY THICK SOLID FUELS: BUOYANT FLOW SUPPRESSION, STRETCH RATE THEORY, AND THE REGRESSIVE BURNING REGIME

Synopsis

In this chapter, the Michigan State University Narrow Channel Apparatus (MSU-NCA) is used to investigate opposed flow flame spread over samples of thermally thick Polymethylmethacrylate (PMMA). Three different fuel thicknesses were tested for mean airflow velocities 8-58 cm/s. The sample thicknesses were 6.6 mm, 12.1 mm and 24.5 mm, respectively. The measured flame position versus time determined the spread rate. Flame spread rates ranged between 0.02 - 0.07 mm/s depending on fuel thickness and mean opposed flow. Complete sample burnout occurred for the 6.6 mm and 12.1 mm samples at the critical flow velocity of 30 cm/s ± 5 cm/s and higher. The flame spread results appeared to be independent of flow velocities for this range (>30 cm/s): this plateau regime is identified as the regressive burning regime. The 24.5 mm thick samples never completely burned through, but they entered the regressive burning regime at 41.4 cm/s flow velocity. The nature of surface regression and its influence on the spread mechanism in this regime at high flow velocities was discussed for completely burned through samples (6.6 mm and 12.1 mm) and partially burned through samples (24.5 mm). For 12.1 mm thick samples, the flame spread results were compared with the same material (PMMA) and similar thickness (12.7 mm) results from the 1981 Fernandez-Pello et al. study. Their tests used a wind tunnel having a different length and cross-section than the MSU-NCA. The comparison was favorable when employing the stretch rate theory of flame spread incorporating the appropriate numerically computed stretch rate. Since buoyancy was an important factor in the 1981 study, when the buoyant stretch was also included, excellent agreement was obtained between the Fernandez-Pello et al. data and the current NCA data. The work presented in this chapter is also published as journal article in Hossain et al. [27].

3.1 Introduction

The propagation of fire in actual or simulated microgravity is different than on Earth. Earth's gravity often dictates many characteristics of diffusion flame behavior during flame spread, even in smaller scale flames. The buoyancy induced flow field on earth can generate a complex flow-flame interaction by modifying the transport processes affecting thermal energy and species transport during flame spread over solid fuels. By contrast, combustion in microgravity, whether actual or simulated, does not show all of these complex phenomena, although there are other complications. Rather, it provides a more symmetric and uniform configuration for examining experimental and theoretical features of diffusion flame spread.

The purpose of this chapter is to make a detailed comparison between the current experimental work, which uses a simulated microgravity apparatus (the Narrow Channel Apparatus, or NCA) in which buoyancy is suppressed, and an acclaimed prior study using a related but different apparatus in which buoyancy was not actively suppressed. Given that the experimental configurations and ranges of validity of these two apparatuses differ the question is, can valid comparisons based on theoretical and numerical analysis be made? This chapter intends to answer that question: (1) by carefully examining flame spread behavior when buoyancy is suppressed (in the current work) and is not suppressed (in the previous work); (2) by attempting to make these comparisons systematically using the stretch rate theory of flame spread; (3) by demonstrating excellent agreement for all of the data except those gathered in the current NCA that suggest the appearance of a type of flame spread herein referred to as the regressive burning regime of flame spread.

In the current flame spread study, the independent parameters (1) sample thickness and (2) opposed flow rate were varied for spread over a nominally thermally thick PMMA sample. Experiments were performed in the Michigan State University NCA facility for a mean inflow oxidizer flow velocity range of 8-58 cm/s over PMMA sample thicknesses of 6.6 mm, 12.1 mm and 24.5 mm.

The structure of this chapter is as follows: Section 3.2 provides a review of previous pertinent work on this and related subjects. Section 3.3 describes the experimental facilities, test procedures, and determinations of possible experimental uncertainty. The data from the NCA tests and experimental results are presented in Section 3.4 and compared with Fernandez-Pello et al. [7] results. In Section 3.5, a CFD analysis and theoretical correlations form the basis for a stretch rate theory comparison of the current flame spread data with the Fernandez-Pello et al. [7] data. Section 3.6 draws some conclusions from this work.

3.2 Previous Work

Several prior theoretical [6, 9, 10, 13, 42] and numerical [43–45] investigations have been conducted to understand the complex interaction between the gas phase and the solid phase during solid fuel flame spread and combustion. Factors that influence the flame spread mechanism include gravity level, pressure, oxygen concentration, flow velocity, velocity gradient, flow orientation (opposed or concurrent), fuel type, and fuel sample dimensions. All of these factors have been studied in past research although a comprehensive understanding is still lacking.

The prior work on which the attention is focused, herein is that of Fernandez-Pello et al. [7], who experimentally studied the influence of opposed flow velocity for thick PMMA (12.7 mm) and thin (0.2 mm) fuel paper sheets in a small wind tunnel which was not, however, a Narrow Channel. They found, for oxygen mass fractions ranging from 0.211 to 0.329, that the flame spread rate is constant in a regime in which buoyancy played an important role and thereafter decreases with continued increase of the flow velocity. As the oxygen mass fraction further increases by steps to unity the flame spread rate first increases with increased opposed flow velocity and then decreases monotonically until final blowout. In general, flame spread on Earth can be strongly influenced by buoyancy which is a dominant factor at low flow velocity/stretch rates, and may result in elevated distances between fuel surface and flame (Figure 3.1 (a)) This feature is different from flame spread behavior in actual and simulated microgravity in the NCA, where the flame appears relatively closer to the fuel surface over the entire length of the flame (Figure 3.1 (b)) because of buoyancy suppression. Several experiments have been conducted in actual and simulated microgravity to study this behavior. Most of the prior studies have considered thin fuel

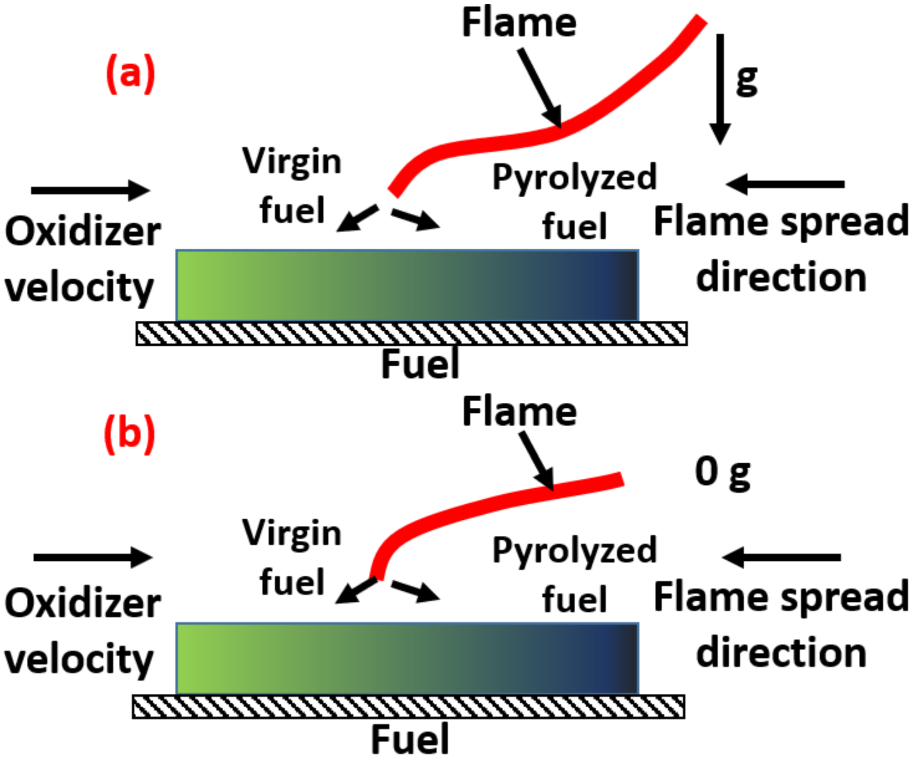

Figure 3.1: Horizontal flame spread mechanism (a) on-Earth (b) in microgravity. In (a) flame attachment at the leading edge occurs further from the surface than in (b) due to buoyancy domination at low opposed flow velocity. The trailing flame is also generally situated further from the surface for (a) (all other factors being equal).

samples, e.g. [21, 26, 28, 30, 31, 33, 46–49]. By comparison, relatively few microgravity flame spread experiments have been performed for thick samples [16, 19, 49–52]. In [50], flame spread over a thick PMMA sample was studied in a quiescent atmosphere (50 % O2 and 50 % N2) at 1 atm pressure. The results showed that during propagation the mass diffusion scale continued to grow over time until the oxygen diffusion rate could no longer sustain it. The flames self-extinguished by excessive radiative heat loss since the weakened flames could not generate sufficient sustaining chemical energy. In [19], thick solid fuel (black PMMA) microgravity surface burning was studied using a variable airflow velocity. In these experiments, the average burn time was approximately six (6) minutes. The results showed a square-root power-law dependence of the flow velocity on flame spread rather than the linear dependence predicted by theory [5]. In [16] a series of concurrent-flow flammability tests were conducted on the International Space Station (ISS) for flow velocities 0 - 55 cm/s for three sizes of clear and black PMMA rods. This work examined flame spread behavior near the quenching and blowoff limits. In [18], flame spread over thick PMMA rods was tested for variable oxygen concentrations (15-21%) and low flow velocities 0.4 - 8 cm/s in microgravity and then compared with normal gravity experiments of similar samples. The results showed that flame spread in microgravity was faster and more sustainable at lower oxygen concentrations than in normal gravity. Experiments [49] were conducted inside an orbiting spacecraft with thick PMMA (10 mm thick) flat samples for concurrent airflow rates between 20-25 cm/s. In BASS-II testing, five thicknesses (1-5 mm) of rectangular PMMA of two widths for both one sided and two sided burning were studied at various oxygen concentration levels [51]. The results showed that for the one-sided burning as the sample thickness increased, the oxygen concentration at extinction decreased but the forced flow velocity at extinction increased. On the other hand, for the two-sided samples the dependency of thickness on flame spread was inconsistent. However, the extinction velocities were significantly lower than for the one-sided samples, indicating, as expected, that heat loss to the substrate for the one-sided flame was greater than for the two-sided flame without a substrate. Microgravity experiments were conducted aboard the SJ-10 satellite by Zhu et al. [52] for 50 mm wide by 10 mm thick PMMA samples. Four oxygen concentrations (40%, 35%, 30% and 25%) and four low flow velocities (9, 6, 3 and 0 cm/s) were used. At a given fixed oxygen concentration, ranging from high to low flow velocity, two distinctive spread modes were observed. These were (1) continuous flame spread and (2) the flamelet mode of flame spread.

It is difficult and expensive to perform true microgravity combustion experiments for thermally thick fuels. Hard impediments for thermally thick experiments in the ISS are short test durations driven by astronaut availability, and limited heating rates driven by size (up mass), limited chamber volumes and heat generation constraints in the closed ISS environment. In contrast, the Narrow Channel Apparatus (NCA) provides an alternative approach to simulate microgravity on earth, allowing an inexpensive experimental approach to study microgravity combustion of thermally thick fuels.

Recent normal gravity horizontal narrow channel experiments using thick fuels in an opposed flow were performed by Matsuoka et al. [53]. Thermally thick (10 mm) PMMA samples were burned for a range of gap heights and two fuel geometries (i.e., sample sizes). The tests showed that for a relatively small gap (1-2 mm) the flame spread rate increases with gap height. As the gap height was further increased, the flame spread rate began to decrease. The transition is a function of the flow velocity and geometrical cross section. For a rectangular channel, the flame spread rate reached a peak value at 4 mm and 3 mm gap heights at 30 and 90 cm/s flow velocities, respectively. The influence of the approach flow velocity was studied in [54] by Matsuoka et al. They varied the flow rate for a 10 mm thick PMMA sample and produced a flammability map as a function of both oxidizer flow velocity and gap height. Zhu et al. [55] investigated flame spread and extinction phenomena over a thick sample of PMMA (10 mm) in both opposed and concurrent flows over low velocity ranges. Since the data in [53–55] used a different sample thickness than the 12.1 mm thickness employed herein, comparisons between these important experiments and the current data are not made.

3.3 Description of Experiment and Test Procedures

3.3.1 Experimental Setup/ Description of NCA Design

All of the experiments discussed herein were conducted in the horizontal Narrow Channel Apparatus (NCA). Figure 3.2 shows a schematic of the NCA test setup, which consists of three main sections: (1) inlet, (2) test section, and (3) outlet. Air is admitted through the entrance ports of the sidewalls and passes through the inlet section into the test section. It travels through six 200 mesh screens and a 3.28 mm cell honeycomb flow straightener, see Figure 3.2 (a). This ensures a straight laminar flow entering the test section. This approach to flow straightening and control has been extensively discussed, and measured using hot wire anemometry, in prior research [33, 56]. There it was also demonstrated that when the NCA cross section is much wider than its height (here of order 100:1), the approach flow at the leading edge of the sample was a laminar, Hagen-Poiseuille flow.

Figure 3.2 (b) shows the test section, which consists of several individual key components, including the top plate, the bottom plate, sidewalls, igniter wire and sample holder. The top aluminum plate contains a slot for the optically accessible quartz window. The bottom aluminum

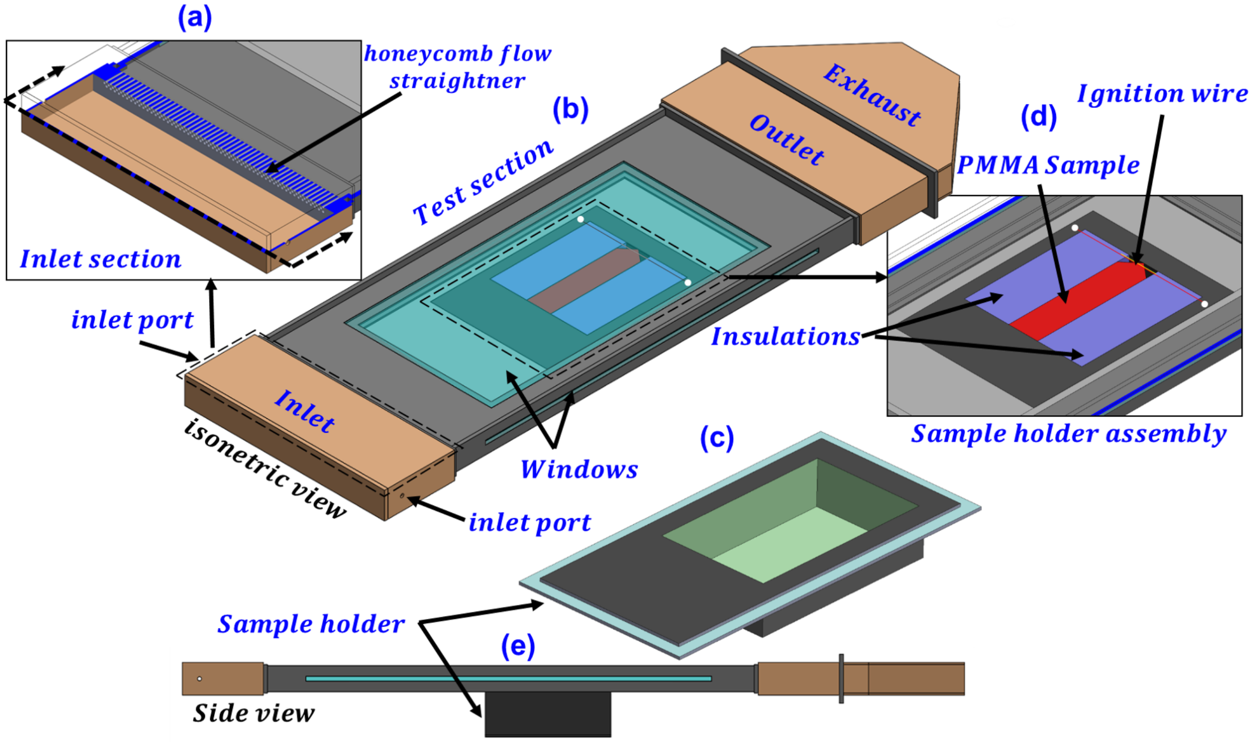

Figure 3.2: Isometric view of the components of the Narrow Channel Apparatus (NCA). The ¾and side views show the inlet, test, exit sections, and the side windows. The (fixed) test section height is h = 5 mm. The sample holder has a recessed section that can accommodate variable thickness samples.

plate of the test section has the same dimensions as the top plate and has a hollow slot in the middle to insert the sample holder. The gap height between the top and bottom plate is fixed at 5 mm. The overall inner test section dimensions are 787.4 mm long, 457.2 mm wide and 5 mm height. Note that width/height = 457.2 mm/5 mm = 91.4 ~ O(100), as claimed above. All experiments are conducted for mean flow velocities 8 - 58 cm/s. For this flow range the Reynolds numbers range from approximately 80 - 680. Thus, the entire flow range for this study is laminar. The required entry length for this laminar flow [33, 56] is 46 - 405 mm. The entrance length of our test section is 419 mm, ensuring a fully developed Hagen-Poiseuille flow profile at the sample leading edge.

The sample holder shown in Figure 3.2 (c) is a 3.2 mm-thick aluminum plate brazed onto a recessed steel section, which holds the test sample. The holder has a long rim in front of the sample leading edge and behind the sample trailing edge. The sample holder section can accommodate samples of several different sizes (l x w) and thicknesses (t). For improved ignitability the samples were machined to triangular shaped at the igniter end (see Figure 2 (d) and also Figure 3, sample trailing edge): the length of each slanted side is 32 mm along the diagonal.

During each test the sample is placed at the center of the holder and then surrounded at its two sides and bottom by calcium silicate insulation boards to reduce heat losses, as shown in Figure 3.2 (d). The side view of the NCA in Figure 3.2 (e) indicates that the sample holder is attached from the bottom of the test section to the hollow slot of the base. Horizontal toggle clamps fasten the sample holder to the base of the test section. In addition, the two aluminum sidewalls contain window slots in which two flush mounted borosilicate windows provide side-viewing capability.

In the outlet, which resembles the inlet, the burned gases exit through a converging sheet metal duct exhaust section. An exit hole in the exhaust section connects to the duct which discharges into the fume hood. There is no flow straightener at the outlet.

3.3.2 Test Procedure and Error Analysis

Consistency of the testing methodology is essential for producing meaningful and repeatable data. Various details of the NCA and lab setup are illustrated in Figure 3.3. During each test, the supply air (shop air, not adjusted for humidity, oxygen mass fraction 0.233) is regulated with a mass flow controller (Alicat MC series 0~100 slpm) before entering the NCA. A LabVIEW Graphical User Interface (GUI) sets the desired flow parameters for the flow through the test section. A 28-gauge Kanthal wire ignites the sample at the trailing edge as shown Figure 3.2 (d) and Figure 3.3. The wire is attached to a conductive cable on both sides of the sample and adjusted to a height of approximately 1 mm above the sample trailing edge. A DC power source supplies the voltage and current through the igniter wire. It is important to note that the igniter wire stretches as current heats it. This movement must be accounted for in the igniter placement. The durability of the wire depends on the applied current level. The wire sags when the current supply is turned on and it touches the sample along with the surrounded insulation. This insulation board prevents the wire from igniting the sample at the side edge. Consequently, each sample is machined to a pointed trailing edge to avoid the contact of insulation and sample: this facilitates the ignition process

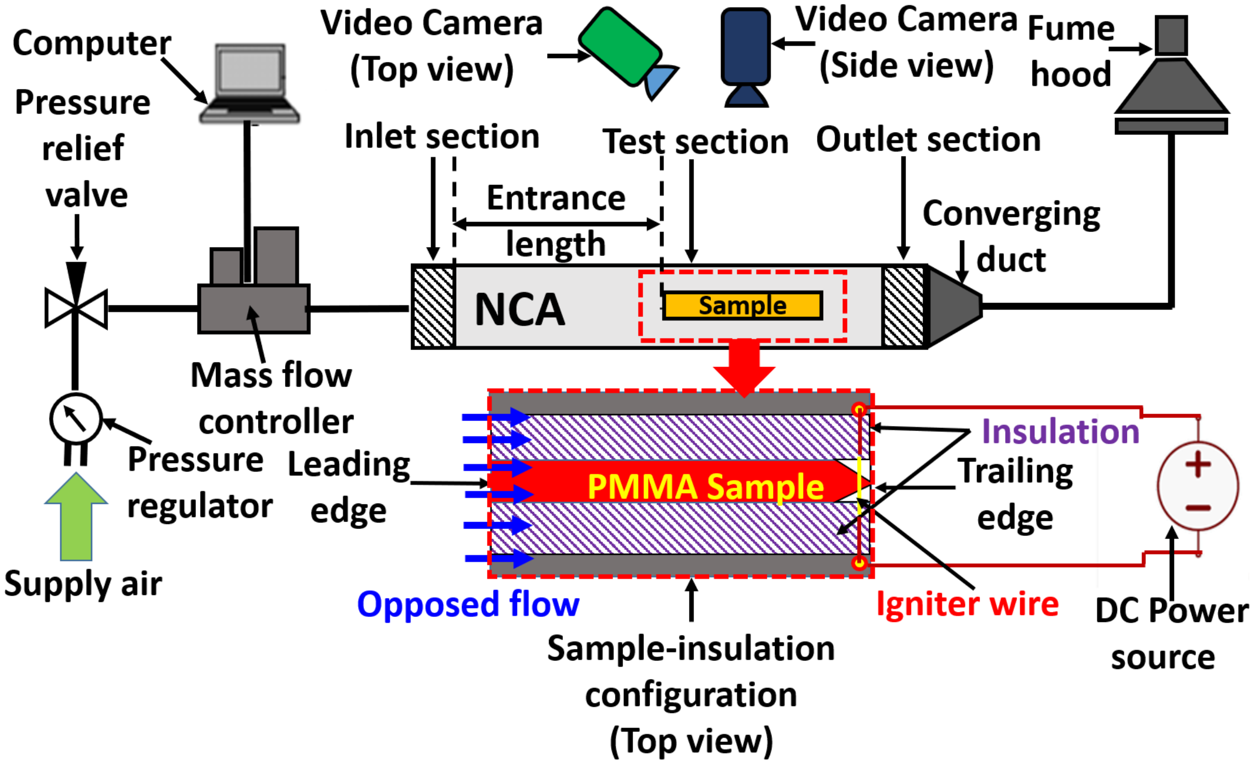

Figure 3.3: Diagrammatic representation of the experimental setup with top view of Narrow Channel Apparatus (NCA). The red arrow indicates the PMMA sample arrangement viewed from above. Note the shape of the pointed sample trailing edge. The tests are recorded from top and side with two video cameras.

(Figure 3.3 inset) and produces a subsequent straight flame front over the sample.

After establishing the desired air flow rate, the DC power supply is activated to ignite the sample. A typical ignition usually occurs between 4 - 5 amps. The DC power supply is turned off once the sample is fully ignited and allowed to burn until the flame front reaches the upstream sample end. Once this happens, the main flow is turned off and the flame extinguishes.

A Sony CX 260 HDR and a Panasonic SDR-T70 video camera record the flame propagation by capturing the view of the experiment from above and the side. The top video camera (see Figure 3.3) is always positioned normal to the NCA top window (Figure 3.2 (b)) and is focused on the surface of the sample. A separate aluminum frame holds this camera above the NCA. The frame structure can slide over the NCA window: this feature is used to change the location of the camera depending on the desired view of the sample. The side video camera is placed normal to one of the NCA side windows using a camera tripod. This camera is focused on the flame's side view. The frame rate was 30 fps for both cameras. Spotlight software and an in-house MATLAB script are used to analyze the videos and to determine the flame spread rate.

The uncertainty of the experimental measurements was estimated. The opposed flow velocity was estimated from the continuity equation, $\overline{V}_g = \frac{\dot{m}}{\rho_\infty A}$. The mass flow rate, $\dot{m}$ was measured with an Alicat MC 6000 series mass flow controller with a full-scale accuracy of ±0.8%. A nominal value that corresponds to the flow velocity of $\overline{V}_g$ is employed to calculate the uncertainty using the method described by Coleman and Steel [57]. The estimated error,±0.8%, assumed the NCA cross-sectional area, A, and the density of air,ρ_∞ were constant. Experiments were repeated 4/5 times to account for any random error of the flame spread rate. The estimated random error for the flame spread rate was calculated to be approximately 6%.

3.4 Experimental Results and Discussion

3.4.1 Flame Visualization

Figure 3.4, Figure 3.5 and Figure 3.6 shows a series of flame images for 6.6 mm, 12.1 mm and 24.5 mm thick PMMA samples. Each image corresponds to a separate experiment for which the corresponding opposed flow velocity is also indicated. One specific frame, selected from each test, shows the flame at a similar location on the sample. During burning, the change in flame brightness, color, and length of the flame are evident. The flame is dim blue near the quenching limit. This suggests an oxygen starvation effect at low flow velocities. As the flow velocity increases, the fuel surface receives sufficient oxygen for continued active burning.

Furthermore, an increase of the flow decreases the gas phase flame standoff distance because the latter is inversely proportional to the surface velocity gradient. Consequently, as the flow rate increases the flame is progressively situated closer to the fuel. As a result, the flame was also brighter at the higher opposed flow velocities. Figure 4 shows that for 26.4 cm/s and higher, the flame has a blue leading edge followed by a bright yellow sooty region. At low flow velocities only, a blue flame appears. The local flow residence time is relatively longer (which would allow any soot that forms to be oxidized) and the lower burning rate (and lower temperature) apparently conspire

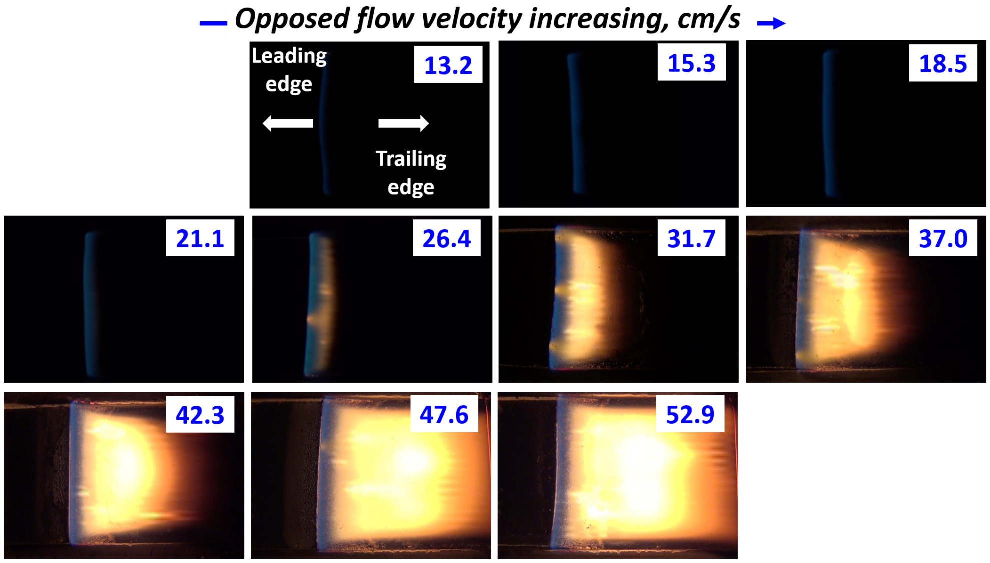

Figure 3.4: Flame images for a 6.6 mm PMMA sample taken from the NCA top window. The images show the indicated range of opposed mean flow velocities increasing from left to right and top to bottom. The surface velocity gradients also increase with opposed flow velocity.

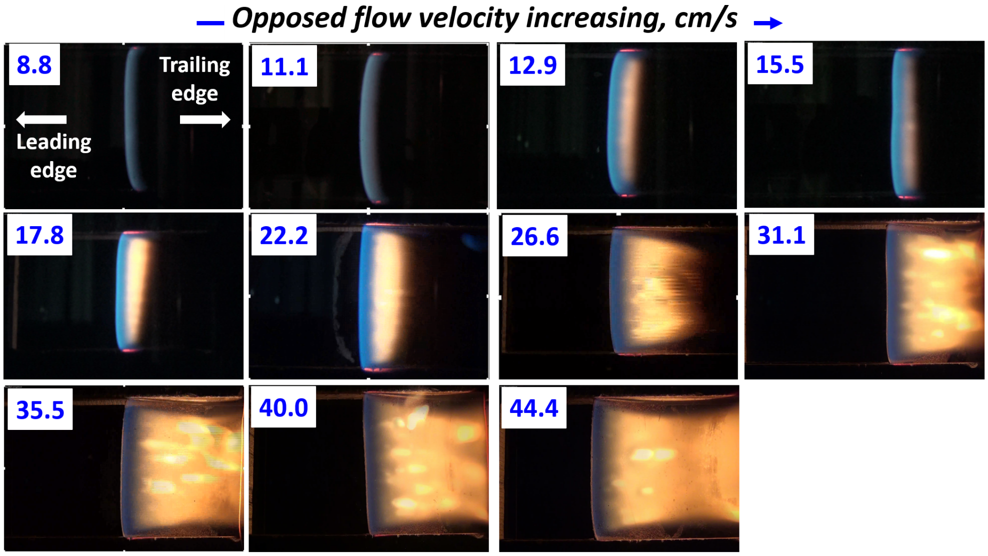

Figure 3.5: Flame images for a 12.1 mm PMMA sample taken from the NCA top window. The images show the indicated range of opposed mean flow velocities increasing from left to right and top to bottom. The surface velocity gradients also increase with opposed flow velocity.

to inhibit soot formation. For a fixed oxygen percentage, the color distribution in the spreading flame appears to be a function of the flow residence time. In the 26.4 and 31.7 cm/s images, one and three semicircular lobes are seen respectively, which may be caused by the bursting of condensed-phase vapor bubbles that had formed in the heated sample (Figure 3.4). In the broader

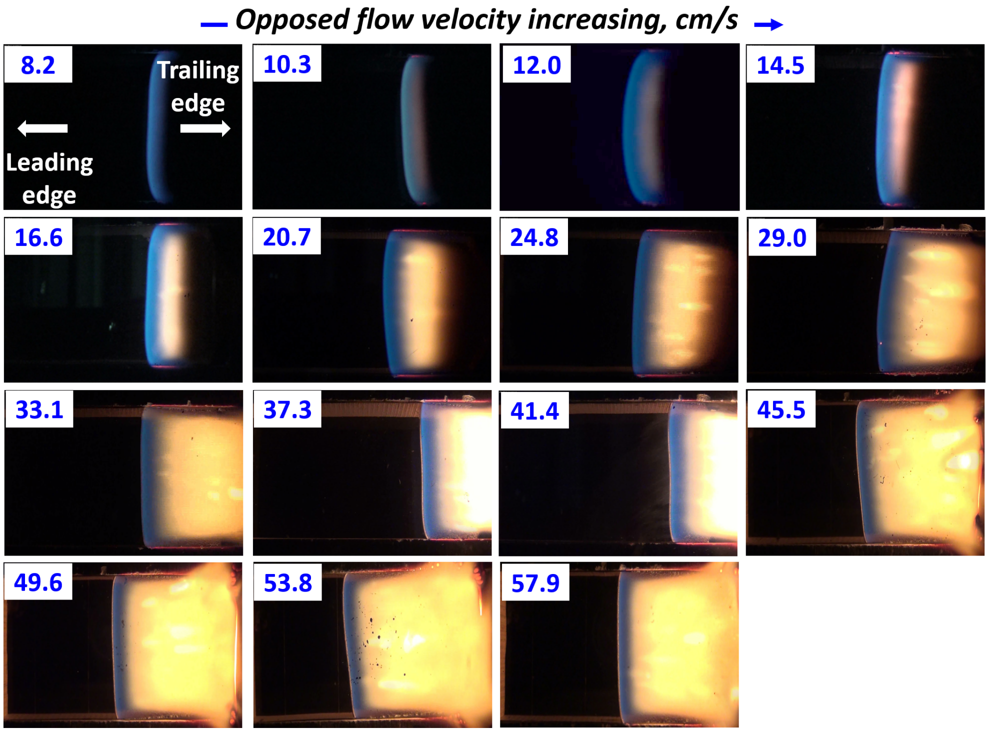

Figure 3.6: Flame images for a 24.5 mm PMMA sample taken from the NCA top window. The images show the indicated range of opposed mean flow velocities increasing from left to right and top to bottom. The surface velocity gradients also increase with opposed flow velocity.

scheme, the flame fronts are essentially flat. However, as indicated here the spreading process is dynamic with multiple physical phenomena occurring simultaneously.

Figure 3.5 represents the flame appearance and length for 12.1 mm thick PMMA samples. These images are similar to those for the 6.6 mm thick PMMA samples shown in Figure 3.4.

The flame spread images for 24.5 mm PMMA samples is shown in Figure 3.6. For 6.6 mm and 12.1 mm PMMA samples, the yellow layer of the flame increases with the flow velocity. The appearance of the flame follows a similar trend to the other two thicknesses. The flames for the flow velocities remain flat although a slight asymmetry can be seen at both edges, and sides, of the sample. It is believed that this asymmetry occurs due to the heat losses between the sample and the insulation interface.

3.4.2 Burnt Samples

The burnt samples are shown in Figure 3.7 (a), (b) and (c) in order of increasing mean flow velocity. The visual appearance of the 12.1 mm thick fuel samples was similar to the 6.6 mm thick samples. The pyrolyzing surfaces for all samples are angled uniformly across the lateral (horizontal) z-direction indicated at the top of Figure 3.7. Figure 3.7 (a) shows that there is complete sample burn through for the flow velocities of 31.7 cm/s or higher. Figure 3.7 (b) shows that complete burn through starts at 26.6 cm/s. None of the samples are completely burned through for the 24.5 mm thick PMMA, see Figure 3.7 (c). Moreover, at 8.2, 10.3 and 12.0 cm/s the thickest samples remain

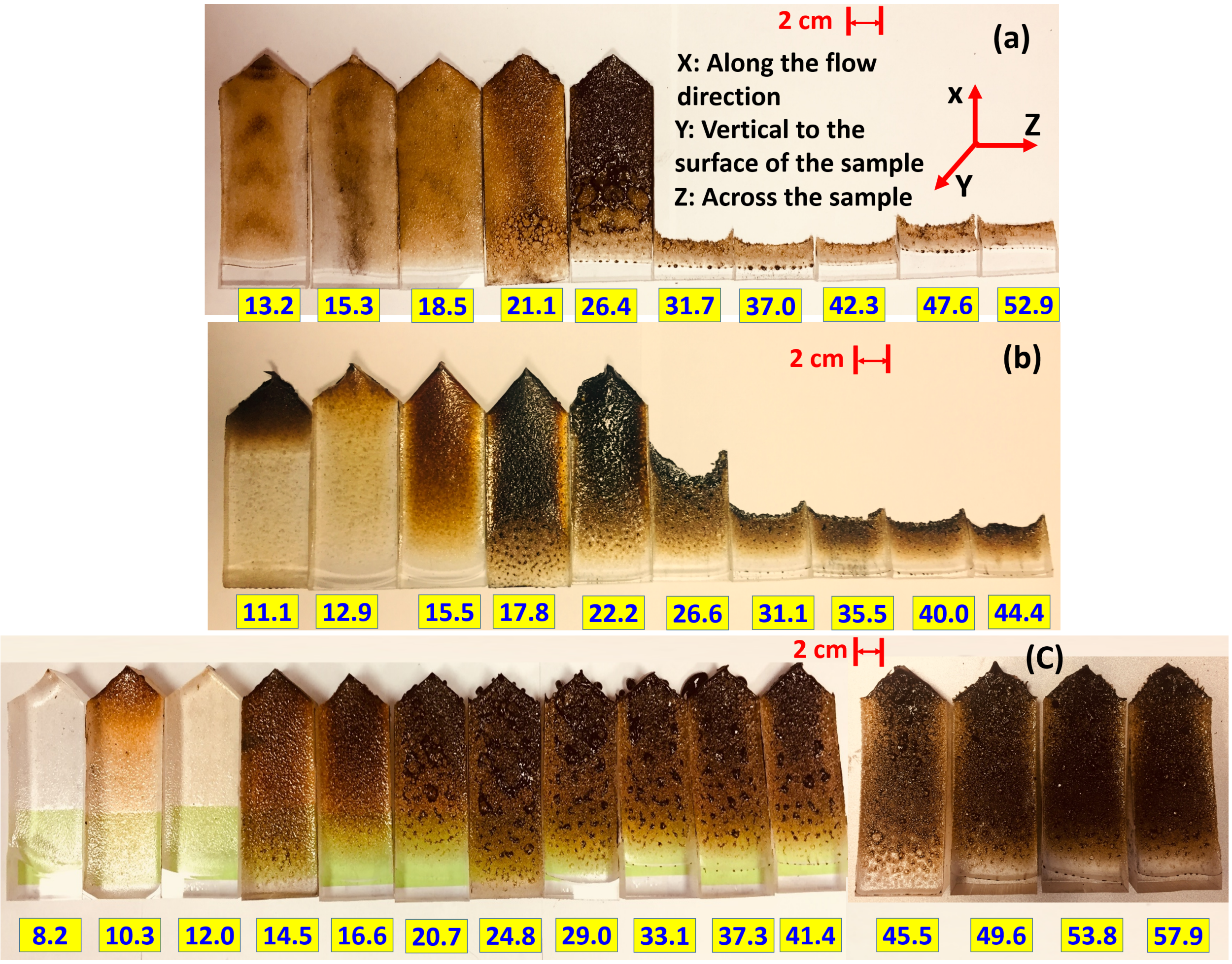

Figure 3.7: Burnt PMMA sample appearance over a range of opposed flow velocities. The velocity values are shown in the yellow boxes in ascending order, left to right. The top row (a) shows burnt samples for 6.6 mm thick case. The middle row (b) shows burnt samples for 12.1 mm thickness. The bottom row (c) shows the burnt samples for the 24.5 mm thick case.

clear and also produce less soot. The proximate cause of this feature may be low flame temperature at these low flow rates.

Figure 3.7 (c) shows that when there is less flame soot the sample remains optically transparent. For some 12.1 mm and 24.5 mm thick samples, a higher ignition flow velocity is used to ignite the samples at low flow velocities. That may be why for some samples there is a dark sooty trailing edge, such as in the 10.3 cm/s case for the 24.5 mm samples in Figure 3.7 (c). After ignition is achieved, the flow velocity is adjusted to the desired velocity and the burnt sample appearance once again becomes transparent.

The black dots on the sample are believed to be related to material swelling caused by bubble formation. During experiments, the bubbles remain below the flame zone. However, once the flow is turned off, the bubbles cool down, they swell up, and they form visible black dots on the surface. The bubbles are continually nucleating, growing, combining, rising and finally rupturing at the surface during burning. Once the sample cools below the degradation temperature, bubbles stop forming. The remaining bubbles are preserved once the sample cools below the glass transition temperature.

3.4.3 Flame Tracking

For each test, flame tracking began after ignition when flame spread is uniform. Uniformity is considered to occur when the flame has spread past the tapered ignition region of the sample and when it becomes flat (or slightly convex) except at the edges due to heat loss.

Figure 3.8 (a) shows a series of images at 1 min intervals for 12.1 mm PMMA samples for an opposed flow velocity of 12.9 cm/s. Initially, the flame is concave upstream but with time it becomes uniform. Visual inspection shows that in this case the uniform flame begins after 10 min into the experiment. Thus, the flame position was tracked forward from the time stamp 10 min. The duration for attaining a uniform flame (5~10 min) varies from test to test and appears to depend mostly on the ignition event. Figure 3.8 (b) shows the flame appearance after it became uniform. This figure is shown as a sequence of images, starting from the 11 min time stamp at 3 min intervals

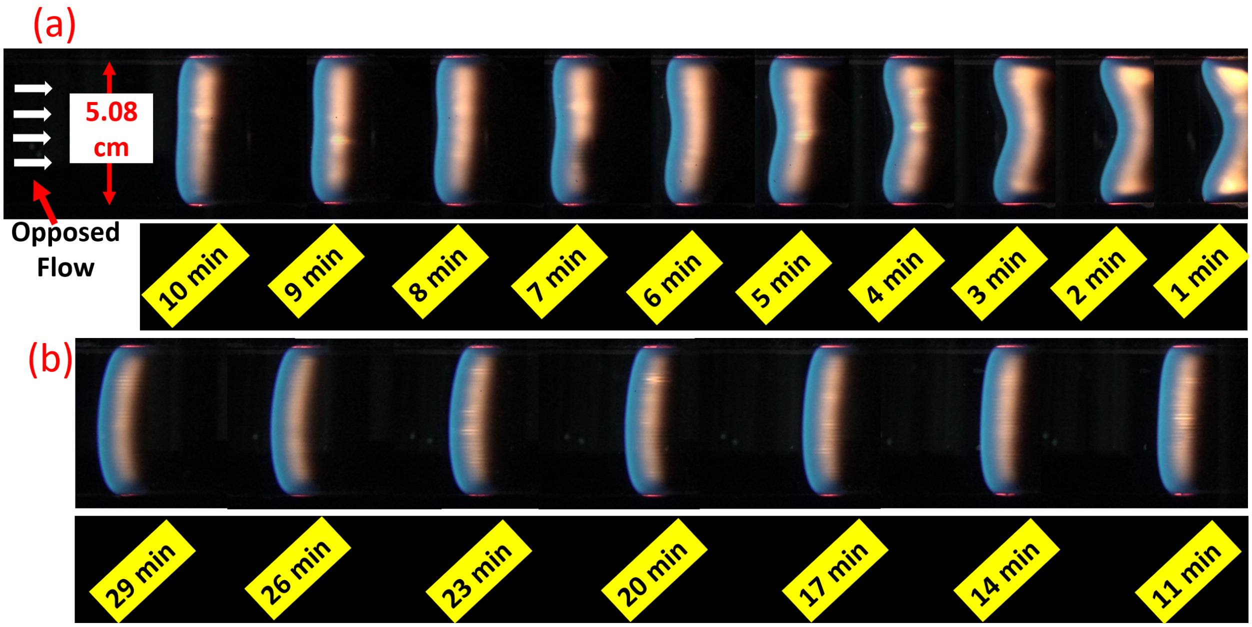

Figure 3.8: (a) Image sequence of flame spread at opposed flow velocity of 12.9 cm/s for 12.1 mm PMMA. The leading edge front is initially concave upstream in the midplane. The image sequence (time increasing right to left) aligns with the actual tests, which are ignited at the right and spread leftward toward the increasing left-to-right flow. (b) Image sequence (time increasing right to left) of flame spread from time stamp 11 min for the same test. The image sequences demonstrate uniform propagation rate between the 11-29 min time stamps.

until the end of the test at 29 min. The flame front was uniform for the entire duration of tracking.

3.4.4 Flame Spread Rate

Flame spread rates were determined by tracking the leading edge position of the flames over the full range of mean opposed flow velocities. The flame leading edge is tracked because of the flame leading edge control the flame spread process [21]. The top view video recordings were considered for each test and tracking began as soon as the flame became uniform. Threshold tracking was used: every frame of the entire test was tracked for all cases. The leading edge position versus time shows excellent linearity over the entire range of flow velocities (see Appendix Figure B.1). Although the overall burning time and the time to establish a uniform flame are both different for each test, tracking was performed for the same time window for all tests. The time history of leading edge tracking was fitted with a line for each flow velocity. Finally, the slope of each line yields the flame

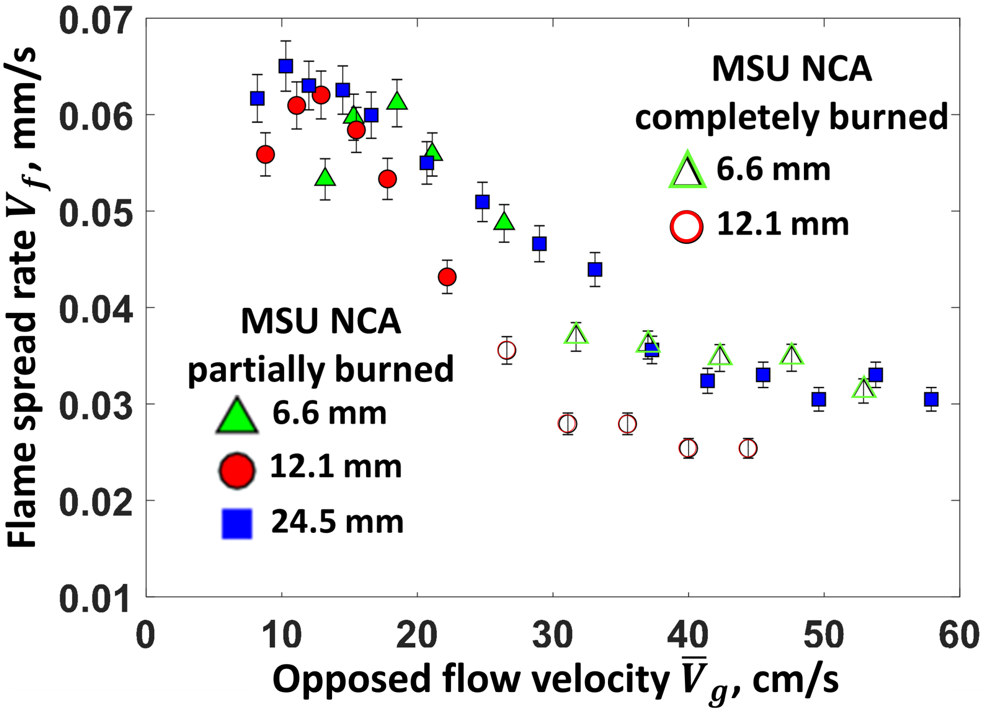

Figure 3.9: Flame spread rate V_f as a function of mean opposed flow velocity $\overline{V}_g$. The experimental uncertainty error is approximately 6% for the flame spread measurements. Data for completely burned through samples are shown with open (hollow) symbols. The 24.5 mm samples never burned through but they entered the regressive burning regime where V_f is independent of $\overline{V}_g$.

spread rate.

Figure 3.9 shows the flame spread rate, V_f, as a function of the mass mean opposed flow velocity,$\overline{V}_g$ Each flame spread data point represents an entire individual test at a particular opposed flow velocity. Several distinct features can be identified from this figure. The maximum flame spread rate for the 6.6 mm samples was observed at $\overline{V}_g$ = 18.5 cm/s (this was averaged over all tests). Prior to this value V_f increased linearly with $\overline{V}_g$ analogous to high oxygen concentration behavior tests in the thermal flame spread regime [7]. When $\overline{V}_g \geq 18.5$ cm/s it is seen that V_f drops monotonically [7].

One difference between the 6.6 and 12.1 mm cases is that the maximum flame spread rate $V_{f,max}$ for 12.1 mm sample occurs at a lower $\overline{V}_g$ = 12.9 cm/s. The flame spread rate for 24.5 mm PMMA sample follows a generally similar trend to the other two smaller thicknesses although important differences are discussed below. The maximum flame spread rate was observed at $\overline{V}_g$ =

10.3 cm/s, continuing the downward trend of $V_{f,max}$ as a function of sample thickness.

In Figure 3.9 the data for the 6.6 mm and 12.1 mm cases are distinguished into two categories. In the first category are the solid triangles and circles denoting flame spread prior to sample burn through. In the second category are the hollow triangles and circles denoting flame spread after sample burn through. In this latter stage (see the images in Figure 3.7 (a) for $\overline{V}_g \geq 31.7$ cm/s. and (b) for $\overline{V}_g \geq 26.6$ cm/ the samples are completely burned through. For the 24.5 mm samples, V_f plateaus after $\overline{V}_g = 41.4$ cm/s without any burn through. The flame is generally hidden behind the sample from the approach flow. As a consequence there is little dependence on the oxidizer flow rate. This stage represents what might be referred to as the extreme limit of the regressive burning stage. Since there is approximately twice as much material to burn for the 12.1 mm samples as for the 6.6 mm samples, the spread rate is slower, though not by half. The 24.5 mm samples also eventually enter the regressive burning regime for oxidizer velocities greater than approximately 40 cm/s, but there is never full sample burnout, as seen in Figure 3.7 (c). Although it is unclear why spread rates are higher for 24.5 mm than for 12.1 mm, it is likely that since less of the 24.5 mm samples burns inwards, the flame spreads more rapidly along the surface than into it.

Figure 3.9 shows that after the peak spread rate, at higher opposed flow velocities, V_f decreased from 6.6 mm to 12.1 mm and then increased for the 24.5 mm samples. As a partial explanation during ongoing research into this behavior, flame spread over a real fuel surface may be viewed as a competition between surface and regressive spread. In the NCA one or the other appears to dominate according to the sample thickness. The intermediate 12.1 mm case, when compared with the 6.6 mm case, presents this competition in the starkest terms. The thickest 24.5 mm case never approaches to the extreme burn through limit and hence the dominant features associated with the classical problem of infinitely thick flame spread are evident nearly throughout the process, even into the regressive burning stage, which never presents as extremely as for the two thinner fuel samples. None of the flame heat used for sample regressions ever completely lost as it is for the thinner samples. It is evident that the flame spread mechanism is different for spread over the substrate (the 6.6 mm and 12.1 mm burn out cases, when flame heat is lost) compared with spreading over the actual sample material (24.5 mm, when heat can be recovered by the sample) in the higher opposed oxidizer velocity range. It is not clear presently how these empirical facts can be related to the thermal responsivity [9, 10, 13] and thermal diffusivity differences between the sample and the insulation.

Finally, sample regression profiles for the thickest samples shows that at approximately 1.5 – 2 cm from the leading edge about 5-6 mm of burned PMMA has been carved out, and at approximately 3-3.5 cm about 10-12 mm of burned PMMA has been carved out of the sample. These distances agree largely with the burn-through distances shown in Figures 3.7 (a) and (b). Once the thin (6.6 mm) sample has burned through the subsequent evolution of the spread rate with flow velocity resembles the thick (24.5 mm) and not the intermediate case (12.1 mm), as shown in Figure 3.9.

3.4.5 Regressive Burning Regime

Prior research has shown that there are at least three flame spread regimes [58]. It was one of the great accomplishments of flame spread research to show that these three regimes can be explained in concert with the Damköhler number, which is the ratio of the characteristic flow to chemical process times. The regimes are: (1) A high Damköhler number regime where the flow is sufficiently slow that the flames can extinguish. A combination of factors including oxygen starvation (slow reaction) and low oxidizer inflow rate (low convection) cause high flame standoff distance that leads eventually to flamelet formation followed soon by extinction: this is the flamelet regime of flame spread [21, 52]. (2) A moderate Damköhler number regime originally referred to as the thermal flame spread regime. Here the flow is sufficiently slow that chemical reaction rate is effectively infinite by comparison. Flame spread was described in a theoretical analysis as a balance between transverse conduction (into both solid and gas) and downstream convection (in solid and gas) [13]. (3) A small Damköhler number regime where finite-rate chemistry alters spread through a greatly reduced flow time (and diffusional transport time scale) along with a fixed characteristic chemical time scale. This regime terminates with eventual flame blowoff. The latter two regimes are extensively discussed in [9]. For the largely flow-driven regimes it is now possible to add a fourth regime, which occurs only for thick, or thicker, fuel samples. Here, mass loss of the fuel behind the flame front produces a carved-out sample profile. The result, as the oxidizer flow rate increases, is a type of flame spread that resembles ablation: the flame shelters itself downstream of the flame front inside the carved-out hollow. In this stage it appears that no matter how large the flow rate is, the flame can comfortably persist in the hollow. It is this new regime of flame spread that the current research describes, most recently in Figure 3.9. Our results appear to identify a plateau in the higher oxidizer velocity range, where the flame spread rate remains unchanged, plateauing as $\overline{V}_g$ is further increased. This occurs in the range $\overline{V}_g$ = 32~58 cm/s and this regime is named as regressive burning regime of flame spread.

In the common understanding of provide by the characterization of flame spread regimes (1) – (3), the availability of oxidizer should increase with $\overline{V}_g$. However, there is no blowoff resembling part (3) of the prior Damköhler number argument. Instead there is a plateau, where the spread rate remains constant as $\overline{V}_g$ is further increased. The appearance of the plateau correlated with the change of sample geometry in the flame zone, i.e., the carved hollow. The altered flow field permits the flow residence time to increase, thereby allowing continued solid fuel consumption. This physical process manifests itself in the visible solid degradation in the downstream under-flame region. In this regressive burning regime, the relatively high speed oxidizer flow pushes the flame towards the fuel surface. This allows enhanced surface degradation which allows the flame to burn while protected in the carved fuel hollow. The idealized fluid flow analogy is the classical backward-facing step problem. Here a region of circulating flow forms behind the step, generating an attached vortex and allows to remain attached throughout any subsequent velocity increase. The analogy in the case of flame spread may not be complete (i.e., it remains to be determined whether or not there actually is an attached, circulating vortex) but it is indicative of an unambiguous alteration of the flame spread mechanism.

Side images are necessary in order to clarify geometric changes of the sample. Here, flame spread over 12.1 mm thick PMMA at 11.1 cm/s (Figure 3.10 (a)) and at 44.4 cm/s (Figure 3.10 (b)) was side photographed to highlight the flame hiding behavior in the regressive burning regime.

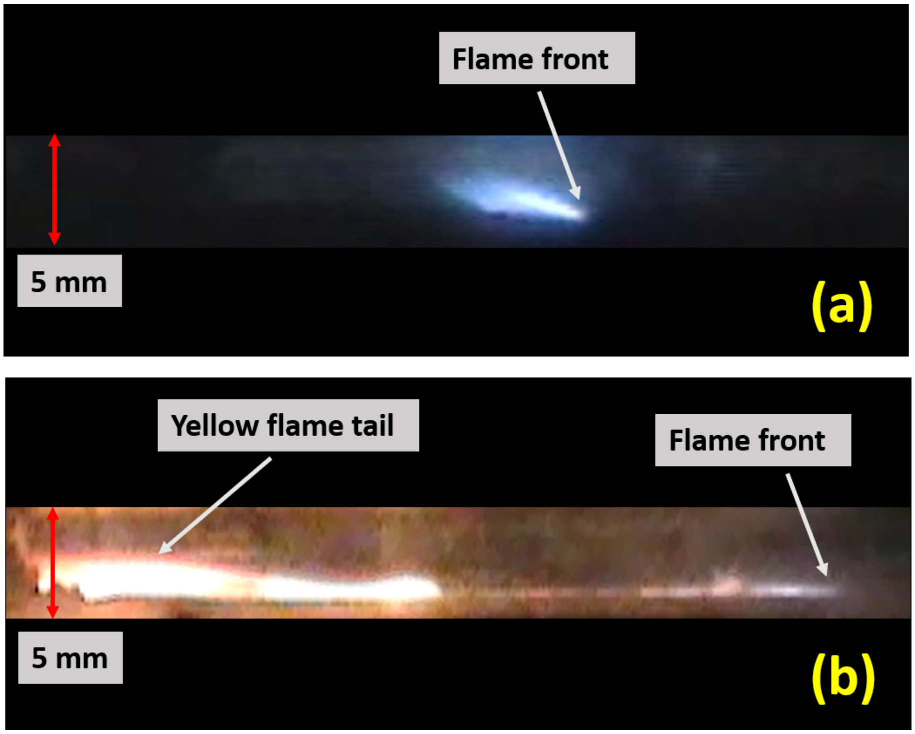

Figure 3.10: Still image showing flame propagation for 12.1 mm thick PMMA from a side video recording at opposed flow (a) $\overline{V}_g = 11.1$ cm/s and (b) $\overline{V}_g = 44.4$ cm/s.

Figure 3.10 (a) shows that the flame projects above, i.e. is visible above, the virgin fuel surface. Figure 3.10 (b) shows that the flame no longer projects above the virgin fuel surface, i.e., it is no longer visible above the plane of the sample. This indicates that it is anchored in the downstream carved fuel hollow near the inclined fuel edge and below the level of the upstream virgin fuel surface. A bright yellow tail is also observed near the trailing edge. This is believed to be caused by vapor jetting. The fast-forwarded side video recording (see Supplementary material 2) is included as supplementary material, which demonstrates that the flame was situated below the fuel surface during the entire test. Note that, a reflection of flame spreading is also visible in the video due to the top window which is cropped from these images.

Hashimoto et al. [59] observed a similar phenomenon for rectangular PMMA samples tested in a narrow duct. They found that the at higher turbulent flow velocities (>18 m/s), an indented area forms at the center of the fuel which is produced by the flame consuming the solid fuel. Furthermore, from a side view the flame cannot be seen above the level of the unburned fuel surface. In this mode of combustion regressive burning is an important mode of solid fuel consumption. Huang et al. [60] observed that thick PMMA rods burning vertically at high $\overline{V}_g$ >100 cm/s are insensitive to $\overline{V}_g$ until the moment of extinction. The flame in this region creates a concave hollow at the end of the downstream rod as opposed to a cone-like burnout shape at lower velocities.

3.4.6 Comparison with FP81 Data

For the 12.1 mm thick samples, a comparison is now made between the MSU NCA flame spread data and the Fernandez-Pello et al. [7] data for their 12.7 mm thick sample tests. These experiments are compared firstly because they use nominally identical thickness samples, and secondly (and more importantly) because being boundary layer flows whose features can be theoretically calculated they provide a consistent basis for comparison. The latter point, which requires explanation, will be elaborated upon below. The purpose of the comparison will be to examine the validity and applicability and predictive capability of the stretch rate theory of flame spread [9, 10, 13].

Figure 3.11 shows the raw flame spread rate data as a function of opposed flow velocity for both the MSU NCA data (Figure 11) and the Fernandez-Pello et al. (henceforth FP81) data [7]. The FP81 data for 23% oxygen mass fraction was selected because the oxidizer for the MSU NCA tests was air. Same markers (circular, red color filled) are used for partially and completely burned samples for the MSU NCA flame spread data for this figure and any other figure onwards where the same data is used.

Despite the nearly identical sample thickness, Figure 3.11 shows that the flame spread behavior for FP81 and the MSU NCA are dissimilar. A possible explanation is the difference in the experimental test section configurations. The small-scale horizontal wind tunnel used in FP81 was 1 m x 5 cm x 4 cm whereas the MSU NCA test section is 78.7 cm x 45.7 cm x 5 mm, nearly the same length but much wider and less tall. The flame spread rate in the wind tunnel is predominantly buoyancy induced at low flow velocity (≤ 30 cm/s), hence the FP81 spread rates in air are largely independent of the flow velocity in that range. However, the condition of the MSU NCA promotes a simulated microgravity condition, where buoyancy is minimized and forced convection is enhanced

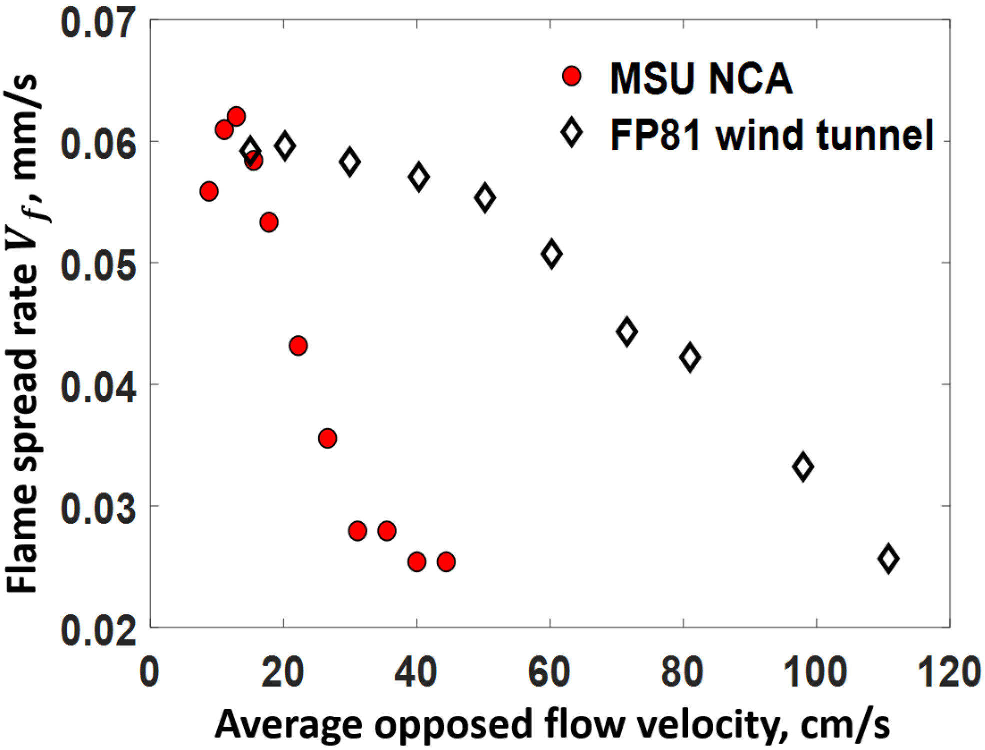

Figure 3.11: Flame spread rate as a function of opposed flow velocity for MSU NCA (same markers are used for partially and completely burned samples) and FP81. The small-scale wind tunnel used in FP81 had dimensions 1 m x 5 cm x 4 cm while the NCA's test section has dimensions 78.7 cm x 45.7 cm x 5 mm.

by comparison. Here the flame spread rate increases (≥ 12.9 cm/s) and then decreases (> 12.9 cm/s) with mean flow velocity. In spite of the difference of these dependencies, the reader will note that the range of flame spread rates for the current study and for FP81 is identical, between 0.02 ∼ .07 mm/s.

A second and more compelling explanation for the discrepancy in the measured flame spread behavior arises when one considers the physical mechanism of the flow stretch rate at the flame leading edge. According to the velocity gradient theory of laboratory scale flame spread [9, 10, 13], the flame stretch exerts a greater influence on the spread rate than the (average) velocity $\overline{V}_g$. For this reason, the stretch rate has been calculated in order to compare the FP81 and MSU NCA data. In a simplified calculation, a parabolic velocity distribution (Poiseuille's equation) was assumed for both the MSU NCA and the FP81 wind tunnel. In the current comparison, the stretch rate was calculated at the flame standoff distance, which correlates with the gas phase characteristic length and is very close to the wall. Since the velocity gradient there is linear, the standoff distance is not crucial to the theoretical calculation and considered as 0.5 mm. For a pressure driven flow, the forced stretch rate (a_f) was calculated using Eq. (3.1)

$$a_f = \frac{6\overline{V}_g}{h}\left(1 - \frac{2s}{h}\right) \tag{3.1}$$

where s=flame standoff distance and h= MSU NCA channel or FP81 wind tunnel height.

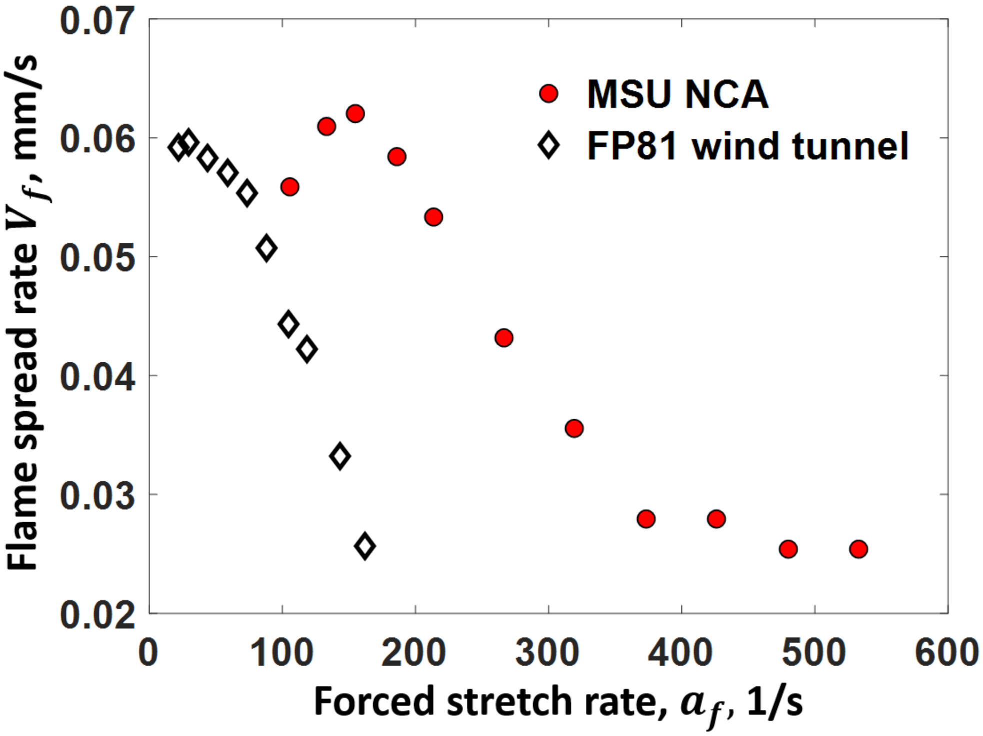

Figure 3.12: Flame spread rate as a function of the opposed forced flow stretch rate, or the near wall velocity gradient. The stretch rate is determined from Eq. (3.1) , where the flame standoffdistance is considered as 0.5 mm. In contrast with Fig. 3.11, the downslope regions of the two curves are now generally parallel.

In Figure 3.12, the flame spread rate (y-axis) results are replotted as a function of the forced opposed flow stretch rate (1/s). It is evident that the NCA produces a higher strain rate compared to the FP81 wind tunnel even though the average flow velocities were much higher in the latter. In contrast to Figure 3.11, the downslope regions of the two curves are now largely parallel: in other words, the stretch rate has “regularized” this functional dependence. Nevertheless, a distinctive offset or gap of the spread rate value exists between the NCA and FP81. Replotting did not reduce the horizontal gap between the two sets of data points.

As qualifiers, it is first noted that the stretch rate was estimated by assuming for both cases a fully developed flow. Secondly, a parabolic velocity distribution was assumed for the NCA, which is valid for a fluid moving downstream between two plates whose length and width are both much greater than their separation distance. As the FP81 wind tunnel's width (5 cm) and height (4 cm) are of the same order of magnitude, the assumption of a velocity gradient that is independent of the lateral location may not be entirely valid. Thus, it was necessary to re-evaluate the cold flow velocity profile for the FP81 wind tunnel in order to more accurately estimate the local stretch rate at the flame leading edge. The following section discusses this estimation.

3.5 Numerical Results and Theoretical Correlations

3.5.1 Numerical Results

In the previous subsection it was demonstrated that an improved correlation of the data was obtained by using the velocity gradient a_f instead of the mean opposed flow velocity $\overline{V}_g$. However, the offset, or gap, still remained (Figure 3.12). The hypothesis is now made that in the FP81 wind tunnel the use of the classical infinitely wide Poiseuille flow formula for a fully developed parabolic flow between parallel plates may not represent the actual flow field in that device (whereas it likely does accurately represent the flow field in the MSU NCA, for which NCA length/NCA height ~ 90). Since there is no such convenient analytical solution for a developing flow in a 2-D rectangular duct, a numerical model was formulated to study the velocity profile.

Computational domain and grid generation:

The computational domain employs the same dimensions of the FP81 wind tunnel, which is 100 cm (1 m) long in the streamwise direction, 5 cm in the lateral direction and 4 cm in the wall-normal direction. A three-dimensional structured grid was developed using ICEM CFD. The number of grid points in the entire domain is approximately 4.2 E+6. Mesh elements consisting of ten prism layers are clustered near the wall in order to resolve the boundary layer. There are 1.91 E+6 control volumes in the entire domain.

Case setup:

A Semi-Implicit Method for Pressure Linked Equation (SIMPLE) solution scheme is used for pressure-velocity coupling with a k-ω SST turbulence model with 0.1% turbulent intensity with air as the working fluid. The experimentally measured FP81 inlet velocity profile was applied at the freestream inlet. A pressure outlet boundary condition was used at the outlet. The commercial finite volume solver (FLUENT) was used to solve the incompressible, steady state Navier-Stokes equations.

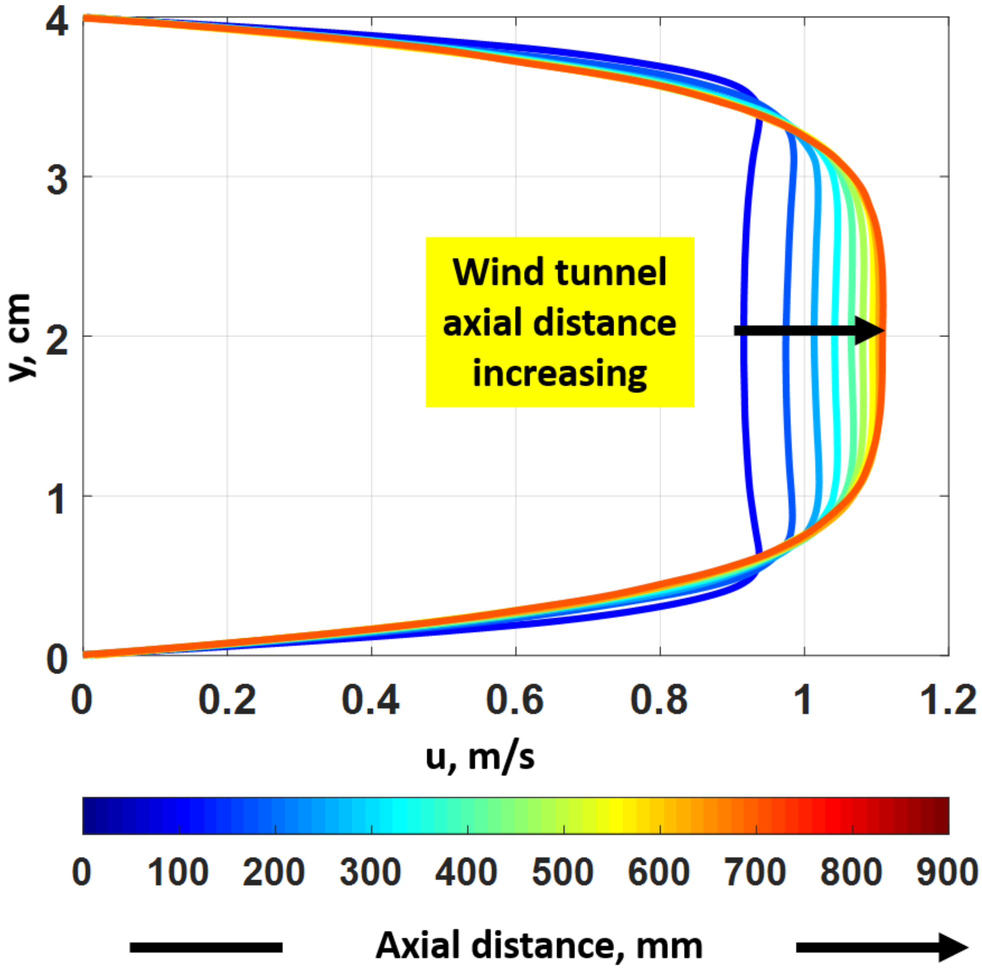

Figure 3.13: Velocity profile at the midplane along the axial distance (streamwise direction) of the FP81 wind tunnel. The inlet velocity boundary condition in this simulation is $\overline{V}_g$ (x = 0) = 80 cm/s . Each line represents a specific velocity profile along the wind tunnel. The color bar represents the length increase of the wind tunnel.

CFD Results:

Velocity distribution results:

Numerical simulations were performed for all of the inlet flow velocities shown in Table 1. Figure 3.13 only shows the evolving velocity distribution in the centerline plane along the wind tunnel for an 80 cm/s inlet velocity. Nine velocity profiles are shown in the axial direction of the wind tunnel at intervals of 100 mm. The results showed a developing boundary layer and confirm that the FP81 velocity profile is not yet fully developed. This trend for the other inlet flow velocities was very similar, hence those results are not shown. Figure 3.13 also shows that the velocity profile near the walls (0 ~ 1 mm) is linear.

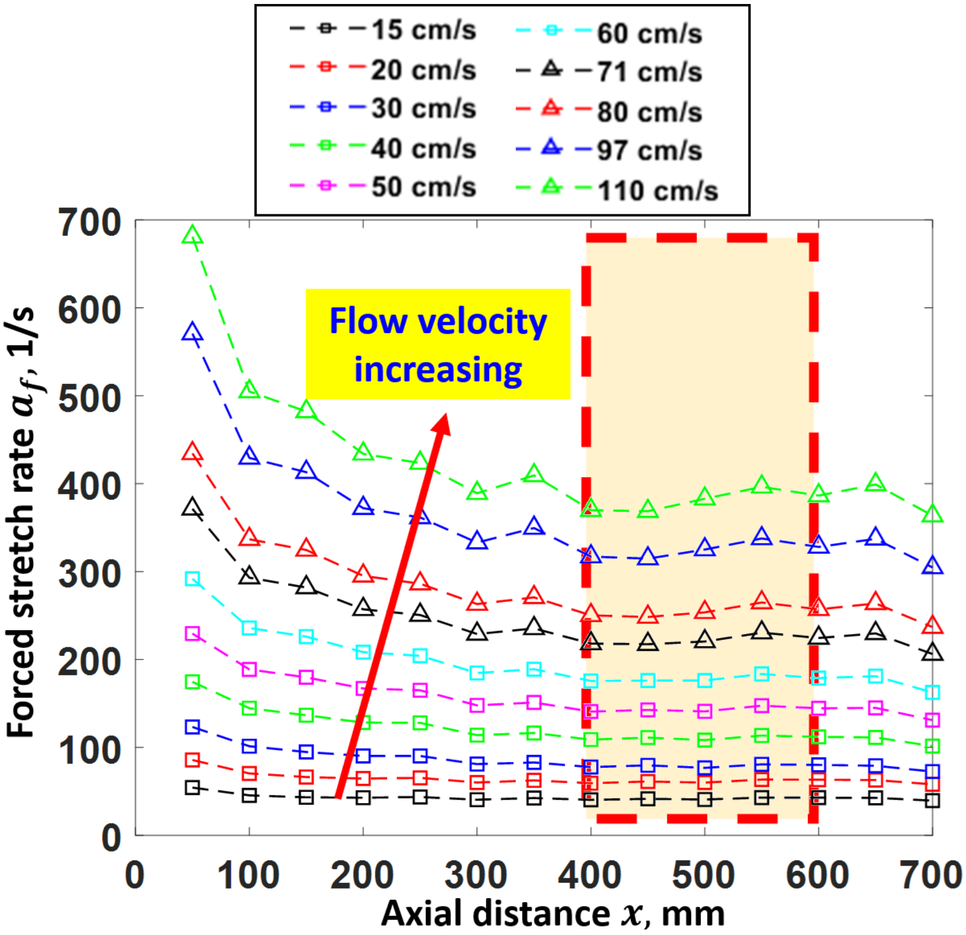

Figure 3.14: Stretch rate along the axial direction, x in the centerline of the wind tunnel for different opposed flow velocities. The thick enclosed dashed lines indicate the sample location, which is called the focus area, in which a_f is nearly constant. The boldface arrow shows the trend of increasing $\overline{V}_g$.

The stretch rate was calculated from the slope of the indicated streamwise velocity profile very close to the wall (0 ~ 1 mm). Figure 3.14 shows the stretch rate as a function of the axial direction x in the wind tunnel for different inlet flow velocities. As shown, the stretch rate increases with the inlet velocity. It is also interesting that at low inlet flow velocities (15 ~ 60 cm/s) there is no significant change in the stretch rate with x where the Reynolds number ranges from 427 to 1707. However, at high flow velocities, the change in stretch rate is much more pronounced. The flow becomes turbulent for the flow velocities 71 ~ 110 cm/s. Here, Re ranges from 1991 to 3130 that falls under the turbulent regime. The sample location in the FP81 wind tunnel in Figure 3.14 lies inside the red dotted region between 400 to 600 mm. In this focus area, a_f is nearly constant.

Figure 3.15 compares the average stretch rate for FP81 wind tunnel estimated from the CFD calculation and an analytical calculation assuming a parabolic velocity distribution (fully developed 1-D flow) considering hypothetical infinitely wide tunnel. As the inlet flow velocity increases, the average stretch rate (predicted by CFD) progressively deviates further from the fully developed 2-D

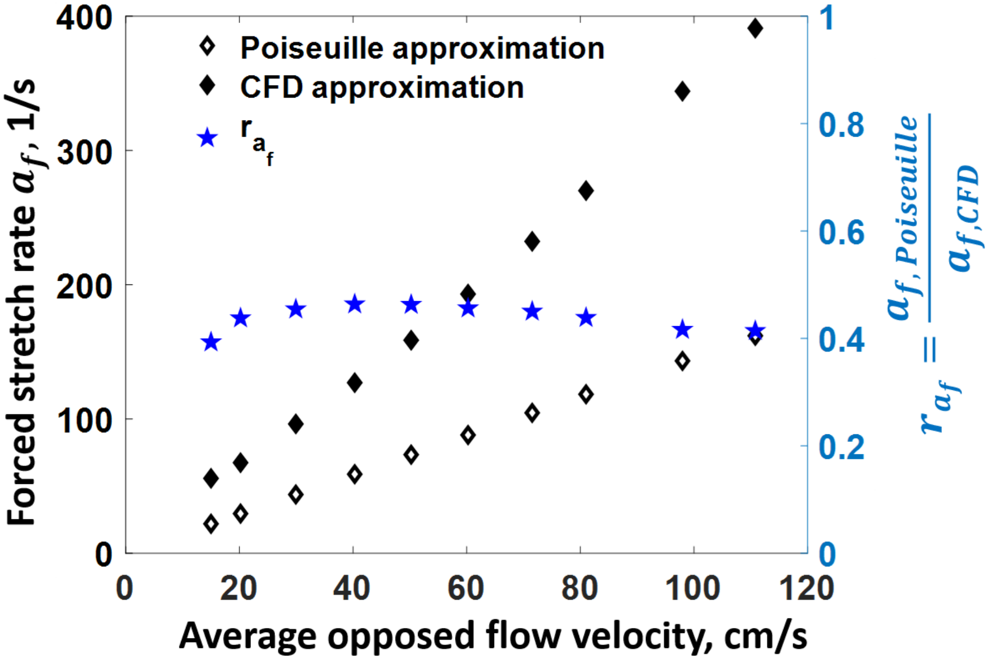

Figure 3.15: Stretch rate a_f as a function of opposed flow velocity $\overline{V}_g$ = 15-110 cm/s estimated from the predicted velocity distribution from CFD and from the Poiseuille approximation (parabolic velocity distribution, Eq. (3.1)) for the FP81 wind tunnel. The secondary axis shows the ratio of the Poiseuille and CFD forced stretch rates as a function of $\overline{V}_g$.

theory. This indicates the presence of an evolving boundary layer, which contributes to the higher stretch rate. The secondary (right) axis shows the forced stretch rate ratio for both the Poiseuille and CFD cases. The ratio, r_{a_f} is nearly constant (0.4 ~ 0.45) throughout the $\overline{V}_g$ range.

Figure 3.16 shows the replotted flame spread rate as a function of the forced stretch rate for the MSU-NCA and the FP81 wind tunnel using the above CFD prediction. The MSU-NCA stretch rates were calculated as before from the analytical velocity profile (Eq. (3.1)) for the flow between two infinitely wide parallel plates.

The CFD prediction produces a spread rate distribution in good agreement with the NCA flame spread rate in the higher opposed flow velocity range. The gap between Figure 3.12 is largely eliminated. There is still a discrepancy in the lower stretch rate range. When $\overline{V}_g < 30$ cm/s, or $a_f < 100$ 1/s, buoyancy plays a role in the FP81 tests. The trend of the data indicates that as the forced flow rate increases the buoyancy effect is gradually overwhelmed and therefore essentially suppressed. This feature of these data was discussed in [13]. Since the FP81 wind tunnel has a

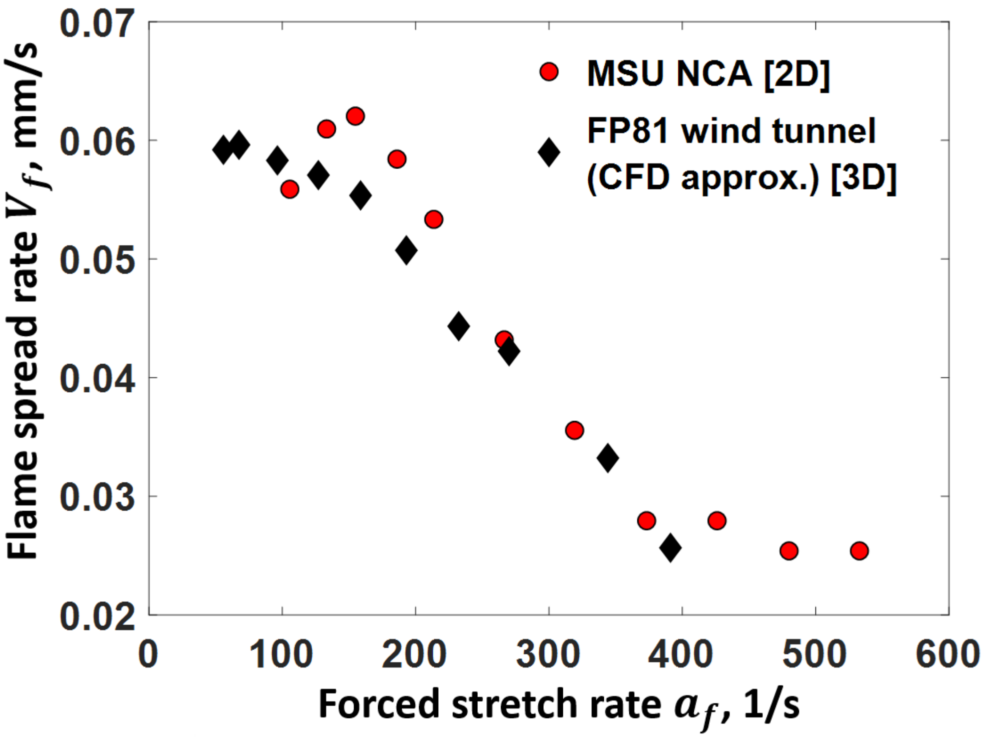

Figure 3.16: Flame spread rate, V_f as a function of forced stretch rate a_f for MSU-NCA and FP81 wind tunnel showing results for both Poiseuille (2-D) and CFD (3-D) solutions.

significant buoyant flow component at lower $\overline{V}_g$ and a_f, discrepancies with the MSU NCA will occur in the low-flow range. The resolution of this discrepancy is the subject of the next subsection.

3.5.2 Theoretical Correlation/Correction

Buoyant Flow Stretch Rate Correction:

Here, a further improvement is made by introducing a correction to the flame stretch as caused by induced buoyant flow. As already discussed, this correction is the most important, and generates its largest effect, in the FP81 low - $\overline{V}_g$range. An orthogonal superposition of the streamwise forced stretch rate a_f and the transverse buoyant stretch rate a_b is used to align the data with the NCA boundary, $a = \sqrt{(a_f^2 + a_b^2)}$ [61].

The buoyant stretch rate at the flame standoff distance, s (referring to [62] [37]) considers a mixed convective flow having $\frac{Gr}{Re^2} \approx 1$. This stipulation leads to $\frac{\frac{\beta g \triangle T y^3}{\nu^2}}{\left(\frac{U_b y}{\nu}\right)^2} \approx 1 =>> \frac{\beta g \triangle T y}{U_b^2} \approx 1$, where U_b is the characteristic buoyant velocity and is representative of its maximum value in a natural convection boundary layer. Solving for U_b gives $U_b = \sqrt{g\beta \triangle T y}$. Replacing, y with s leads to $U_b = \sqrt{g\beta \triangle T s}$. Differentiating this buoyant velocity gives the buoyancy induced stretch rate Eq. (3.2):

$$a_b = \left(\frac{\delta U_b}{\delta y}\right)_{y=s} = \frac{1}{2}\sqrt{\frac{g\beta(T_w - T_\infty)}{s}} = \frac{1}{2}\sqrt{\frac{g(\rho_\infty - \rho)}{\rho_\infty s}} = C\sqrt{\frac{g}{s}} \tag{3.2}$$

Using values a_b = 105 1/s (a preliminary order of magnitude estimate) with g = 9.81 m/s and s = 0.5 mm, the constant C is estimated to be 0.75. By varying the flame standoff distance between s= 0.5 to s=1 mm a buoyant stretch rate range is found as a_b = 75 1/s to 105 1/s. Instead of considering all the values between the range (a_b = 75 ~ 105 1/s), the lower (75 1/s) and upper (105 1/s) limits are used to adjust the stretch rate for the final comparison (Figure 3.17). By including the buoyant stretch rate, the mixed stretch rate improves the agreement of flame spread rate between MSU-NCA and FP81 wind tunnel (recall that a_f is computed numerically). As seen in Figure 3.17 a shift range 75 1/s < a_f < 105 1/s accounts for the buoyant stretch and serves to better align the FP81 data

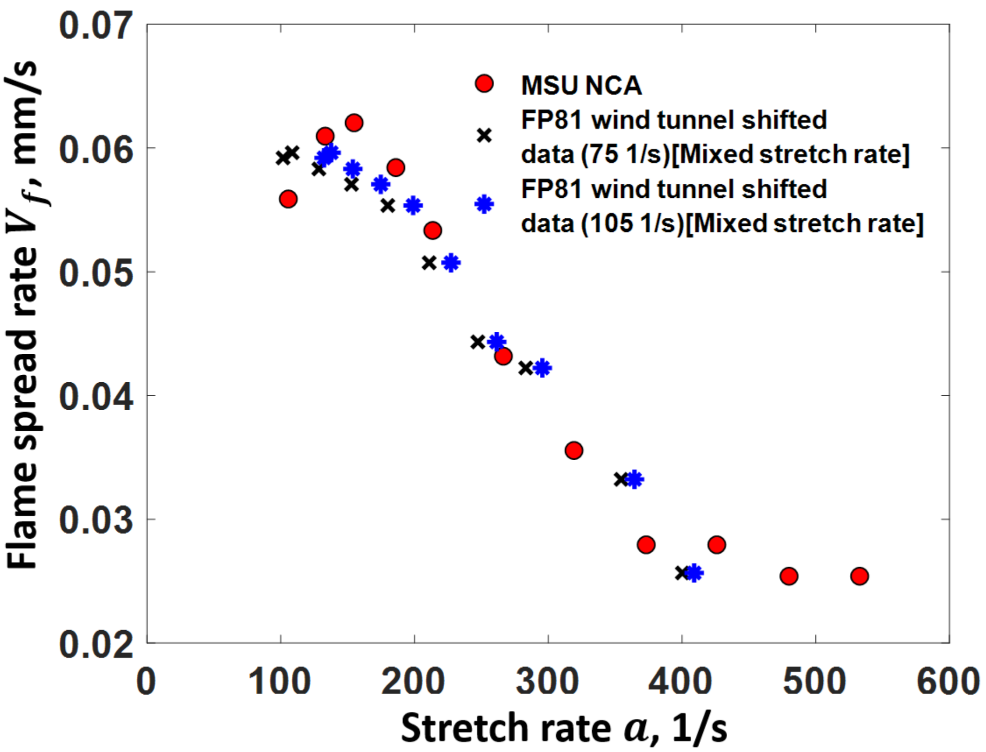

Figure 3.17: Flame spread rate as a function of mixed (bouyant and forced) stretch rate. The gap between the two sets of data in Fig. 16 is essentially eliminated over the entire a_f range.

with the MSU NCA data. Table 3.1 shows the least squared error between the MSU NCA data and FP81 wind tunnel data with and without buoyant stretch rate inclusion. It is evident that the error with a_b is lower than without a_b. The correlation provides improved agreement with MSU NCA and FP81 data.

Table 3.1: Least squared error as a function of buoyant stretch rate factor. The buoyant stretch rates, a_b 0, 75 and 105 1/s are used to calculate the least square error.

Buoyant stretch rate factor (1/s)	Least-Square Error
0	$4\,x10^{-3}$
75	$3.2\,x10^{-3}$
105	$3.2\,x10^{-3}$

3.6 Summary

Flame spread rates were measured experimentally for PMMA sample thicknesses 6.6 mm, 12.1 mm and 24.5 mm. A series of experiments was conducted for opposed flow velocities between 8 - 58 cm/s. The MSU NCA, which will suppress buoyancy, can simulate the microgravity environment spread rate. Major observations are listed below:

The NCA tests provide valuable information on thick fuel flame spread in simulated microgravity. The flame spread rate results show that for the 6.6 mm thick samples, the maximum flame spread rate occurs at 18.5 cm/s. For the 12.1 mm and 24.5 mm samples, the maximum spread rate occurs at 12.1 cm/s and 10.3 cm/s, respectively. Thus, the maximum spread rate occurs at lower flow velocities for thicker fuels although one expects an asymptote as the thickness becomes very large. Consistent with the concept of a maximum flame spread rate, as the flow velocity is further increased the spread rate drops for all samples. However, this drop is not monotonic with sample thickness. A flame spread regime called the regressive burning regime is observed for all PMMA samples tested here.

From the qualitative observation of the flame, the flame luminosity increases with the opposed flow velocity for all sample thicknesses. The leading edge of the flame is always blue. With increases in flow velocity, a bright-yellow flame along with a blue leading-edge flame is formed. The yellow flame tail grows with increased opposed flow velocity whereas the blue flame length seems to be nearly constant.

Flame spread results from the NCA (simulated microgravity) are compared with normal gravity wind tunnel results [7] for the same material (PMMA) and for the similar sample thickness. Numerical results show that a developing boundary layer forms in the FP81 wind tunnel, which alters substantially the local forced flow stretch rate, a_f. The a_f value obtained from the CFD analysis is higher than the a_f value using only the Poiseuille approximation (Figure 3.15). Incorporated into the stretch rate theory of flame spread, the computationally determined a_f for the FP81 data produces good agreement with the NCA results in the high stretch rate range of the data. It also eliminates the large gap in the data seen in Figure 3.11 and Figure 3.12. To account for the buoyancy effect inherent to normal gravity, the FP81 results were shifted by using a calculated buoyant stretch rate, a_b in a mixed stretch rate expression using orthogonal (streamwise + transverse) superposition, $a = \sqrt{(a_f^2 + a_b^2)}$. When this modification was made to the stretch rate the result was in excellent agreement between the two sets of data (Figure 3.17). In particular, there was marked improvement in the low flow velocity data range.

More generally than specific experimental tests using particular facilities, this work has demonstrated that the difficult task of making comparisons — of correlating the measurements with a valid theory — can be accomplished for laboratory scale flame spread studies in carefully controlled flow fields. The broader question addressed herein has been: How is one set of flame spread data to be compared with a different set of flame spread data? This can only be achieved when there is a common basis for comparison. The current work has shown that a common basis for comparison is the stretch rate theory of flame spread, which, implemented in the form of a correlation, is capable of producing agreement between two seemingly disparate sets of measurements. As discussed herein, there are many substantive differences between the FP81 and MSU NCA configurations but the unifying thread was the stretch rate concept. Importantly, the two data sets disagree only when the geometry of spread in the NCA changes from horizontal to regressive burning (see the high stretch rate data in Figure 3.17).

In Chapters 2 and 3, the investigations are focused on flame spread for thin fuel and thick fuel, respectively. The thick fuel flame propagation study indicates that the flame spreading is influenced by regression (transverse) along with propagation (longitudinal). This surface regression is contributing to a tunneling effect of flame, where the flame hides below the fuel surface level. As a result, flame blow-off was not observed for the tested range of flow velocities. The burnt PMMA samples of thickness 24.5 mm from thick fuel study will be analyzed in Chapter 4. The primary focus of the next study is to examine and measure the surface regression profile near the flame leading edge.

CHAPTER 4

EXPERIMENTAL INVESTIGATION OF SURFACE REGRESSION FOR THICK PMMA IN OPPOSED FLOW NARROW CHANNEL FLAME SPREAD

Synopsis

In this chapter, surface regression by sample mass loss was studied during opposed flow flame spread over polymethyl methacrylate (PMMA) under variable forced flows inside a Narrow Channel Apparatus (NCA). Experiments were perfomed in a horizontally configured NCA. The flow velocities were varied between 8 - 45 cm/s, the PMMA sample nominal thickness was 2.54 cm and the burned samples were examined for the regressed surface shape and slope. A theoretical expression, Eq. (4.1), was developed to estimate the mass loss rate from the curved regressed surface after burning. The theoretical correlation shows that in order to calculate the mass loss rate, it is necessary to measure both the flame spread rate and the regression depth. The flame spread rate is determined by analyzing the entire video record. The sample surface regression profile is measured from the post-burn sample. The results showed that the regression depth increases with increased average flow velocity. The mass loss rate along the sample center line is flow dependent. For flow velocities less than or equal to 12 cm/s, the average power law exponent for mass loss rate approximates closely to -1/2. In this case the surface barely regresses (2 mm). This result is similar to that in the theoretical literature for flame spread over ideal vaporizing and non-regressing solids. For average flow velocities higher than 24.8 cm/s, the average power law dependency is approximately -1/4. At these opposed flow velocities the regression depth is a prominent physical feature of the burned sample. Comparisons of current results are made with power laws produced in previous flame spread research. The transition from the -1/2 power to -1/4 power occurs over a limited range of velocity gradients and mean flow velocities.

4.1 Introduction

As seen in the previous two chapters, solid fuel combustion and flame spread is a complex process of chemical reactions and transport processes in the solid and gas phases. During solid combustion the gas phase provides the driving heat flux to the condensed fuel, which raises the temperature, initiates solid phase degradation, and produces a mass flux of volatile gas species into the gas. The gaseous fuel molecules react with the inflowing oxidizer to maintain flame spread. The fuel mass flux from the solid influences flame propagation, flame shape and flame character, and the gas and solid phase process are strongly coupled.

4.2 Literature Review

An initial "flame spread" model was formulated by Emmons for the forced flow combustion of an idealized liquid fuel [63]. This model was based on laminar boundary layer (LBL) theory and Spalding's flame sheet droplet combustion theory [64] which introduced the mass transfer number B. Variable property influences were included through the Howarth transformation [63]. The Emmons solution was later used as a baseline for studies of the steady burning of vertical plates [65] subject to the LBL and flame-sheet approximations. A key feature in this and almost all subsequent models of flame spread was the hypothesis of a flat, non-regressing under-flame sample surface.

The analysis by Singh et al. [66] produced a relation between the local mass-burning rate and the local temperature gradient at the condensed phase fuel surface for flames over vertical solid fuel surfaces. This relationship depends upon a suitably defined B-number.

Other studies have examined the mass loss rate on vertical, burning PMMA samples. Orloff et al. [67] measured the mass loss per unit area as a function of time at four different heights of a vertical PMMA sheet. Singh et al. [66] and Pizzo et al. [68] measured the steady downward burning rate of vertical PMMA samples under natural convection. The sample mass burning rate [66, 68] follows the respective power law decay dependencies $x^{-0.349}$ and $x^{-0.37}$, with x measured from the flame leading edge. Carmignani et al. and Huang et al. [60, 69] measured the downward burning rate of vertical PMMA slabs and PMMA cylinders, respectively. In ref. [69] a burning rate formula was derived that contained the flame spread rate and the sample regression angle. Moreover, the regression angle was linear in x [69], viz. $y(x) = -\beta x$, where β = const. In [60] an important distinction was made between a flame spread regime and a fuel regression regime for downward burning vertical rods where the transition occurs at 100 cm/s flow velocity. Concerning forced flow experiments, Ndubizu et al. [70] burned PMMA plates and measured the transient local regression rate in 90,150 and 200 cm/s.

In this work, a series of flame spread experiments were performed in the MSU NCA for horizontal thick PMMA samples for several mass averaged opposed airflow velocities. Videos of the flame spread process and post burn sample images were used to derive an expression for the local solid mass loss rate. The results showed that the flame spread rate, regression depth and mass loss rate vary with average flow velocity and therefore surface velocity gradient. The final results are presented in terms of the velocity gradient, which research [9, 11, 26] has demonstrated is a viable measure of the flow/combustion interaction during laboratory-scale flame spread for diverse macro gas flow fields.

4.3 Experimental Description

4.3.1 Experimental Facility & Test Procedure

The experiments were conducted in the horizontal Narrow Channel Apparatus (NCA), which consists of inlet, test, and outlet sections. The dimensions and details of this apparatus are described in previous chapter. The test section has dimensions $L \times W \times H$ = 78.7 cm × 45.7 cm × 5 mm. For the 8-45 cm/s flow velocity range the Reynolds number varied between 80 - 500 where the hydraulic diameter was 10 mm (2h). Since the required entry length for fully developed flow is 4.6 - 30.5 cm, and the entrance length is 41.9 cm, the channel flow was fully developed over the sample. Also as air passes through the inlet towards the test section, it travels through flow straighteners to ensure that a uniform flow enters the test section. For viewing during tests, the top plate of the test section holds a quartz window and the two side plate hold borosilicate windows.

The commercially cast PMMA sheets of thickness 2.54 cm (1 in) was ordered from the vendor. However, the actual thickness of the sheets was 2.49 cm (under-size by 0.05 cm). Samples roughly 12.1 cm (4.75 in) long by 5.1 cm (2 in) wide were cut from the flat sheets.

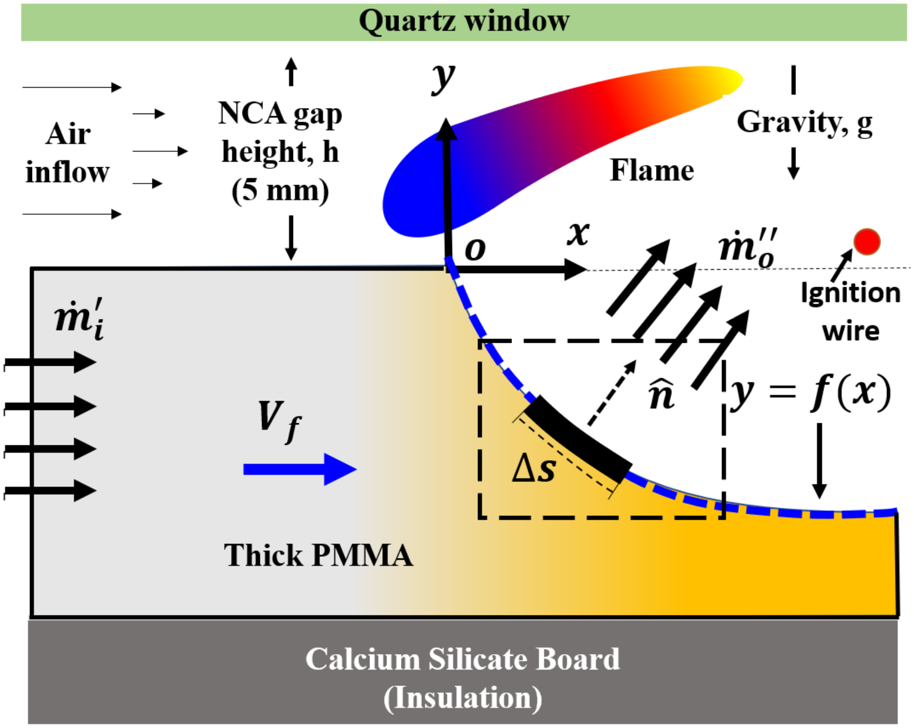

Figure 4.1: Schematic of the unscaled side view of experimental set up for Narrow Channel Apparatus (NCA). After ignition the flame spreads upstream (to the left) towards the incoming fully developed air flow having velocity distribution $u(\tilde{y}) = \frac{3}{2}\overline{V}_g(1 - 4\tilde{y}^2/h^2)$ (Note: $\tilde{y}$ is measured from centerline, y is measured from the surface). The 2.54 cm PMMA sample is considered to be thermally thick [11]. The sample is surrounded on three sides by calcium silicate insulation.

During each test the sample was surrounded (two sides and bottom) by insulation boards to prevent heat losses. In each test the supply air was regulated with a mass flow controller before entering the NCA. All tests were recorded from above (top view, see Figure 4.1) with a Sony CX 260 HDR video camera with frame rate 30 fps. The scaling size was slightly different for different tests and varied between 17-19 pixels/mm. Spotlight 16 software and MATLAB script were used to analyze the videos and estimate the spread rate V_f, which previous chapter has demonstrated is very nearly constant, i.e., steady spread. All experiments were repeated at least three times to assess repeatability. The random error for the flame spread rate is estimated as ≈ 6%.

Also shown in Figure 4.1 is the gap height (fixed at $h = 5mm$), the opposed-flow spreading flame, the consumption of the sample surface denoted by the curve $y = f(x)$, the local normal $\hat{n}$ to this curve and the local mass flux $\dot{m}_o''$ from the curved surface into the gas. In a coordinate system fixed to the sample leading edge the sample inflow speed is V_f. In this flame-fixed coordinate system, the air inflow is V_f plus the fully developed parabolic channel profile.

Experiments were conducted for inflows having $\overline{V}_g$ = 8.2, 10.3, 12, 14.5, 20.7, 24.8, 29, 37.3, 41.4, 45.5 (cm/s). The corresponding surface shapes after the experiments had ended and the samples had cooled were measured by imaging the sliced sample, then analyzing the image with an in-house MATLAB script to determine the surface shapes $y = f(x)$. The MATLAB script served to systematically process the digital images. Each photographic image was transformed into a gray level image with black background contrasted with white sample. The estimated error for mass loss rate is ≈ 8%.

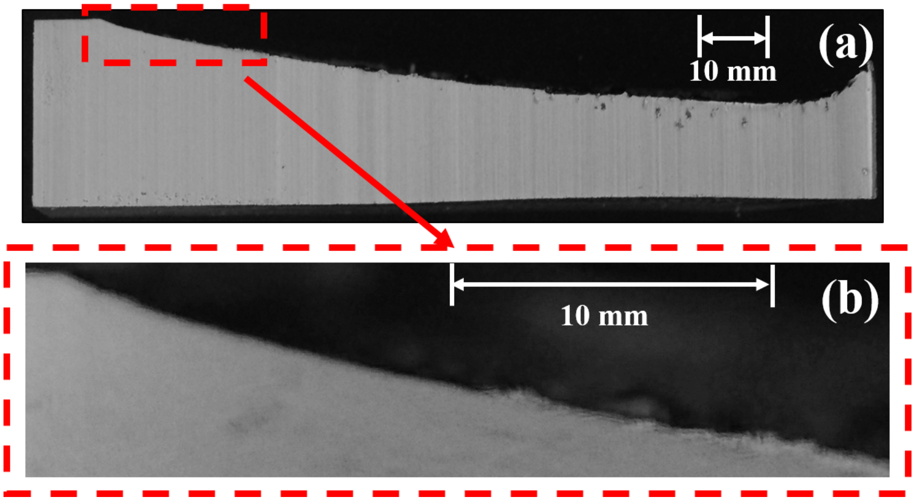

Figure 4.2: (a) Cutaway profile of entire burned sample (flame spread leftward). The burnt sample images were taken with a high resolution mirrorless Olympus OM-D E-M5 Mark II camera. The resolution of the images were 4608 x 3456 pixels. The scaling size was 114 pixels/mm. The expanded view (b) shows the detailed region to be examined, which does not include the trailing edge where $y = f(x)$ no longer monotonically decreases.

4.3.2 Surface Shape Measurement Technique & Mass Flux Correlation

A burned sample surface $y = f(x)$ is shown in Figure 4.2. The profile cross section is obtained by slicing the sample in half after a spread test. The principal hypothesis herein is that $y = f(x)$ is a negative, monotonically decreasing function of distance x measured from the leading edge. The solid mass flux $\dot{m}_i'' = \rho_s V_f$ crossing the area $\Delta y \cdot 1$ equals the mass flux leaving in the local $\hat{n}$ direction: $\rho_s V_f \Delta y \cdot 1 = \dot{m}_o'' \Delta s \cdot 1$. Thus,

$$\dot{m}_o'' = \frac{\rho_s V_f |f'(x)|}{\sqrt{1 + f'(x)^2}}, \tag{4.1}$$

which gives the local mass flux leaving the solid surface downstream of the flame leading edge.

It will be seen in Section 4.4.1 that the regressed shape has the power law form $y = |f(x)| = Cx^n; 0 < n < 1$. The expression is substituted from $|f'(x)| = nC/x^{1-n}$ into Eq. (4.1) and evaluate the average $\overline{\dot{m}_o''}$ over the length L from the definition $\overline{\dot{m}_o''} \equiv \frac{1}{L}\int_0^L \dot{m}_o'' dx$. For small L — for which $|f'(x)| = nC/x^{1-n}$ in the integrand is large — we find $\overline{\dot{m}_o''} \approx$ const. For large L — for which $|f'(x)| = nC/x^{1-n}$ in the integrand becomes small — we find $\overline{\dot{m}_o''} \approx \text{const.} \cdot L^m$, where m is negative and satisfies $|m| + n = 1$. The latter limit case suggests that if the power law for the slope function $f(x)$ is n, then the resultant power law dependence from Eq. (4.1) for the mass flux $\dot{m}_o''$ is $-m = 1 - n$. In other words, the powers can potentially obey the fixed relation $|m| + n = 1$. It will be seen from Table 4.1 that in fact $|m| + n \neq 1$ and that neither the small nor large L limits are precisely true.

4.4 Experimental Results

Here the regressed surface shapes $y = f(x)$ are first measured and then used in order to evaluate $\dot{m}_o''$ by using Eq. (4.1). It is not assured that all of the emitted mass will burn at the flame, some may be swept from the NCA as unburned hydrocarbons.

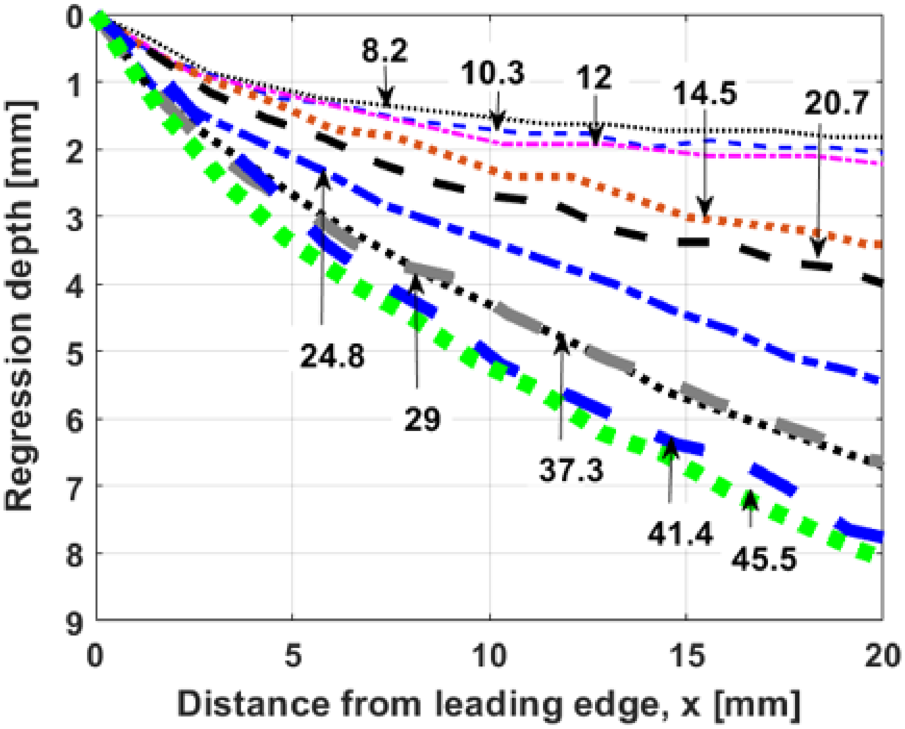

Figure 4.3: Surface regression profiles $y = f(x)$ along the center line for the ten test $\overline{V}_g$ values (cm/s). As $\overline{V}_g$ increases the regression depth $|f(x)|$ increases.

4.4.1 Surface Regression Profiles

Shown in Figure 4.3 are the experimental data (broken lines) for the surface regression profiles in a 20 mm streamwise segment (see Figure 4.2 (b)) of the burned surface. The $\overline{V}_g$ values (cm/s) are indicated by arrows pointing to each curve. The best fit lines (not shown in Figure) are formed from the power law $|f(x)| = Cx^n$. The constants C and n are shown in the second and third columns of Table 4.1 for each regression profile.

Shown in Figure 4.4 are the local slopes in the indicated region of Figure 4.3 for all of the opposed velocities. Figure 4.3 shows that the larger is $\overline{V}_g$, the deeper is the surface regression profile. The three lowest opposed flow velocities $\overline{V}_g$ = 8.2, 10.3, 12 cm/s cluster together, as do the next two, $\overline{V}_g$ = 14.5 and 20.7 cm/s. Clustering also occurs but is less obvious for the last five cases, $\overline{V}_g$ = 24.8, 29, 37.3,41.4 and 45.5 cm/s. The local slopes were calculated from the power fit equation of the regression depth. As in Figure 4.3 the lowest three velocities cluster together. The lowest R^2 values are for $\overline{V}_g$ = 8.2, 10.3, 12 cm/s for which the powers n average to 0.41 ± 0%. For

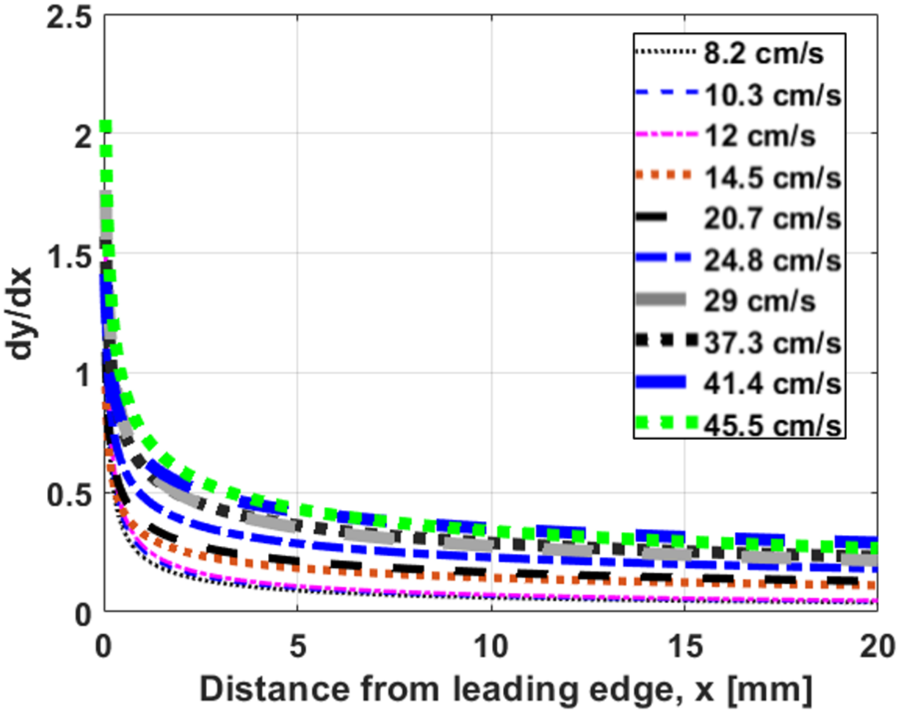

Figure 4.4: Local slopes $dy/dx = f'(x)$of the regression depthas a function of distance from the leading edge for various opposed flow velocities, in cm/s. These are used in Eq. (4.1) to evaluate the local mass flux.

the next two velocities, $\overline{V}_g = 14.5$ and 20.7 cm/s, the average n is 0.64 ± 0%. For the remaining five velocities, $\overline{V}_g = 24.8, 29, 37.3, 41.4, 45.5$ cm/s, the average n is 0.672 ± 4.7%.

4.4.2 Volatile Mass Flux Distributions

Using the slope of surface shape profiles of Figure 4.4 and documented in Table 4.1, Eq. (4.1) generates the mass flux profiles in Figure 4.5. Shown here is the local mass flux along the sample centerline during steady state flame spread. Flow velocities $\overline{V}_g$ are shown in boldface letters. The best fit lines (not shown in Figure 4.5) are also formed here using power law $\dot{m}_o'' = Dx^m$. However, the fit parameters are shown in the D, m, R^2 columns of Table 4.1 for which $R^2 > 0.97$. The results show average powers $m = -0.51 \pm 1.6\%$ over the first three conditions ($\overline{V}_g = 8.2, 10.3, 12$ cm/s), $m = -0.315 \pm 1.6\%$ for $\overline{V}_g = 14.5, 20.7$ cm/s, and $m = -.246 \pm 10.4\%$ for $\overline{V}_g = 24.8, 29, 37.3, 41.4, 45.5$ cm/s. The initial and final $\dot{m}_o''$ power dependencies $m = -0.51$ and $m = -.246$ bracket a transition region having $m = -.315$.

Table 4.1: Shown are $\overline{V}_g, V_f$, the correlation coefficients C, D, E, the exponents n, m, p and R^2 values for regression depth, mass loss rate and theoretical correlations for ten $\overline{V}_g$ values. The average values of n for the first three is 0.41. For $\overline{V}_g = 14.5$ and 20.7 cm/s the average n is 0.64. The last five five $\overline{V}_g$ values give an average n of 0.672 (±4.7% variance). The average values of m for the first three is -0.51 (±1.6% variance), for the next two is -0.315 (±1.6% variance) and for latter five is -0.246 (±10.4% variance). Over the first three entries $n + |m| = 0.92$, for fourth and fifth entries it is$n + |m| = 0.955$ and over the last five entries $n + |m| = 0.92$. These sums are close to but not equal to unity, as per the discussion of Section 4.3.2. Also shown are deduced parameters for the theoretical average heat flux $\overline{\delta \dot{q}''}$ that generates $\dot{m}_o''$. Note that $p = n - 1$.

V_g	V_f	Regression fit			Mass loss fit			Theoretical		
	$\times 10^3$							considerations		
[cm/s]	[cm/s]	$y = Cx^n [mm]$			$\dot{m}_o'' = Dx^m [g/m^2 s]$					
		C	n	R^2	D	m	R^2	E	p	$\overline{\delta \dot{q}''}$ $[kW/m^2]$
8.2	6.17	0.57	0.41	0.953	13.5	-0.52	0.986	24.0	-0.59	3.9
10.3	6.5	0.63	0.41	0.963	15.62	-0.51	0.983	28.0	-0.59	4.6
12	6.3	0.69	0.41	0.978	16.37	-0.5	0.97	30.2	-0.59	4.9
14.5	6.26	0.52	0.64	0.996	20.05	-0.32	0.994	35.4	-0.36	7.4
20.7	5.99	0.6	0.64	0.993	21.44	-0.31	0.991	38.6	-0.36	8.1
24.8	5.10	0.72	0.67	0.997	20.35	-0.27	0.988	37.5	-0.33	8.2
29	4.66	0.91	0.67	0.998	22.1	-0.25	0.981	43.3	-0.33	9.5
37.3	4.39	0.97	0.64	0.998	20.25	-0.27	0.976	40.1	-0.36	8.4
41.4	3.56	0.89	0.73	0.99	18.73	-0.2	0.986	36.9	-0.27	8.9
45.5	3.30	1.15	0.65	0.996	18.93	-0.24	0.969	39.9	-0.35	8.5

Figure 4.6 shows the comparison of the power fit exponent of mass loss rate during opposed flow flame spread between the horizontal channel flow MSU NCA, the vertical plate natural convection correlation and the horizontal forced convection theoretical predictions of [63]. The comparison is made as a function of velocity gradient because it is the only fluid-dynamical feature that is common to all configurations. This statement is now explained.

For the NCA, the incoming flow is fully developed and the velocity gradient is determined from $u(\tilde{y}) = \frac{3}{2}\overline{V}_g[1 - 4\tilde{y}^2/h^2]$ where $\tilde{y}$ is measured from the NCA centerline and the velocity gradient is evaluated at the sample surface $\tilde{y} = -h/2$ (the $x - y$ system of coordinates is fixed to the leading edge, see Figure 4.1).

The $-1/2$ exponent for $\dot{m}_o''$ applies for forced flow fields of the Blasius LBL type [63]. This value is shown in Figure 4.6 as the black dashed line. The NCA results show that at low $\overline{V}_g$ values

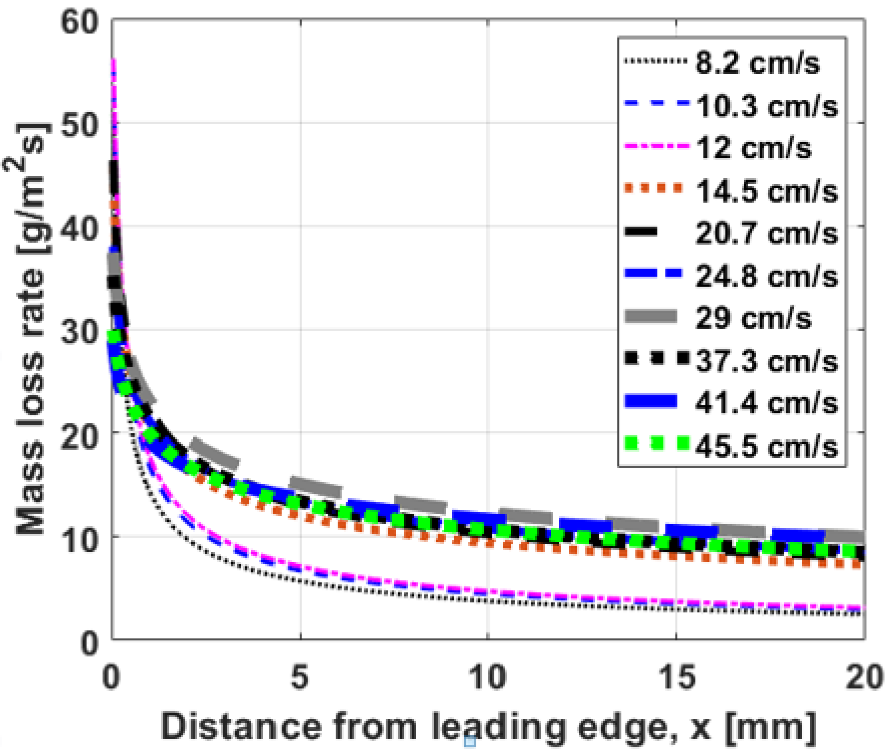

Figure 4.5: Local mass loss rate along the centerline as a function of distance from the leading edge for different opposed flow velocities (cm/s).

8.2, 10.3 and 12 cm/s, the mass flux exponents are close to the predicted $x^{-1/2}$ dependence, whose theoretical basis is the non-regressing surface. Looking back at the regression depth in Figure 4.3 it is seen that the maximum regression depth over the 12.1 cm length of the sample for these low- $\overline{V}_g$ values is less than 2 mm, i.e., an approximately 1.5% regression. Thus, the theoretical non-regressing fuel result agrees with the low-$\overline{V}_g$ NCA experiments. However, for $\overline{V}_g$ = 14.5 and 20.7 cm/, the exponents average to -0.315, which is in the vicinity of the Singh et al. [66] exponent of -0.349 for downward flame spread under natural convection.

For $\overline{V}_g \geq 24.8$ cm/s the $\dot{m}''_o$ exponents averaged to $m = -0.246$. Here, finite-rate chemical kinetics may be important although the 5 mm height of the NCA decreases the flame standoff distance significantly. From side visual observation, it is seen that for larger $\overline{V}_g$ the flame anchors itself along the regressing surface below the unburned fuel surface height. In this region, which qualitatively resembles the fluid mechanical backward facing step, there is possible flow recirculation [11]. Continuous vapor jetting was also observed. These fluid mechanical processes, which

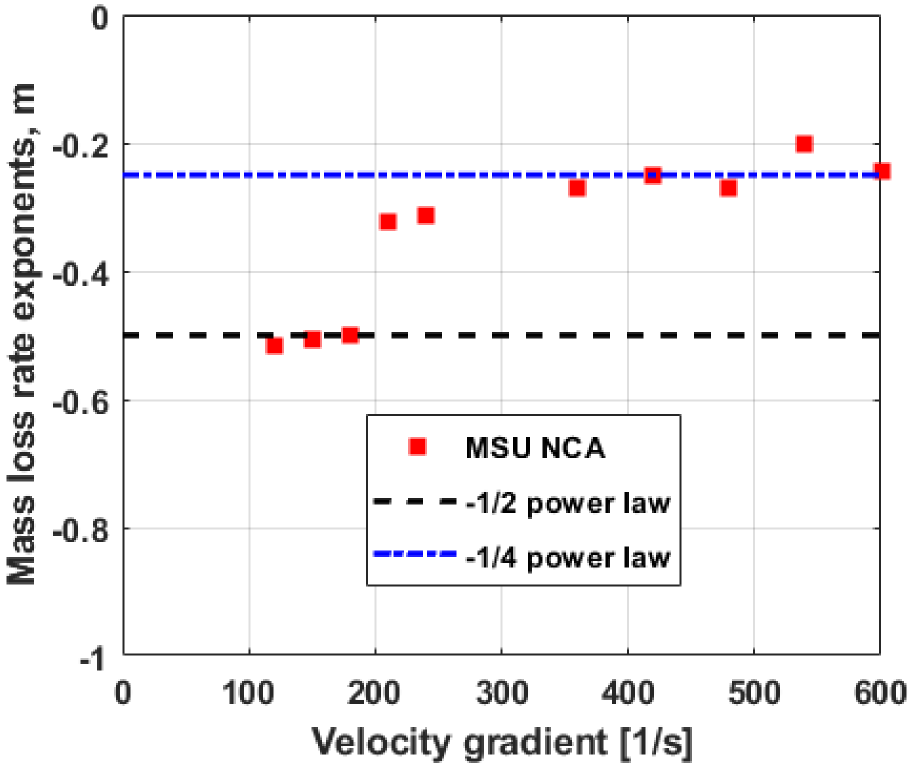

Figure 4.6: Comparison of mass loss rate exponents with the $x^{-1/2}$ boundary layer theory [63] and the $x^{-1/4}$ natural convection heated flat plate.

seriously upset the notion of both a mean mass flow $\overline{V}_g$ as well as the notion of a surface velocity gradient that can reliably be estimated from the Hagen-Poiseuille theory, could seriously alter the leading edge flame spread and surface regression characteristics and produce the $m \approx -1/4$ functional dependence.

The influence of NCA gap height to suppress the buoyancy is examined in ref. [26].The high regression depth (> 5 mm) at high flow velocity (> 24.8 cm/s) contributes to alter the NCA gap height. It is an indication that for thick samples at high flow velocities the NCA is perhaps not suppressing buoyant flow. Hence the $\dot{m}_o''$ deviates from [66] and instead produces a result that is in functional agreement with the classical natural convection heated vertical plate, which gives an $x^{-1/4}$ dependence. Here $m = -0.246$.

4.5 Discussion

Here the experimental results are discussed in the context of the theoretical framework.

4.5.1 Mass Flux Optimization

The mass flux $\dot{m_o}''$ of volatiles gases from the surface of the decomposing solid fuel is given by Eq. (4.1). Mathematically, this expression can be written as $g(x, y') = y'(x)/\sqrt{1 + y'(x)^2}$. An extremum for $g(x)$, i.e. of $\dot{m_o}''$, is obtained when $g(x, y')$ satisfies the differential equation $g - y'\partial g/\partial y' = \text{const.}$ [71]. A direct calculation gives $y'(x) = \text{const.}$ Thus, the optimum $\dot{m_o}''$ occurs when the sample consumption produces the surface regression function $y(x) = -\beta x, \beta \geq 0$, for which $\dot{m_o}'' = \rho V_f \beta/\sqrt{1 + \beta^2}$ increases as β increases. Figures 4.1, 4.2 and 4.3 show that the surface regression process is not optimal.

4.5.2 Mass Flux by Surface Decomposition & Relationship to Heat Flux

The following theoretical development is based on the boundary condition at the solid/gas interface. This is evaluated immediately before and after the solid surface begins losing mass to the gas at $x = 0$. Before surface degradation occurs, the incoming heat flux from the flame and hot gases, $\dot{q}''_{f+g}$, is balanced by heat conduction into the solid phase, $\dot{q}''_{cond,s}$. After degradation occurs, the incoming flux (whose value is nearly the same as it was when there was no degradation) is now balanced by a diminished $\dot{q}''_{cond,s}$ (plus) the heat liberated to the gases by the evolved mass, $\dot{m_o}''\mathcal{L}_v$. After regression commences the net heat into the surface $\delta\dot{q}'' \equiv \dot{q}''_{f+g} - \dot{q}''_{cond,s}$ balances the evolved mass flux enthalpy, viz.,

$$\delta\dot{q}'' = \dot{m_o}''\mathcal{L}_v = \rho_s\mathcal{L}_v \left|\frac{dy}{dt}\right|. \tag{4.2}$$

Converting from time to position using $|dy/dt| = V_f|dy/dx| = V_f|f'(x)|$ and writing the net heating function as $\delta\dot{q}''(x) = Ex^p$ in Eq. (4.2) gives $Ex^p = (\rho_s\mathcal{L}_v V_f)|dy/dx|$, which is integrated to give

$$y(x) = -\left(\frac{E}{(p+1)\rho_s\mathcal{L}_v V_f}\right)x^{p+1} = -Cx^n. \tag{4.3}$$

The correspondence between the theoretical parameters of Eq. (4.3) and C and n of Table 4.1 is apparent: $p = n - 1$ and $E = n\rho_s\mathcal{L}_v V_f C$. Values of E for the three data groupings can be calculated from the empirical data of Table 4.1, and the corresponding $\delta\dot{q}''$ evaluated. The result is a generally increasing quantity having plausible magnitude $\overline{\delta\dot{q}''} \approx 5 - 10kW/m^2$.

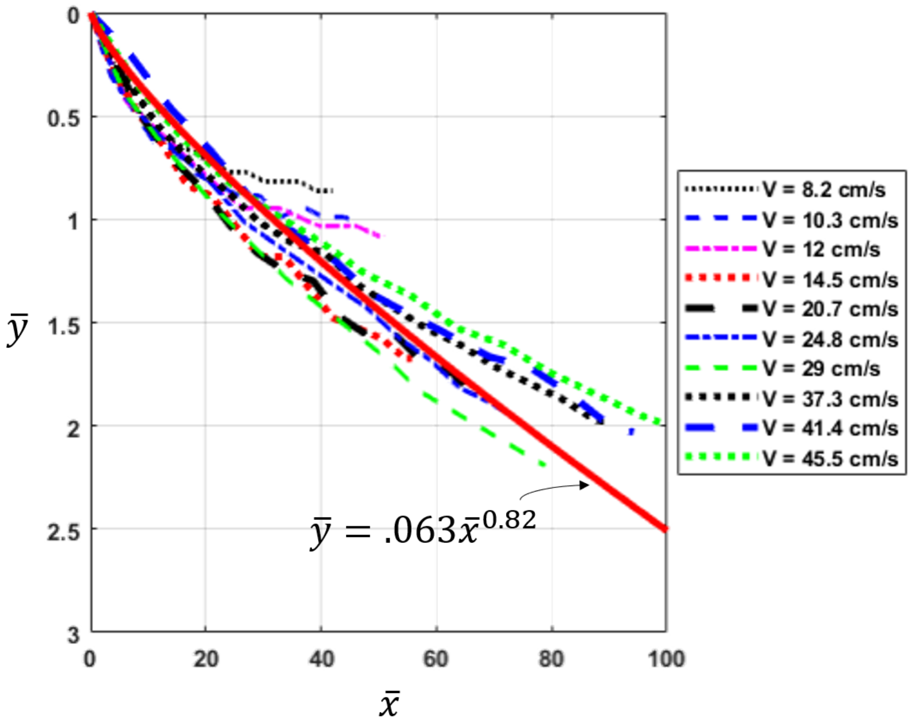

Figure 4.7: Surface regression profiles, $\bar{y}$ in dimensionless form along the center line for the ten test $\overline{V}_g$ values (cm/s) where $\bar{y} = \frac{y}{\frac{\alpha_s}{V_f}}$ and $\bar{x} = \frac{x}{\sqrt{\frac{\alpha_g}{a}}}$. The red line shows the empirical correlation $\bar{y} = 0.063\bar{x}^{0.82}$.

4.5.3 Dimensionless Regression Profile

Assuming, $\bar{y} = \frac{y}{L_y}$ and $\bar{x} = \frac{x}{L_x}$ where L_x is the characteristic gradient length and L_y is the solid conduction length. For fully developed air flow, the velocity distribution $u(\tilde{y}) = \frac{3}{2}\overline{V}_g(1 - 4\tilde{y}^2/h^2)$. Then, $a = \frac{\partial \tilde{u}}{\partial \tilde{y}}(\tilde{u} = -h/2) = \frac{6\bar{V}_g}{h}$. Thus

$$\bar{y} = -\frac{CL_x^n}{L_y}\bar{x}^n \tag{4.4}$$

Using $L_x = \sqrt{\frac{\alpha_g}{a}}$ and $L_y = \frac{\alpha_s}{V_f}$

Figure 4.7 shows dimensionless regression depth, $\bar{y}$ as a function of dimensionless distance, $\bar{x}$. The scaling is based on the thick fuel assumption where both solid and gas phases are dominant.

The non-dimensionalization of the lengths collapsed regression profiles on each other for different flow velocities. The scaled data generate the empirical correlation as $\bar{y} = 0.063\bar{x}^{0.82}$.

4.6 Summary

The combined empirical and theoretical analysis presented herein shows that the mass loss rate depends on sample density, flame spread rate and the geometry of surface regression. The density of the PMMA is approximately constant (1190 kg/m^3), whereas the V_f and surface regression are functions of the flow. The results show that a larger $\overline{V}_g$ generates a larger regression depth. Surface regression increases with x for all values of $\overline{V}_g$.

Three different data groupings of surface regression were observed. The first data grouping has $\overline{V}_g$ =8.2, 10.3, 12 cm/s. The maximum surface regression of this group is approximately 2 mm. The second data grouping has $\overline{V}_g$ =14.5 and 20.7 cm/s: the maximum regression depth is approximately 4 mm. The third data grouping has $\overline{V}_g$ = 24.8, 29, 37.3, 41.4 and 45.5 cm/s. These data are not so closely clustered as the two previous although there is functional similarity in the regression profiles.

The influence of the power of the fuel surface mass efflux was discussed and compared with the $x^{-1/2}$ behavior found for the case of the "ideal vaporizing solid" [11] and whose implications were examined in [72].

The appearance of the $x^{-1/4}$ power in the mass flux dependence on downstream distance does not mean that this regime of flame spread (which has slightly higher $\overline{V}_g$ than the two regimes preceding it) is akin to the vertical constant temperature heated plate. More likely, there is a complex flow pattern within the curved-out sample (see Figure 4.3) that generates the -1/4 power-law dependence. The implications for flame spread, heat transfer and general flame/solid interaction remain yet to be studied for this complicated flow pattern, which may involve flow separation and recirculation in addition to the above-mentioned jetting.

Furthermore, the examination on post-burn sample is continued to the next Chapter 5. During the test, it is observed that the fuel samples melt and have significant vapor jetting (shooting flame).

The attributes of molten layers for thick materials are not fully understood. Close inspection of the tests revealed the boiling of the molten samples. A thick bubble layer is found by observing the post-burn sample. This bubble formation plays a significant role on heat transfer process consequently fuel to vapor production. The next study is the first to characterize and quantify these internal bubbles.

CHAPTER 5

EXPERIMENTAL STUDY OF MOLTEN BUBBLE LAYER GROWTH AND BUBBLE SIZE DISTRIBUTION IN POST-FLAME-SPREAD PMMA SAMPLES

Synopsis

Thermoplastics are polymers that are moldable to create above their liquification certain temperature. They have a wide array of applications. The burning of thermoplastics show some unique characteristics. For PolyMethylMethAcrylate (PMMA), a molten layer of bubbles in-liquid develops during burning, which has a profound effect on flame spread and stability. The in-depth bubble layer reduces solid phase conduction both forward (lateral) and downward (transverse) which can alter the overall nature of flame spreads. This study is primarily focused on the bubble formation and distribution inside a burnt PMMA sample. Experiments were conducted in the Michigan State University (MSU) Narrow Channel Apparatus (NCA). The burnt samples were analyzed by dividing the sample image into eight equal sections. Bubble sizes and counts were determined using digital image analysis (DIA). The frequency of the bubble size distribution was analyzed and compared for each of the eight segments. Standard distribution functions were fitted against the empirical probability density function (PDF) for the bubble size distribution. The Log-normal distribution provides a good prediction for the bubble size distribution for all segments.

5.1 Introduction

Thermoplastics (polymers) have numerous applications in the construction industry, for transport vehicles, the electro-technical industry, aircraft windows and household materials. However, thermoplastics are highly flammable and can also constitute a major fire hazard.

Thermoplastic combustion is a complicated process, involving both solid and gas phase reactions. Some thermoplastics form char layers in the condensed phase, e.g. cellulosic fuels, while others form internal bubbles, undergo bubble bursting, sputtering of the surrounding gases, and swelling or intumescence.

For non-charring thermoplastics, the exothermic chemical reactions in the gas phase flame act as an external heat flux and liquefy a layer near the surface of the thermoplastic [73]. Thus, for some thermoplastics a large amount of bubble growth can occur inside the molten layer. These bubbles transport volatile gases through the liquefied molten liquid layer to the liquid layer surface where they burst. The molten liquid bubble layer reduces the conductivity by acting as an insulator at the thermoplastic surface [74]. It also plays a role in altering the burning rate through the mechanism of surface mass transport during regression [75].

The phenomenon of bubble layer formation has not been thoroughly considered in flame spread theory. In advanced flame-spread models of the future, the inclusion of bubbles will likely be key factor for making accurate flame spread rate, burning rate predictions. Although numerous heat transfer models have been developed, insufficient attention has been paid to the study of bubble formation during thermoplastic pyrolysis and combustion, which is necessary for the development of accurate models of flame spread over thermoplastic materials. This study is meant to address this knowledge gap.

Here, the attention is confined to bubble formation in non-charring thermoplastics. A representative thermoplastic is cast Polymethylmethacrylate (PMMA) which is formed by either casting or extrusion. The constituents of PMMA thermal degradation or decomposition are approximately 80% MMA gas when the temperature is greater than 500 °C [76]. Cast PMMA does not char or drip during combustion. By contrast, extruded PMMA does drip because their aligned polymer chains produce a relatively low glass transition temperature of the solidified polymer compared with the pyrolysis temperature [77]. Cast PMMA yields a harder, sturdier and more homogeneous material with higher molecular weight and longer polymer chains. Due to these attractive properties and burning characteristics, cast PMMA is suitable for space flight experiments and simulated zero-g testing.

It is noted that of the many types of materials that can be used in scientific studies of flame spred, PMMA appears to best conform to what has been referred to as the "ideal vaporizing solid" [11].

That is to say, it begins gasifying and continues to gasify/vaporize at a nearby constant temperature of 668 K. The liquid melt layer (which contains the bubbles) is quite viscous and does not drip or run in downward spread, and there is almost no charring. In addition, under what can be referred to as “ordinary” conditions, the gasifying surface does not regress significantly. All of these factors make PMMA an excellent (“ideal”) material with which to compare experiment and theory.

5.2 Literature Review

Numerous studies have been conducted over many decades to study the flame spread mechanism over thermoplastic surfaces especially for PMMA [7, 18, 27, 44, 50, 52–55, 60, 61, 68, 78–92].

Usually those studies were categorized into two flame spread groups depending on the thickness of the specimens: Thermally thin spread occurs when the temperature distribution across the specimen is uniform. Thermally thick spread occurs when the temperature distribution has no influence at the bottom sample surface. A fuel specimen, whether thermally thin or thick, can be categorized using the equation:

$$L_s \sim \sqrt{\frac{\alpha_s \alpha_g}{V_f U}}, \tag{5.1}$$

where, α_g is the thermal diffusivity in the gas, α_s is the thermal diffusivity in the solid, V_f is the flame spread rate and U is the oxidizer velocity. If the preheat length L_s is less than the fuel thickness, the fuel may usually be considered as thermally thick.

In addition, the flame spread mechanism of PMMA depends on the placement of the specimen: vertical (downward and upward) [16, 18, 60, 68, 78, 81, 82, 85, 89, 90] and horizontal (opposed and concurrent) [7, 27, 44, 55, 78–80, 82, 91] flame spread. There are also studies where the angle of the sample placement is varied [93].

Kashiwagi and Ohlemiller [94] investigated the effects of gas phase oxygen concentration on the rate of gasification and surface temperature of PMMA (4 x 4 x 1.5 cm). In addition, low density PE samples (4 x 4 x 1.25 cm) were investigated transient, non-flaming heating under thermal radiation fluxes of 1.7 and 4 W/cm^2 with five different ambient gas mixtures. In this work, no flame is involved but the external thermal radiation source mimics the primary mode of energy transfer in the developing fire. They reported occasional bursting of large bubbles in the nitrogen environment, which caused irregular surface temperatures. Some bubbles burst through small neck-like holes into the near surface and vented their contents to the gas phase. This process was violent. In 1994, Kashiwagi described the significance of the bubble study on the internal transport mechanism for flammable polymers [95].

Regarding in-depth bubble formation, Wichman [73] developed a theoretical model to describe the response of a flammable thermoplastic such as PMMA to an incident heat flux. The model attempted to describe the influence of bubble formation on the heat and mass transport processes involved in sample gasification. Bubble nucleation, growth, convection and collisions were included in the derived bubble number distribution function. The mass flux of volatile gases and the bubble void fraction were developed from the equations for conservation of mass, momentum, species and energy to predict the steady-state surface regression rate. Some of the notions discussed in [73] are examined here, such as the bubble distribution function.

In the context of established burning, not transient flame spread, Yang et al. [96,97] investigated the burning characteristics of polymer spheres (PMMA), Polypropylene (PP) and Polystyrene (PS) having diameters 2-6.35 mm in low gravity under oxygen concentrations 19-30%. The dynamic events of bubbling, sputtering, vapor jetting, soot shell formation and breakup were observed during combustion. Bubble bursting contributes to the dynamic ejection events during polymer combustion and were observed quite spectacularly, as highly transient to the flame surface.

The active suppression of bubble formation was studied in an idealized, 1-D, low pressure pseudo microgravity environment. The investigations [98] introduced a fuel layered approach where a molten layer is coated over the non-combustible solid PMMA sphere to suppress bubble formation. They showed that bubble formation and bursting can be suppressed by decreasing the ambient pressure. Bubble formation was observed at atmospheric pressure (~100 kPa), however at reduced pressure (50 and 20 kPa), bubble bursting at the sample surface barely occurred.

The influence of the molten bubble layer on diffusion flames over PMMA was studied at low stretch rates in a microgravity environment [74]. Initially, sample surface swelling was observed due to bubble layer development during ignition. Sample swelling showed a direct proportionality with bubble formation in the low Peclet number range. Buoyancy was determined to play a small role (compared to thermocapillary forces and surface regression) on vertical bubble migration, in fact a higher rate of surface bubble bursting was seen at low gravity. Therefore, bubble surface bursting shows an apparently greater influence on low gravity polymer combustion.

A comprehensive three-dimensional model including bubble effects on a burning spherical thermoplastic in microgravity was developed by Butler [75]. The model employes the finite element method to solve the one-dimensional radial equation for the temperature field in order to describe bubble nucleation, growth and migration. It was found that bubble bursting influences pyrolysis significantly. The bubbles release gases having low thermal conductivity, which acts as a gas-phase insulator film. As a result the heat transfer to the solid slows down and the mass loss rate decreases.

Johnston [99] described internal bubble formation for spherical PMMA shells. A bubble layer is obtained using CT scan analysis after each drop test near the surface. This work showed that the bubble density and bubble sizes variable, as is the bubble layer depth.

5.3 Experimental Description and Image Acquisition

All experiments were conducted in the horizontal Narrow Channel Apparatus (NCA) where the main test section has dimensions 78.7 cm × 45.7 cm × 5 mm. A detailed description of the NCA setup and characteristics can be found in Ref. [27]. The fuel samples used in this experiment were rectangular bars extracted from commercially cast PMMA flat stock sheets (30cm × 30cm × 2.54cm). The final samples were roughly 12.1 cm long and 5.1 cm wide. Although the original PMMA stock thickness was listed as 2.54 cm, the actual thickness of the sheets was 2.49 cm which was within the reported vendor tolerances. The sample was surrounded (two sides and bottom) by insulation boards to prevent heat losses. A 28-gauge Kanthal wire was used to ignite the sample that was placed at the near or downstream side of the sample (with respect to the opposed oxidizer inflow). The igniter wire was connected to a DC power supply. Each test started with supply air entering the NCA controlled by a mass flow controller. After establishing the desired flow rate, the DC power supply was activated in order to ignite the sample. This permits opposed flow flame spread to occur over the sample.

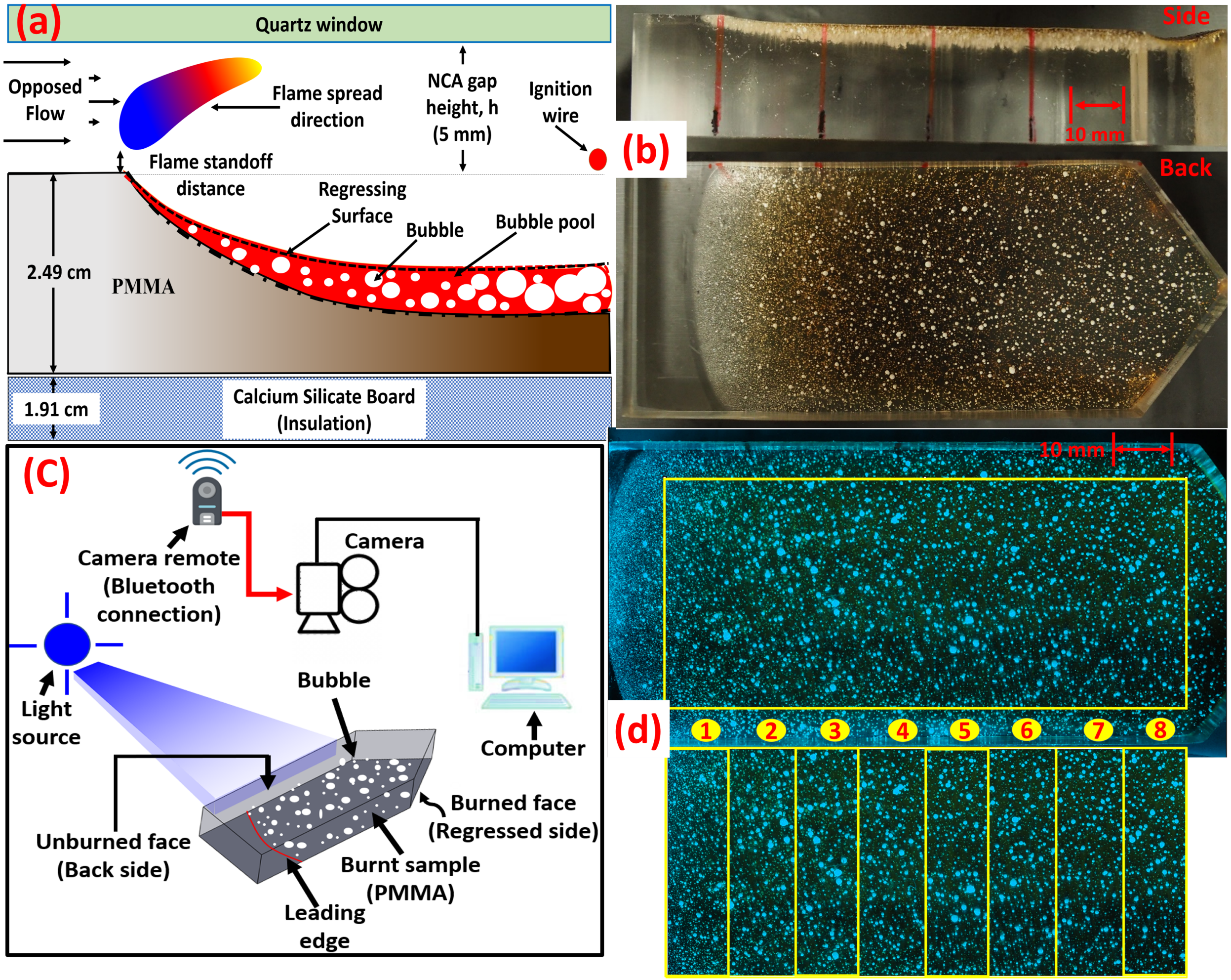

Figure 5.1: (a) Schematic of the unscaled view of the experimental setup of the Narrow Channel Apparatus. After ignition the flame spreads upstream (to the left) from the "rear" to the "front" of the sample. The 2.54 cm PMMA sample is considered to be thermally thick. The sample is surrounded on three sides by calcium silicate insulation. The schematic shows a conceptual side view of bubble formation and regression of the burning PMMA specimen. (b) A digital image of the post-burn sample. The top photograph is the side view of the sample, which shows the bubble layer, compare with (a) the bottom photograph is the back view, which shows the bubble distribution. (c) Schematic of the camera and light settings to capture the high resolution monochromatic image. (d) High resolution monochromatic image with indicated Region of Interest, ROI (top image), and division of the ROI into eight (8) separate segments (bottom image).

Figure 5.1 shows a (a) schematic side view of opposed flow flame spread over a thermoplastic solid. The flame consumes the solid sample and causes its surface to regress. Inside the sample a bubble layer is formed adjacent to the interface. The heat transferred by conduction melts the sample surface, creating a molten layer which allows the formation of internal bubbles, see e.g., Refs [73, 75]. The samples were allowed to burn until the flame front reaches the leading, upstream or front edge of the sample. Once this happens, the main flow is turned off and the flame extinguishes. The customary test duration was approximately 30 minutes. The burned thermoplastic was removed for examination from the NCA after it had completely cooled to a solid.

Figure 5.1 (b) shows an image of the post-burn sample from the side (top image) and back (bottom image). This sample was tested at an opposed flow velocity (left to right) of 15 cm/s. The side view of the post-burn sample shows that the bubbles reside within a thin surface layer. The view from the back or under side shows a mottled and dark caramel colored residue on the burned surface. The black region is the consequence of soot deposition on the molten surface. The caramel color is from condensed products of reaction from the flame. Note that the bubbles near the leading curved edge were transparent whereas further downstream they appeared to be white.

Digital image analysis was used to evaluate the number of bubbles and their corresponding size distributions in the post-test PMMA specimen. A bench top setup was constructed to capture digital images (Figure 5.1 (c)) of the burnt sample. Images were captured from the back side using a high-resolution mirrorless Olympus OM-D E-M5 Mark II camera. The camera was remotely operated through a Bluetooth connection in order to avoid noise. A LED light source (11Watts) illuminated the surface to produce improved contrast between bubbles and background.

The resolutions of the images were 4608 x 3456 pixels where each pixel represents 0.022 mm x 0.022 mm area (Figure 5.1 (d), top). A high aperture value of f/20 was used to increase the depth of field of the bubbles in the thin layer (Figure 1(b), top). The high aperture closes the lens which in turn may cause insufficient lighting. To ensure proper lighting, a high exposure time of ½ second was used which was very sensitive to vibration. Therefore, a remote-controlled shutter was used to capture images. The software packages ImageJ and MATLAB were used to process the digital images.

A rectangular Region of Interest (ROI) image is considered for two reasons. One reason is to avoid the edge effect that occurs during burning. In addition, a cropped portion of the actual image is selected to avoid additional bias error since the light distribution was nonuniform during image capture. The resolution of the ROI was 3564 x 1902 pixels (previous dimensions). The rectangular ROI is divided in to eight equal sections. The area of each section is approximately 425 mm^2. The sample segments were numbered 1 to 8 from upstream to downstream (left to right) as shown in Figure 5.1 (d).

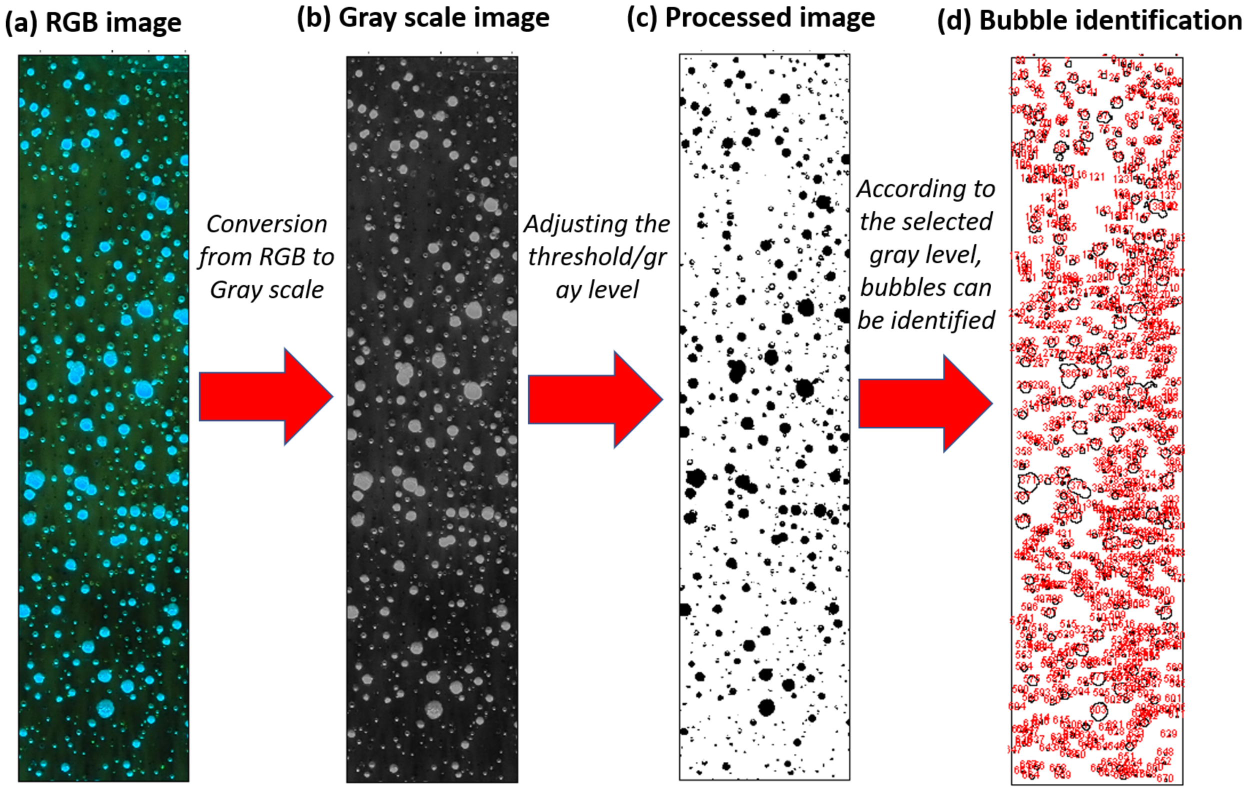

Figure 5.2: A typical bubble identification process from a raw high resolution digital image-(a) Raw RGB image segment (b) 8-bit Gray scale conversion (c) Processed image after thresholding (d) Final converted image with identified bubbles.

Figure 5.2 shows the consecutive steps of image processing. First, each slice of the image was converted from RGB (Figure 5.2 (a)) to 8-bit grayscale (Figure 5.2 (b)). Next, an image thresholding method was adopted to identify the bubbles. The 8-bit grayscale images possess a unique set of grayscale values assigned to every feature. The grayscale values range from 0 to 255, where 0 represents absolute black and 255 represents absolute white. These unique grayscale values are distinguished from other features by the thresholding, which separates some pixels within a desired range of grayscale values from the other pixels, as shown in Figure 5.2 (c). An optimum gray level value was selected during calibration. An edge detection algorithm was developed and employed, which identified all possible boundaries of the bubbles while blocking other features (see Figure 5.2 (d)).

5.4 Results

5.4.1 Bubble Statistics

Three PMMA samples having similar dimension (~ 12.1 × 5.1 × 2.49 cm) were studied. As per the previous section, they were burned at an average opposed flow velocity of 15 cm/s. Here, the bubble statistics (bubble frequency, PDF, fitting with standard function, root mean square difference) of these post-burn PMMA samples will be studied. Samples 2 and 3 produce similar results as of sample 1 for different bubble statistics. That's why, only the results from sample 1 has been shown and discussed in the following sub sections and the results from samples 2 and 3 have been included in the Appendix C to avoid redundancy.

5.4.1.1 Frequency Distribution

Figure 5.3 shows the variation of the bubble size distribution in the ROI of the burnt PMMA sample 1 shown in Figure 5.1 (d). To construct the frequency distributions, the discrete bubble sizes were tabulated in ascending order of area. Then they were grouped into size bins of 5×10^{-3} mm^2 over the range from 2×10^{-3} to 52×10^{-3} mm^2. For the sake of clarity, bubble sizes that are greater than 52×10^{-3} mm^2 were eliminated due to their statistical insignificance. Bubble size distributions appear to be asymmetrical and positively skewed (to the left) for each of the eight segments. Here, "frequency" means the number of members in each bin. The figure shows a general trend of decreasing frequency with bubble size for all segments.

The bubble frequency for the smallest size range ($(2-7) \times 10^{-3}$ mm^2) appears to be insensitive to segment number (2 to 8) except for segment 1 for which has the highest frequency.

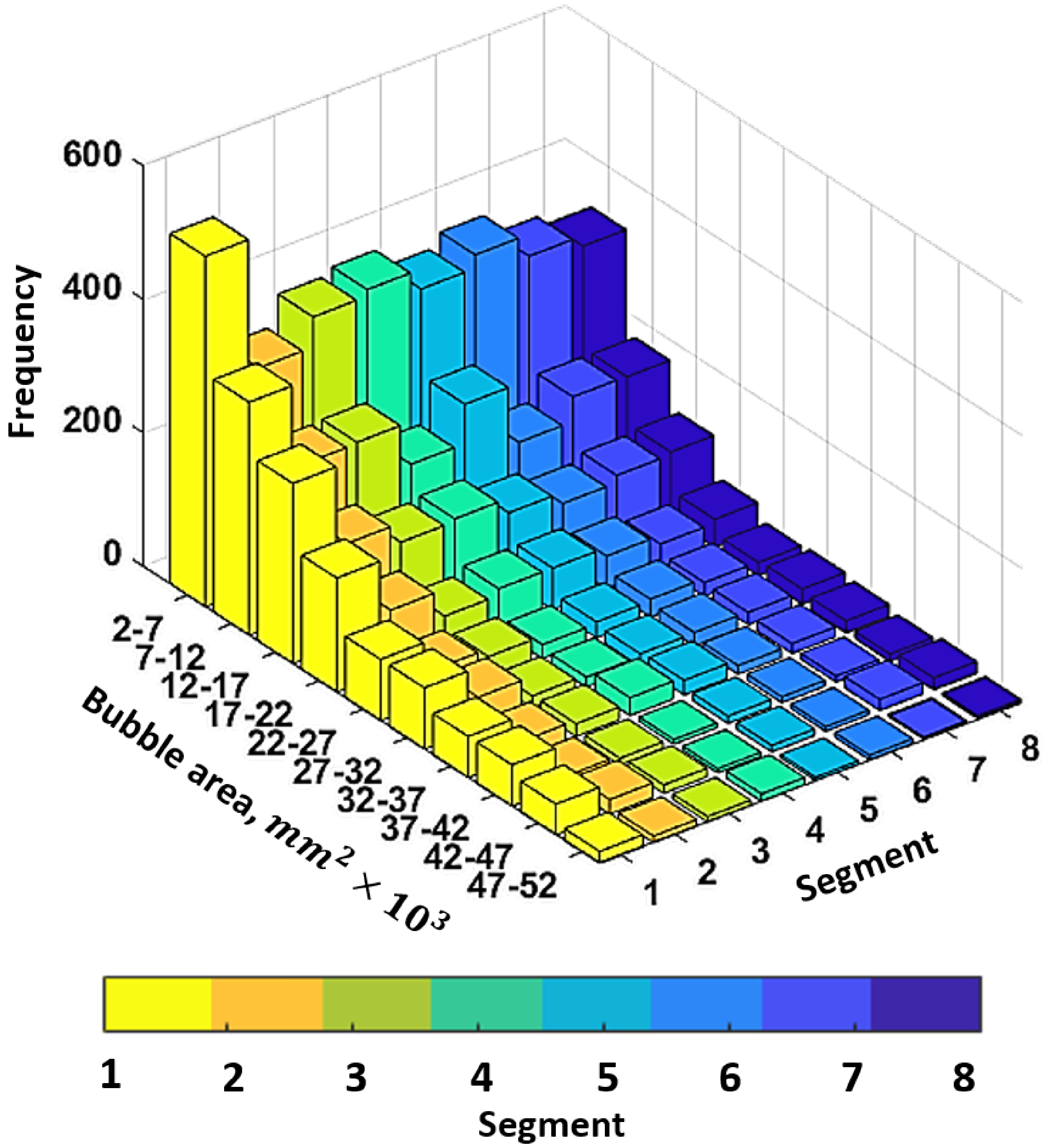

Figure 5.3: Bubble area frequency distribution. The color represents the specific segment (1-8). Yellow is segment 1 (curvy-edge side, far left segment), while violet is segment 8 (far right segment). The bubble area is divided into 10 different size ranges or bins. Each bin width is 0.005 mm^2.

During opposed flow flame propagation, the leading edge of the flame faces toward the oxidizer flow (see Figure 5.1 (a)). Bubble formation/nucleation in this segment starts earlier which results in a higher bubble frequency. The bubbles near the leading edge do not have sufficient time to coalesce or merge. Also, since bubble bursting at the interface occurs at a lower rate, it is reasonable that the bubble frequency in this region should be higher. As the oxidizer passes into the flame and the hot products of combustion are swept across the downstream surface, molten layer becomes thicker, and the bubbles have more room to collide and grow.

It was observed after flame extinguishment that some bubbles near the surface had burst and vented gaseous MMA monomer for several minutes thereafter. As a result, the bubble frequency remains smaller further downstream of the flame leading edge.

5.4.1.2 Probability Density Functions for Bubble Area Distributions

In general, the Probability Density Function (PDF) was estimated for each frequency distribution. The bubble size histogram (Figure 5.3) shows that the bubble area distributions are typically non-normal, positively skewed, and positive-definite (diameters are always positive). Figure 5.4 shows the estimated PDF as a function of bubble area. Here, the PDF is determined from the histogram of the bubble sizes. Equation (5.2) below is used to estimate the PDF:

$$\text{PDF} = \frac{\text{No of bubble in each bin}}{\text{Total no of bubbles} \times \text{Bin width}} \tag{5.2}$$

Here, the bin width is $5 \times 10^{-3}\ mm^2$ for all segments, whereas the number of bubbles varies in each segment. For clarity, the total number of bubbles in every slice is indicated in the legend. In Figure 5.4 the PDFs in each group are plotted against the median of the corresponding group. The PDFs are skewed toward smaller rather than the larger bubble areas. In addition, the trends are nearly identical for all segments. There are noticeable PDF peaks for all segments at the same bubble area. Although the frequency distribution shows that segment 1 has the maximum number of smallest size bubbles, the PDF for segment 1 is minimum for this range of bubble sizes. This confirms that the frequency of smaller size bubble formation is higher in segment 1 than the other segments. Figure 5.4 shows that the PDFs become nearly insensitive with segment number from approximately 0.025 to 0.05 mm^2 bubble size (area).

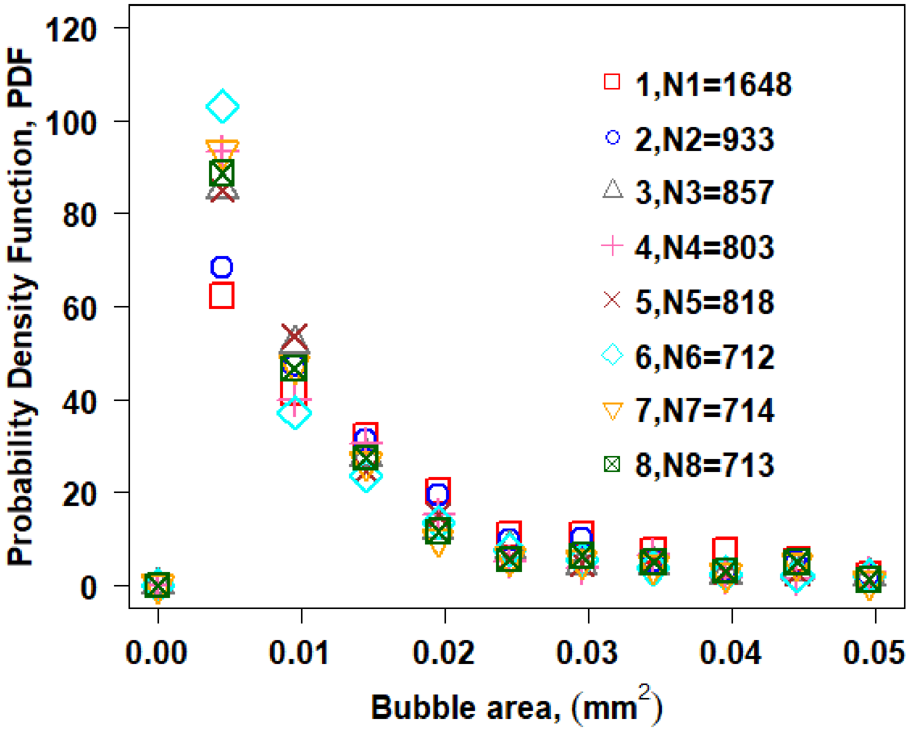

Figure 5.4: Probability Density Function (PDF) for bubble area for each segment 1-8. Bin width is .005 mm^2. Eight different markers are used in the legend to show the eight segments. The PDF in each bin is plotted with respect to the median value in that bin.

5.4.1.3 Fitting Procedure and Criteria

The above size distributions are compared with several standard distribution functions. Three distribution functions having different underlying theoretical assumptions and mathematical structure were evaluated using the data derived from the procedures described above. The functions are two-parameter functions: Weibull, Gamma and Log-normal. Each function was fitted using an iterative nonlinear optimization algorithm to the experimental PDF data of the bubble area distribution. Values of the fitting parameters that provided the closest fit between the estimates and the empirical data were assessed using the statistical software platform, R. The parity of model predictions with empirical data was ascertained using the Root Mean Square Deviation (RMSD), viz.,

$$\text{RMSD} = \sqrt{\frac{\sum_{i=1}^{N}(x_i - \hat{x}_i)^2}{N}} \tag{5.3}$$

where, N is the number of data points, i is the variable, x_i is the empirical PDF from the experiment and $\hat{x}_i$ is the estimated PDF from the distribution function.

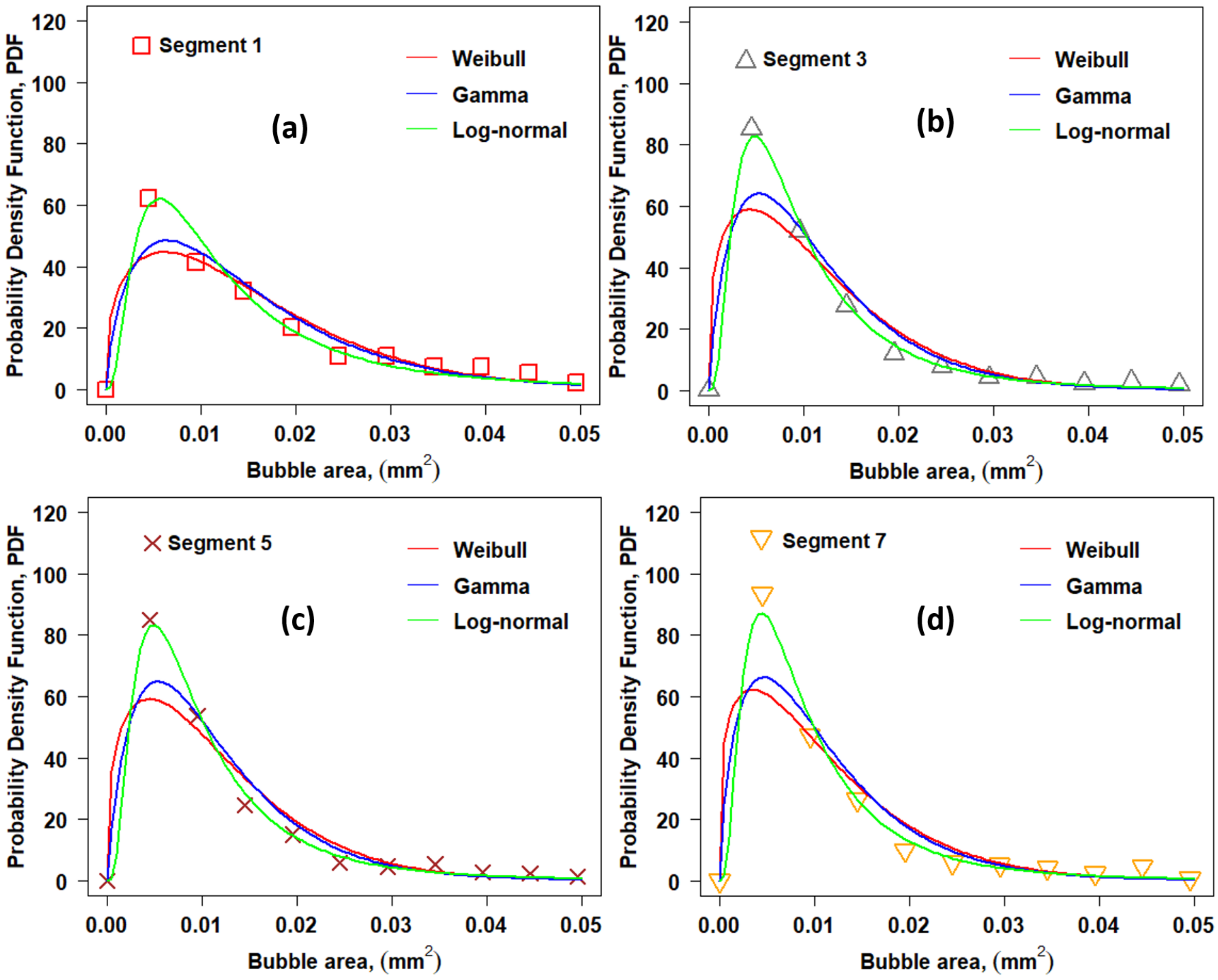

Figure 5.5: The empirical Probability Density Function (PDF) versus bubble area is compared with the Weibull, Gamma and Log-normal functions. Bin width is 0.005 mm^2. The PDF in each bin is plotted with respect to the median value of the bin. Here only four segments are shown. (a) segment 1, (b) segment 3, (c) segment 5 and (d) segment 7.

Figure 5.5 shows the empirical PDF comparison with the Weibull, Gamma and Log-normal functions for (a) segment 1, (b) segment 3, (c) segment 5 and (d) segment 7. It is evident that the PDFs match better with the log-normal function relative to the other two distribution functions. To avoid redundancy, segments 2, 4, 6 and 8 are not shown here, however the log-normal remains the most suitable function for those segments as well. Figure 5.6 shows the empirical PDF comparison with the Weibull, Gamma and Log-normal functions for samples 1, 2 and 3 for segment 8. It shows that the Log-normal function is also a better match for other samples for segment 8. Other segments were analyzed for samples 2 and 3 and found that Log-normal provides the best fit.

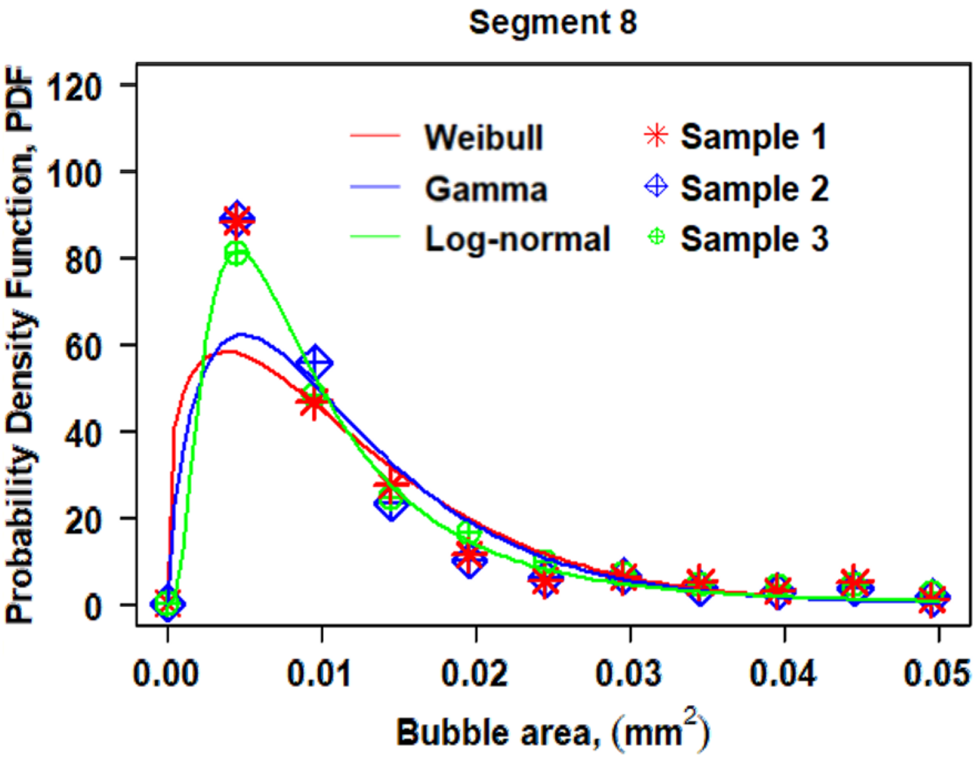

Figure 5.6: The empirical Probability Density Function (PDF) versus bubble area is compared with the Weibull, Gamma and Log-normal functions for samples 1, 2 and 3. Bin width is 0.005 mm^2. The PDF in each bin is plotted with respect to the median value of the bin. Here only segment 8 is shown for all samples.

Quantitative results of the fitting performances of the distribution functions for the PDF data sets are shown in Figure 5.7. Overall RMSD values obtained from the regression analysis between the estimated and the empirical PDF ranged from 2 to 13. The trends of the RMSDs were largely similar. Segment 6 with 712 bubbles, followed by segment 4 with 803 bubbles, shows the highest deviation for each function. The lowest RMSD values were obtained for every segment from the two parameter Log-normal function, followed by the Gamma and Weibull functions. Comparatively, the worst fits were obtained with the Weibull functions.

5.4.2 Bubble Quantity

Here, the overall bubble quantities (bubble count and bubble area) will be studied of these post-burn PMMA samples. Each burnt sample image was cropped such that the ROI was divided into eight

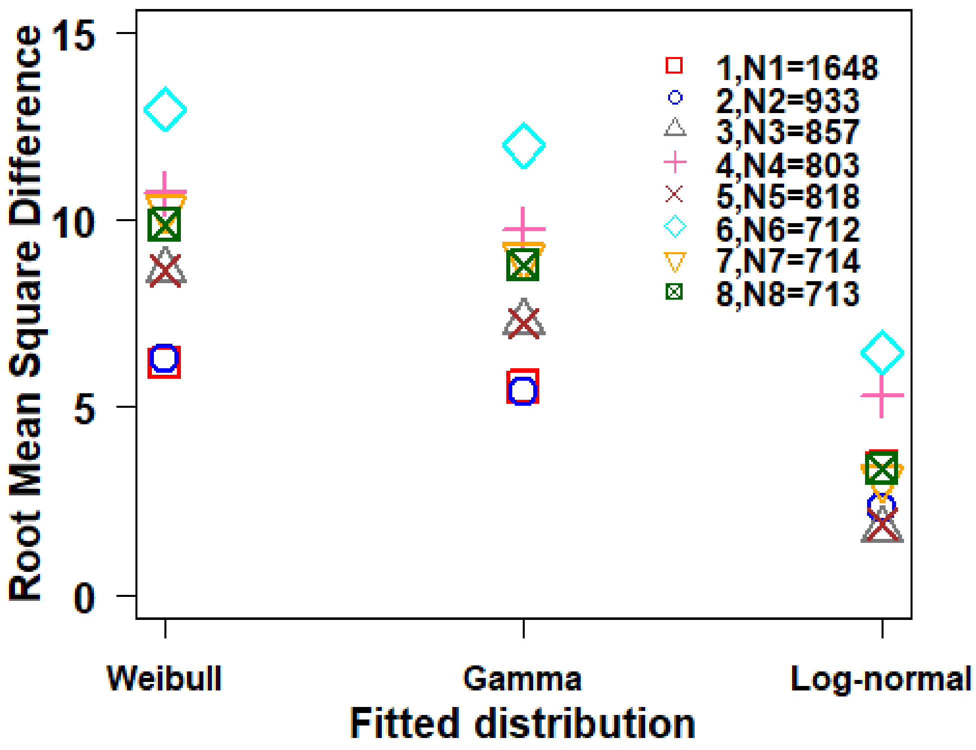

Figure 5.7: Performance of the three distribution functions fitted to the PDF of the bubble area in terms of the Root Mean Square Deviation (RMSD) (see Eq. (5.3)). Eight different markers are used to indicate the eight (8) separate segments.

equal sections (see Section 3).

5.4.2.1 Bubble Count

Figure 5.8 (a) shows the bubble count for the eight separate segments. Three different markers represent the three samples: blue circles, red triangles and green rectangles represent samples 1, 2 and 3 respectively. Each bubble is counted by identifying their (i.e. its projected area) edge from image processing as described in the previous section.

The bubble count is always highest in segment 1. It abruptly reduces from segment 1 to segment 2 possibly because the leading-edge effect is no longer dominant. The bubble count appears to be insensitive in the remaining segments (segments 3 - 8) further downstream. Note from Figure 5.8 that a slight offset in bubble count was observed for sample 3 when compared with sample 1 and 2. One possible reason for this discrepancy could be the burning time. Although the three samples

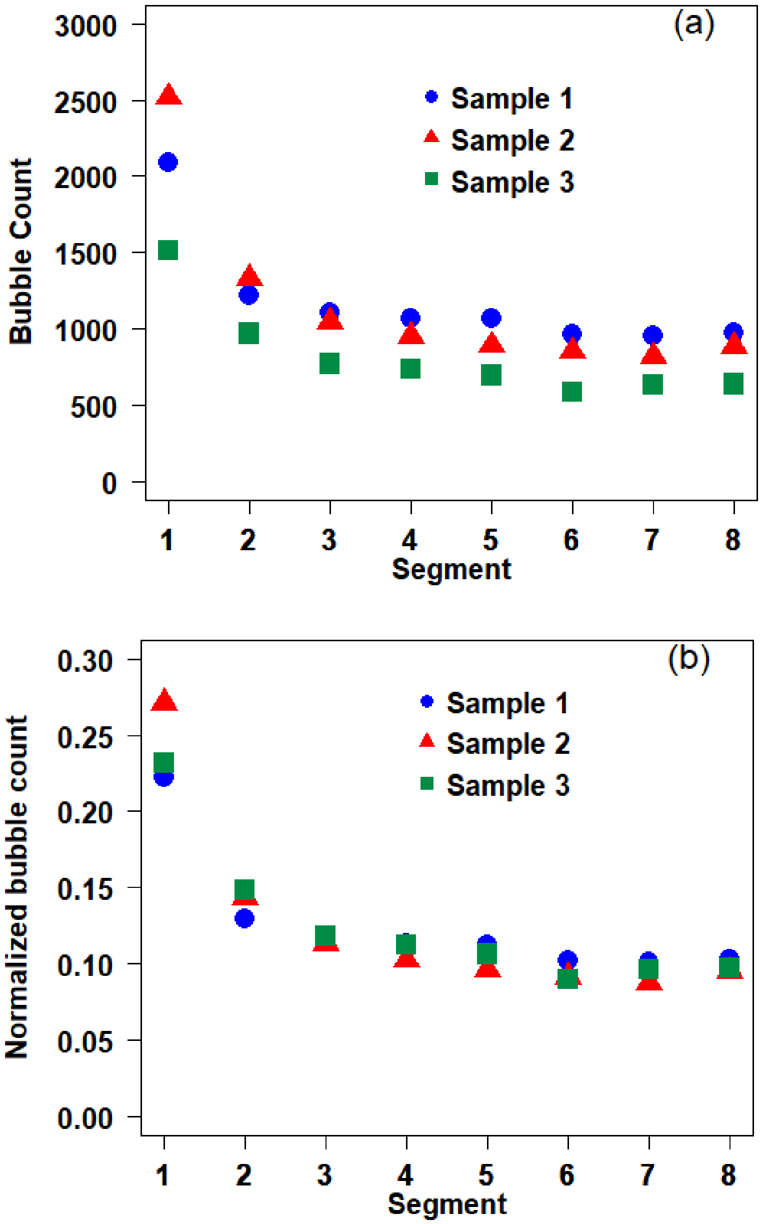

Figure 5.8: (a) Bubble count for segments (1-8). The blue circle, red triangle and green rectangle markers represent sample 1, sample 2 and sample 3, respectively. Note the offset between samples 1, 2 and sample 3 (b) Normalized bubble count. Normalization was performed with the total number of bubbles of that respective sample.

were tested using identical opposed flow velocities, samples 1 and 2 were burnt longer than sample 3. The test duration for sample 1 and 2 was 30 minutes whereas for sample 3 it was 25 minutes. It appears that the longer burning time causes additional bubble formation for samples 1 and 2. In an attempt to factor out this difference, each segment's bubble count was normalized by the total bubble count of the corresponding sample. Figure 5.8 (b) shows the normalized bubble count for the three samples. In addition to largely eliminating the offset in Figure 5.8 (a), this figure shows a sharp decay from segment 1 (~ 0.25) to 2 (~ 0.15), then a long plateau (~ 0.12). The uncertainty in bubble count measurement is ~ 10 %, which was empirically assessed from several tests of repeatability.

5.4.2.2 Bubble Area

Figure 5.9 (a) shows the total bubble area for the eight separate segments. The bubble area is obtained by thresholding the bubble's pixel value in order to distinguish it from the background values. The pixel value is converted to the millimeter unit scale in order to estimate the area. Finally, each identified bubble area is summed in order to calculate the total bubble area for a given segment.

Figure 5.9 (a) exhibits a slower decay in bubble area for sample 1 and 2, whereas a linear and pronounced decay is observed for sample 3. Note that, although segment 1 has mostly small bubbles (Figure 5.3), the significantly higher bubble count (Figure 5.8) produces a high bubble area. By contrast, segment 8 has a higher bubble area instead of a lower bubble count. Careful visual observation revealed relatively bigger bubbles in the segments located near the trailing edge. A possible explanation could be trailing edge ignition. Olson et al. described a unique phenomenon called sample swelling during ignition and solid phase heat up, which contributes to bubble development [74]. The flame moves away from the surface as the solid is heated due to the solid phase warming during the swelling period. However, sample swelling was not observed in this study, although there might be unrealized swelling balanced by sample regression. It is believed that, the bubble layer evolves and some bubbles coalesced during sample heat up, which may result in larger bubbles.

The percentage of surface area is occupied by bubbles, which is defined mathematically as

$$\% \text{ of bubble area} = \frac{\text{Total bubble area of a segment}}{\text{Total area of that segment}} \times 100. \tag{5.4}$$

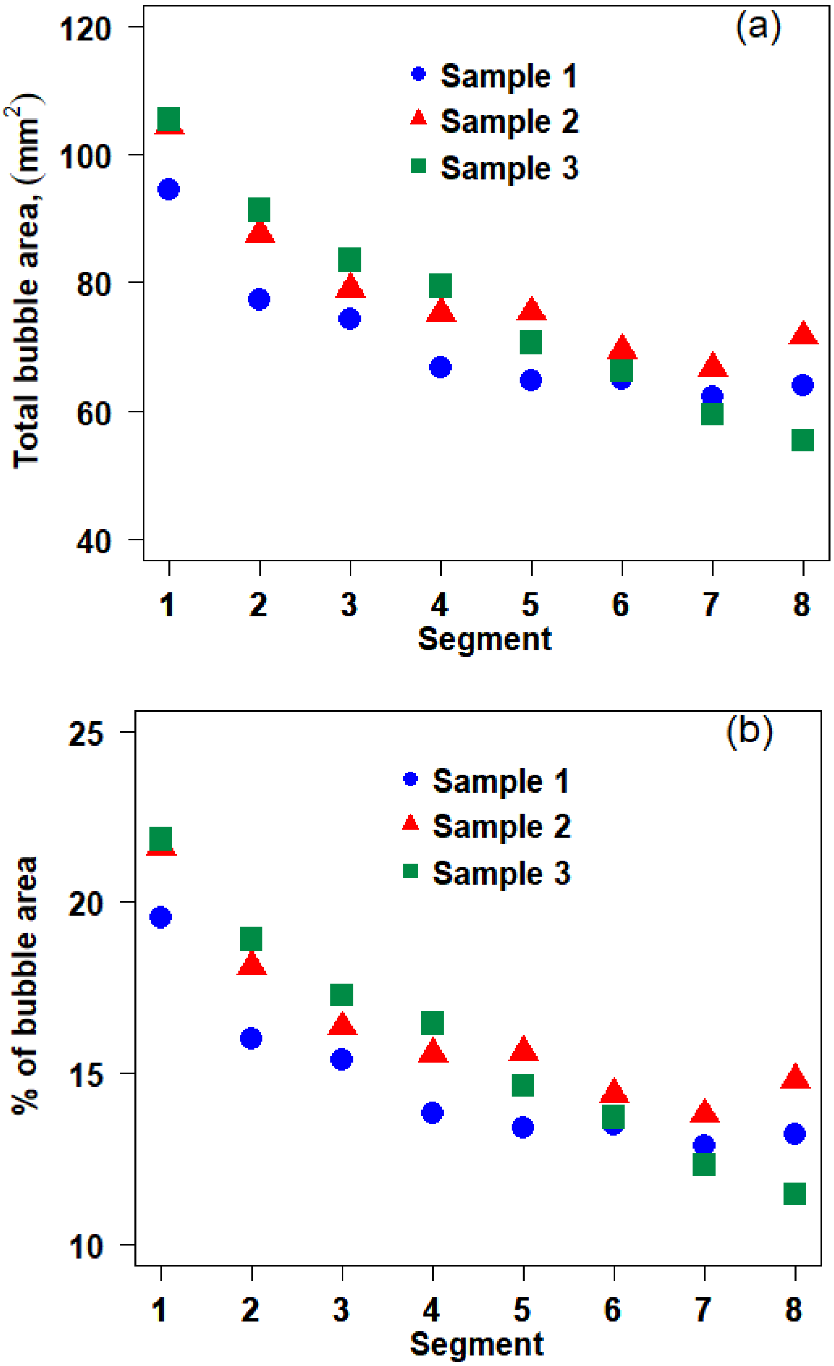

Figure 5.9: (a) Total bubble area for different sample segments. The blue circle, red triangle and green rectangle markers represent sample 1, sample 2 and sample 3, respectively. (b) Percentage of bubble area versus number of segments. The total areas for each segment for sample 1, sample 2 and sample 3 are 425 mm^2, 423 mm^2 and 422 mm^2.

Figure 5.9 (b) shows the percentage of bubble area for the three samples. The percent of bubble area is determined from Eq. (5.4). Segment 1 has the maximum bubble count as well as the highest bubble area percentage (~ 22%) for all samples. Figure 5.9 (b) has a similar trend as Figure 5.9 (a). The overall percentage of bubble area is between 12 – 22%.

5.4.2.3 Bubble Volume

In the previous subsection, two characteristic bubble quantities (count and area) were measured and analyzed. A digital mirrorless camera was used to observe the bubbles and measure their size (area). However, the measurement was conducted by viewing a projection of the bubbles from the back of the sample. To calculate the bubble volume, it is crucial to identify their shape, which is not possible from this 1-sided, 2D non-intrusive measurement. Therefore, a simplified attempt was developed to estimate the bubble volume. This methodology is described below.

First, it is assumed that the bubbles are regularly shaped for example as cylinders, cones, cubes or spheres. Side observation revealed that the bubbles can be broadly categorized into two shapes: (1) round bubbles that can be assumed to be spherical and (2) elongated bubbles that can be considered to be cylindrical. The average bubble diameter for these two limiting geometries is determined from the projected (surface) area.

The projected area is that of a circle and this diameter represents an overall average characteristic length. The bubble count and area are used to calculate the diameter. Then, the equation for this quantity is

$$d_{avg} = \sqrt{\frac{4A}{\pi N}}, \tag{5.5}$$

where, d_{avg} is the average bubble diameter, A is the total bubble area (mm^2) and N is the number of bubbles.

Figure 5.10 shows the average bubble diameter. Although sample 1 and 3 show a non-monotonic increase in bubble diameter, sample 2 shows a pronounced increase in average diameter up to segment 5, then it begins to plateau.

This average bubble diameter is used to calculate the total volume of the bubbles in each segment. Assuming all bubbles are spherical, the equation used to determine the total bubble

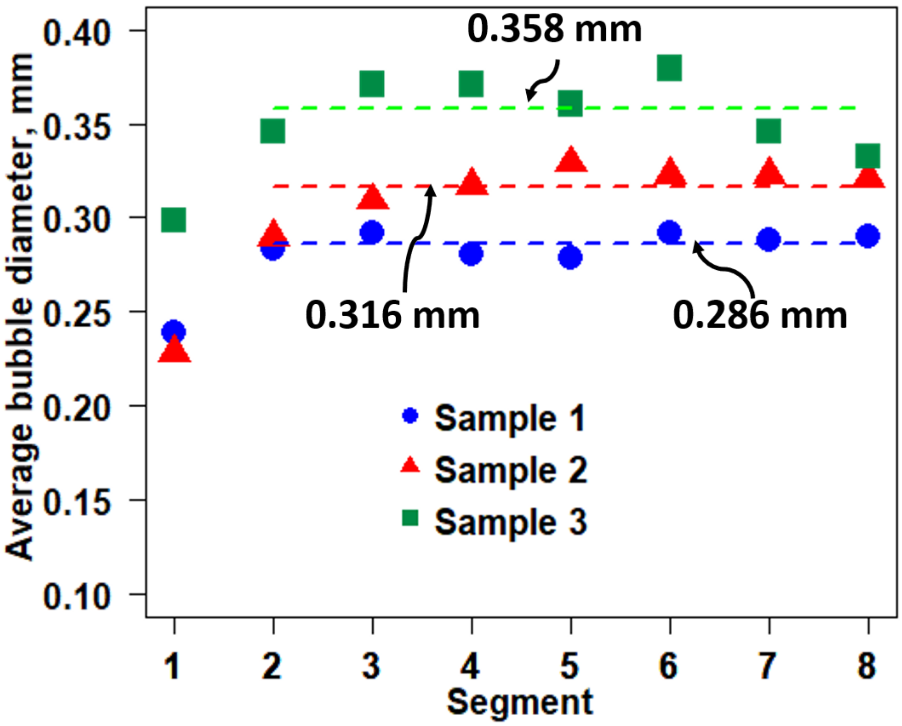

Figure 5.10: Average bubble diameter versus the segment number. The blue circle, red triangle and green rectangle markers represent sample 1, sample 2 and sample 3, respectively. The blue, red and green dashed lines are the average between segments 2 to 8 for samples 1, 2 and 3, respectively. The percentages of errors (variations in average diameter) from segments 2 to 8 based on least squared method are 1.7%, 3.8% and 4.3% for samples 1, 2 and 3, respectively. Note the relative plateau after segment 1, for all samples as the errors are relatively low.

volume is given by

$$V_{sphere} = \frac{1}{6}\pi d_{avg}^3 N. \tag{5.6}$$

Assuming, all bubbles are cylindrical, the total volume of bubble is given by

$$V_{cylinder} = \frac{\pi}{4} d_{avg}^2 h_b N, \tag{5.7}$$

where h_b is the bubble layer depth.

The common factor appearing Eq (5.6) and Eq (5.7) is $\frac{1}{2}\pi d_{avg}^2 N$. Therefore, the bubble volume is dictated by the factors $\frac{1}{3}d_{avg}$ and $\frac{1}{2}h_b$ when the bubble shape is spherical and cylindrical, respectively. In this work, this is called the “shape factor”.

The equivalent sphere volume ranges from 20 to 45 mm^3, whereas the equivalent cylinder volume between 210 to 350 mm^3 is larger by a factor of 10. The higher shape factor results in

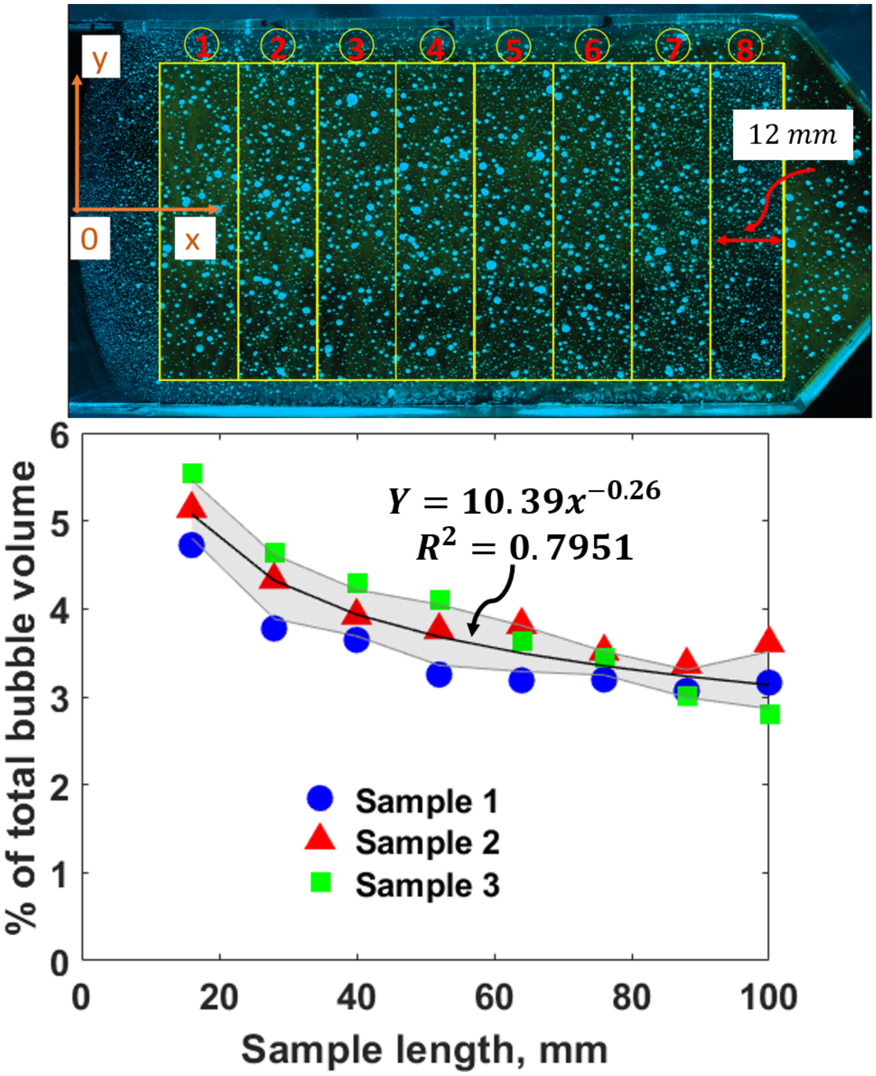

Figure 5.11: The percentage of total bubble volume is plotted against the median value of that segment. The sample length is measured from the leading edge shown with the axis of top photograph of the sample. Each segment length is approximately 12 mm. The blue circle, red triangle and green rectangle markers in the plot represent sample 1, sample 2 and sample 3, respectively. Eq. (5.9) is used to determine the total bubble volume. The solid black line is the power curve fit, which gives approximately an $x^{-1/4}$ dependence. The shaded area is the local Root Mean Square Error (RMSE) for the individual segments.

a significantly higher bubble volume for the assumed cylindrical shape. In actuality, the bubbles are neither always spherical nor cylindrical, but some fraction of these shapes (assuming these are the dominant two). Thus, some bubbles are spherical and others are cylindrical. However, it is not possible to know their respective counts from the current work (which considers only their projections). To estimate the bubble volume, a percentage of bubbles, x, is assumed to be cylindrical. Based on this assumption, the total bubble volume can be estimated from the following equation

$$V_b = V_{sphere} + V_{cylinder} = \frac{1}{6}\pi d_{avg}^3 N(1-x) + \frac{\pi}{4} d_{avg}^2 h_b N x. \tag{5.8}$$

Finally, the percentage of total bubble volume in each segment, ψ, is given by

$$\psi = \frac{V_b}{V_{slice}} = \frac{\frac{1}{6}\pi d_{avg}^3 N(1-x) + \frac{\pi}{4} d_{avg}^2 h_b N x}{w_b \times l_b \times t_b} \times 100\%. \tag{5.9}$$

Figure 5.11 shows the percentage of bubble volume for all three samples. Here, x = 0.2 is used for cylindrical bubbles. This figure exhibits a slow decay along its length from 6 to 3% for all samples.

5.5 Average Area from Bubble Distribution Function

The calculations of the preceding section are extended to calculate the bubble average area from the PDF of the bubble distribution. By the above described section fitting and procedure (section 5.4.1.3), it was determined that bubble area distribution was best described with the log-normal function. The PDF equation for this well known function is

$$\text{PDF} = \frac{1}{A\sigma\sqrt{2\pi}}\, exp\left(-\frac{(lnA-\mu)^2}{2\sigma^2}\right) \tag{5.10}$$

where A is the bubble area, μ is the mean of the bubble area and σ is the standard deviation of the bubble area. By multiplying this PDF by the bubble area and integrating over the total area, the average bubble surface area can be calculated from the formula

$$\text{Average Area, } \overline{A} = \int_{A=a}^{A=b} A \frac{1}{A\sigma\sqrt{2\pi}}\, exp\left(-\frac{(lnA-\mu)^2}{2\sigma^2}\right) dA. \tag{5.11}$$

where $A = a$ and $A = b$ are the integration limits. Evaluation of this integral gives

$$\overline{A} = -\frac{1}{2} e^{[\mu+\sigma^2/2]} \left[\text{erf}\left[\frac{\mu + \sigma^2 - \ln A}{\sqrt{2}\sigma} \right] \right]_{A=a}^{A=b}. \tag{5.12}$$

Equation (5.12) is a 2-parameter formula. The mean of the bubble area, μ and standard deviation of the bubble area, σ for each segment can be obtained experimentally. The integration limits, a

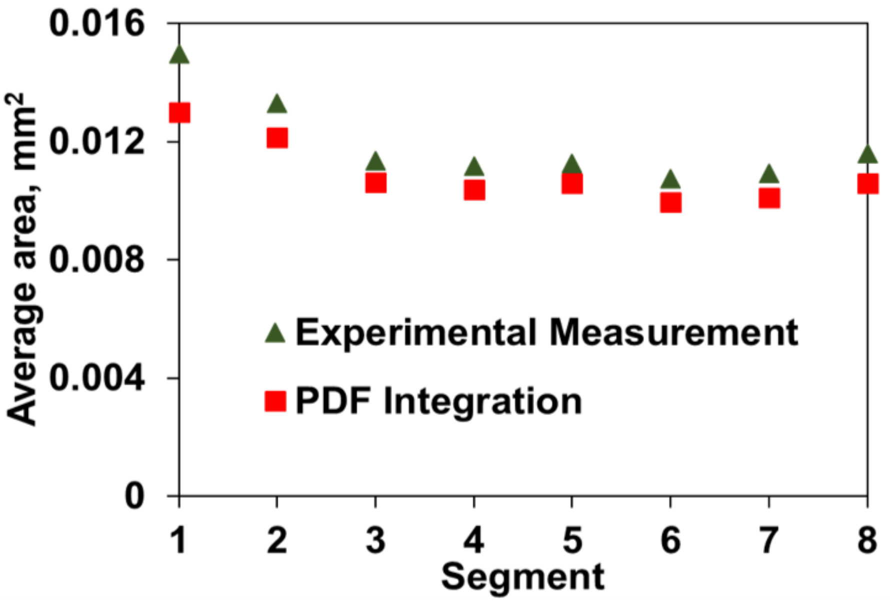

Figure 5.12: Average bubble area for sample 1 from experimental measurement and PDF integration.

and b would be the lower and upper boundaries of bubble area of each segment. Here, the average bubble area were analyzed over the range of $(2 - 52) \times 10^{-3}\ mm^2$ due to statistical significance. Thus, $a = 2 \times 10^{-3}\ mm^2$ and $b = 52 \times 10^{-3}\ mm^2$ is considered for Eq. (5.12).

Similarly, the bubble average area can be determined from the experimental measurement. The average area will be the total bubble area over the total number of bubbles.

$$\text{Average bubble area} = \frac{\text{Total bubble area of a segment, } A}{\text{Total bubble count of that segment, } N}. \tag{5.13}$$

Figure 5.12 shows the sample 1 average per-segment area of the bubbles. The triangles and squares represent the area from experimental measurement and the PDF estimation, respectively. The average area is highest in segment 1. This figure exhibits minimal change in average area with segment number. The measured average area is always slightly smaller than the PDF estimation. The average difference between these two sets of estimations is approximately 4.5%

5.6 Summary

Bubble formation in PMMA burning were studied experimentally through a high resolution photographic method. Here, the samples were burnt in a Narrow Channel Apparatus at an opposed flow velocity of 15 cm/s. Major observations of this study are listed below:

The bubble area frequency distribution of post-burn PMMA samples is determined from experimental measurement for 8 separate segments. Each histogram is positively skewed and they are all qualitatively similar. Segment 1 has slightly higher bubbles compared to other segments due to being on the active oxidation zone of reaction prior to the extinction of the flame. Furthermore, PDF is estimated from the histogram to compare our results with three standard distribution functions. A two-parameter log-normal function was best described the nature of density functions for bubble sizes less than 0.052 mm^2.

In addition, the results provide important information on bubble formation inside PMMA thermoplastics. Primarily, bubble count and bubble area were determined from the image analysis. Both bubble count and area results show a decreasing trend from segment 1 to 8. The normalized form of bubble count provides minimal variation between segment 2 to 8. On the other hand, the bubble area continuously drops for all samples from segment 1 to 7.

A semi-empirical scaling analysis was conducted to estimate the bubble volume. Here, an average diameter is determined from the bubble count and area. Two different shapes, sphere and cylinder are considered to estimate the bubble volume and the bubble volume fraction of the bubble layer.

In Chapters 4 and 5 the post-flame-spread sample was inspected and analyzed. In Chapter 4, the experimental features of sample regression is examined. The mass flux comes out of the burnt surface is also determined. Chapter 5 describes the role of the molten bubble layer. These past two chapters have been rather a thorough look at the surface phenomena occurring during thick flame spread. In chapter 6, the goal is to consolidate some of the observation in the form of a theoretical model of surface regression which will be compared with experimental measurements.

CHAPTER 6

MODELING OF TRANSIENT REGRESSION WITH PHASE CHANGE

Synopsis

In this chapter, a simplified one-dimensional model of heat transfer and material regression is examined under a constant heat flux that simulates heat transfer from the flame to the surface for non-charring materials. For this purpose, a theoretical and numerical model is formulated that incorporates the solid to gaseous transformation of solid fuels in two stages: (1) the pre-vaporization (heat up stage) and (2) the vaporization stage. The analysis examines the influence of heat flux on thermal regression for a finite length solid fuel. This problem is described by a parabolic partial differential equation along with the appropriate boundary and initial conditions. An energy balance is employed to track the moving boundary. A variable spaced grid method and boundary immobilization method are used to fix the moving boundary and solve a nonlinear coupled system of equations.

6.1 Introduction

When a material is subjected to a high heat flux, it can be ignited when it decomposes to gaseous volatiles that are transported by diffusion and convection into the surrounding oxidizing gas. The ignition of the flame may lead to subsequent flame spread while the gaseous fuel reacts with surrounding oxidizer and maintains the flame. Surface ignition at a point is often associated with an induced inflow of oxidizer. The effect of oxidizer inflow on flame spread rate have extensively analyzed in chapter 3. Subsequently, the influence of flame spread rate on surface regression also analyzed in chapter 4.

Most theoretical models of flame spread rate have used the flat-surface approximation in which the surface of the fuel surface does not regress [5, 10, 11, 63, 100]. The surface shape can exert a crucial influence during flame spreading by altering substantively the incoming air flow at the flame leading edge. Solving a flame spread model that includes surface regression may involve complicated pyrolysis, solid-phase chemical reaction, phase change, and complex heat and mass transport processes. Instead of solving a complicated elliptic boundary value problem, a set of parabolic conservation equations can be formulated, which balance cross-stream conduction and convection process. The purpose is to model the transient regression process, in order to develop an understanding of the complicated nature of the regression process in flame spread over non-charring thermoplastics.

6.2 Compatibility of Energy Equation & Energy BC

A theoretical and numerical basis is sought that is minimally sufficient to predict a material degradation during flame spread i.e., the regressive burning regime discussed in chapter 3. Since PMMA requires external heating to enable flame spread, which eventually causes regression, this will be a necessary component of the subsequent analysis.

The principal theoretical feature of the solid phase problem is the transition from a non-regressing solid, whose surface temperature rises and where the solid phase surface heat flux q'' is constant (the impulsively heated constant flux solid), to a regressing surface whose temperature is now constant with the value T_v (Figure 6.1).

A one-dimensional model is considered of the transient heating process. The solid transient heat equation is

$$\frac{\partial T}{\partial t} = \alpha \frac{\partial^2 T}{\partial y^2}, \tag{6.1}$$

where $\alpha = k/\rho c$ is the thermal diffusivity, ρ is the density, c is the specific heat, and k is the thermal conductivity. All thermal properties are assumed to remain constant throughout the process. In the pre-vaporization stage, $T(0,t) < T_{vap}$, $0 < t < t_v$ and the other boundary conditions are

$$-kT_y(0,t) = q^{''}, \quad T_y(-L,t) = 0, \tag{6.2}$$

where, $q^{''}$ is the constant external heat flux. The initial condition describes an initially cold sample,

$$T(y,0) = T_\infty. \tag{6.3}$$

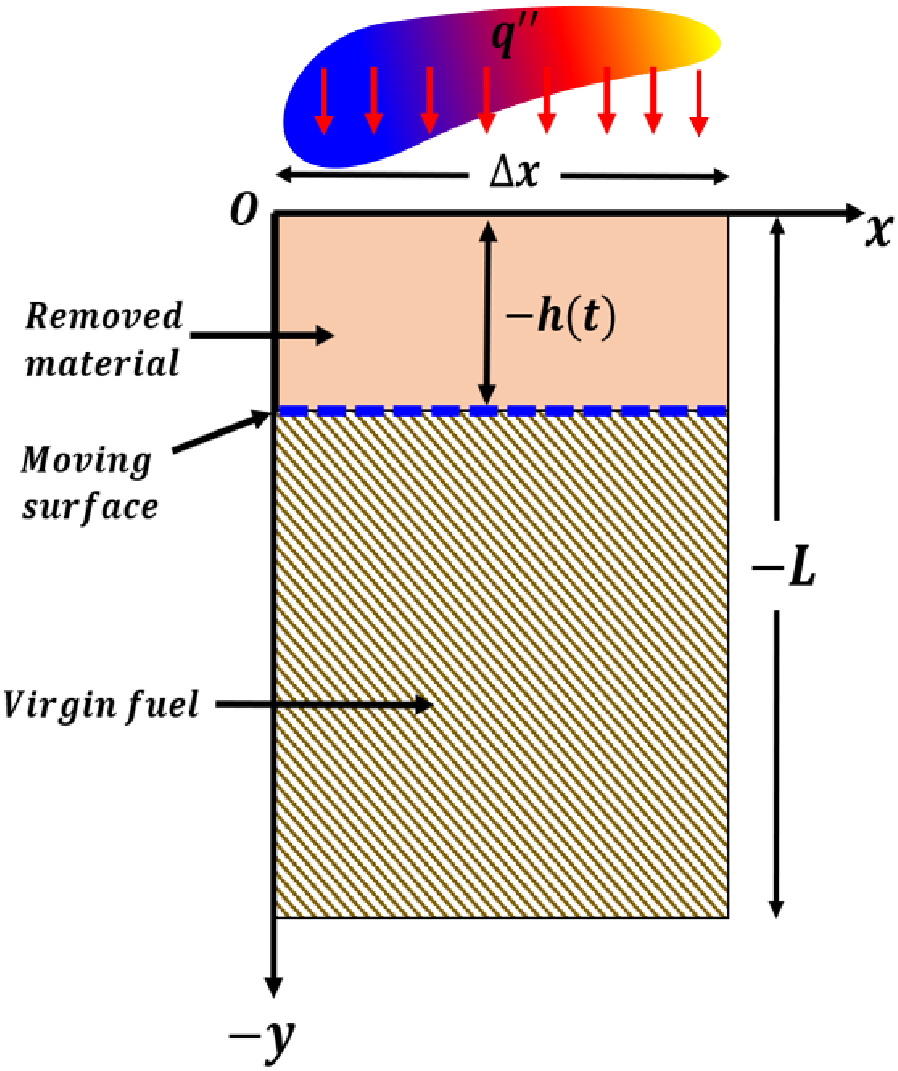

Figure 6.1: The simplified 1-D regression model

The vaporisation stage begins when $T = T_{vap}$ at the surface, which occurs when $t = t_v$, the vaporization time. For $t > t_v$, and $-h(t) < y < -L$, the boundary conditions are

$$T_y(-L,t) = 0, \quad T(-h(t),t) = T_v, \tag{6.4}$$

where $h(t)$ is the depth of the regressed surface after it has began vaporizing or gasifying (see Figure 6.1). The initial condition is

$$T(y,t_v) = T_0(y), \tag{6.5}$$

where, once again $h(t)$ is the solid-vapor interface position. The surface regression rate measures the moving boundary of the domain. The temperature in the material at the time t_v is described as

$T_0(y)$ within the slab. This distribution is obtained from the solution of Eqs (6.1), (6.2) and (6.3). At the moving solid-vapor interface, the heat balance equations apply:

$$-kT_y(-h(t),t) = q'' - \rho L_v \frac{d(-h(t))}{dt}, \tag{6.6}$$

where L_v is the latent heat of vaporization. The initial condition is

$$h(t_v) = o. \tag{6.7}$$

In the following section, the above problem is analyzed. In the pre-vaporization stage, an analytical solution is found using the separation of variables method. Though the problem is simplified, it is still a challenging exercise to find the solution for the vaporization stage, since this is a moving boundary problem.

6.3 Non-dimensionlization

The governing equations are non-dimensionalized in order to analyze the physical mechanisms that may subsequently influence regression. The dominant mechanism of heat transfer in the thick solid from the imposed heat flux (mimicking the flame) is solid conduction. The interaction between the solid and gas phases determines the nature of flame growth and spreading and it is postulated herein that a related interaction will ultimately dictate the regression phenomenon. Gas phase conduction is dominant in thermally thin flame spread and becomes weaker as the fuel thickens [37]. Therefore, the gas phase conduction is considered negligible and the sole mechanism of gas-phase transfer is the incident flame heat flux, see Figure 6.1.

Based on this idea, the problem formulation in dimensionless form is given by

Pre-vaporization/regression stage:

Governing Equation:

$$u_{\eta\eta} = u_\tau, \quad 0 < \eta < 1, 0 < \tau < \tau_v, \tag{6.8}$$

Boundary Conditions:

$$u_\eta(0,\tau) = -Q'', u_\eta(1,\tau) = 0, \quad 0 < \tau < \tau_v, \tag{6.9}$$

Initial Condition:

$$u(\eta, 0) = 0, \quad 0 \leqslant \eta \leqslant 1. \tag{6.10}$$

Vaporization stage:

Governing Equation:

$$u_{\eta\eta} = u_\tau, \quad h(\tau) < \eta < 1, \tau > \tau_v, \tag{6.11}$$

Boundary Conditions:

$$u_\eta(1, \tau) = 0, u(h(\tau), \tau) = 1, \quad \tau > \tau_v, \tag{6.12}$$

Initial Condition:

$$u(\eta, \tau_v) = u_0(\eta), \quad h(\tau) < \eta < 1, \tag{6.13}$$

Energy Balance Equation:

$$-u_\eta(h(\tau), \tau) = Q'' - r\frac{dh(\tau)}{d\tau}, \tag{6.14}$$

Initial Condition for Moving Boundary:

$$h(\tau_v) = 0. \tag{6.15}$$

The various dimensionless groups are defined as follows:

$$u(\eta, \tau) = \frac{T(y,t) - T_\infty}{T_v - T_\infty}, \tag{6.16a}$$

$$\eta = \frac{-y}{-L}, \tag{6.16b}$$

$$\tau = \frac{\alpha t}{L^2}, \tag{6.16c}$$

$$\tau_v = \frac{\alpha t_v}{L^2}, \tag{6.16d}$$

$$Q'' = \frac{Lq''}{k(T_v - T_\infty)}, \tag{6.16e}$$

$$h(\tau) = \frac{-h(t)}{-L}, \tag{6.16f}$$

$$r = \frac{L_v}{c_p(T_v - T_\infty)}. \tag{6.16g}$$

6.4 Pre-Vaporization Stage

Solution for u

The pre-vaporization stage heat conduction problem, Eqs (6.8) - (6.10), is solved using separation of variables. The solution procedure is described below:

The heat conduction equation, Eq (6.8), is a second order non-linear equation with inhomogeneous boundary condition. To solve this problem, first an arbitary function, $w(\eta, \tau)$, is considered that satisfies the inhomogeneous, time-dependent boundary conditions. The solution $u(\eta, \tau)$ that is sought is then decomposed into a sum of $w(\eta, \tau)$ and another function $v(\eta, \tau)$, which satisfies the homogeneous boundary conditions. When these two functions are substituted into the heat equation, it is found that $v(\eta, \tau)$ must satisfy the heat equation subject to a source that may be time dependent but must be homogeneous. This heat conduction function, $v(\eta, \tau)$ is solved using eigenfunction expansions. The arbitary function obtained from trial and error is

$$w(\eta, \tau) = \frac{Q''\eta^2}{2} - Q''\eta + Q''\tau.$$

Using $w(\eta, \tau)$, the boundary conditions are reduced to the form

$$w_\eta(0, \tau) = -Q'', \quad w_\eta(1, \tau) = 0$$

The initial condition becomes

$$w(\eta, 0) = \frac{Q''\eta^2}{2} - Q''\eta$$

Consider $u(\eta, \tau) = w(\eta, \tau) + v(\eta, \tau)$ as the new dependent function. Then, Eqs (6.8) - (6.10) become

$$w_{\eta\eta} + v_{\eta\eta} = w_\tau + v_\tau,$$

$$v_{\eta\eta} = v_\tau,$$

where $w_{\eta\eta} = w_\tau = Q''$.

$$BC: u_\eta(0, \tau) = -Q'' = w_\eta(0, \tau) + v_\eta(0, \tau) = -Q'' + v_\eta(0, \tau) \Rightarrow v_\eta(0, \tau) = 0$$

$$u_\eta(1, \tau) = 0 = w_\eta(1, \tau) + v_\eta(1, \tau) = 0 + v_\eta(1, \tau) \Rightarrow v_\eta(1, \tau) = 0$$

$$IC: u(\eta, 0) = 0 = w(\eta, 0) + v(\eta, 0) = \frac{Q''\eta^2}{2} - Q''\eta + v(\eta, 0) \Rightarrow v(\eta, 0) = -\frac{Q''\eta^2}{2} + Q''\eta$$

Thus the following initial boundary value problem is needed to solve for $v(\eta, \tau)$:

$$\begin{aligned} v_{\eta\eta} &= v_\tau, && 0 < \eta < 1, \tau > \tau_v, \\ v_\eta(0,\tau) &= 0, v_\eta(1,\tau) = 0, && 0 < \tau < \tau_v, \\ v(\eta, 0) &= -\frac{Q''\eta^2}{2} + Q''\eta, && 0 < \eta < 1. \end{aligned} \tag{6.17}$$

Function $v(\eta, \tau)$ can be found using an eigenfunction expansion.

The above homogeneous problem for $v(\eta, \tau)$ can be solved with a separation of variable procedure. Let $v(\eta, \tau) = y(\eta)t(\tau)$, and substituting in Eq. (6.17) to obtain

$$\frac{y''(\eta)}{y(\eta)} = \frac{t'(\tau)}{t(\tau)} = -\lambda_n^2.$$

Rearranging

$$y''(\eta) = -\lambda_n^2 y(\eta) \quad and \qquad t'(\tau) = -\lambda_n^2 t(\tau),$$

$$y''(\eta) + \lambda_n^2 y(\eta) = 0 \quad and \quad t'(\tau) + \lambda_n^2 t(\tau) = 0.$$

The general solution of $y(\eta)$ and $t(\tau)$ is

$$y(\eta) = Asin(\lambda\eta) + Bcos(\lambda\eta), \tag{6.18}$$

and

$$t(\tau) = Ce^{-\lambda_n^2 \tau}. \tag{6.19}$$

After applying the boundary conditions to Eq. (6.18)

$$y'(0) = \lambda_n[Acos(\lambda_n 0) - Bsin(\lambda_n 0)] \Rightarrow A = 0$$

$$y'(1) = \lambda_n[Acos(\lambda_n 1) - Bsin(\lambda_n 1)] \Rightarrow Bsin(\lambda_n) = 0$$

$$B \neq 0 \quad and \quad sin(\lambda_n) = 0 = sin(n\pi) \Rightarrow \lambda_n = n\pi$$

Thus,

$$y(\eta) = Bcos(n\pi\eta),$$

$$t(\tau) = Ce^{-(n\pi)^2 \tau}.$$

Finally, $v(\eta, \tau) = Bcos(n\pi\eta)Ce^{-(n\pi)^2\tau}$

For n^{th} normal mode

$$v_n(\eta,\tau) = \sum_{n=0}^{\infty} B_n cos(n\pi\eta) e^{-(n\pi)^2\tau}$$

Therefore

$$v_n(\eta,\tau) = B_0 + \sum_{n=1}^{\infty} B_n cos(n\pi\eta) e^{-(n\pi)^2\tau} \tag{6.20}$$

After applying the initial condition

$$v_n(\eta,0) = -\frac{Q''\eta^2}{2} + Q''\eta = B_0 + \sum_{n=1}^{\infty} B_n cos(n\pi\eta) e^{-(n\pi)^2\tau}.$$

The cosine series Fourier transform for B_0 and B_n will be

$$B_0 = \int_0^1 \left(-\frac{Q''\eta^2}{2} + Q''\eta\right) d\eta \Rightarrow B_0 = \frac{1}{3}Q'',$$

$$B_n = 2\int_0^1 \left(-\frac{Q''\eta^2}{2} + Q''\eta\right) cos(n\pi\eta) d\eta \Rightarrow B_n = -\frac{2Q''}{n^2\pi^2}.$$

Substituting B_0 and B_n in Eq. (6.20) gives

$$v_n(\eta,\tau) = \frac{1}{3}Q'' - \sum_{n=1}^{\infty} \frac{2Q''}{n^2\pi^2} cos(n\pi\eta) e^{-(n\pi)^2\tau}.$$

The final solution becomes

$$u_n(\eta,\tau) = \frac{Q''\eta^2}{2} - Q''\eta + Q''\tau + \frac{1}{3}Q'' - \sum_{n=1}^{\infty} \frac{2Q''}{n^2\pi^2} cos(n\pi\eta) e^{-(n\pi)^2\tau}. \tag{6.21}$$

τ_v calculation

Vaporization/regression starts when $u(\eta = 0) = 1$ and that time is the non-dimensional pyrolysis time, τ_v. Applying this condition to Eq. (6.21) gives

$$\tau_v + \frac{1}{3} - \frac{1}{Q''} - \frac{2}{\pi^2} \sum_{n=1}^{\infty} \frac{1}{n^2} e^{-(n\pi)^2\tau_v} = 0. \tag{6.22}$$

Therefore, τ_v is only a function of the dimensionless heat flux Q''. Equation (6.22) can be greatly simplified by neglecting the decaying exponential terms,

$$\tau_v \cong \frac{1}{Q''} - \frac{1}{3}. \tag{6.23}$$

However, Eq. (6.23), the approximate solution for τ_v, is only valid for $Q'' \leq 3$. It is also possible to solve for τ_v with the exponential term (Eq. (6.22)) using an iterative Newton-Raphson method. The procedure is now explained. Let

$$f(\tau_v) = \tau_v + \frac{1}{3} - \frac{1}{Q''} - \frac{2}{\pi^2}\sum_{n=1}^{\infty}\frac{1}{n^2}e^{-(n\pi)^2\tau_v}. \tag{6.24}$$

The derivative of $f(\tau_v)$ is

$$f'(\tau_v) = 1 + 2\sum_{n=1}^{\infty} e^{-(n\pi)^2\tau_v}. \tag{6.25}$$

The Newton-Raphson method defines

$$\tau_v^{n+1} = \tau_v^{n} - \frac{f(\tau_v)}{f'(\tau_v)}. \tag{6.26}$$

Then Eq. (6.27) will be

$$\tau_v^{n+1} = \tau_v^{n} - \frac{\tau_v + \frac{1}{3} - \frac{1}{Q''} - \frac{2}{\pi^2}\sum_{n=1}^{\infty}\frac{1}{n^2}e^{-(n\pi)^2\tau_v}}{1 + 2\sum_{n=1}^{\infty} e^{-(n\pi)^2\tau_v}}. \tag{6.27}$$

Figure 6.2 shows the solution algorithm for τ_v using the Newton-Raphson iterative process. The first three exponential terms were included. The initial input is a guess value for τ_v and an error limit, ϵ is prescribed. Usually the solution converges sooner than the highest iteration value. As soon as the error becomes smaller than the limit ϵ, iteration is stopped and the solution is obtained. The τ_v value is determined for different heat fluxes with another For-Loop condition.

6.5 Vaporization Stage

Coordinate Transformation

It is assumed that the vaporization starts once the surface temperature of the slab reaches the material vaporization value. As already discussed, it is difficult to find the analytical solution for this stage. Therefore, a numerical approach is considered. It is seen that Eqs. (6.11) - (6.15) describe a moving boundary problem. In order to fix the moving boundary, a coordinate transformation is introduced, viz.,

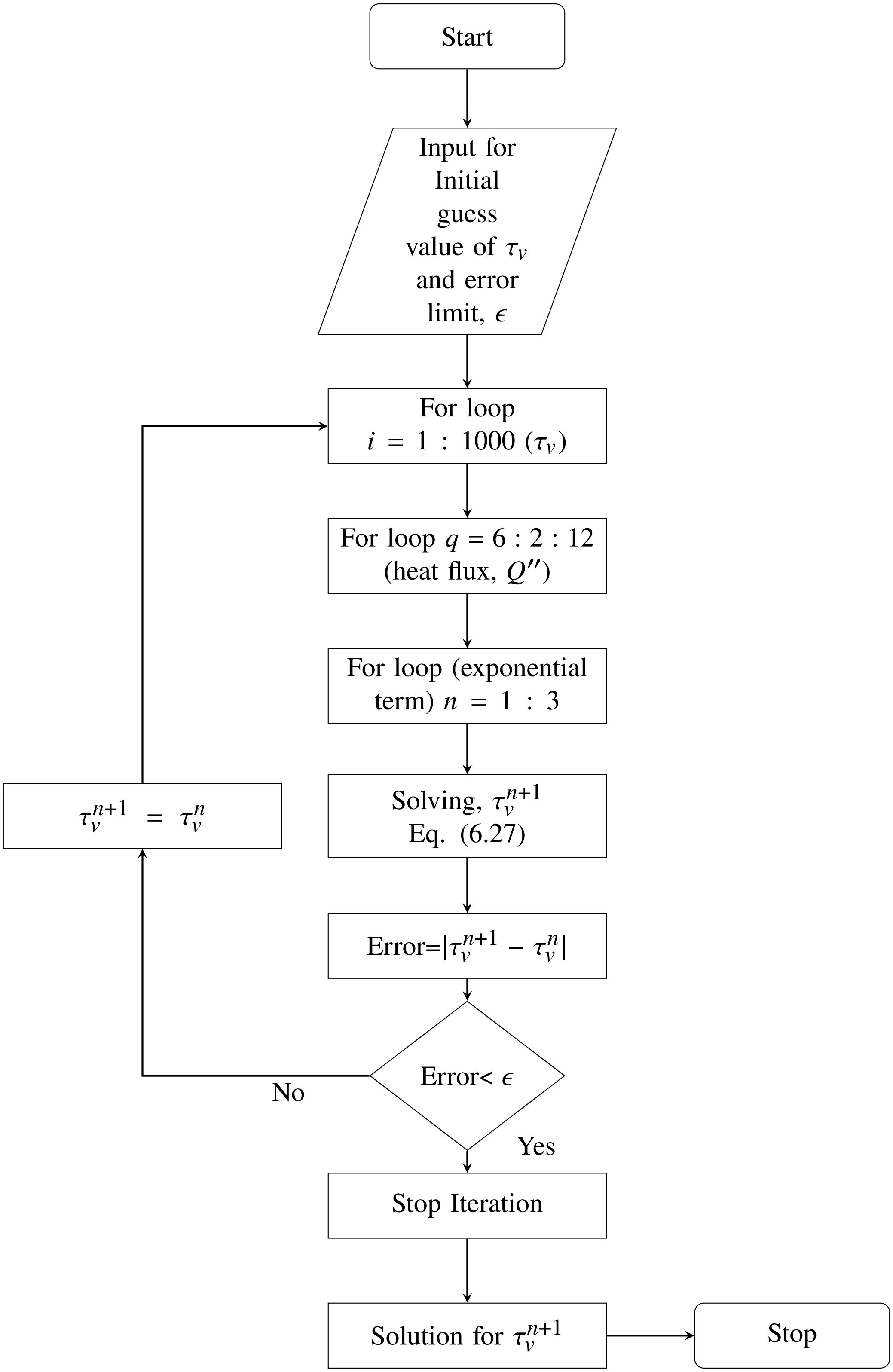

Figure 6.2: Numerical algorithm for the solution of τ_v

In terms of the new independent variables ξ and τ the following relations are deduced.

$$\xi = \frac{1-\eta}{1-h(\tau)}, \tag{6.28a}$$

$$\frac{\partial^2 u}{\partial^2 \eta} = \frac{1}{(1-h(\tau))^2}\frac{\partial^2 u}{\partial^2 \xi}, \tag{6.28b}$$

$$\left(\frac{\partial u}{\partial \tau}\right)_\eta = \left(\frac{\partial u}{\partial \tau}\right)_\xi + \frac{\xi}{1-h(\tau)}\frac{\partial u}{\partial \xi}\frac{dh(\tau)}{d\tau}. \tag{6.28c}$$

Then, Eqs. (6.11) - (6.14) are transformed into the following fixed boundary problem by using Eqs (6.28)

Governing Equation:

$$\left(\frac{\partial u}{\partial \tau}\right)_\xi + \frac{\xi}{1-h(\tau)}\frac{\partial u}{\partial \xi}\frac{dh(\tau)}{d\tau} = \frac{1}{(1-h(\tau))^2}\frac{\partial^2 u}{\partial^2 \xi} \quad 0 < \xi < 1, \tau > \tau_v, \tag{6.29}$$

Boundary Conditions:

$$u_\xi(0,\tau) = 0, u(1,\tau) = 1, \quad \tau > \tau_v, \tag{6.30}$$

Initial Condition:

$$u(\xi,\tau_v) = u_0(\xi), \quad 0 < \xi < 1, \tag{6.31}$$

Energy Balance Equation:

$$-u_\xi(1,\tau) = Q'' - r\frac{dh(\tau)}{d\tau}. \tag{6.32}$$

Note that the system of Eqs (6.29) - (6.32) are nonlinear.

Numerical Discretization

Equation (6.29) is solved with BCs Eq. (6.30), IC Eq. (6.31) and energy balance Eq. (6.32) on a grid using the finite difference method. Discretization of ξ for $0 < \xi < 1$ and τ for $0 \leqslant \tau \leqslant T$ are conducted. To simplify the discretization process, consider that the vaporasation starts at $\tau = 0$.

Space is discretized with grid spacing $\triangle\xi = 1/(n+1)$. Let $\xi_i = i \triangle \xi$, where $0 \le i \le n+1$. A time marching solution employs an explicit 2^{nd} order scheme method to solve for the dimensionless temperature, u, viz.,

$$\frac{\partial u_i}{\partial \tau} = \left[\frac{\xi_i}{1-h_i}\right] \underbrace{\left[\frac{u_{i+1}-u_{i-1}}{\triangle\xi}\right]}_{1^{st} order\ central\ differencing} \frac{dh_i}{dt} + \left[\frac{1}{(1-h_i)^2}\right] \underbrace{\left[\frac{u_{i+1}-2u_i+u_{i+1}}{(\triangle\xi)^2}\right]}_{2^{nd}\ order\ central\ differencing} \tag{6.33}$$

$$u(\tau + \triangle\tau) = u(\tau) + \frac{\partial u_i}{\partial t}\triangle\tau \tag{6.34}$$

Boundary conditions:

$$\begin{aligned} &\frac{\partial u}{\partial \xi}(0,\tau) = 0, \\ &\frac{u_{i+1}-u_i}{\triangle\xi} = 0, \\ &u_{i+1} = u_i, \\ &u_2 = u_1, (i = 1), \end{aligned} \tag{6.35}$$

$$\begin{aligned} &u(1,t) = 1, \\ &u_N = 1, (i = N), \end{aligned} \tag{6.36}$$

Initial condition:

$$u(\xi, 0) = u_0(\xi), \tag{6.37}$$

Energy balance equation

$$\begin{aligned} \frac{dh(\tau)}{d\tau} &= \frac{1}{r}\left[Q'' - \frac{1}{1-h}\frac{\partial u}{\partial \xi}(1,\tau)\right], \\ \frac{dh_i(\tau)}{d\tau} &= \frac{1}{r}\left[Q'' - \frac{1}{1-h_i^\tau}\frac{u_N^\tau - u_{N-1}^\tau}{\triangle\xi}\right], \end{aligned} \tag{6.38}$$

$$h(\tau + \triangle\tau) = h(\tau) + \frac{dh_i(\tau)}{d\tau}\triangle\tau. \tag{6.39}$$

Here the mesh Fourier number has been defined as

$$F = \alpha\frac{\triangle\tau}{\triangle\xi} \tag{6.40}$$

F is a dimensionless number that lumps the key physical parameters in the problem, α, the thermal diffusivity, and the discretization parameters, $\triangle\xi$ and $\triangle\tau$, into a single parameter. Therefore, $\triangle\xi$

and $\triangle\tau$, are chosen in such a way that $F \leq 1/2$, since the solution is explicit. The algorithm will not produce meaningful results unless this $F \leq 1/2$, which is a stability criteria for the explicit method.

The computational algorithms are developed in MATLAB. The numerical calculations are performed for various values of Q''. The computed ranges of these dimensionless parameters are 0 to 1. The accuracy is tested by changing the grid resolution. Convergence is attained if the absolute error of the dimensionless temperature between two grid resolution is less than $1x10^{-5}$. The numerical algorithm for the solution procedure is shown in Figure 6.3. All input variables are initialized at the outset. The position of the moving boundary is set to its previous value, h_{old}. By solving the moving boundary $h(\tau)$, the regression depth is obtained. This regression depth of that time step is the boundary condition for solving the temperature equation. The temperature u is updated for the next time step, $\tau + \triangle\tau$. The computation is performed until $\tau = \tau_{final}$.

6.6 Results and Discussion

6.6.1 Pre-Vaporization Stage

In the pre-vaporization stage, the boundary of the slab slowly reaches T_{vap}. In non-dimensional form, $u = 1$ is achieved at the surface at $\eta = 0$ when vaporization starts. Figure 6.4 represents the exact solution, given by Eq. (6.21). Here, the finite slab is heated with a constant imposed heat flux 6 kW/m^2 to the top (left) boundary ($\eta = 0$). The dotted black line shows the temperature profile within the slab when the regression process starts at $\eta = 0$. These $u(\eta, \tau)$ profiles are evaluated for several heat flux values 8, 10 and 12 kW/m^2.

Figure 6.5 shows the dimensionless temperature distribution in the finite slab when the boundary $\eta = 0$ reaches $u = 1$ for heat fluxes, $q'' = 6, 8, 10, 12$ kW/m^2. This figure shows a decreasing trend for all heat flux as the right boundary, $\eta = 1$ is adiabatic. Figure 6.5 shows a pronounced decay in dimensionless temperature with higher imposed heat flux. The likely reason could be the low heat flux which contributes to the higher τ_{vap}. This means that a longer time is required to achieve vaporization when a low heat flux is implied. In such cases, the low heat flux has sufficient time to

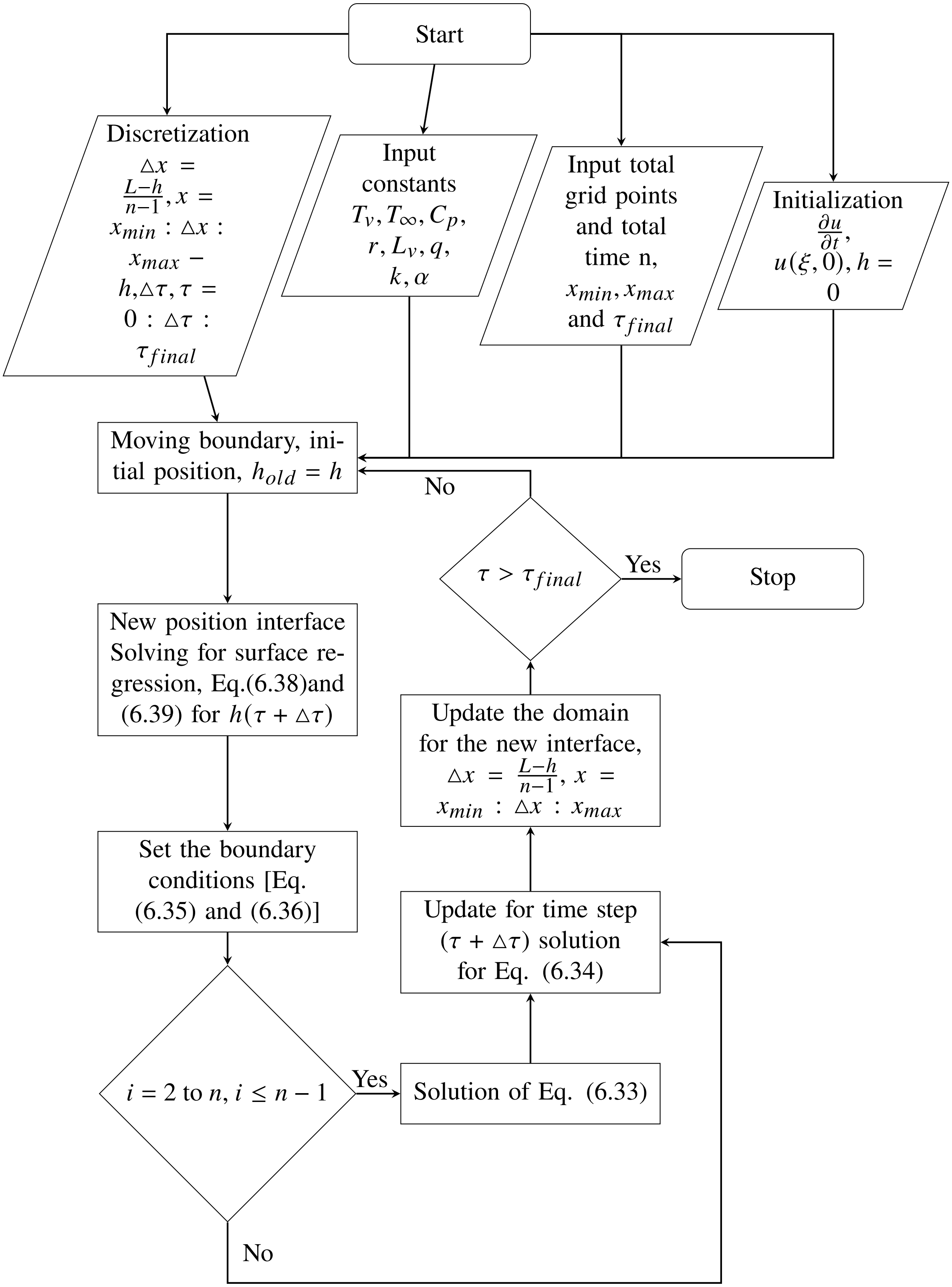

Figure 6.3: Numerical algorithm for the solution of vaporization/regressing stage.

penetrate into the slab, thereby producing a more uniform sample temperature. On the other hand, the time to achieve surface vaporization τ_{vap} is low when the external heat flux is high. As a result the boundary $\eta = 0$ attains the vaporization process much sooner than the low heat flux. However, the heat imputed to the solid surface has less time to penetrate the slab. That is the reason for the observed stronger decay of the dimensionless temperature, u with heat flux increment.

In Figure 6.6, the dimensionless temperature from Figure 6.5 is plotted against the transformed coordinate $\xi = \frac{1-\eta}{1-h(\tau)}$. This dimensionless temperature profile is considered as the initial temperature, $u_0(\xi)$ and is used as the in-sample initial condition for the subsequent vaporization/regression stage.

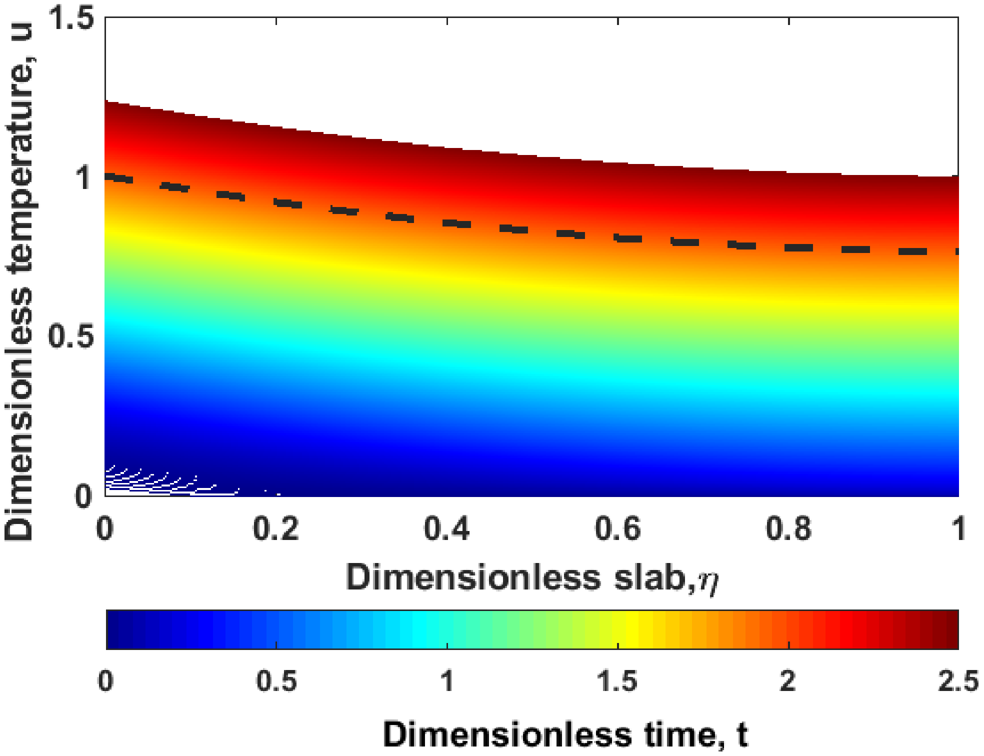

Figure 6.4: Color contour plot for the space-time evolution of the sample temperature for external heat flux 6 kW/m^2 in the pre-vaporization stage. The dotted line represents the temperature distribution within the finite slab when the temperature reaches to T_{vap} at $(u(\eta = 0) = 1)$ when vaporization starts.

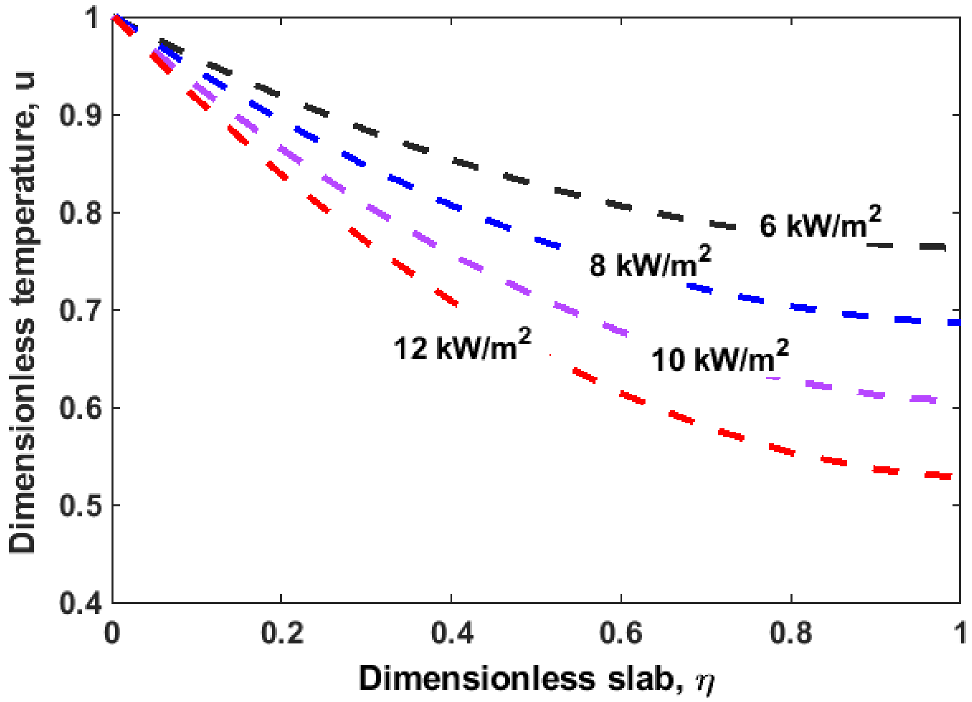

Figure 6.5: Dimensionless temperature, u vs dimensionless slab, η for heat flux 6, 8, 10 and 12 kW/m^2.

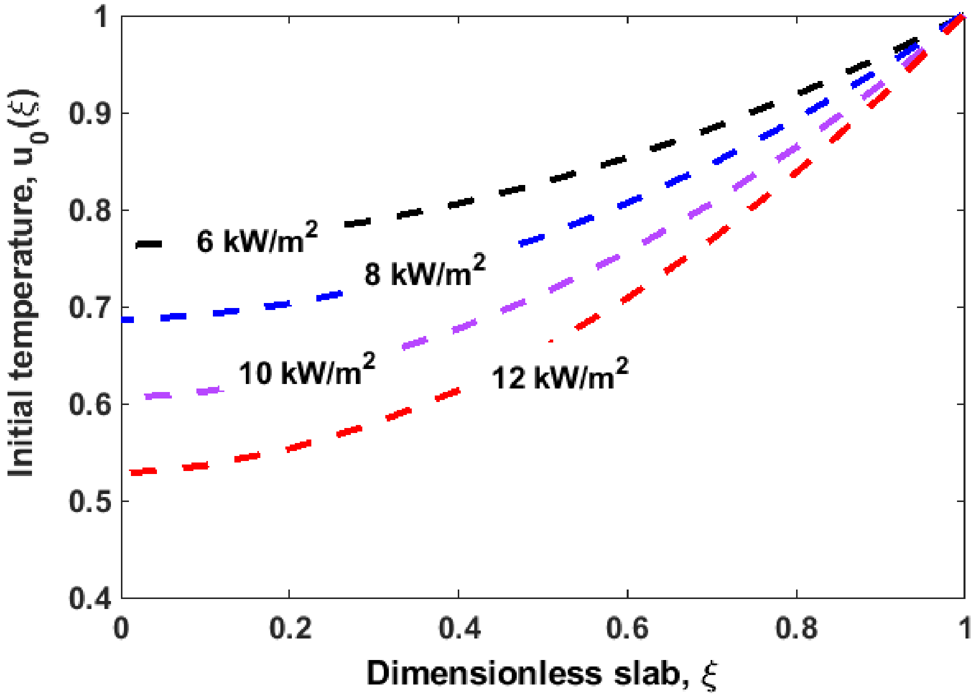

Figure 6.6: Initial temperature for vaporisation stage in transformed coordinate for heat flux 6, 8, 10 and 12 kW/m^2

6.6.2 Vaporization Stage

In order to study the vaporization process, numerical computations were performed as described previously, for the solution of Eqs. (6.33) - (6.39). Some of the results are depicted here. Figure 6.7, for example shows the position of the regressed interface versus time (dimensionless form) for heat fluxes 6, 8, 10, 12 kW/m^2. Note that the time in Figure 6.7 begins at zero instead of τ_{vap}. It is observed that the heat flux exerts a strong influence on regression. For a higher flux, regression of the boundary is deeper, meaning that the sample mass loss (and its rate) are higher. Figure 6.7 shows that the regression slope is steeper for a higher heat flux. Note that from $\tau = 1.75$ onward, regression plateaus for all heat fluxes except 6 kW/m^2. As discussed in Figure 6.5, the higher heat flux reaches the vaporization temperature earlier, however, this heat does not have sufficient time to penetrate through the depth of the slab. In the initial (vaporization) stage, the solid surface temperature increases faster than the conduction resistance of the vaporized layer with increased

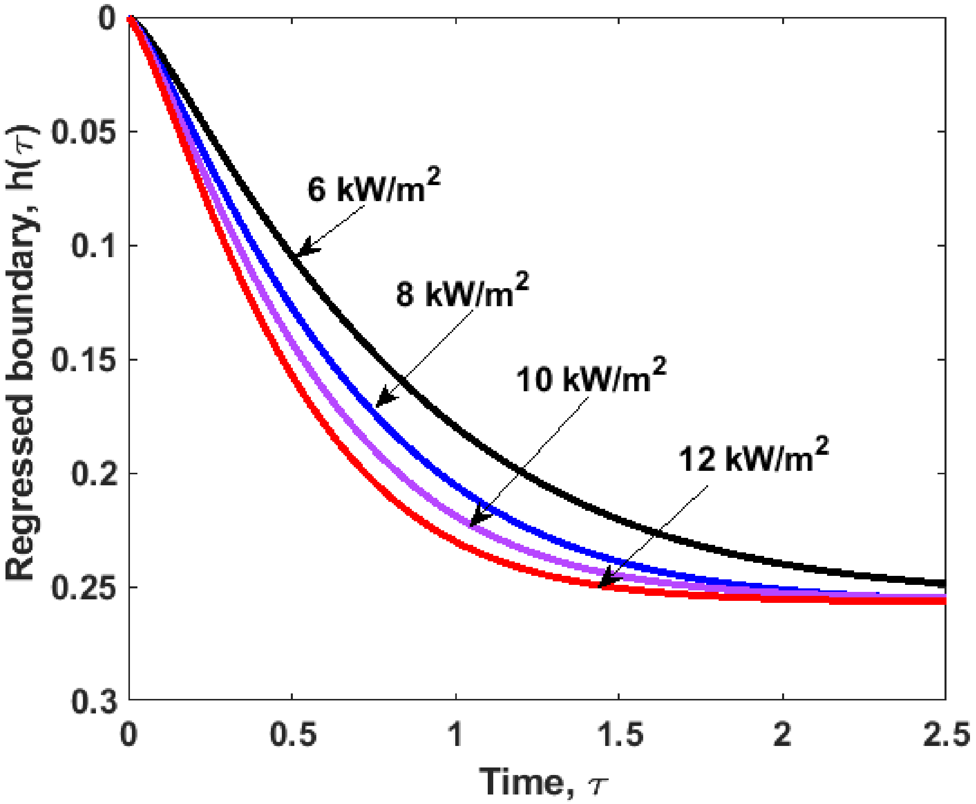

Figure 6.7: Dimensionless regressed boundary position with time for heat flux 6, 8, 10 and 12 kW/m^2

heat flux, hence regression is faster. But as the vaporization process proceeds, the increase in the vaporized layer thermal resistance surpasses any further increase in solid temperature and thus the regression process stalls and plateaus. The estimate $\tau \simeq 1.75$ characterizes the time needed to achieve this plateau.

6.7 Scaling Analysis

The purpose of the scaling analysis is to correlate the current modeling results with the experimental data. In addition, the scaling analysis examines the feasibility of basic flame spread assumptions for the prediction of observed surface regression.

From the experimental work described in chapters 3 and 4, observations were recorded on the post-burn samples. Regressions distances (depths = profiles) were measured for samples that had already been burned (i.e., tested) at different opposed flow velocities. Therefore, to additional transient measurements were involved. On the contrary, the model is transient, enabling computation from constant heat flux to phase change and eventual thermal degradation and regression. The goal is to scale the equations and deduce parameters that permit making preliminary comparisons with

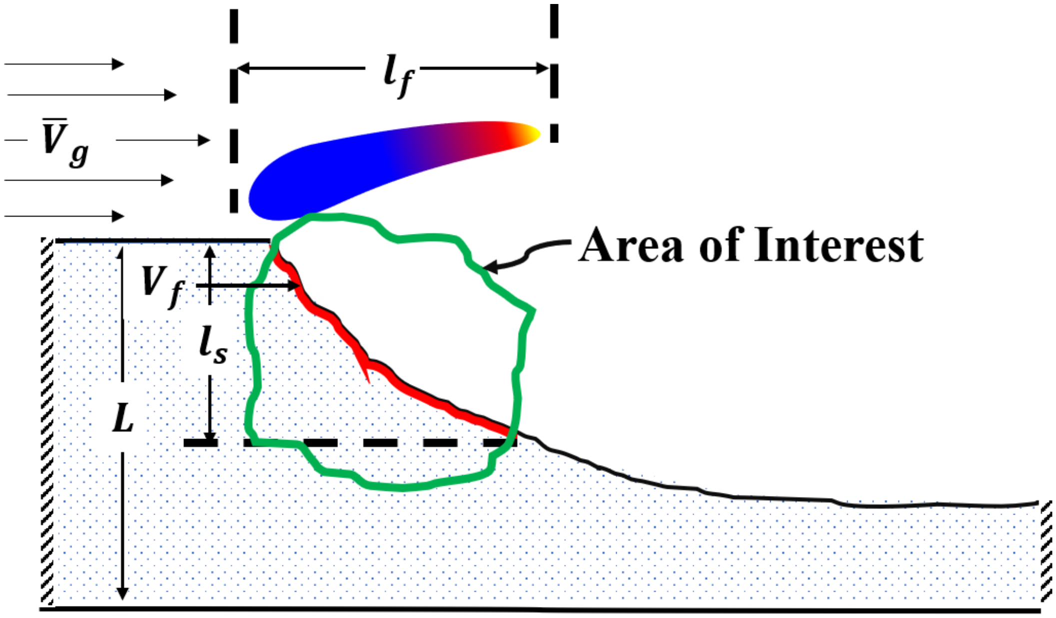

Figure 6.8: Schematic of the flame leading edge showing the flame length l_f, and the characteristic solid length scale, l_s. The flame is anchored near the leading-edge, moving right to left towards the opposed flow.

the experimental data.

The diagram in Figure 6.8 shows a flame spreading over a regressing fuel surface. The schematic shows that the tip on leading edge of the flame is anchored to the solid fuel at an attachment point. The solid regresses due to the combustion process (the corrugated slanted surface). In particular, the schematic represents the flame instance before the flame spread experiment has been terminated. The flame has traveled over the fuel surface, a steady (plateau) level of regression has happened. As seen, regression depth has increased in the solid fuel longitudinal direction (x-direction) and eventually reaches a plateau.

The non-dimensional variable representing space and time are $\eta = y/L$ and $\tau = \frac{\alpha t}{L^2}$. In dimensional form, $y = \eta L$ and $t = \frac{L^2 \tau}{\alpha}$. When $L = 25.4$ mm (thickness of the tested PMMA sample) and $\alpha = 1.62 \times 10^{-7} m^2/s$ (thermal diffusivity of PMMA), the time scale becomes $L^2/\alpha = 3.98 \times 10^3 s \sim 4 \times 10^3 s \sim 1 hr$. The entire test time scale is approximately one hour. This overall time scale is viable for describing the regression profile for the entire test. However, the measurements focused on regression that is motivated by the spread of the flame. The shorter time and space scales ("flame-level") dictate a redefinition of the scaling parameters . In the region of interest, near the flame leading edge, spread occurs over an effectively "infinitely thick" sample. In other words, there is no physical thickness relevant to the spread process. The relevant normalization variables (scales) are V_f and α_s, such that

$$Length : l_s = \alpha_s / V_f, \tag{6.41a}$$

$$Time : t = l_s / V_f. \tag{6.41b}$$

Characteristic parametric magnitudes can be estimated. Thus, $\alpha_s \sim O(10^{-7})\ m^2/s$ and $V_f \sim O(10^{-5})\ mm/s$ leads to

$$Length : l_s \sim \frac{O(10^{-7})}{O(10^{-5})} \sim O(10^{-2}) m \sim O(10^{1}) mm, \tag{6.42a}$$

$$Time : t \sim \frac{10^{-7}}{(10^{-5})^2} \sim O(10^{3}) s. \tag{6.42b}$$

The scaled time and space ranges in our area of interest, namely the actively regressing region near the flame leading edge (Figure 6.8) are, therefore $O(0)$ to $O(10^3)s$ and $O(10^0)$ to $O(10^1)mm$.

Therefore, l_s and t greatly reduced the length and the time scale. Figure 6.9 shows the dimensional regression with time using the reformed scaling parameters. The regression depth is approximately 2 mm for heat fluxes 8,10 and 12 kW/m^2 at 600 s and steady state is attained after that time (between 600 to 1000 s). The experimentally measured surface regression depth (Chapter 4, Figure 4.3) shows regression depths between 1 mm to 8 mm in a 20 mm streamwise segment for several opposed flow velocities. The experimental work examined sample regression after burning.

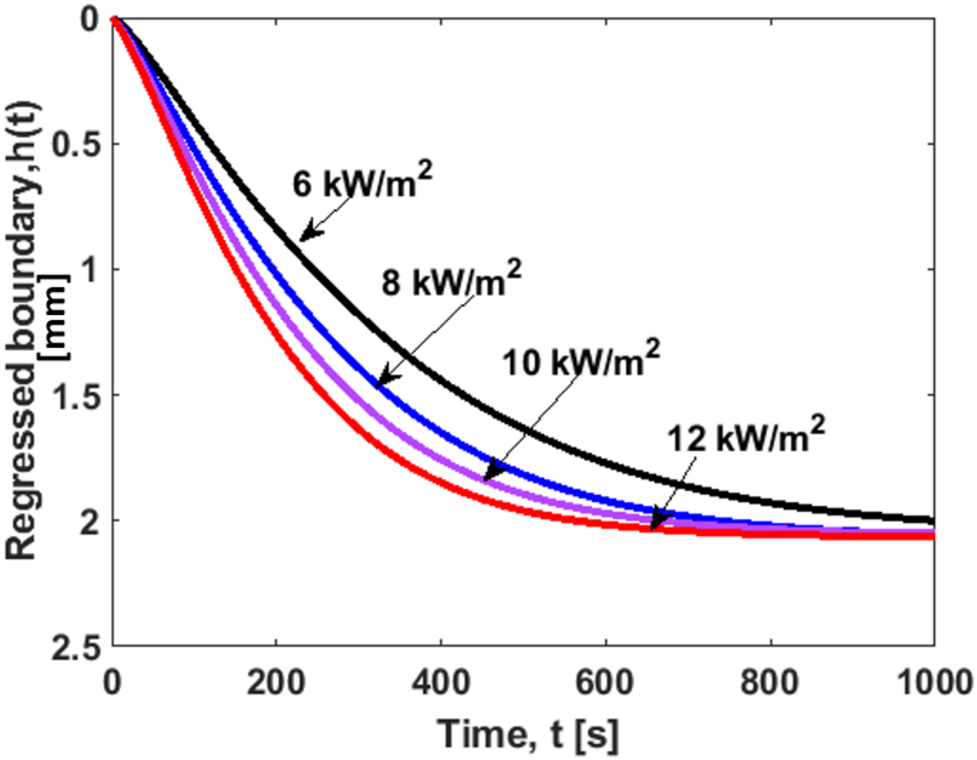

Figure 6.9: Regressed boundary position with time for heat flux 6, 8, 10 and 12 kW/m^2.

Transient surface regression profiles were not measured due to experimental limitations. However, a Galilean transformation from time to spatial co-ordinate of the model can be achieved by multiplying time in the Figure by flame spread rate V_f. By using, hypothetical $V_f \cong 0.02$ mm/s, to the x-axis co-ordinate ranges between 0 ~ 20 mm. Figure 6.10 shows the regression versus position x, which is considered as distance from the leading edge as shown in Figure 6.8.

Figure 6.11 shows a comparison between the modeling results and the experiment data. The regression depths for the cases of opposed flow velocities 8.2, 10.3 and 12 cm/s were used for the

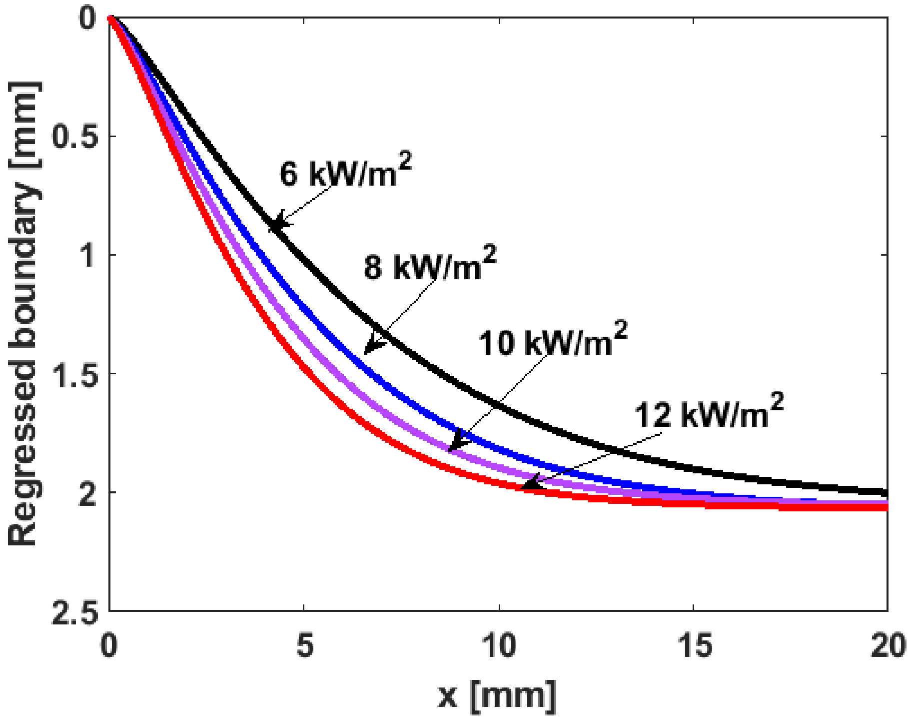

Figure 6.10: Regressed boundary position with space for heat flux 6, 8, 10 and 12 kW/m^2

purpose of comparison. This figure indicates that the modeling results can adequately characterize the regressed surface profile for low opposed flow velocity cases when the latter are suitably scaled. The essence of the scaling is to use scale factors that are appropriate to an "infinitely thermally thick" solid fuel, as given by Eqs. (6.42 a) and (6.42 b).

6.8 Summary

Transient flame growth over a solid fuel is of fundamental and practical importance for fire safety. The objective of this work was to determine the material response to external heat flux by the flame. The basic assumption of the material that it is considered as an "ideal vaporizing fuel" [11]. As the fuel/material decomposed it produced vapor from solid.

The transient one-dimensional model was divided into two stages. In the first stage, where no regression is involved, the solid boundary is heated by the external heat flux. After a certain time the surface attains the vaporization temperature and triggers the regression process. This second stage is identified as the vaporization stage. The imposed heat flux plays an important role in

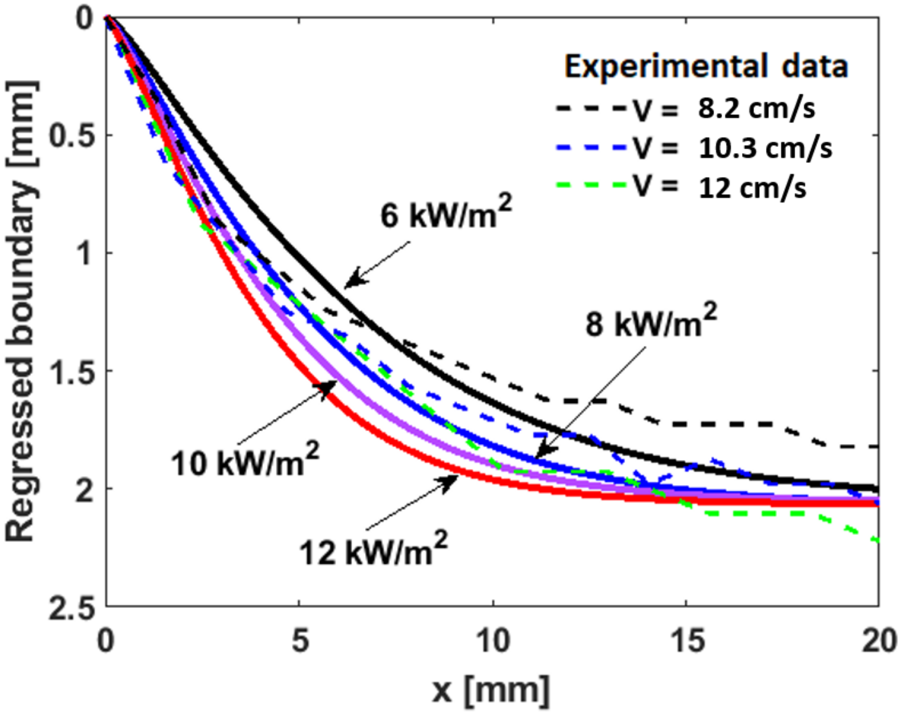

Figure 6.11: Comparison between experimental regression depths for flow velocities 8.2, 10.3 and 12 cm/s with the theoretically modeled regressed boundary shape for heat fluxes 6, 8, 10 and 12 kW/m^2.

determining the vaporization time, τ_v. The higher is the heat flux, the lower is τ_v period. Results showed, as expected, that the solid fuel temperature distribution is sensitive to the imposed heat flux.

In order to correlate experimentally measured sample regression profiles (Chapter 4) with the model predictions, a scaling analysis was conducted in the vicinity of the flame leading edge. The semi-empirical scaling analysis manages to successfully compare the measured data with the modeled results for a characteristic flame spread rate of V_f = 0.02 mm/s.

CHAPTER 7

CONCLUSION

Despite several decades of research which involves experimentation and development of analytical and numerical models, the complexity of opposed flow flame spread continues to merit attention in the combustion research community. Most of our research revolves around the ability to extract trends out of complicated data sets. The trends that is extracted from these observations form the basis for correlations and theories that help us to understand the underlying fire physics.

7.1 Concluding Remarks: Chapter 2

The Narrow Channel Apparatus has been under investigation as a possible test method for screening material for space flight applications. A key objective is to determine whether the gap height of the NCA can be chosen to suppress buoyancy without causing excessive heat losses to the inert top and bottom of the NCA. Experiments were performed on thin Whatman 44 filter paper for opposed flow velocities ranging from 1 to 40 cm/s and different NCA gap heights (3, 5, 7 and 9 mm). Flame spread rates measured from video analysis ranged from 0.12 to 0.37 cm/s. Side view images were used to qualitatively assess the influence of buoyancy on the flame shape. The influence of the gap height on the overall equivalence ratio is determined from a scaling analysis which showed the higher the gap height, the (globally) leaner is the flame.

A scaling analysis is performed for gas preheat length scale calculation with a parabolic flow distribution, which leads to good agreement with the Linear gradient A and Linear gradient B models which are based on the linear velocity gradient assumption. This agreement is encouraging, since flame spread in spatially variable velocity fields is a relatively unexplored topic of research. A significant observation is that the solid preheat lengths are an order of magnitude smaller than the gas preheat lengths. This means that a higher thermal diffusivity of the gases has a larger impact on the length scales than the higher flow velocity.

Heat losses in the NCA are analyzed by a control volume analysis. Convective heat loss, radiative heat loss and enthalpy rise of the gas and solid were considered as contributing factors. It is found that the heat loss can be minimized for all gap heights for a particular opposed flow velocity. A heat loss analysis demonstrated that a small gap height led to a high heat loss from the flame to the wall, which consequently led to flame quenching. Among the gap heights, 5 mm appears to yields the best compromise between the NCA wall heat loss (undesirable) and buoyancy suppression (desirable).

7.2 Concluding Remarks: Chapter 3

In Chapter 3, opposed flame spread over PMMA is investigated by varying the sample thickness and flow velocities. Three different fuel thicknesses (6.6, 12.1, 24.5 mm) were tested over a range of airflow velocities from 8-52 cm/s. The primary emphasis was to focus on the general issue of flame spread measurement. However, eventually the study was extended to compare results with the previous literature. In order to do that, numerical and theoretical calculations were also performed.

The flame position was tracked from the test videos to determine the flame spread rate. Results showed that the flame spread rate varies between 0.02 - 0.07 mm/s. Different flame spreading regimes are identified and discussed in the context of the Damkohler number.

Flame images and burnt samples for all thickness samples and all velocities were carefully examined. The flame brightness increases with a growing yellow tail as the opposed flow velocity increases for all sample thicknesses. From visual inspection of the post-burn samples, it is found that the soot production is low at a low opposed flow velocity. For 6.6 and 12.1 mm thick samples, complete burn out was observed for flow velocities greater than 31 and 26 cm/s. In this region, the flame spread rate was unaffected by the opposed flow velocity, identified here as the regressive burning regime. A semi-constant flame spread rate was observed for 24.5 mm thick samples for velocities greater than 41.4 cm/s, but complete burn out was not observed. In the regressive burning regime, the solid fuel regression plays a dominant role compared to the flame spread rate where the flame consumed the fuel and spread slowly.

In this chapter, the NCA results were compared with prior study by Fernandez-Pello et al. [7].

A detailed procedure involving numerical and theoretical analysis was shown to favorably compare two disparate set of measurements: results from NCA (a buoyancy suppression device) and data from the Princeton wind tunnel (buoyancy not suppressed). The stretch rate is shown to be a viable parameter for comparing the results and correlating the results. The analysis demonstrates that, when properly interpreted and analyzed, the data can be fitted in a universal fashion showing excellent agreement, with divergence only occurring when the new "regressive burning regime" was encountered.

7.3 Concluding Remarks: Chapter 4

In Chapter 4, a technique is presented to measure the surface regression to determine the mass loss rate. The process is based on measurements of the regressing surface location as a function of distance from the sample leading edge. The PMMA samples of thickness 24.5 mm were burned in the NCA for opposed flow velocities 8-45 cm/s. Each post-burn sample is analyzed. An image processing algorithm is employed to obtain the surface regression shapes.

The mass loss rate of opposed spreading flames was determined by formulating a semi-empirical correlation. Experimental results shows that surface regression increases with flow velocity. Three distinctive clusters of data were observed. For flow velocity < 12 cm/s which was the first cluster, the regression is approximately 2 mm. The mass loss results were fitted against power-law functions and an average -0.515 power dependence was found. The mass loss rate results were compared with Emmon's formula [63] where the power dependence is $x^{-1/2}$ for downstream distance. This $x^{-1/2}$ dependence shows excellent agreement with low flow velocity results. As the regression is minimal, the solid fuel can be considered as an "ideal vaporizing solid" [11] which is also the modeling basis of Emmon's work [63].

The second cluster is for opposed flow, $\overline{V}_g = 14.5$ and 20.7 cm/s where the mass loss rate follows the power dependency average of -0.315. Finally, for $\overline{V}_g = 24.8$, 29, 37.3, 41.4 and 45.5 cm/s the average power dependency is -.246. Here, regression is dominant approximately 8 mm and, contributes to a higher gap height of the narrow channel. As discussed in Chapter 2, the buoyancy suppression is related to the gap height of the NCA. The regression depth for this range of flow velocities, alters the NCA gap height. Therefore, it appears that in this instance the NCA would not be able to suppress buoyancy as effectively. As a result, the mass loss rate power law dependency resembles that for a natural convection heated vertical plate $x^{-1/4}$ for flow velocities $\overline{V}_g$> 24.8 cm/s.

7.4 Concluding Remarks: Chapter 5

Thick solid PMMA has been burned inside NCA to assess different flame spread related issues. A close inspection of the post-burn sample led to the analysis, described in this chapter. The examination of the burnt samples revealed the presence of internal bubbles in the PMMA. Three samples were investigated, burned at a flow velocity of 15 cm/s in the NCA. The samples were analyzed using a 2D digital image processing technique by dividing the sample into eight separate segments.

The results showed the bubble size distribution of the post-burn PMMA samples can be described by a two parameter log-normal density function for bubble size less than 0.052 mm^2 and bin width 0.005 mm^2. The results are consistent for all 8 segments. The bubble count and bubble area are determined by an edge detection algorithm for analyzing the images. An overall descending trend is observed from segments 1 to 8. Segment 1 is the nearest to the leading edge of the flame. Here, bubbles nucleate and due to insufficient time did not fully form, merge or coalesce. Furthermore, the bubble volume is determined from a scaling analysis. The goal was to calculate the bubble volume fraction, which was varied between 3-6%.

7.5 Concluding Remarks: Chapter 6

In Chapter 6, a thermo-diffusive analysis of a model problem simulating a diffusion flame has been conducted. This study consisted of two parts.

The first part is a simplified 1-D model comprised of two stages. The preliminary pre-vaporization stage describes a pre-heating phenomenon by the external heat flux. This stage was solved theoretically. The later vaporization stage describes the regression/vaporization process at a constant temperature subject to a constant heat flux. The process enables conductive and convective heat transfer exchanges between the flame and the surface. An explicit finite definite scheme is used to numerically model this stage. The numerical study examines transient regression for different constant heat fluxes. This 1D model is used to investigate the details of the regression process under heating with constant physical properties.

The second part is a semi-empirical scaling analysis to compare the transient model results with experimental NCA results. Chapter 4 examines regression near the leading edge of a spreading flame in an opposed flow is examined. A length and time scale are formulated using the flame spread rate, which dimensionalizes the regression from the analytical-numerical modeling. The scaling analysis establishes a procedure for interpreting the model. The results show good agreement between the NCA measurements and the model.

CHAPTER 8

FUTURE WORK

The results from this research could be extended in the future into the following areas:

8.1 Recommendations for Future Work: Chapter 2

In this study, Whatman 44 filter paper of thickness 0.17 μm is burnt inside NCA. Different types of thin fuel can be examined to solidify the conclusion regarding the gap height.

Our control volume heat loss analysis can be expanded with a numerical model. A numerical effort at full-scale simulation can be attempted with variable NCA gap height.

NCA construction is very crucial to simulate microgravity conditions. In this work, opposed flow velocity is varied for different NCA gap heights. Spacecraft environment also fall along the normoxic curve at 34% oxygen concentration and 56.5 kPa. Future extensive testing along normoxic curve would provide more realistic conditions of the spacecraft environment to select a gap height.

Infrared Radiation (IR) camera can be used to get temperature distribution of the flames.

Another possible expansion of this work is an analytical scaling analysis which is in development phase. The goal of our analysis is to determine the optimum channel height for minimum heat loss by balancing the convection and buoyant heat loss. The heat losses caused from the buoyant flow induced by the flame in a channel of height h, and then add those losses to the losses caused by forced convection to both the upper and lower channel walls. Once theses heat losses are added, the total losses, can be minimized by choosing an optimal channel height.

8.2 Recommendations for Future Work: Chapter 3

The newly found regressive burning regime is required to analyze extensively. It is hypothesized that the flame is hiding behind a “curved hollow” during spreading. The test observation from side is presented to support the hypothesis. The validation work with legacy result shows deviation near regressive regime. It indicates that the this regime can not be described with flame spread theories rather new form of flame spread interpretation is required. After analyzing the post-burn sample, it is found that the regression depth is substantially high in this regime. In contrast, the flame spread rate is constant and relatively low (approximately 0.02 mm/s). It is evident that the high regression rate is altering the flame spreading process. An extensive experimentation and theoretical work is needed to properly explain the associated phenomenon. It is not possible to run high flow velocity experiments with the current mass flow controller. A setup is being developed with higher range mass flow controller by this author. Future students will be able to perform high flow velocity experiments to study the regressive regime.

Flame-to-flamelet transition has been studied for thin combustible fuels for years. Similar behaviors can be studied for thick fuel in the near-limit regime. This author has performed experiments at low flow velocity ($\overline{V}_g$) < 8 cm/s. Instabilities prior to extinction, gradual break up of the continuous flame front leading to extinction is observed. The preliminary results are not included in the main body of this dissertation, they are presented in the Appendix D Section D.1. It is believed that more experiments needs to be conducted for better understanding in this regime.

Flame area is an important parameter which can be an indication of the presence of soots, can locate the reaction zone. To the knowledge of the author, there are few studies available for flame area measurement on thin fuel [101, 102]. The author made an attempt to measure the flame area for thick fuel. It is found that the flame area is a dynamic process, changes with time. Although, our measured flame spread rate for thick PMMA for all opposed flow velocities was steady. The flame area indicates variation with time. Flame images demonstrate that the flame consists of a blue and yellow region. An image processing algorithm is developed to measure the flame area. The measurement process and preliminary results are reported in the Appendix D Section D.2 . This work has an excellent potential to be considered as future research.

8.3 Recommendations for Future Work: Chapter 4

The significance of the regressive burning regime can be assessed with regression depth and mass loss rate along with flame spread rate. Future experiments may solidify the knowledge by analyzing the regression shape. The test results will be important in developing theoretical understanding for this regime.

Future work is needed to address the effect of sample width on horizontal opposed flow flame spread process over solid fuel. The regression depth and mass loss rate will be further explored in order to establish a methodology for fire scenario for different scaled materials.

8.4 Recommendations for Future Work: Chapter 5

The post-burn thick PMMA samples were studied for internal bubble formation. Bubble study is specially important in providing benchmark information for the future numerical model. The bubble formation needs to be considered for the model development for flame spread rate. The bubble frequency distribution, bubble counts, bubble sizes derived from experimental observations will be crucial information for modeling.

The scaling analysis to calculate the bubble volume fraction is of great importance. A 2D measurements were conducted and available shapes (sphere and cylinder) were considered to scale the bubble volume. In reality, bubble shapes are far more complex. A robust measurement system such as Computer Tomography (CT) scan will be appropriate to identify the bubble shapes. To do so, micro-CT (μ-CT) scanner located at Case Western Reserve University (CWRU) is used to scan one of our samples to obtain preliminary results. This author has performed basic post-processing on CT-scanned images and laid out the methodology for the future students (see Appendix E).

8.5 Recommendations for Future Work: Chapter 6

Future work is needed to focus on two dimensional simplified models of the flame spread process. The future model can shed more light on the spread mechanism and may also produce correlations from numerical and experimental data. A more realistic 2D time-dependent model of opposed flow flame spread over non-charring materials. Radiation is one of the important mechanism that can alter the flame spread mechanism at low flow velocity. Radiation mechanisms can be included in the numerical model. In the analytical work, the thermal properties are considered constant. In actual burning process, thermal properties vary with time. The variation and the effect of thermal properties on flame spread mechanism can be of great interest for research in future.

APPENDICES

APPENDIX A

CORRELATION PROOF: GAS LENGTH SCALE

The dimensionless form of Eq. (2.14) for the gas preheat length scales is given by

$$\hat{\delta}^3_{g,NCA} + C_2\hat{\delta}^2_{g,NCA} - C_1\hat{\delta}_{g,NCA} + C_0 = 0$$

where $\hat{\delta}_{g,NCA} = \frac{\delta_{g,NCA}}{h}$, $C_2 = \frac{1}{c_q}$, $C_1 = \left(\frac{1}{6c_q^2}\right)\left(\frac{V_f}{\overline{V}_g}\right)$, $C_0 = \left(\frac{c_g}{6c_q^2}\right)\left(\frac{\alpha_g}{6\overline{V}_g}\right)$

This cubic can easily be rearranged as

$$n^2 - 1 = a_1(n^3 - \frac{a_2}{a_1}n)$$

where the constants are $a_1 = \sqrt{c_g c_q}\sqrt{\frac{\alpha_g}{6\overline{V}_g h}}$ and $a_2 = \frac{1}{\sqrt{c_g c_q}}\frac{V_f}{\overline{V}_g}\sqrt{\frac{6\overline{V}_g h}{\alpha_g}}$

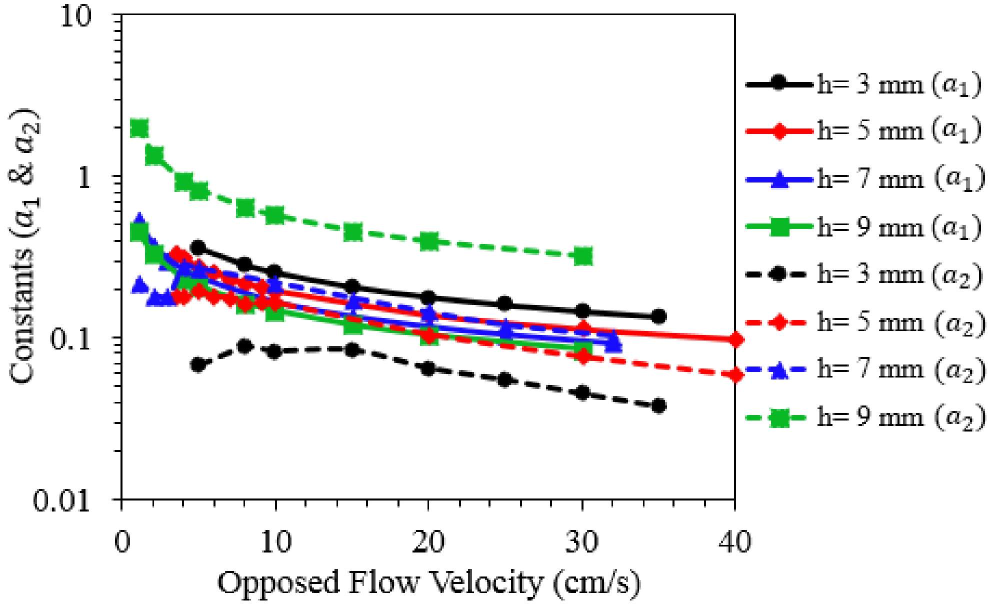

Figure A.1: Constants a_1 and a_2 versus opposed flow velocity for different h values. The solid lines are for a_1. The dashed lines are for a_2.

In Figure A.1, a_1 and a_2 are shown as functions of $\overline{V}_g$ where it is seen that both are between $O(10^{-1})$ and $O(10^0)$. This ratio of a_2/a_1 is generally of order unity and cannot be neglected. Expanding n as $n = n_0 + a_1 n_1 + ...$ and substituting into the cubic leads to $n = 1 + \frac{a_1}{a_2+2}$. The dimensionless gas preheat length for narrow channel becomes, approximately,

$$\hat{\delta}_{g,NCA} = \sqrt{\frac{c_g \alpha_g}{6\bar{V}_g h c_q}} \left[1 + \frac{\sqrt{c_g c_q} \sqrt{\frac{\alpha_g}{6\bar{V}_g h}}}{\frac{1}{\sqrt{c_g c_q}} \frac{V_f}{\bar{V}_g} \sqrt{\frac{6\bar{V}_g h}{\alpha_g}} + 2} \right] \tag{A.1}$$

APPENDIX B

FLAME POSITION VS TIME

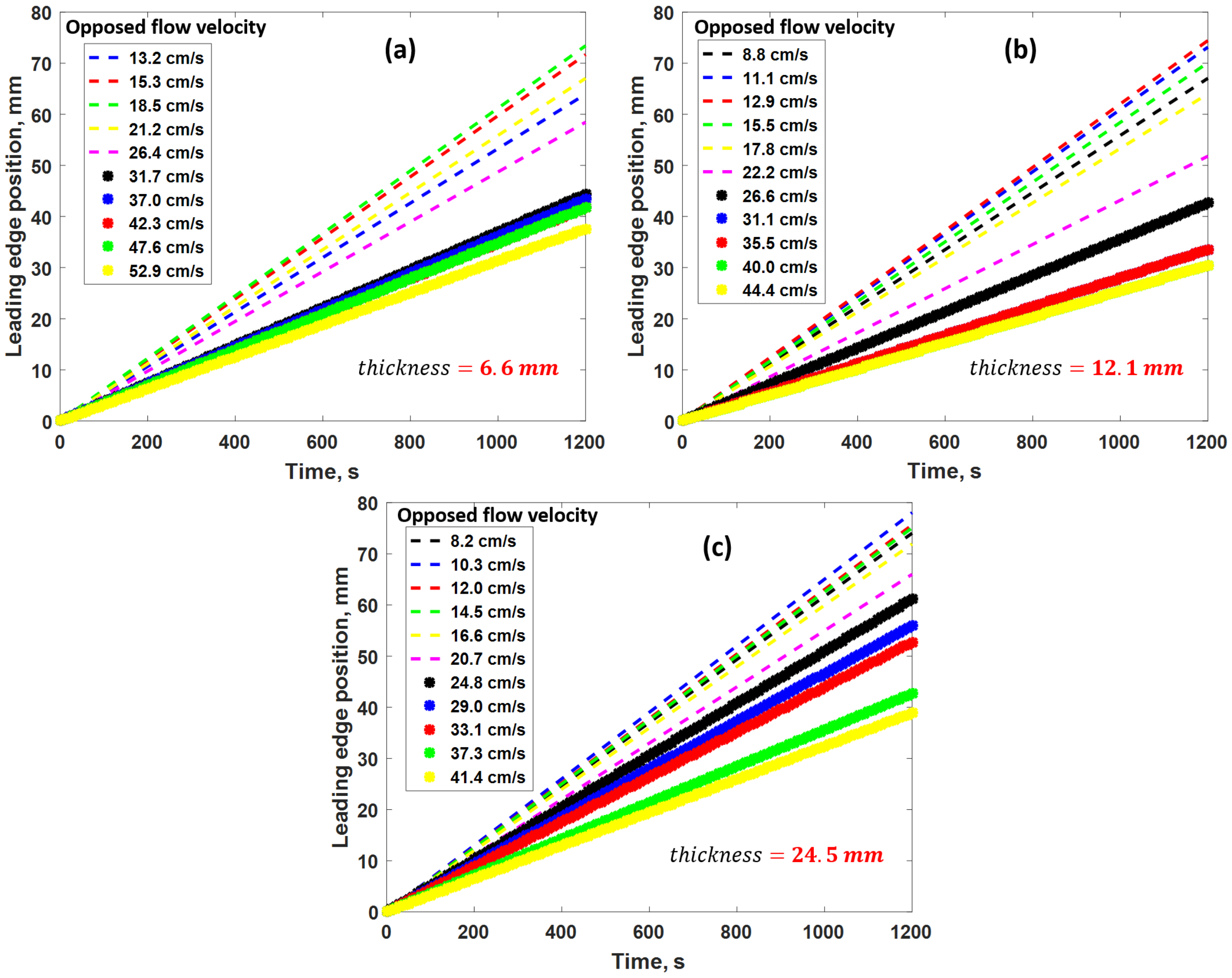

Figure B.1: Flame leading edge position as function of time a range of opposed flow velocities for (a) 6.6 mm thick PMMA, (b) 12.1 mm thick PMMA and (c) 24.5 mm thick PMMA. The slope of each curve yields the flame spread rate, which is nearly constant for each test.

Figure B.1 shows the relative flame position as a function of time for 6.6, 12.1 and 24.5 mm (Figure B.1 (a), (b) & (c) respectively) PMMA samples over the range 8-52 cm/s of opposed flow velocities. The initial time ($t = 0$) was designated as the time when the flame tracking began, and the corresponding flame location was considered as the initial tracking point ($x = 0$). Threshold tracking was used for all cases. As a result, the tracking shows excellent linearity over the entire range of flow velocities. Although the overall burning time is different for each test, tracking was performed for the same time window for all tests. Each line on the plot is for constant opposed flow velocity, and the corresponding slope indicates the flame spread rate.

APPENDIX C

BUBBLE STATISTICS FOR SAMPLE 2 AND 3

C.1 Frequency distribution for Sample 2

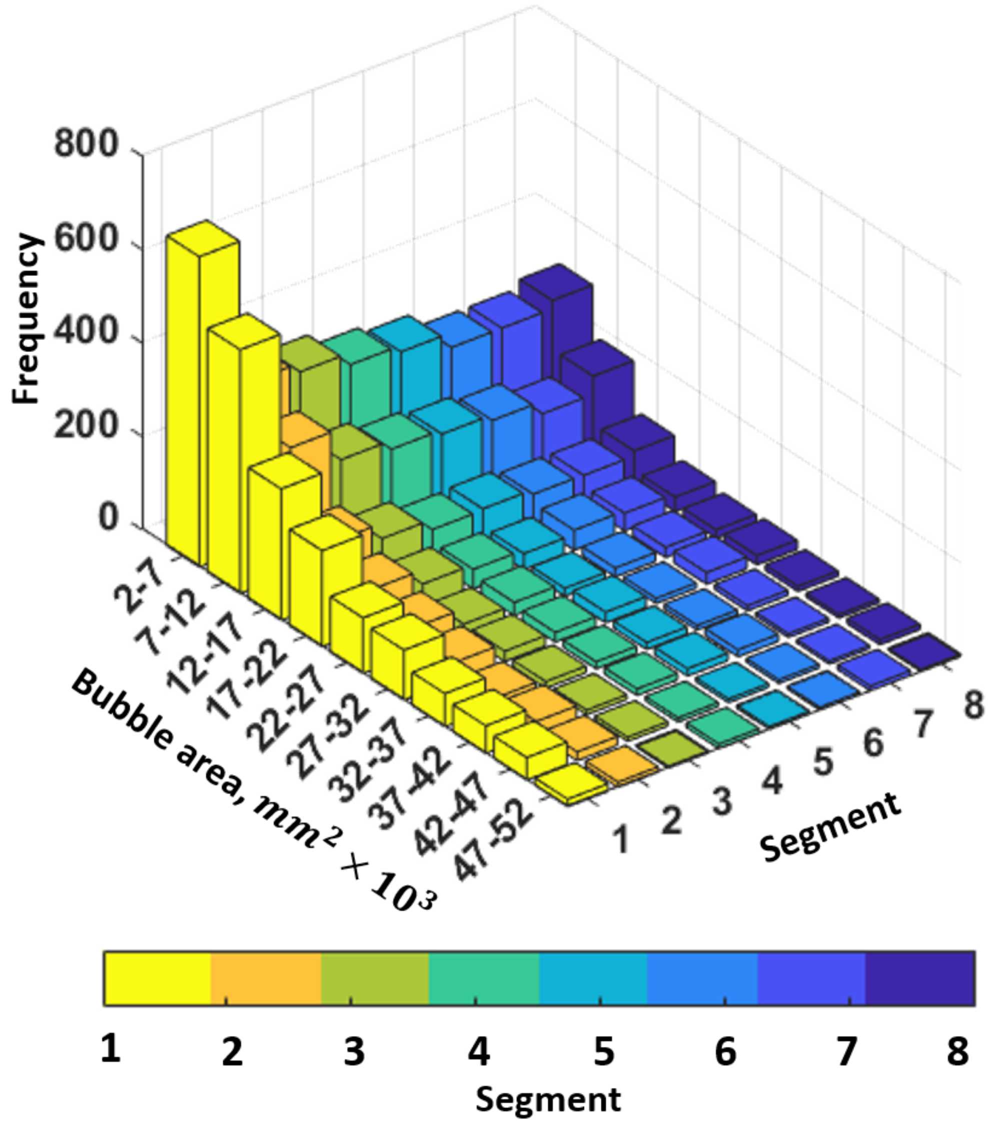

Figure C.1: Bubble area frequency distribution for sample 2. The color represents the specific segment (1-8). Yellow is segment 1 (curvy-edge side, far left segment), while violet is segment 8 (far right segment). The bubble area is divided into 10 different size ranges or bins. Each bin width is 0.005 mm^2.

C.2 Frequency distribution for Sample 3

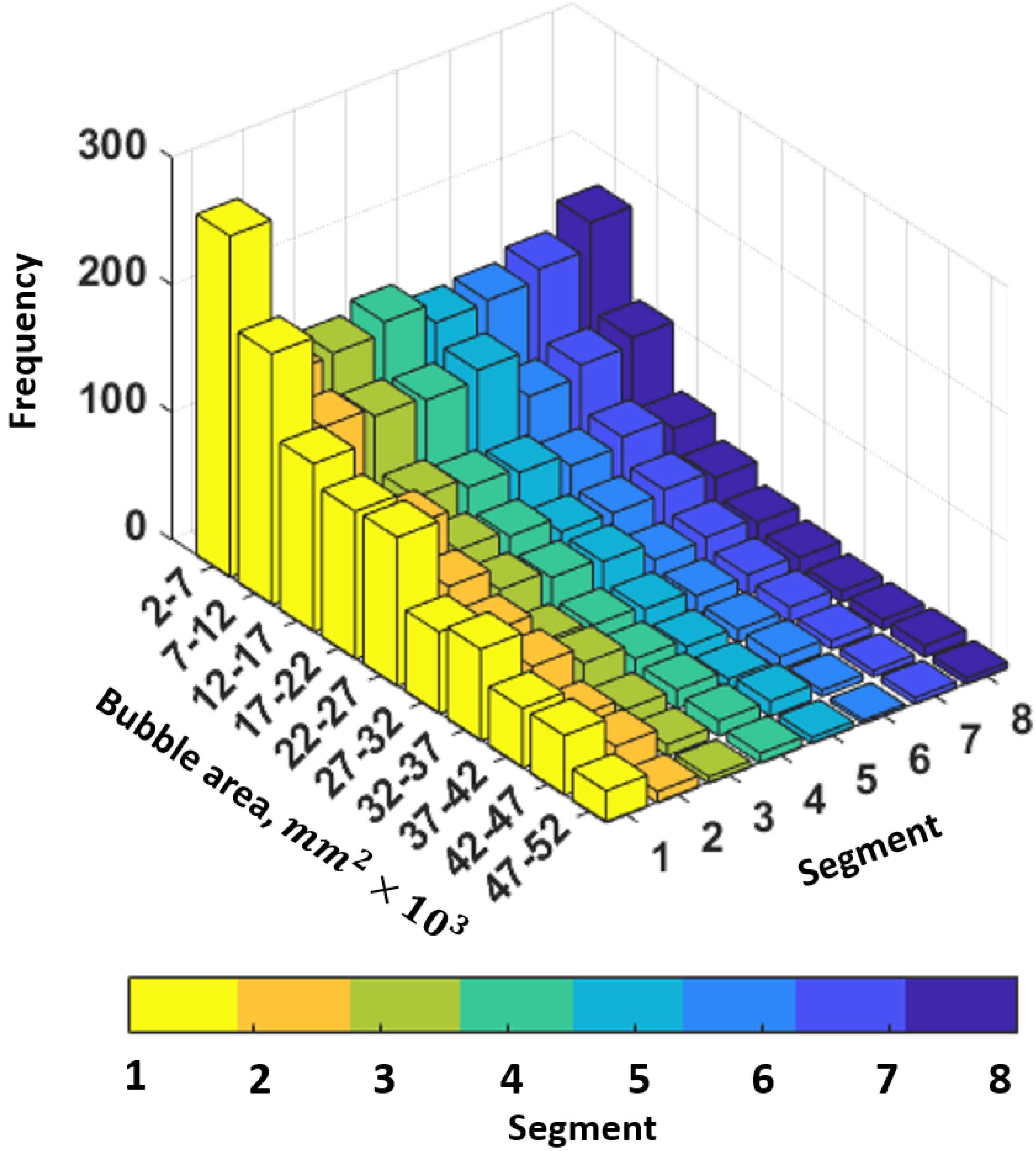

Figure C.2: Bubble area frequency distribution for sample 3. The color represents the specific segment (1-8). Yellow is segment 1 (curvy-edge side, far left segment), while violet is segment 8 (far right segment). The bubble area is divided into 10 different size ranges or bins. Each bin width is 0.005 mm^2.

C.3 PDF for Sample 2 and Sample 3

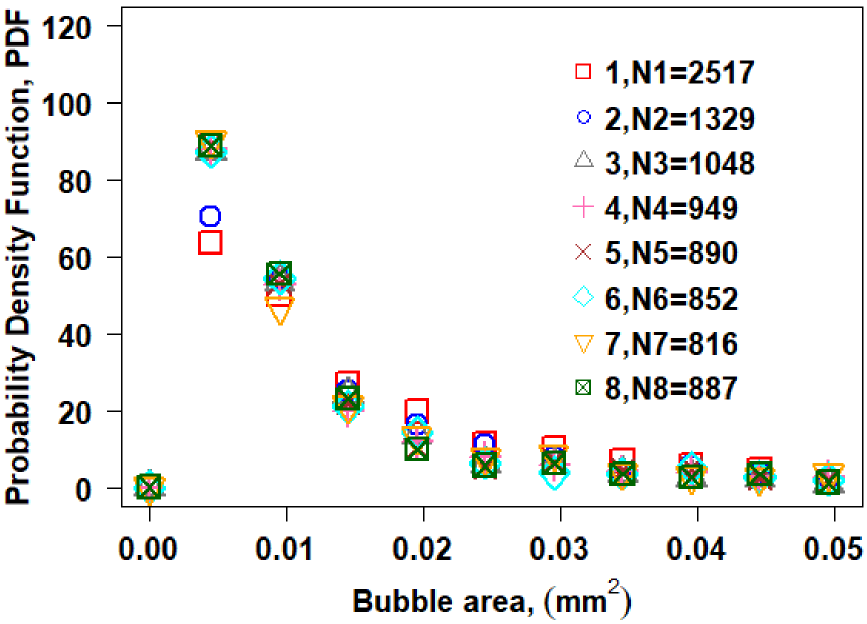

Figure C.3: Probability Density Function (PDF) for bubble area for each segment 1-8 for sample 2. Bin width is .005 mm^2. Eight different markers are used in the legend to show the eight segments. The PDF in each bin is plotted with respect to the median value in that bin.

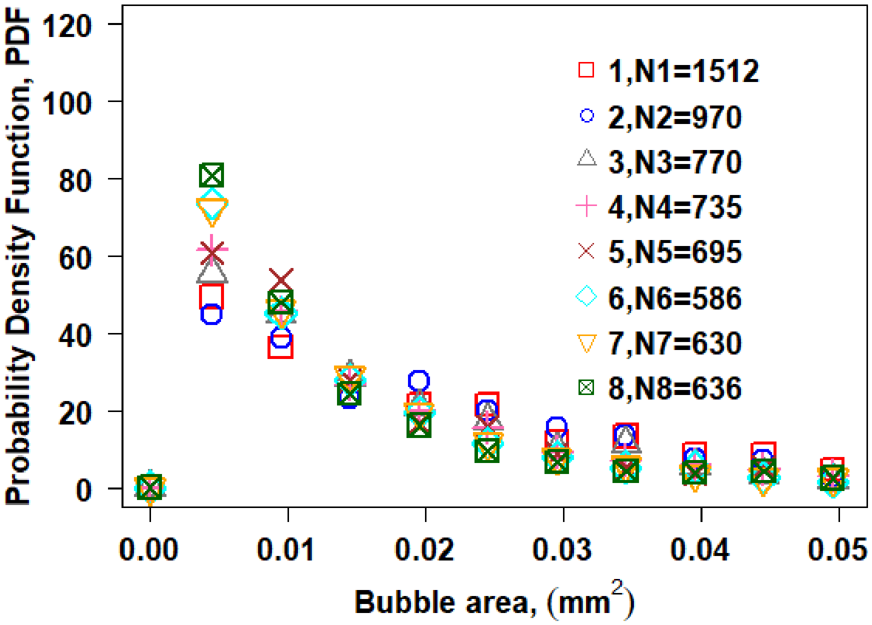

Figure C.4: Probability Density Function (PDF) for bubble area for each segment 1-8 for sample 3. Bin width is .005 mm^2. Eight different markers are used in the legend to show the eight segments. The PDF in each bin is plotted with respect to the median value in that bin.

C.4 Fitting with Standard functions for Sample 2

C.4.1 Segment 1, 2, 3 & 4

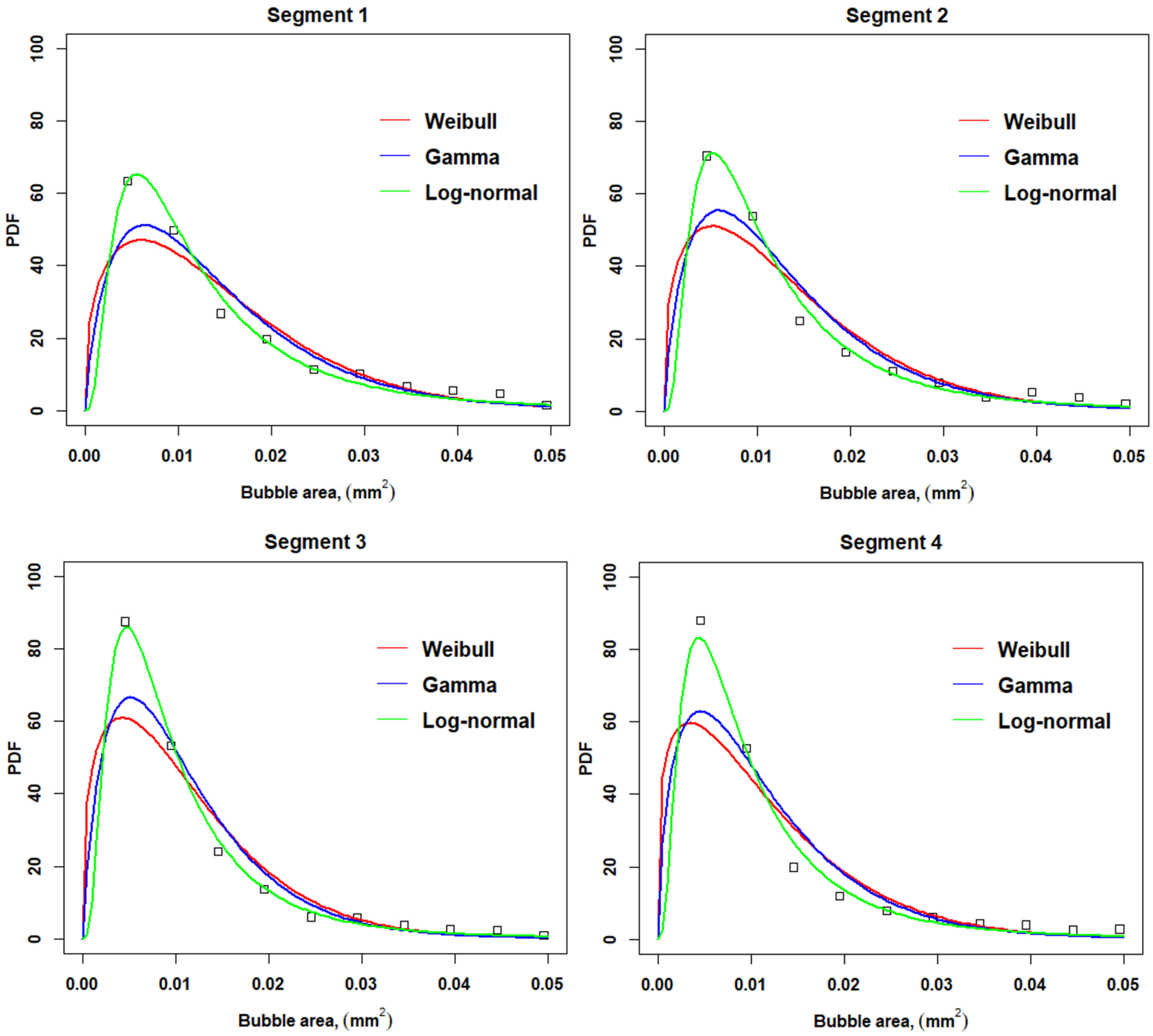

Figure C.5: The empirical Probability Density Function (PDF) versus bubble area is compared with the Weibull, Gamma and Log-normal functions for sample 2. Bin width is 0.005 mm^2. The PDF in each bin is plotted with respect to the median value of the bin.

C.4.2 Segment 5, 6, 7 & 8

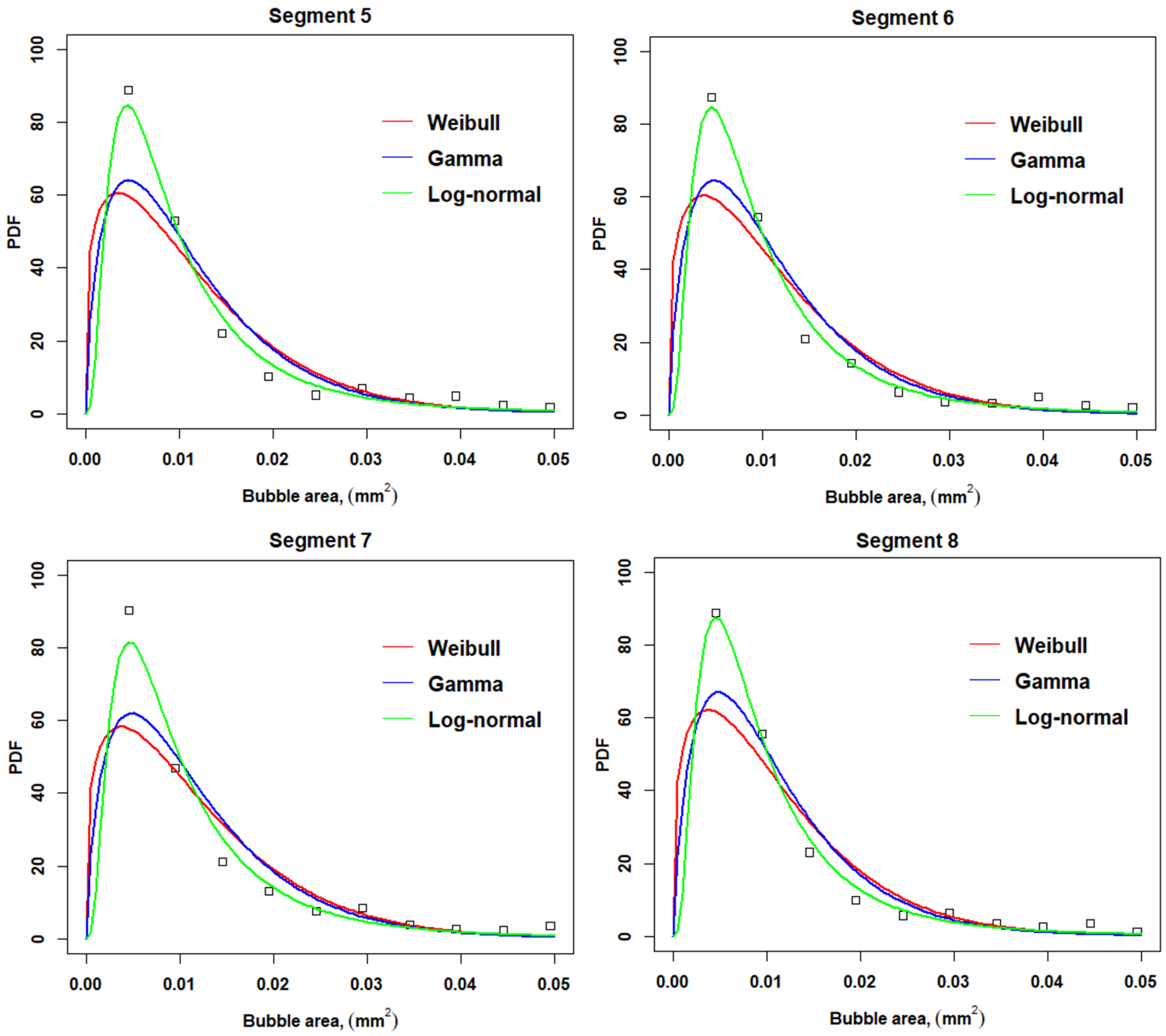

Figure C.6: The empirical Probability Density Function (PDF) versus bubble area is compared with the Weibull, Gamma and Log-normal functions for sample 2. Bin width is 0.005 mm^2. The PDF in each bin is plotted with respect to the median value of the bin.

C.5 Fitting with Standard functions for Sample 3

C.5.1 Segment 1, 2, 3 & 4

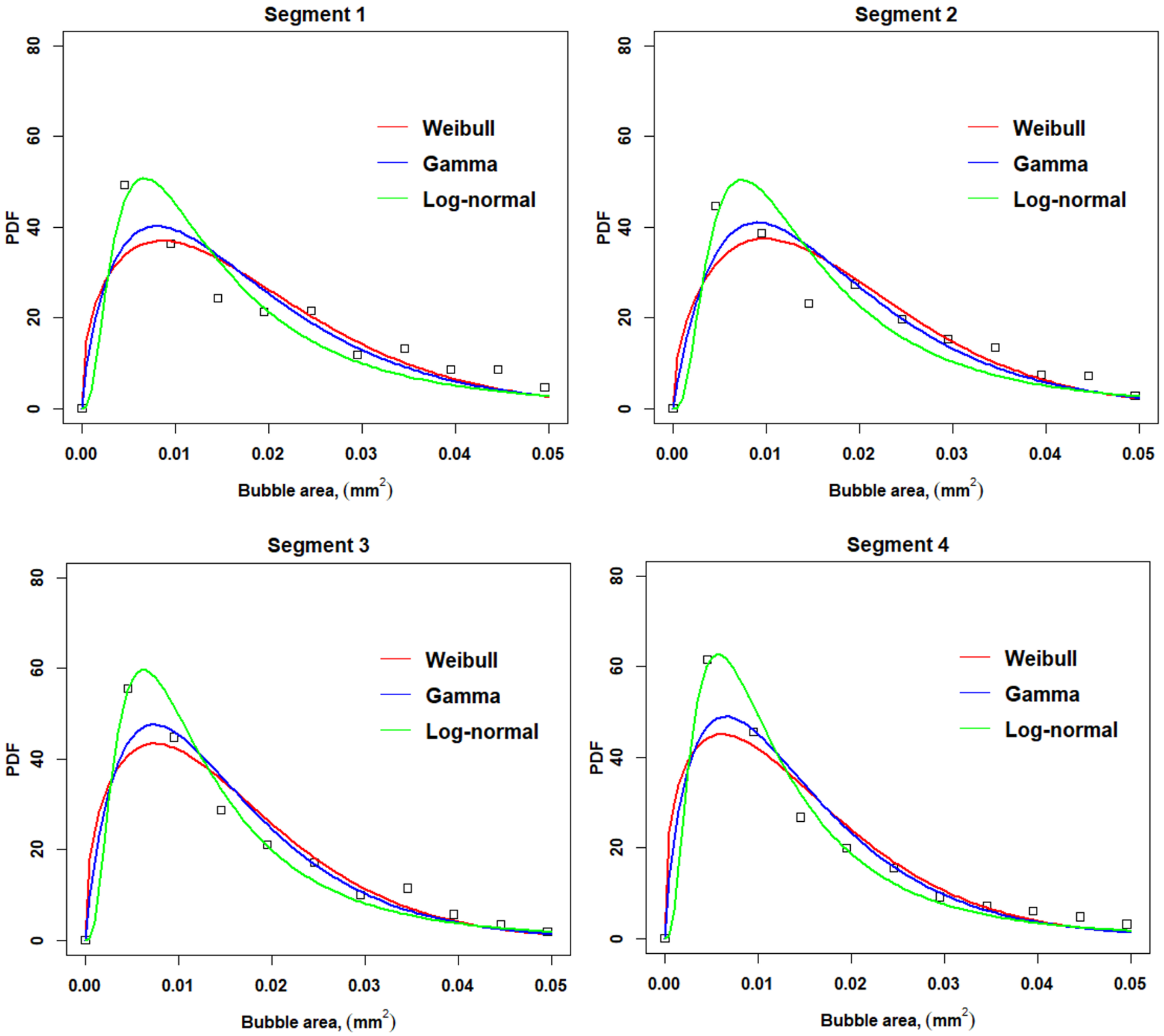

Figure C.7: The empirical Probability Density Function (PDF) versus bubble area is compared with the Weibull, Gamma and Log-normal functions for sample 3. Bin width is 0.005 mm^2. The PDF in each bin is plotted with respect to the median value of the bin.

C.5.2 Segment 5, 6, 7 & 8

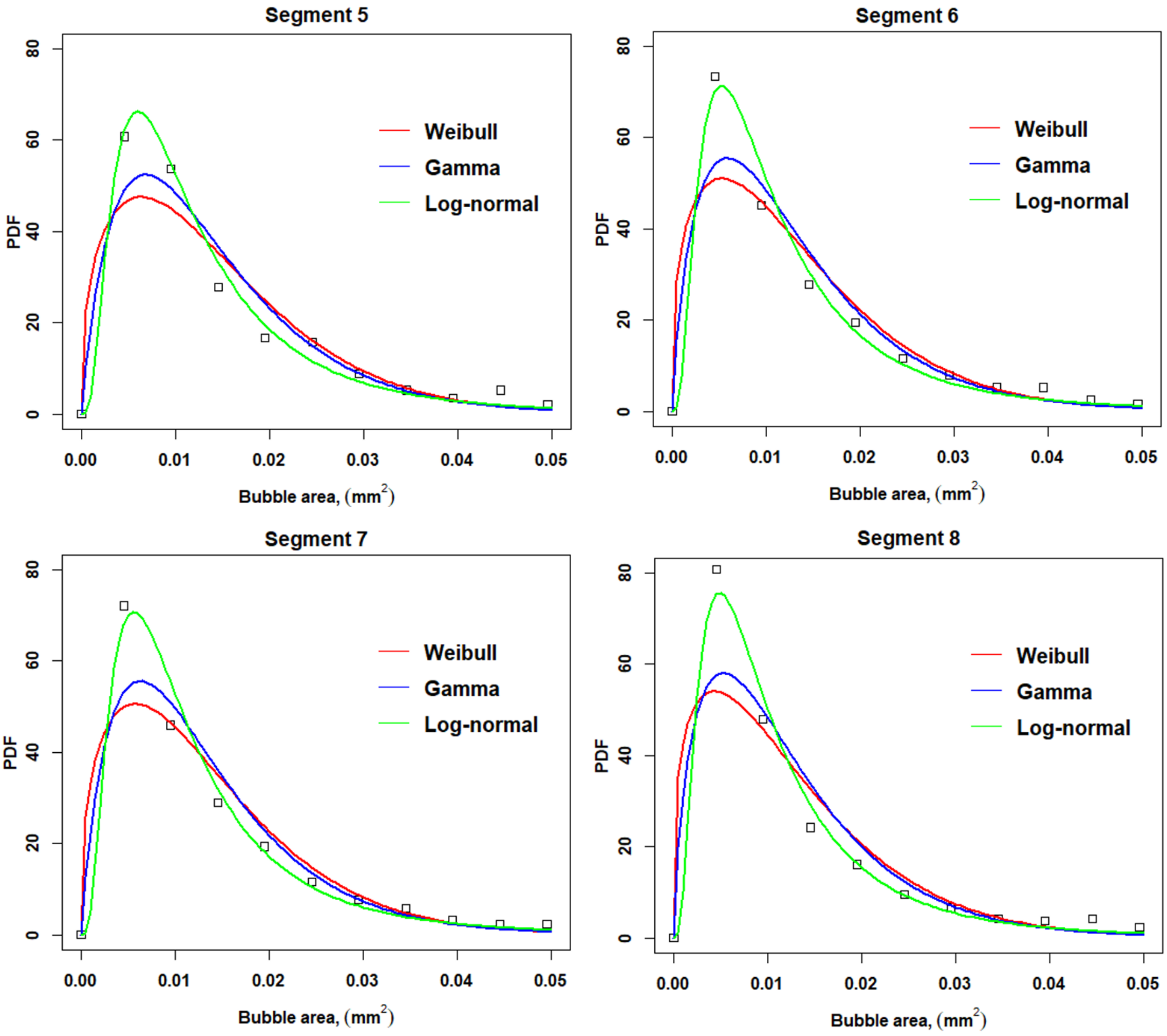

Figure C.8: The empirical Probability Density Function (PDF) versus bubble area is compared with the Weibull, Gamma and Log-normal functions for sample 3. Bin width is 0.005 mm^2. The PDF in each bin is plotted with respect to the median value of the bin.

C.6 RMSD for Sample 2 and Sample 3

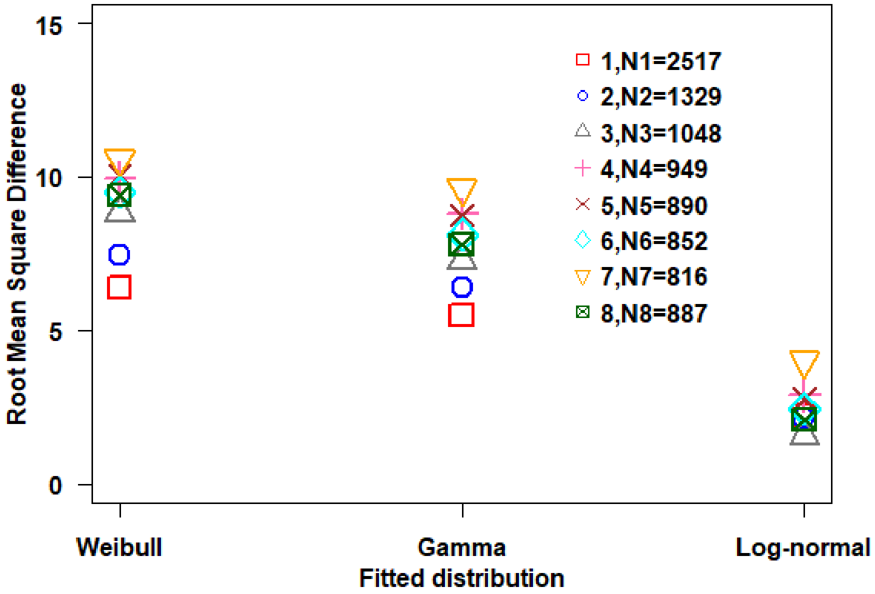

Figure C.9: Performance of three distribution functions fitted to the PDF of the bubble area in terms of the Root Mean Square Deviation (RMSD) (see Eq. (5.3)). Eight different markers are used to indicate the eight (8) separate segments for sample 2.

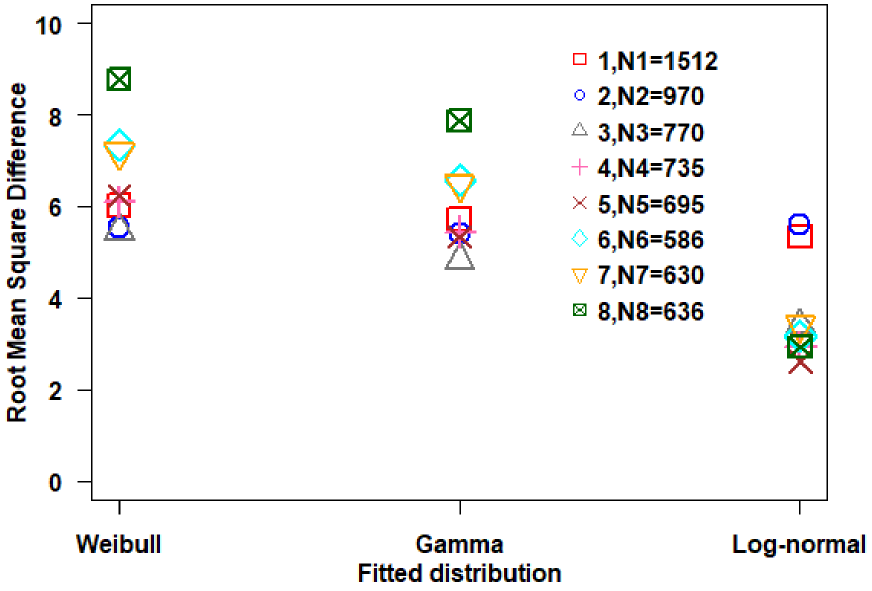

Figure C.10: Performance of three distribution functions fitted to the PDF of the bubble area in terms of the Root Mean Square Deviation (RMSD) (see Eq. (5.3)). Eight different markers are used to indicate the eight (8) separate segments for sample 3.

APPENDIX D

FLAME INSTABILITY AND FLAME AREA

D.1 Flame Instability

The process of flame instability and eventual extinction was studied. Figure D.1 shows a sequence of images for a 6.6 mm thick PMMA sample at a flow velocity of 7.8 cm/s. Each image was extracted 1 min apart from the video. Image brightness was corrected for better visualization. Note that it is difficult to ignite the PMMA sample at the low flow velocities. Therefore, a slightly higher flow velocity was considered to avoid extinction during the ignition process. After the ignition, once the flame begins to spread (right to left) and becomes a uniform flame against the flow velocity the flow velocity is reduced to the desired velocity, $\overline{V}_g$ =7.8 cm/s. The time stamp shown in Figure D.1 is the time when the flow velocity dropped to a desired value which is 7.8 cm/s. It is evident that the flame becomes non-uniform along the bottom edge as the flame propagates over time. Flame flickering can be seen near the bottom edge at time, t = 12 min. This instability contributes to the formation of flamelet at t = 14 min. The flame eventually separates from the bottom edge and becomes very small and weak. The flame finally extinguishes after 17 min of propagation.

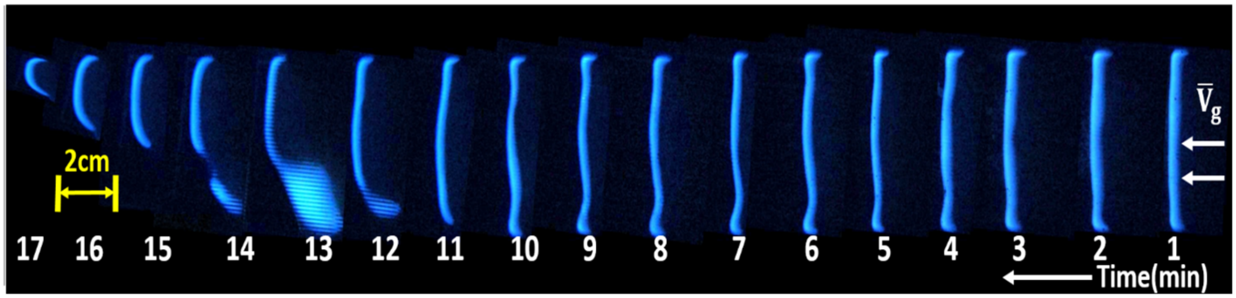

Figure D.1: Image sequence of flame spread at opposed flow velocity, 7.8 cm/s for 6.6 mm thick PMMA.

It is noteworthy that the flame propagation mechanism is different for low opposed flow velocity.

The flame becomes significantly weak and moves away from the fuel surface at low opposed flow velocity. The flame moves outward from surface seeking for oxygen continuously. As the flame moves away from the surface, the heat transfer from flame to the surface decreases primarily by radiation. This causes a very slow flame spread and eventually the flame extinguishes at low flow velocity before reaching out to the other end of the sample.

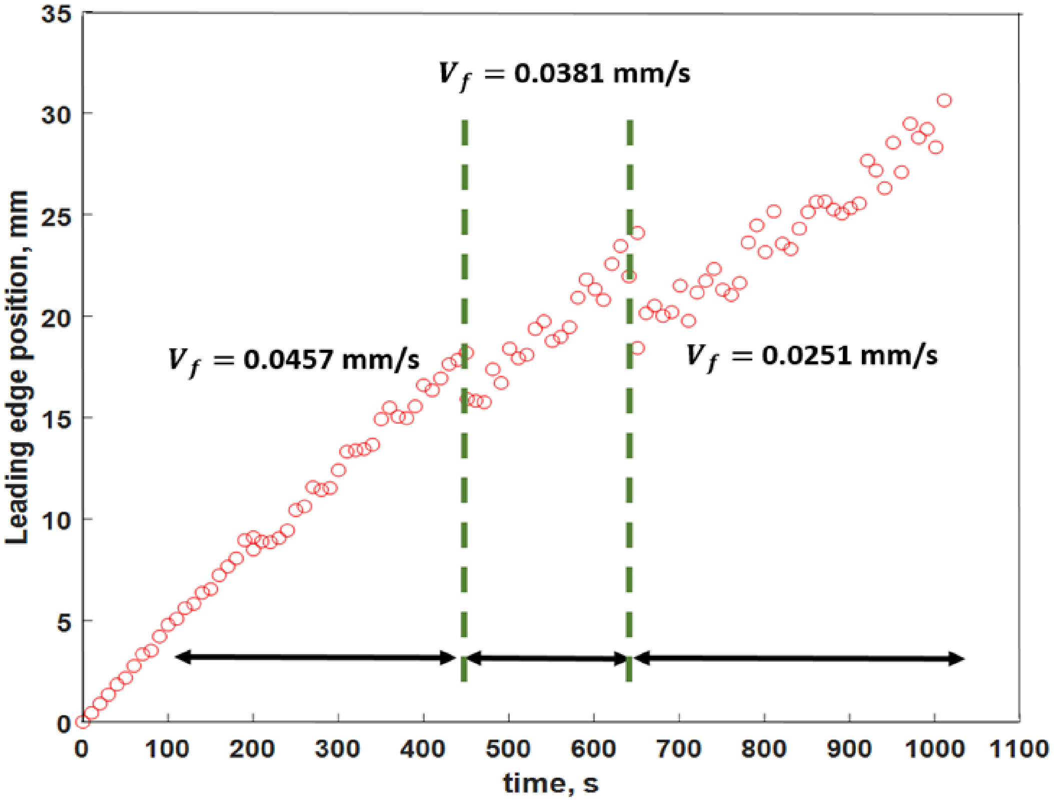

Figure D.2: Leading edge flame tracking as a function of time for 6.6 mm thick PMMA for opposed flow velocity 7.8 cm/s. The flame spread is determined from this tracking and continuous decrement of flame spread is found.

The temporal dependency on flame spread rate estimation was determined by tracking the flame leading edge over time. Figure D.2 shows the flame leading edge position as a function of time for an opposed flow velocity of 7.8 cm/s for a 6.6 mm thick PMMA. The flame tracking sequence starts once the opposed flow velocity becomes settled at 7.8 cm/s and a uniform flame front appears. Initial tracking shows good linearity at the first 100 seconds. As the time increases, the flame tracking shows non-linear behavior over time which is evident in Figure D.2. Unlike, Figure B.1 when the opposed flow velocity was relatively high, the flame tracking showed good linearity.

However, Figure D.2 does not depict linearity as time progresses. It is also observed that, the flame becomes weaker over time and it eventually extinguishes. Figure D.2 can be divided into three distinct regions. The flame spread rate (slope of each region) is calculated in each region by linear regression. A decreasing trend in flame spread is also observed from the result.

The continuous progression of flame becomes weaker (Figure D.2) that contributes to decrease in flame spread rate at low opposed flow velocity. Because of the less availability in oxidizer at low flow velocity, the slow transport of oxidizer to the reaction zone contributes to the formation of weaker flame. Thus, the flame extinguishes by heat losses to the surrounded gas due to a slow reaction rate.

D.2 Flame Area

D.2.1 Measurement Technique

Top videos and high resolution still images were analyzed using the ImageJ and MATLAB image processing algorithm for flame area measurement. Flame area were estimated for a range of opposed flow velocities. Entire test video was tracked for each opposed flow velocity. Figure D.3 (a) shows a sample raw flame image captured from a test video for flow velocity 14.5 cm/s, 24.5 mm thick PMMA. The raw image was then converted into a gray image for further processing which is shown in Figure D.3 (b).

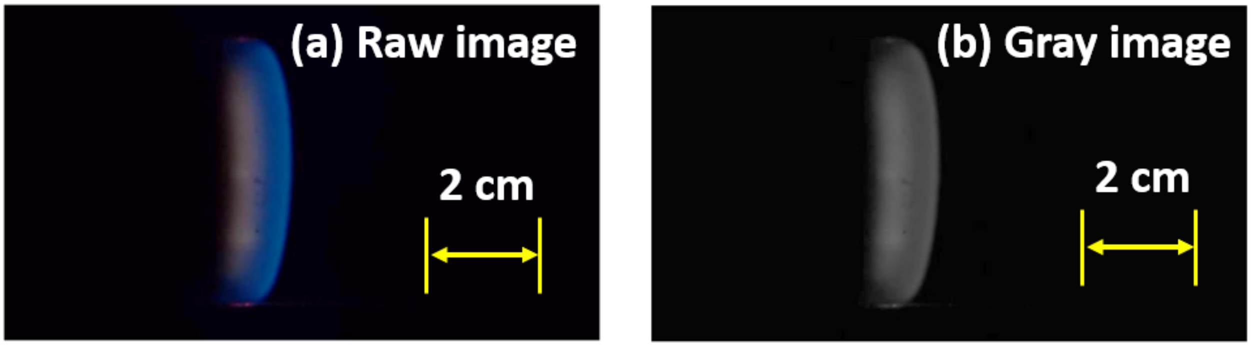

Figure D.3: Image processing for flame area analysis. (a) the raw image recorded from the top. (b) the gray image.

The 8-bit grayscale image have unique set of grayscale values from 0 to 255. By excluding the unique grayscale values that are assigned to the flames, characteristics part of total region and yellow region can be isolated and measured (Figure D.4). Blue flame region is identified by subtracting the yellow region from the total flame region. The evolution in time of flame area were obtained by repeating the process for each frame.

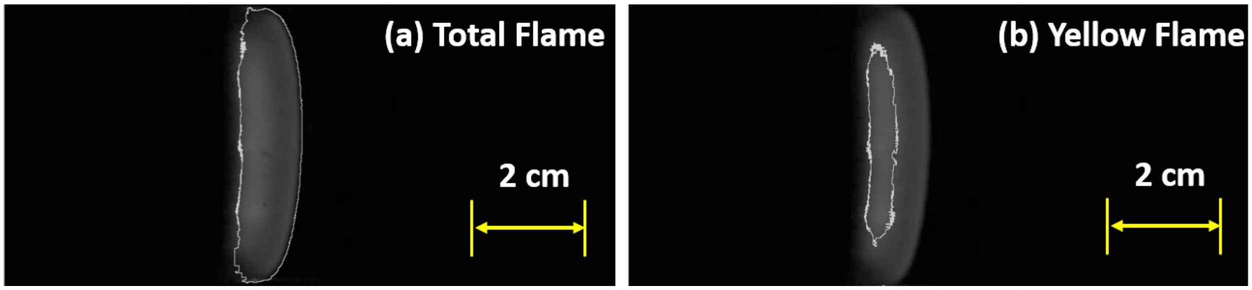

Figure D.4: Image processing for flame area identification. (a) the total flame region. (b) the yellow flame region.

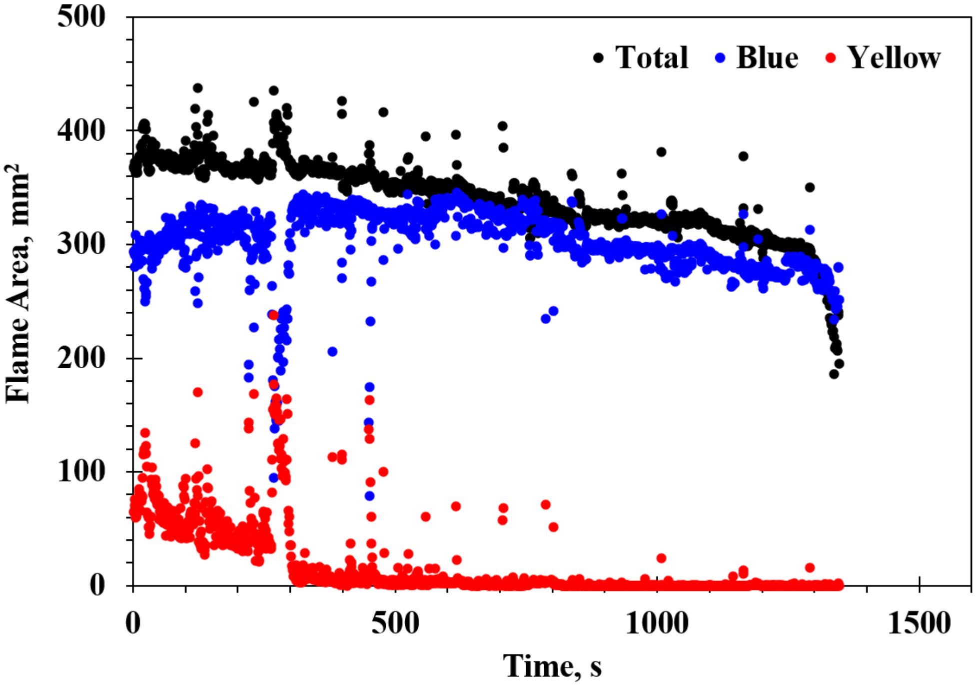

Figure D.5: Flame area vs time for opposed flow velocity 8.2 cm/s. The black, blue and yellow marker represents total, blue and yellow flame region respectively.

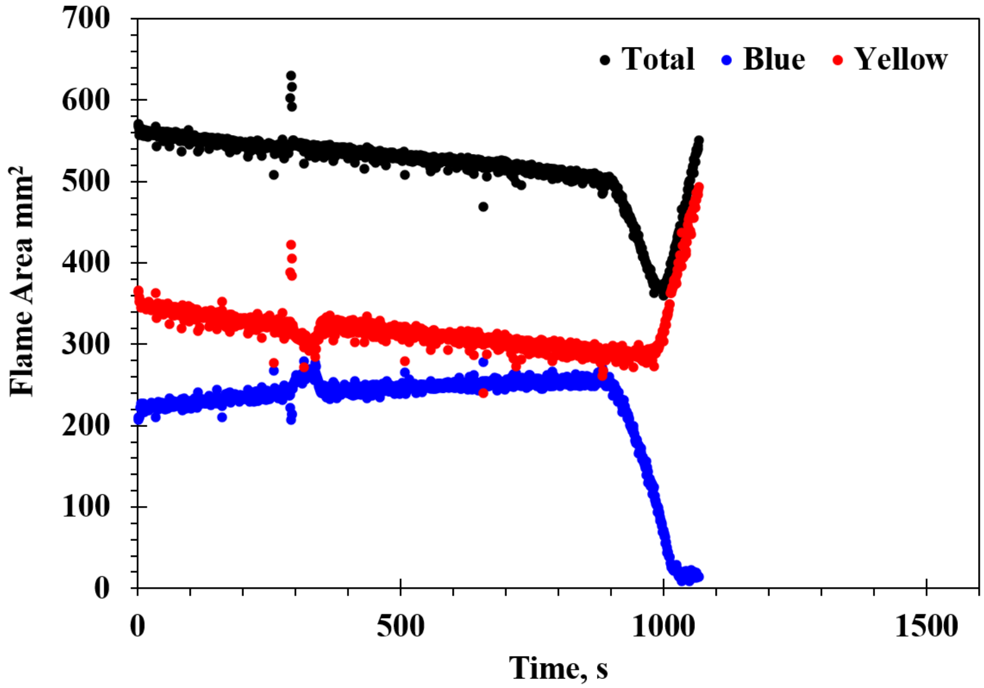

Figure D.6: Flame area vs time for opposed flow velocity 14.8 cm/s. The black, blue and yellow marker represents total, blue and yellow flame region respectively.

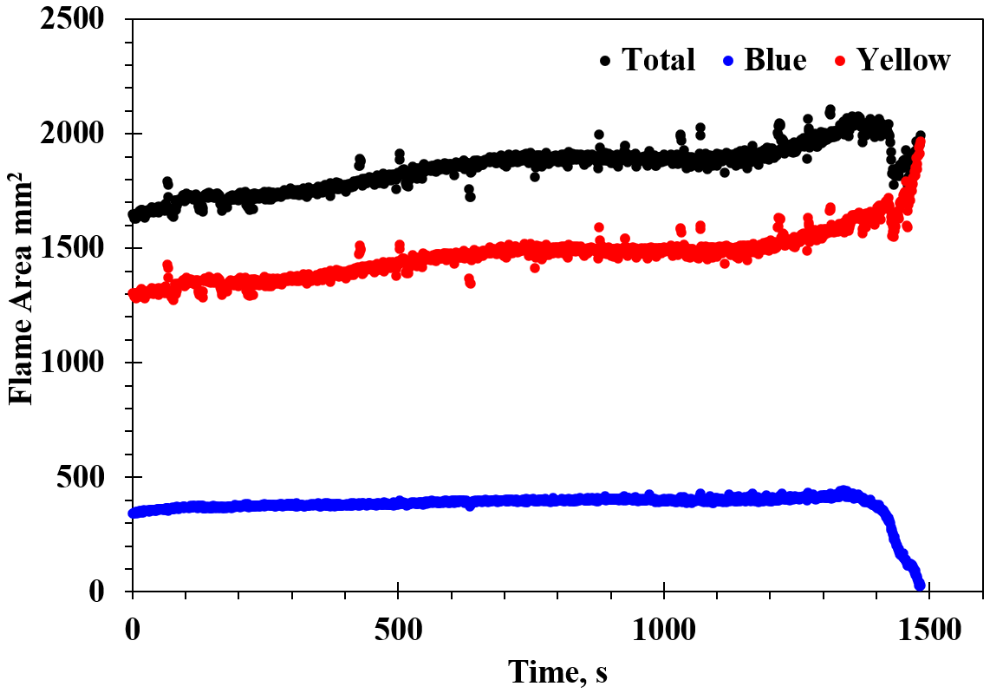

Figure D.7: Flame area vs time for opposed flow velocity 24.5 cm/s. The black, blue and yellow marker represents total, blue and yellow flame region respectively.

D.2.2 Preliminary Results

The analysis shows the evolution of flame areas (total and yellow) with respect to time for 24.5 mm thick PMMA at flow velocities $\overline{V}_g$ = 8.2, 14.5 and 24.5 cm/s. Figure D.5, D.6 and D.7 show results for total flame, blue flame and yellow flame area for flow velocities 8.2, 14.5 and 24.5 cm/s, respectively. A particular flow velocity is used which found effective for ignition of the sample. For these tests, a flow velocity of 15 cm/s is used at the beginning of the test. After few minutes, the flow velocity was set to the desired one. Note that t = 0 is defined at the moment the experiment was set to the desired flow velocity. The final tracking time depends on the test duration. Therefore, the tracking window is different for each opposed flow velocity.

APPENDIX E

CT SCAN MEASUREMENT

An Inveon-PET-CT scanner located at Case Center for Imaging Research (CCIR), CWRU is used to examine the bubble structure of the post-burn PMMA sample. The sample is placed on the CT sample bed and slided into the scanner. The ultimate goal of this work is to assess the topology of the bubbles and measure the bubble volume fraction. In order to achieve the goal, first step is to accurately process the CT scanned images. This author has developed a detail methodology which is presented below.

The scanned image data are in Digital Imaging and Communications in Medicine (DICOM) format. This special type of file format can be read with ImageJ software. The data are imported as an image sequence with 3D reconstruction option. The sample is scanned with a low resolution settings of 84 μm in order to keep the file size manageable. A binning factor of 2 is selected during reconstruction.

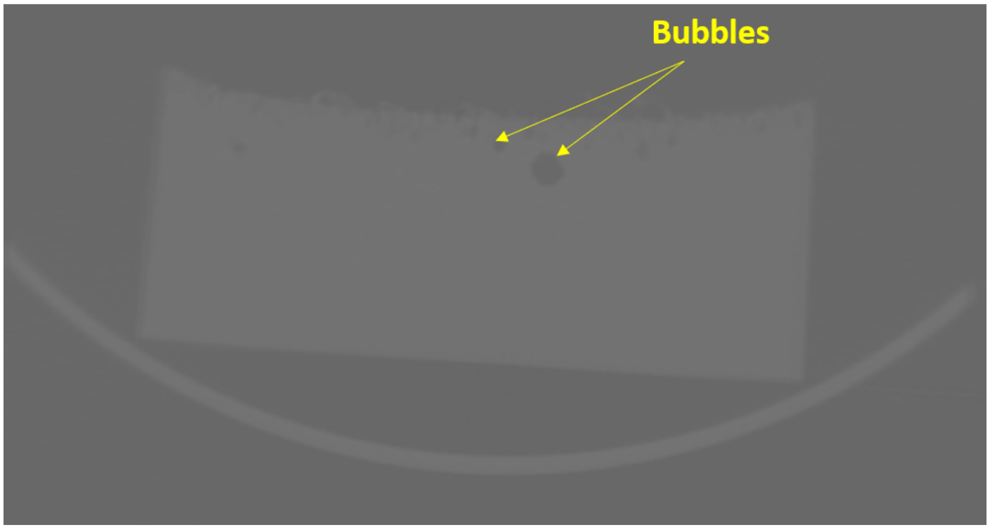

Figure E.1: A cross-sectional view of the CT-scanned post-burn PMMA sample. The light gray part is the PMMA sample which has higher density (1190 kg/m^3) than the dark dots whcih are the bubbles with lower density (1.29 kg/m^3).

The images are 32-bit images with 1024 x 1024 x 1024 pixels. Each pixel represents 0.084 mm x 0.084 mm x 0.084 mm. The 32-bit images are converted to 8-bit images where the gray scale value in between 0 to 255.In a CT scanned image, the grayscale pixel values are representation of the x-ray absorption of the material's density. High x-ray absorption represents high density materials which stands for high grayscale values (bright) and low density materials represents low grayscale values (dark) in the image. The bubble density is substantially lower than the PMMA density. So the bubble will have low grayscale value which can be distinguished from the sample by setting up a thresholding technique. Figure E.1 shows a cross-section of the front view from a 3d constructed system.

BIBLIOGRAPHY

BIBLIOGRAPHY

[1] U.S. Fire Adminstration. *https://www.usfa.fema.gov/data/statistics/*, 2021.

[2] D. Williams. Apollo 1. *https://nssdc.gsfc.nasa.gov/planetary/lunar/apollo1info.html.*

[3] D. Williams. Apollo 13 accident. *https://nssdc.gsfc.nasa.gov/planetary/lunar/ap13acc.html.*

[4] K. Veronese. Mir space station. *https://io9.gizmodo.com/that-one-time-a-fire-almost-destroyed-the-mir-space-sta-5978305.*

[5] J. N. De Ris. Spread of a laminar diffusion flame. *Symposium (International) on Combustion*, 12(1):241 – 252, 1969.

[6] F. A. Williams. Mechanisms of fire spread. *Symposium (International) on Combustion*, 16(1):1281 – 1294, 1977.

[7] A. C. Fernandez-Pello, S. R. Ray, and I. Glassman. Flame spread in an opposed forced flow: the effect of ambient oxygen concentration. *Symp. (Int.) Combustion*, 18(1):579 – 589, 1981.

[8] I. S. Wichman and F. A. Williams. A simplified model of flame spread in an opposed flow along a flat surface of a semi-infinite solid. *Combust. Sci. Technol.*, 32(1-4):91–123, 1983.

[9] I. S. Wichman. A model describing the influences of finite-rate gas-phase chemistry on rates of flame spread over solid combustibles. *Combust. Sci. Technol.*, 40(5-6):233–255, 1984.

[10] I. S. Wichman. Flame spread in an opposed flow with a linear velocity gradient. *Combustion and Flame*, 50:287 – 304, 1983.

[11] I. S. Wichman. Theory of opposed-flow flame spread. *Prog. Energy Combust. Sci.*, 18(6):553 – 593, 1992.

[12] F. P. Incropera and D. P. Dewitt. Fundamentals of heat and mass transfer, 6th ed. 2007.

[13] I. S. Wichman, F. A. Williams, and I. Glassman. Theoretical aspects of flame spread in an opposed flow over flat surfaces of solid fuels. *Symposium (International) on Combustion*, 19(1):835 – 845, 1982. Nineteenth Symposium (International) on Combustion.

[14] M. A. Delichatsios, R. A. Altenkirch, M. F. Bundy, S. Bhattacharjee, L. Tang, and K. Sacksteder. Creeping flame spread along fuel cylinders in forced and natural flows and microgravity. *Proceedings of the Combustion Institute*, 28(2):2835 – 2842, 2000.

[15] K. Pickett, A. Atreya, S. Agrawal, and K. Sacksteder. Burning and suppression of solids – ii fire safety investigation for the microgravity science glovebox. *29th annual meeting of the American Society for Gravitational and Space Research (ASGSR) and the 5th International Symposium on Physical Sciences in Space (ISPS), Orlando, FL*, 2013.

[16] S. L. Olson and P. V. Ferkul. Microgravity flammability boundary for pmma rods in axial stagnation flow: Experimental results and energy balance analyses. *Combust. Flame*, 180:217 – 229, 2017.

[17] S. Bhattacharjee, A. Simsek, F. J. Miller, S. L. Olson, and P. V. Ferkul. Radiative, thermal, and kinetic regimes of opposed-flow flame spread: A comparison between experiment and theory. *Proceedings of the Combustion Institute*, 36(2):2963 – 2969, 2017.

[18] S. Link, X. Huang, A. C. Fernandez-Pello, S. L. Olson, and P. V. Ferkul. The effect of gravity on flame spread over pmma cylinders. *Nature Scientific Reports*, 8(120):2963 – 2969, 2018.

[19] S. L. Olson, U. Hegde, S. Bhattacharjee, J. L. Deering, L. Tang, and R. A. Altenkirch. Sounding rocket microgravity experiments elucidating diffusive and radiative transport effects on flame spread over thermally thick solids. *Combustion Science and Technology*, 176(4):557–584, 2004.

[20] Zero gravity research facility. *https://www1.grc.nasa.gov/facilities/zero-g/.*

[21] S. L. Olson, F. J. Miller, S. Jahangirian, and I. S. Wichman. Flame spread over thin fuels in actual and simulated microgravity conditions. *Combust. Flame*, 156(6):1214 – 1226, 2009.

[22] F. Karmali and M. Shelhamer. The dynamics of parabolic flight: Flight characteristics and passenger percepts. *Acta Astronautica*, 63(5):594 – 602, 2008.

[23] D. Mulville. *NASA-STD-6001*, 1998.

[24] K. E. Lange, A. T. Perka, B. E. Duffield, and F. F. Jeng. Bounding the spacecraft atmosphere design space for future exploration missions. *NASA Johnson Space Center; Houston, TX, United States*, page 53.

[25] I. S. Wichman, L. Oravecz-Simpkins, and S. L. Olson. Design and fabrication of a hele-shaw apparatus for observing instabilities of diffusion flames. *NASA/CP, 210826 2001*, 2001.

[26] S. Hossain, I. S. Wichman, G. W. Sidebotham, S. L. Olson, and F. J. Miller. Influence of gap height and flow field on global stoichiometry and heat losses during opposed flow flame spread over thin fuels in simulated microgravity. *Combust. Flame*, 193:133 – 144, 2018.

[27] S. Hossain, I. S. Wichman, F. J. Miller, and S. L. Olson. Opposed flow flame spread over thermally thick solid fuels: buoyant flow suppression, stretch rate theory, and the regressive burning regime. *Combustion and Flame*, 219:57 – 69, 2020.

[28] J. Pepper, F. J. Miller, S. L. Olson, and I. S. Wichman. A study of the effectiveness of a narrow channel apparatus in simulating microgravity flame spread over thin fuels. *42nd Int. Conf. Environ. Syst. San Diego Calif.*, 2012.

[29] G. W. Sidebotham and S. L. Olson. Microgravity opposed-flow flame spread in polyvinyl chloride tubes. *Combust. Flame*, 154(4):789 – 801, 2008.

[30] B. Comas, A. Carmona, and T. Pujol. Experimental study of the channel effect on the flame spread over thin solid fuels. *Fire Safety Journal*, 71:162 – 173, 2015.

[31] K. Kuwana, K. Suzuki, Y. Tada, and G. Kushida. Effective lewis number of smoldering spread over a thin solid in a narrow channel. *Proceedings of the Combustion Institute*, 36(2):3203 – 3210, 2017.

[32] R. Klimek and T. Wright. Spotlight–8 image analysis software. pages 1–60, 2006.

[33] I. S. Wichman, S. L. Olson, F. J. Miller, and S. A. Tanaya. Experimental evaluation of flame and flamelet spread over cellulosic materials using the narrow channel apparatus. 2013.

[34] S. L. Olson, F. J. Miller, and I. S. Wichman. Characterizing fingering flamelets using the logistic model. *Combustion Theory and Modelling*, 10(2):323–347, 2006.

[35] G. W. Sidebotham and I. Glassman. Flame temperature, fuel structure, and fuel concentration effects on soot formation in inverse diffusion flames. *Combustion and Flame*, 90(3):269 – 283, 1992.

[36] S. L Olson, T. Kashiwagi, O. Fujita, M. Kikuchi, and K. Ito. Experimental observations of spot radiative ignition and subsequent three-dimensional flame spread over thin cellulose fuels. *Combustion and Flame*, 125(1):852 – 864, 2001.

[37] A. C. Fernandez-Pello and T. Hirano. Controlling mechanisms of flame spread. *Combustion Science and Technology*, 32(1-4):1–31, 1983.

[38] C. Huggett. Estimation of rate of heat release by means of oxygen consumption measurements. 4(2):61–65, 1980.

[39] D. Elpidorou, V. Prasad, and V. Modi. Convection in a vertical channel with a finite wall heat source. *International Journal of Heat and Mass Transfer*, 34(2):573 – 578, 1991.

[40] I. S. Wichman. On diffusion flame attachment near cold surfaces. *Combustion and Flame*, 117(1):384 – 393, 1999.

[41] I. S. Wichman, N. Lakkaraju, and B. Ramadan. The structure of quenched triple flames near cold walls in convective flows. *Combustion Science and Technology*, 127(1-6):141–165, 1997.

[42] S. Bhattacharjee and R. A. Altenkirch. A comparison of theoretical and experimental results in flame spread over thin condensed fuels in a quiescent, microgravity environment. *Symposium (International) on Combustion*, 24(1):1669 – 1676, 1992. Twenty-Fourth Symposium on Combustion.

[43] C. Jiang, J. S. Tien, and H. Shih. Model calculation of steady upward flame spread over a thin solid in reduced gravity. *Symposium (International) on Combustion*, 26(1):1353 – 1360, 1996.

[44] S. Bhattacharjee, A. Simsek, S. L. Olson, and P. Ferkul. The critical flow velocity for radiative extinction in opposed-flow flame spread in a microgravity environment: A comparison of experimental, computational, and theoretical results. *Combustion and Flame*, 163:472 – 477, 2016.

[45] Y. T. Liao and J. S. T'ien. A numerical simulation of transient ignition and ignition limit of a composite solid by a localised radiant source. *Combustion Theory and Modelling*, 17(6):1096–1124, 2013.

[46] S. Wang, J. Hu, Y. Xiao, T. Ren, and F. Zhu. Opposed-flow flame spread over solid fuels in microgravity: the effect of confined spaces. *Microgravity Sci. Technol.*, 27:329–336, 2015.

[47] S. Hossain, G. W. Sidebotham, I. S. Wichman, S. L. Olson, and F. J. Miller. Gap height influence on thin fuel flame spread in a narrow channel. *10th US Natl. Combust. Meet.*, 2017.

[48] S. Hossain and I. S. Wichman. Heat transfer optimization in simulated microgravity combustion. *West. States Sect. Combust. Inst. Laram. WY*, 2017.

[49] D. L. Urban, P. V. Ferkul, S. L. Olson, G. A. Ruff, J. Easton, J. S. T'ien, Y. T. Liao, C. Li, A. C. Fernandez-Pello, J. L. Torero, G. Legros, C. Eigenbrod, N. Smirnov, O. Fujita, S. Rouvreau, B. Toth, and G. Jomaas. Flame spread: Effects of microgravity and scale. *Combustion and Flame*, 199:168 – 182, 2019.

[50] R. A. Altenkirch, L. Tang, K. Sacksteder, S. Bhattacharjee, and M. A. Delichatsios. Inherently unsteady flame spread to extinction over thick fuels in microgravity. *Symposium (International) on Combustion*, 27(2):2515 – 2524, 1998.

[51] S. Link, X. Huang, A. C. Fernandez-Pello, S. L. Olson, and P. V. Ferkul. Flammability limits from bass ii testing in microgravity compared to normal gravity limits. *49th Int. Conf. Environ. Syst.*, pages paper ICES 2019–101, 2019.

[52] F. Zhu, Z. Lu, S. Wang, and Y. Yin. Microgravity diffusion flame spread over a thick solid in step-changed low-velocity opposed flows. *Combustion and Flame*, 205:55 – 67, 2019.

[53] T. Matsuoka, K. Nakashima, T. Yamazaki, and Y. Nakamura. Geometrical effects of a narrow channel on flame spread in an opposed flow. *Combustion Science and Technology*, 190(3):409–424, 2018.

[54] T. Matsuoka, K. Nakashima, Y. Nakamura, and S. Noda. Appearance of flamelets spreading over thermally thick fuel. *Proceedings of the Combustion Institute*, 36(2):3019 – 3026, 2017.

[55] F. Zhu, Z. Lu, and S Wang. Flame Spread and Extinction Over a Thick Solid Fuel in Low-Velocity Opposed and Concurrent Flows. *Microgravity Science and Technology*, 28(2):87–94, May 2016.

[56] S. A. Tanaya. Examination of a simulated micro-gravity device for evaluating flame instability transitions and flame spread over thin cellulosic fuels. *MSc Thesis, Michigan State Univ. United States.*, 2004.

[57] H. W. Coleman and W. G. Steele. Experimentation, validation, and uncertainty analysis for engineers 3rd edition. 2009.

[58] S. L. Olson. Mechanisms of microgravity flame spread over a thin solid fuel: Oxygen and opposed flow effects. *Combustion Science and Technology*, 76(4-6):233–249, 1991.

[59] N. Hashimoto, H. Nagata, T. Totani, and I. Kudo. Determining factor for the blowoff limit of a flame spreading in an opposed turbulent flow, in a narrow solid-fuel duct. *Combustion and Flame*, 147(3):222 – 232, 2006.

[60] X. Huang, S. Link, A. Rodriguez, M. Thomsen, S. L. Olson, P. V. Ferkul, and C. Fernandez-Pello. Transition from opposed flame spread to fuel regression and blow off: Effect of flow, atmosphere, and microgravity. *Proceedings of the Combustion Institute*, 37(3):4117 – 4126, 2019.

[61] S. L. Olson and J. S. T'ien. Buoyant low-stretch diffusion flames beneath cylindrical pmma samples. *Combustion and Flame*, 121(3):439 – 452, 2000.

[62] S. L. Olson. Buoyant low stretch stagnation point diffusion flames over a solid fuel,. *Ph.D. Thesis, Case West. Reserv. Univ. United States – Ohio*, 1997.

[63] H. W. Emmons. The film combustion of liquid fuel. *ZAMM - Journal of Applied Mathematics and Mechanics*, 36(1-2):60–71, 1956.

[64] D. B. Spalding. The combustion of liquid fuels. *Symp. (Int.) Combust.*, 4(1):847 – 864, 1953. Fourth Symposium (International) on Combustion.

[65] P. J. Pagni and T. M. Shih. Excess pyrolyzate. *Symp. (Int.) Combust.*, 16(1):1329 – 1343, 1977.

[66] A. V. Singh and M. J. Gollner. Estimation of local mass burning rates for steady laminar boundary layer diffusion flames. *Proc. Combust. Inst.*, 35(3):2527–2534, 2015.

[67] L. Orloff, A. T. Modak, and R. L. Alpert. Burning of large-scale vertical surfaces. *Symp. (Int.) Combust.*, 16(1):1345 – 1354, 1977.

[68] Y. Pizzo, J. L. Consalvi, P. Querre, M. Coutin, L. Audouin, B. Porterie, and J. L. Torero. Experimental observations on the steady-state burning rate of a vertically oriented pmma slab. *Combust. Flame*, 152(3):451 – 460, 2008.

[69] L. Carmignani, B. Rhoades, and S. Bhattacharjee. Correlation of burning rate with spread rate for downward flame spread over pmma. *Fire Tech.*, 54(3):613–624, May 2018.

[70] C. C. Ndubizu, R. Ananth, and P. A. Tatem. Transient burning rate of a noncharring plate under a forced flow boundary layer flame. *Combust. Flame*, 141(1):131 – 148, 2005.

[71] J. David Logan. Applied mathematics: A contemporary approach. *John Wiley, NY*, pages 85–150, 1987.

[72] L. Yang and I. S. Wichman. Theoretical and numerical analysis of a spreading opposed-flow diffusion flame. *Proc. R. Soc. A.*, 465, 2009.

[73] I. S. Wichman. A model describing the steady-state gasification of bubble-forming thermoplastics in response to an incident heat flux. *Combustion and Flame*, 63(1):217 – 229, 1986.

[74] S. L. Olson and J. S. T'ien. Near-surface vapour bubble layers in buoyant low stretch burning of polymethylmethacrylate. *Fire and Materials*, 23(5):227–237, 1999.

[75] K. M. Butler. A numerical model for combustion of bubbling thermoplastic materials in microgravity. *Journal of Fire Sciences*, 2002.

[76] W. Zeng, S. Li, and W. K. Chow. Review on chemical reactions of burning poly(methyl methacrylate) pmma. *Journal of Fire Sciences*, 20:401 – 433, 2002.

[77] S. G. Link. Piloted ignition and flame spread over clear and black pmma cylinders in opposed flows. *MSc. Thesis, UC Berkeley*, 2015.

[78] A. C. Fernandez-Pello and F. A. Williams. Laminar flame spread over pmma surfaces. *Symposium (International) on Combustion*, 15(1):217 – 231, 1975. Fifteenth Symposium (International) on Combustion.

[79] A. Fernandez-Pello and F. A. Williams. Experimental techniques in the study of laminar flame spread over solid combustibles. *Combustion Science and Technology*, 14(4-6):155–167, 1976.

[80] M. Sibulkin and A. G. Hansen. Experimental study of flame spreading over a horizontal fuel surface. *Combustion Science and Technology*, 10(1-2):85–92, 1975.

[81] M. Sibulkin, J. Kim, and J. V. Creeden. Jr. The dependence of flame propagation on surface heat transfer i. downward burning. *Combustion Science and Technology*, 14(1-3):43–56, 1976.

[82] S. R. Ray, A. C. Fernandez-Pello, and I. Glassman. A study of the heat transfer mechanisms in horizontal flame propagation. *J. Heat Transfer*, 102(2):357–363, 1980.

[83] A. Ito and T. Kashiwagi. Temperature measurements in pmma during downward flame spread in air using holographic interferometry. *Symposium (International) on Combustion*, 21(1):65 – 74, 1986. Twenty-First Symposuim (International on Combustion).

[84] A. Ito and T. Kashiwagi. Characterization of flame spread over pmma using holographic interferometry sample orientation effects. *Combustion and Flame*, 71(2):189 – 204, 1988.

[85] K. K. Wu, W. F. Fan, C. H. Chen, T. M. Liou, and I. J. Pan. Downward flame spread over a thick PMMA slab in an opposed flow environment: experiment and modeling. *Combustion and Flame*, 132(4):697 – 707, 2003.

[86] S. Bhattacharjee, M. D. King, and C. Paolini. Structure of downward spreading flames: a comparison of numerical simulation, experimental results and a simplified parabolic theory. *Combustion Theory and Modelling*, 8(1):23–39, 2004.

[87] N. Iqbal and J. Quintiere. Flame heat fluxes in pmma pool fires. *Journal of Fire Protection Engineering*, 6(4):153–162, 1994.

[88] S. I. Stoliarov and R. N. Walters. Determination of the heats of gasification of polymers using differential scanning calorimetry. *Polymer Degradation and Stability*, 93(2):422 – 427, 2008.

[89] Y. Pizzo, C. Lallemand, A. Kacem, A. Kaiss, J. Gerardin, Z. Acem, P. Boulet, and B. Porterie. Steady and transient pyrolysis of thick clear pmma slabs. *Combustion and Flame*, 162(1):226 – 236, 2015.

[90] I. T. Leventon and S. I. Stoliarov. Evolution of flame to surface heat flux during upward flame spread on poly(methyl methacrylate). *Proceedings of the Combustion Institute*, 34(2):2523 – 2530, 2013.

[91] L. Carmignani, F. Lotti, and S. Bhattacharjee. Comparison of flame spread and blow-off extinction over vertical and horizontal pmma samples. *Mechanical Engineering Journal*, 3(6):16–00277–16–00277, 2016.

[92] S. Hossain, I. S. Wichman, S. L. Olson, and F. J. Miller. Opposed flame spread over thick pmma fuel samples in the narrow channel apparatus (simulated microgravity). *11 th US National Combustion Meeting, Pasedena, CA*, 2019.

[93] I.S. Wichman and K. Saito. An experimental study of the effects of gravity on flame spread in high oxygen concentration environments. *Combustion and Flame*, 52:291 – 297, 1983.

[94] T. Kashiwagi and T. J. Ohlemiller. A study of oxygen effects on nonflaming transient gasification of pmma and pe during thermal irradiation. *Symposium (International) on Combustion*, 19(1):815 – 823, 1982. Nineteenth Symposium (International) on Combustion.

[95] T. Kashiwagi. Polymer combustion and flammability—role of the condensed phase. *Symposium (International) on Combustion*, 25(1):1423 – 1437, 1994. Twenty-Fifth Symposium (International) on Combustion.

[96] J. C. Yang and A. Hamins. Combustion of a polymer (pmma) sphere in microgravity. *Third International Microgravity Combustion Workshop, NASA Lewis Research Center, Cleveland, Ohio, April 11-13*, 1995.

[97] J. C. Yang, A. P. Hamins, and M. K. Donnelly. Combustion of a polymer (pmma) sphere in microgravity. *NIST Interagency/Internal Report (NISTIR) - 6331*, 1999.

[98] T. Migita, T. Yamahata, T. Matsuoka, Y. Nakamura, and P. Strempfl. Methodology to achieve pseudo 1-d combustion system of polymeric materials using low-pressured technique. *Fire Technol*, 56:229–245, 2020.

[99] M. C. Johnston. Growth and extinction limits: ground based testing of solid fuel combustion in low stretch conditions in support of space flight experiments,. *Ph.D. Thesis, Case West. Reserv. Univ. United States – Ohio*, 2018.

[100] C. Kumar and A. Kumar. Gravity modulation study on opposed flame spread over thin solid fuels. *Proceedings of the Combustion Institute*, 34(2):2675–2682, 2013.

[101] L. Carmignani, K. Dong, and S. Bhattacharjee. Radiation from flames in a microgravity environment: Experimental and numerical investigations. *Fire Tech.*, 56(3):33–47, June 2020.

[102] A. Vetturini, W. Cui, YT. Liao, S. L. Olson, and P. Ferkul. Flame spread over ultra-thin solids: Effect of area density and concurrent-opposed spread reversal phenomenon. *Fire Tech.*, 56:91–111, June 2020.